MACRO AND MICRO CHARACTERIZATION OF POWDER MIXING PROCESSES

By

JUAN GUILLERMO OSORIO CAICEDO

A Dissertation submitted to the

Graduate School – New Brunswick

Rutgers, The State University of New Jersey

in partial fulfillment of the requirements

for the degree of

Doctor of Philosophy

Graduate Program in Chemical and Biochemical Engineering

written under the direction of

Professor Fernando J. Muzzio

and approved by

_____

_____

_____

_____

New Brunswick, New Jersey

May 2014

ABSTRACT OF THE DISSERTATION

Macro and Micro Characterization of

Powder Mixing Processes

by JUAN GUILLERMO OSORIO CAICEDO

Dissertation Director:

Fernando J. Muzzio, PhD

Powder mixing is a critical operation in pharmaceuticals and other industries. Despite much research, there is still a lack of understanding of the mixing mechanisms, their effects on blend properties, and how these affect the quality of the final product. In addition, commonly used and new batch mixing technologies are not well established to handle the growing number of products involving cohesive and highly potent active pharmaceutical ingredients (APIs).

The work presented in this dissertation focuses on the macro- and micro-mixing characterization of a resonant acoustic mixer (RAM), and the micro-mixing dynamic characterization of bin-blending for pharmaceutical powders, with an emphasis on mixing cohesive APIs. First, the mixing performance of the RAM as a function of processing parameters (acceleration, fill level and blending time) was characterized. Then the effects of the RAM processing parameters on the final blend properties, and tableting

and tablet characteristics were investigated. This was followed by the micro-mixing characterization of blends obtained from the RAM using near-infrared chemical imaging (NIR-CI). In the second part of this dissertation, the micro-mixing dynamics of three APIs, chlorpheniramine maleate (very cohesive), acetaminophen (cohesive) and caffeine (slightly cohesive), were characterized using *in situ* NIR-CI and compared.

Overall, blends in the RAM reached the required blend uniformity (RSD < 5%) in as low as 30 seconds. Resonant acoustic mixing significantly affected the final properties of lubricated blends, increasing their density with increases in acceleration and blending time. These changes in blend properties affected the final properties of tablets by increasing weight, decreasing hardness, and decreasing dissolution. All blend and tablet properties, except hydrophobicity, followed a power law when correlated to the energy per unit mass. The aggregation of the API in the blends decreased with increasing mixing intensity (acceleration) and blending time. In the bin-blending studies, the most cohesive API followed the expected trends (e.g. higher RSDs and larger aggregate sizes), while the trends for APAP and caffeine were dependent on their concentrations. NIR-CI was useful in monitoring the distribution and aggregate size of APIs and excipients, demonstrating agglomeration as a function of cohesion and API concentration in the blends.

ACKNOWLEDGEMENTS

Throughout my time at Rutgers, I was very fortunate to have the support, mentorship, guidance and friendship of many exceptional individuals. First, I would like to thank my advisor, Professor Fernando J. Muzzio, for his guidance, support, and motivation. Fernando, thanks to you, I have not only improved my technical, writing and presentation skills but I have also grown as a person. You have served me as a role model. I, without a doubt, have been highly motivated by your successful career in academia. I also thank the members of my thesis committee, Professor Marianthi Ierapetritou, Professor Rohit Ramachandran and Professor James D. Litster, for their time, support and feedback. It has been a pleasant and rewarding experience working with you these years.

I would like to acknowledge the National Science Foundation's Engineering Research Center for Structured Organic Particulate Systems (ERC-SOPS) and Integrative Graduate Education and Research Traineeship (IGERT) Fellowship Program in NanoPharmaceutical Engineering and Science for providing financial support for this work, and the numerous travel and career-development opportunities. I would like to thank all the academic and industry members and staff involved in the ERC-SOPS. I want to express my gratitude to Dr. Eric H. Erenrich, Dr. Douglas B. Hausner, Mrs. Aisha Lawyrey, and Mrs. Charanjeet Kaur for their help and support throughout the years at Rutgers.

I would like to give special thanks to Professor Rafael Mendez for his help, mentorship and friendship since the beginning of my graduate studies. Rafa, working with you at Rutgers taught me how to be a diligent and independent researcher while working in teams. Thanks for all the advice and help during all these years. I would also

like to express my gratitude to Professor Rodolfo Romañach and his students, Yleana Colon, Eduardo Hernandez, Andres Roman, Indira Jerez, and Jenny Gonzalez. All, Thank you for receiving me in your lab and for your help with NIR spectroscopy, NIR chemical imaging and chemometrics.

I would like to thank all the undergraduate and master students that helped with experimental work during my PhD. I would like to recognize Koushik Sowrirajan and Jonathan Colon for their hard work. Koushik and Jonathan, thank you for your help in the lab and, especially, with writing the articles. I also want to recognize all my colleagues at Rutgers. I am very grateful to have learned a great deal from each of you and to have counted with your friendship. Thanks to Dr. Aditya Vanarase, Dr. Alisa Vasilenko, Dr. Fani Boukouvala, Dr. Yijie Gao, Dr. Atul Dubey, Prof. Kalyana Pingali, Dr. Marcos Llusa, Dr. Athanas Koynov and Dr. Matthew Metzger. A special thanks to those who are still at Rutgers. Thanks to Sara Koynov, Abhishek Sahay, Bill Engisch, Sarang Oka, Pallavi Pawar, Yifan Wang, Krizia Karry, Dr. Heather Emady, Dr. Kellie Anderson, and Dr. James Scicolone. Thank you all for your help in the lab, with NIR, with DEM, with writing and, especially, your friendship. A special mention to Dr. Heather Emady for her help with the revision of parts of this dissertation and postdoctoral fellowship applications.

Last but not least, I want to thank my family and those few friends, who have been like my family, for their unconditional support and trust during my graduate studies. I dedicate my PhD to all of you. Without you in my life, I could not have done this. I specially want to thank my father, Guillermo Osorio, and sister, Claudia Osorio, for always, always being here for me. Only you know what we have been through; it was

your endless encouragement that has made this possible. This is for the two of you. This also goes to my mother, Mirtha Caicedo, and my little sister, Maria Bolaños, for always showing me love and support from far away. I also want to share this accomplishment with my little brother, David Osorio. Maria and David, to serve you as a role model and inspiration is my greatest reward. Finally, I want to thank the greater being, God, for giving me the opportunity to be in the place I am now. "¡Gracias, totales!"

TABLE OF CONTENTS

LIST OF TABLES

LIST OF FIGURES

Chapter 1 Introduction

Powder mixing is one of the most important processes in many industries, including pharmaceuticals, food, catalysts, cement, chemicals, cosmetics, energetics, and plastics, to name a few. The global production of powder-based materials is over ten billion metric tons, most of which requires one or multiple powder mixing stages [1]. The goal of a mixing process is to yield a sufficiently uniform mixture with desired material properties. However, "sufficient" and "desired" depend on the specific industry, the final product and its application(s). In the pharmaceutical industry alone, around 80% of all finished products are manufactured in solid dosage forms composed of powder blends, which commonly undergo more than one mixing step [2]. Surprisingly, despite the prevalence of this process, powder mixing remains a poorly understood process [3] and, up to very recently, most industries neglected its importance and complexity [4]. Most research in powder mixing in the past 20 years has been driven by the pharmaceutical industry and its regulatory agencies [5]. This can be attributed to numerous production batch failures and marketed product recalls, with extensive economic costs, most of which have been caused by unexplained measured variability during mixing [6].

The intricacy of powder mixing processes is caused by several factors. First, powders have complex material characteristics, and chiefly among them, rheological properties [7]. The wide range of material properties such as particle size distribution, particle shape, particle density, surface properties, powder cohesion, and variable bulk density make powder mixing a complicated process. In fact, powders may exhibit solid-like, liquid-like, and gas-like behaviors all in one process (Figure 1-1), depending on the rate of shear, the extent of compaction of the bed, and the geometry in which the bed is

confined [8, 9]. In addition, the high blend uniformity standards required by regulatory agencies and needed to ensure high quality products (especially in pharmaceuticals), make powder mixing a challenging task [10]. To add more complexity to powder mixing processes, the development of highly potent, cohesive active pharmaceutical ingredients (APIs) is becoming increasingly prevalent in the pharmaceutical industry [11, 12]. This requires mixing small amounts of tiny particles (API) within a matrix of much larger ingredients [13].

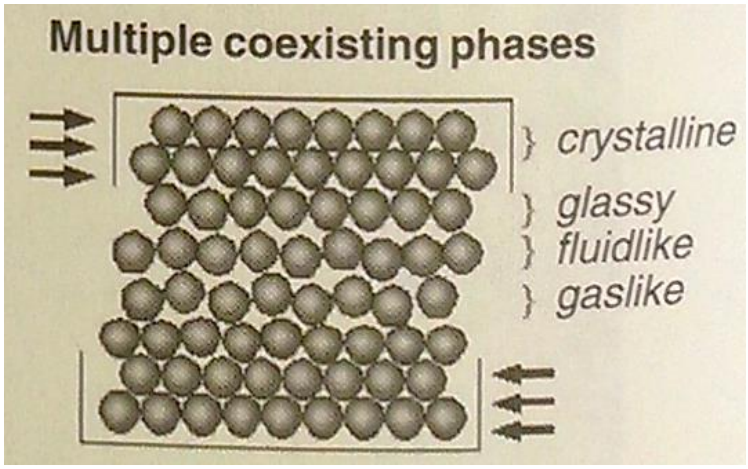

Figure 1-1. Coexisting phases in powder flow behavior and mixing. Crystalline (solid), glassy/fluidlike (liquid) and gaslike. Image taken from [9].

In most situations in practice, powder mixing involves both macro-mixing as well as micro-mixing processes. Macro-mixing focuses on the quantification of the evolving bulk blend uniformity of relevant ingredients. Micro-mixing is the process that describes how particles from different ingredients interact with each other to form a blend with certain properties such as degree of agglomeration [12], segregation [14], cohesion [15], hydrophobicity [16], and electric conductivity [17]. Significant advances have been made in understanding macro (bulk) mixing and segregation of free-flowing particles [18-23]

and, to a much smaller extent, bulk mixing of cohesive powders [24-27]. On the other hand, micro-mixing (e.g. agglomeration) of powder blends have received substantially less attention [28, 29].

Overall, numerous batch blenders, varying in size, geometry and mixing mechanisms have been studied. Out of all types of mixers used in the pharmaceutical industry, the most common are tumble mixers and convective mixers. Tumble mixers induce gentle mixing, reducing the risk of overheating the materials, and are relatively easy to clean [30]. Convective mixers are used for materials that cannot be easily mixed in tumble mixers, such as materials that are prone to segregation or to agglomeration [9]. However, convective mixers often exhibit "dead" spots and can cause over-lubrication issues due to the presence of high shear zones. The mechanisms and performance of these blenders have been investigated and reported in the literature, including V-blenders [19, 20, 23, 27, 31], bin-blenders [3, 18, 24, 30, 31], double-cone blenders [22, 32] and ribbon blenders [2, 33].

Much of the advancement in characterizing powder mixing has focused on determining the bulk efficiency and "mixing curves" (the evolution of a variability index in the concentration of the "critical" ingredient in the blend, typically described using the relative standard deviation of samples, as a function of mixing time) of the aforementioned blenders. To visualize what is meant by the bulk efficiency characterization, a typical mixing curve from a blender is shown in Figure 1-2 [30]. This curve shows a fast-decaying zone (convective mixing) followed by a slower decaying and fluctuating zone in which dispersive mixing of the powder occurs. In all cases, the blend uniformity of the active pharmaceutical ingredients (APIs) and, occasionally, of the

lubricant (magnesium stearate, MgSt) was determined as a function blender design, rotation rate, fill level and fill pattern. While the bulk efficiency determination of commercially available blenders is necessary, it does not guarantee that materials with a wide range of properties will properly mix and yield a high quality blend. In addition, the bulk efficiency does not serve as a complete method to predict the behavior of the final blend in consecutive unit operations.

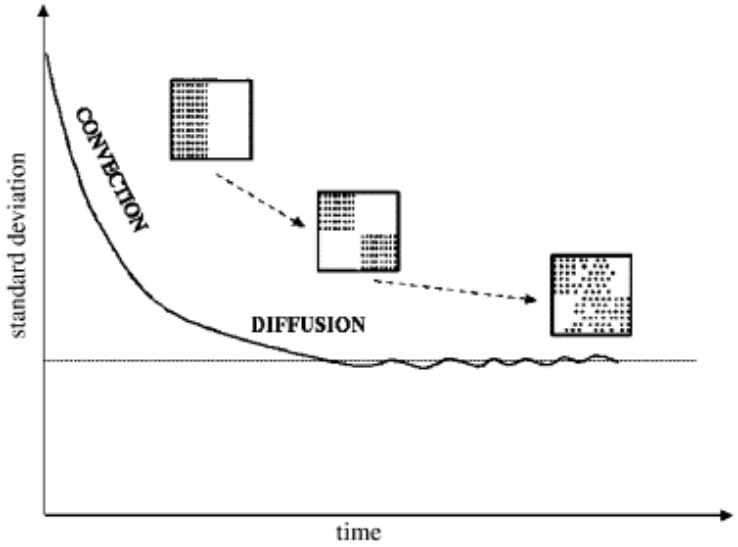

Figure 1-2. Typical mixing curve showing the variability (in this case the standard deviation) as a function of time. The two distinct mixing regimes, convection and diffusion (dispersion), are indicated [30].

Overall, several issues are often encountered during powder mixing, affecting both the properties of final blends and the quality of finished product (e.g. tablets). These issues include, but are not limited to, non-uniformed blends caused by insufficient mixing time or agglomeration [11], poor final blend performance (e.g. flowability [34], segregation [14] and over-lubrication [35]), and poor finished product performance (e.g. tablet hardness and dissolution) [36]. Thus, new technologies that can improve mixing efficiency and performance are of significant interest. However, since introducing new

technologies to such a strictly regulated industry can be difficult, further understanding of the most common processes (e.g. bin-blending) is also critical. The work presented in this dissertation focuses on the macro- and micro-mixing characterization of a new mixing technology, the resonant acoustic mixer (RAM), and the micro-mixing dynamics in a bin-blending process for pharmaceutical powders. This work furthers the understanding of powder mixing of cohesive APIs. Although the work presented in this dissertation is based on pharmaceutical processing, the methods are general and apply to other industries as well.

No studies on the RAM have been reported in peer-reviewed publications for any type of application. The RAM works on the application of low frequency, high intensity acoustic field facilitating the movement of the loose powder mass to induce fast motion and mixing [37]. The RAM can potentially be used to mix low concentrations of potent, cohesive APIs during pharmaceutical product development where the amount of API is limited. In this dissertation, the effects of resonant acoustic mixing on final blend and tablet properties are studied. Micro-mixing studies of blends and tablets from the RAM, and of blends in a bin-blending process are performed using near-infrared chemical imaging (NIR-CI). The work presented here aims to study, characterize, and introduce a new blending technology for pharmaceutical and general powder applications. In addition, micro-mixing dynamic studies in bin-blending add substantial understanding and knowledge of this process.

The three specific aims of this dissertation are as follows:

Specific Aim I: To characterize the macro-mixing performance and effects of resonant acoustic mixing on pharmaceutical powder blends and tablets. This aim characterizes and

analyzes for the first time the macro- (bulk) mixing performance of resonant acoustic mixing by quantifying the blend uniformity of critical ingredients in two studies. The first study considers a fractional factorial experimental design with three APIs (micronized acetaminophen, caffeine, and granulated acetaminophen) varying in material properties in a common blend with three concentrations (3%, 10%, 30% w/w) as a function of mixing parameters (fill level and acceleration) and blending time. The second part of the study uses a full factorial experimental design to fully characterize the macro-mixing dynamics of a cohesive API (3% w/w acetaminophen, APAP) and lubricant (1% w/w magnesium stearate – MgSt) in the resonant acoustic mixing process. These two studies are described in Chapter 3. In addition, the effects of resonant acoustic mixing parameters on the material properties of blends and tablets, obtained from the second part of the study, are considered. The latter is discussed in Chapter 4.

Specific Aim II: To examine the micro-mixing state of blends from resonant acoustic mixing using near-infrared chemical imaging. This aim reports the micro-mixing state of pharmaceutical blends, from a cohesive API blend (3% w/w APAP) and lubricant (1% w/w MgSt), as a function of resonant acoustic mixing parameters. This aim is presented in Chapter 5.

Specific Aim III: To study the micro-mixing dynamics of cohesive active pharmaceutical ingredients in a bin-blending process using *in situ* near-infrared chemical imaging. This aim characterizes the micro-mixing dynamics of three cohesive APIs, categorized as very cohesive (chlorpheniramine maleate), cohesive (acetaminophen), slightly cohesive (caffeine), in a bin-blending process as a function of blend

concentration (3%, 10%, and 30% w/w) and rotation rate. This aim is summarized in Chapters 6 and 7.

Chapter 2 Literature review and technical considerations

In this chapter, a brief summary of important literature on the subjects studied in this dissertation is discussed. Each subsection discusses the significance and novelty of the work being presented here, establishing the conceptual framework of this dissertation. The following sections summarize the fundamentals of powder mixing mechanisms (Section 2.1), powder mixing (including micro-mixing and macro-mixing) in relation to the pharmaceutical industry (Section 2.2), and the importance of material properties of powders and powder blends (Section 2.3).

2.1 Mixing Mechanisms

Recent powder mixing research has focused on characterizing the mixing and mechanisms found in mixers commonly used in a wide range of industries. Three mechanisms have been proposed for powder mixing: convection, dispersion and shear [38]. Convective mixing (macro-mixing) occurs when groups of particles are transported from one location to another by the bulk flow. Dispersive mixing (micro-mixing) refers to the dispersive comingling of individual particles due to velocity fluctuations. Shear mixing, which is also a micro-mixing effect, is caused by slipping planes within the powder bed, provoked by the same external forces (e.g. gravity) that drive convective and dispersive mixing. In most applications, these mechanisms act concurrently and interact in complex ways, and their relative importance is scale-dependent. Thus, the interactions of different mixing mechanisms along with the complex rheological properties of powders make powder mixing a difficult process to predict and control. As an example,

powders are compared to fluids and solids (Figure 2-1) showing that fluids regain their initial state while powders change due to handling [39].

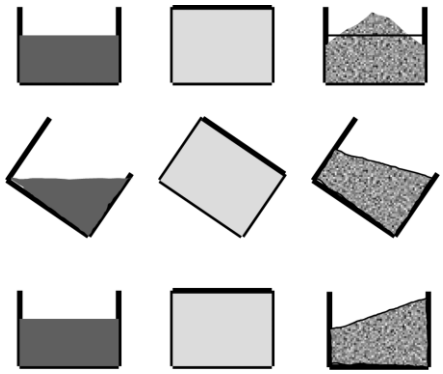

Figure 2-1. Possible process feed formulations. From left to right: a Newtonian liquid, gas and bulk powder. From top to bottom: before, during and after tilting [39].

Depending on the external force that drives the flow (e.g. gravity or shear), one mechanism will usually dominate, but the others will also still occur. For illustration purposes, let us consider the most common mixers used in batch mixing applications by the pharmaceutical industry: tumbling mixers (e.g. V-blenders, tote-blenders and double-cone blenders, shown in Figure 2-2a) and convective mixers (e.g. ribbon and Nauta mixers, Figure 2-2b). Tumbling mixers (gravity driven) have fast convection, while dispersion is much slower. In order to induce higher dispersion in tumbling mixers, asymmetric vessels, internal baffles and/or rotating impellers are used. Convective mixers (agitated mixers) have faster dispersion due to the use of impellers (mechanical means), but might lead to both high shear zones and stagnant unmixed areas, which could affect the final quality of the mixture [9]. Shearing occurs in all types of mixers, especially in convective mixers due to the rapid impeller velocities used. Further characterization of

powder mixtures and mixing mechanisms as related to free-flowing particles and slightly cohesive materials can be found elsewhere [9, 40].

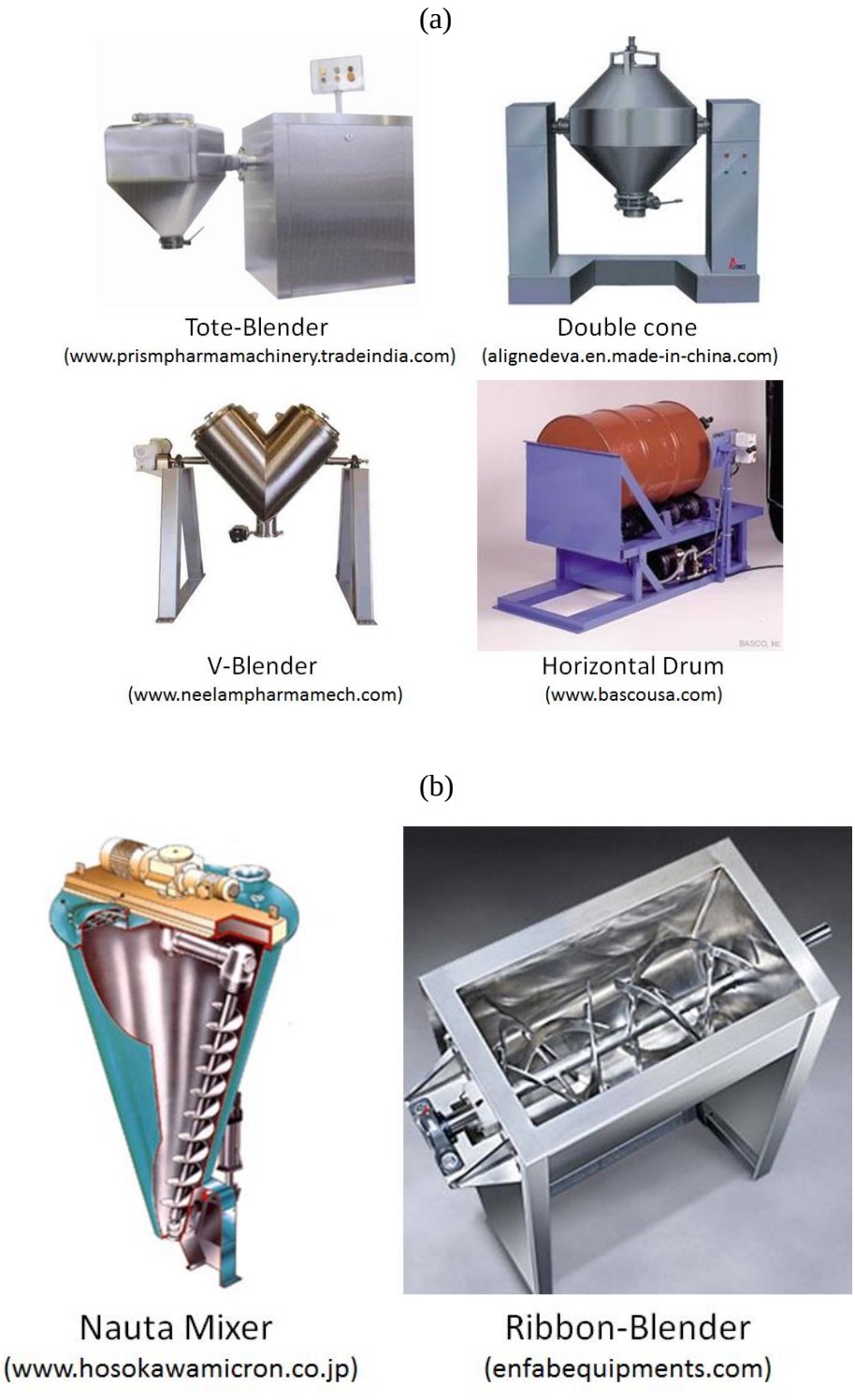

Figure 2-2. Examples of (a) tumbling mixers and (b) convective mixers.

In the work presented in this dissertation, a new type of mixer (resonant acoustic mixer - RAM) and one of the most common tumbling mixers (tote- or bin-blender) used in the pharmaceutical industry are studied. The RAM mixer flow patterns are unknown and should be studied using other techniques (e.g. numerical simulation) that are out of the scope of the objectives of this dissertation. Nevertheless, it is important to recall that the RAM works on a different principle than any commonly used blender in the pharmaceutical industry. The RAM uses resonant vibration to induce fast motion and homogenization of powders. All three mixing mechanisms (convection, dispersion and shear) are expected to be present during resonant acoustic mixing. Diffusive mixing and shearing must be studied using numerical techniques. These mechanisms are most likely caused by the rapid movement (~61 Hz) in the RAM inducing shearing and strong interactions between single and small groups of particles. The bin-blending process studied in this dissertation only considers tumbling and does not use any type of high shear facilitators. This enables to study the effect of API cohesion on the micro-mixing dynamics in the bin-blending process.

2.2 Powder Mixing in the Pharmaceutical Industry

In past decades, powder-based manufacturing has predominantly been done through batch processing. This is particularly true in the pharmaceutical industry, where a series of batch processes (unit operations) are carried out in sequence to convert APIs into products suitable for administration [41]. Although most other industries have been transitioning to continuous manufacturing in the last 30 years, the pharmaceutical industry is still at an early stage in this regard [42]. Batch processing is still predominant, even if some unit operations are intrinsically continuous (i.e., milling, tableting, capsule

filling, roller compaction). The Food and Drug Administration (FDA) has defined batch as "a specific quantity of a drug or other material intended to have uniform character and quality, within specified limits and is produced according to a single manufacturing order during the same cycle of manufacture" [43, 44]. To understand the role mixing plays in this manufacturing order, the most common manufacturing routes in the pharmaceutical industry are considered. These are (in order of prevalence) wet granulation, direct compression and dry granulation [45]. Regardless of the manufacturing route used, powder mixing or blending is always required; usually more than once within a single batch.

For illustration purposes, let us consider the direct compression and wet granulation scenarios. In direct compression, the sequence is as follows: 1) mixing of main components and API, 2) lubrication (mixing) of the blend using a solid lubricant, and 3) compression [46]. Most often, mixing and lubrication are done in a single blender; nevertheless, the mechanisms during the main mixing step and lubrication are largely different [47]. For wet granulation, the sequence is as follows: 1) mixing, 2) wet granulation (mixing), 3) milling, 4) drying (mixing), 5) milling, 6) further mixing, 7) lubrication (mixing), and 8) compression [48]. Hence, mixing is required in several stages throughout pharmaceutical processing, where the powder blend material properties are changing from one unit operation to another, even during storage and/or transport [49].

Generally, in any batch mixing step, a specific total amount of ingredients are mixed in an individual vessel. The ingredients are loaded and agitated for a certain amount of time until a uniform mixture is obtained. Subsequently, the blend is discharged out of the

vessel for the next unit operation (e.g. granulation or compression). But powder mixing, as previously stated, is not a simple process. The mixing mechanisms depend on the material properties of the API and excipients (i.e. any inactive substance in the blend alongside the API), the blender type, and blender operating parameters (such as rotation rate, impeller speed, fill level and filling pattern). For example, the mixing of free-flowing particles substantially differs from the mixing of cohesive particles. Cohesive particles most commonly agglomerate. This is caused by the large attractive interactions (e.g. capillary forces) between cohesive particles [50]. Free-flowing particles do not form aggregates, but they tend to segregate, which is most commonly caused by differences in size and/or density [51]. To remediate these issues, either a tumbling or a high-shear (convective) blender is used keeping in mind that their design and mixing parameters determine their performance.

Next, a brief discussion of how powder blend uniformity (or mixing performance) is characterized followed by a discussion on the Quality-by-Design (QbD) initiative developed by the FDA and adapted by the pharmaceutical industry. Then, a summary of the macro-mixing characterization studies for a variety of blender types and materials is given. At the end of this section, a brief summary of the micro-mixing characterization of powder mixing is described.

2.2.1 Powder Blend Uniformity

Batch powder blending involves both macro-mixing processes as well as micro-mixing processes. Macro-mixing, which has been the emphasis of most recent studies, focuses on the quantification of the evolving bulk blend uniformity of the relevant constituents. Correspondingly, its scale of scrutiny (the sample size) is typically the same

size as the finished product (e.g. a tablet or a capsule) [52]. Good blend uniformity must be achieved to ensure that the right amount of drug is delivered every time. The indicator of blend uniformity (or content uniformity in tablets) is usually the relative standard deviation (RSD) of the concentration of the critical component measured. The RSD can be considered as a good macro-mixing indicator at the scale of scrutiny of the sample size [52].

The RSD is the sample standard deviation of the concentration (s) normalized by the sample mean concentration ($\bar{C}$) of the critical component (e.g. API) measured (Eq. 2-1).

$$RSD = \frac{s}{\bar{C}},\ where\ s = \sqrt{\frac{\sum_1^N (C_i - \bar{C})^2}{N-1}}, \tag{2-1}$$

where C_i is the concentration of sample i and N is the number of samples used in the measurement. The usual criterion used to determine if a blend is "uniform" is that the RSD must be less than 5%. In the case of content uniformity of tablets, the RSD must be less than 6% [53]. Usually, the RSD estimated from a set of samples is different from the true RSD. Provided that sampling error is small, the estimated RSD approaches the true RSD as the number of samples measured increases [54]. Ideally, the estimated RSD is one value within a range of possible RSDs. In general, the number of samples must large enough, unbiased enough, and representative enough to provide an accurate estimate of the true concentration and true blend uniformity of the mixture. In practice, this is an elusive goal that is sometimes not achieved, and is rarely demonstrated.

The determination of the blend uniformity by means of the RSD does not specify anything about the micro-mixing state of the final blend. Blends can have identical macro-mixing states (same bulk concentration and RSD), but differ in the micro-mixing

state, which may result in different product quality and performance (Figure 2-3) [52]. Intuitively, it is expected that a larger energy input should yield better blend uniformity. However, in some cases, this intuition is wrong. Depending on the materials and the geometry of the blender used, de-mixing (segregation) can be induced, sometimes after the most homogeneous blend might have been achieved, occurring after a specific level of total energy input [14]. High-energy inputs might also lead to over-shearing a blend, causing particle attrition and/or over-lubrication, affecting the desired material properties of the final blend and product [55].

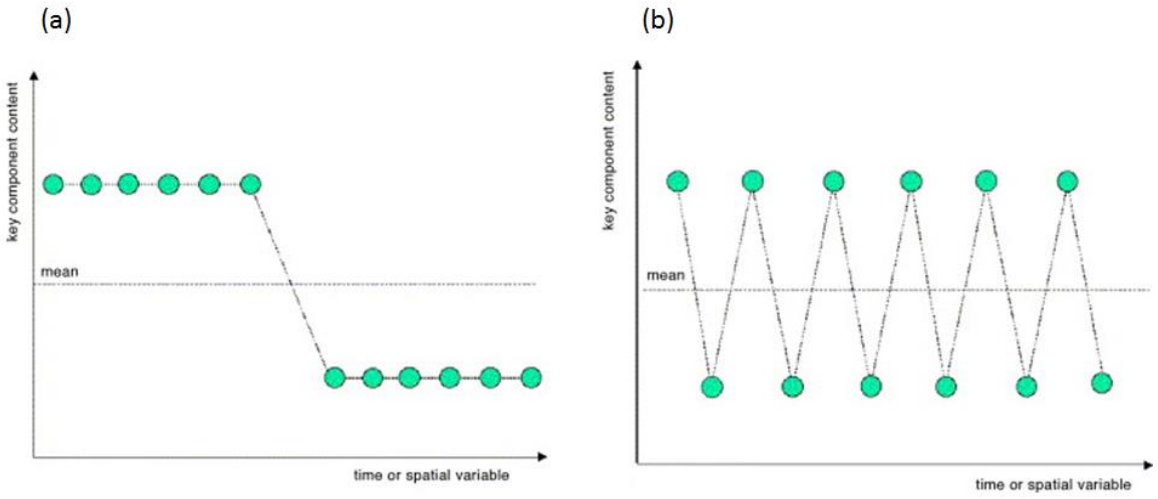

Figure 2-3. Two mixtures (a and b) of equal macro-mixing state can show different micro-mixing states that can affect the final quality and performance [52].

2.2.2 Quality-by-Design

Powder mixing used to be more an art than a science. It used to be empirically "optimized" for the specific formulation under study [11]. Once a specific powder mixing process that yielded the desired blend uniformity and material properties was defined and validated, additional changes to the mixing process were very difficult to implement. This

was due to both the regulatory agencies guidelines, and to the reluctance of pharmaceutical companies to expose themselves to increased regulatory scrutiny and to risk having to repeat expensive clinical studies in case something was changed in the process [52]. Thus, the approach to pharmaceutical manufacturing design was to start with specified raw materials and put them through a non-varying process to "ensure" non-varying final product. Not being able to change the process often led to batch failures without clear causal explanations. In fact, since the process had to remain "unchanged", it could not accommodate variability derived from changes in raw material properties and/or environmental conditions [9]. This compromised quality due to unidentified variability still causes extensive costs for the pharmaceutical industry. It is estimated that expenses of rejected batches, reworked products and extensive investigations of failure consume as much as 25% of some companies revenue [41].

Recently, The FDA reconsidered previous strict guidelines with the recognition that "increased testing does not improve product quality" in fixed processes [55]. Thus, the FDA introduced the Quality-by-Design (QbD) initiative for the development and manufacturing of drug products [56]. QbD describes pharmaceutical quality "as a product that is free of contamination and reproducibly delivers the therapeutic benefit promised on the label to the consumer" [55]. Quality is a function of the API, excipients, manufacturing, and packing. QbD focuses on building quality into a product by achieving a thorough understanding of the process in which it is developed and manufactured, including knowledge of the process risks involved in manufacturing the product and the best possible solutions to reduce or mitigate those risks [57]**.** QbD enables a host of new methods to study and improve pharmaceutical powder mixing. These methods most

commonly include the use of process analytical technology (PAT) tools, such as near-infrared spectroscopy, and design of experiments.

PAT has been defined by the FDA “as a mechanism to design, analyze and control pharmaceutical manufacturing processes through measurement of critical process parameters which affect the critical quality attributes” of the product, in this case powder blends and tablets [58]. For instance, batch powder mixing requires understanding the effect of process parameters on the mixing process itself, on blend uniformity and on the material properties of the final blend and finished product. Therefore, the development, use and implementation of experimental techniques and theories that can predict the final outcome of powder mixing are desired throughout the pharmaceutical industry as well as any other powder-based industry. Such experimental techniques can include the use of in-line NIR as a PAT tool as well as the use of design of experiments to understand the effect of critical process parameters (e.g. blending time, mixing intensity, material properties of API) on the critical quality attributes (e.g. blend uniformity and tablet dissolution).

2.2.3 Macro-mixing Characterization

Powder mixing has been given a great deal of attention in the last two decades. The development of more sophisticated products required greater control and efficiency of this process [59]. Since then, experimental characterization of commercially available and new blenders has been performed by various groups. Much effort was devoted to understanding the mixing and de-mixing of free-flowing particles in many different types of blenders [18-23, 60]. Although substantial knowledge was gained about the mixing mechanisms of such particles in a variety of blenders, many ungranulated pharmaceutical

powders (including APIs and excipients) do not fall into the “free-flow particle” category. Therefore, the past decade saw an increase in studies and understanding of the mixing of slightly cohesive to cohesive materials [3, 24-27, 30, 60]. Most studies have focused on understanding the evolution of the blend uniformity (i.e. RSD) as a function of blending time, blender design and process parameters. Despite this, predictive modeling, control and scale-up of batch mixing is still far from being fully implemented [9].

An example, experimental results in a tote-blender are shown in Figure 2-4 [60]. Here, the RSD is measured as a function of the number of revolutions. Differences in the mixing curves are obtained from variations in the fill level and rotation rate. The results presented in these mixing curves were obtained for free-flowing materials which were loaded side-by-side. The mixing of free-flowing particles is typically independent of rotation speed. One of the most important considerations in tumbling blenders is the loading pattern. When a tumbling blender is symmetrically loaded in a top/bottom fashion versus a side-by-side fashion, the mixing rates are greatly increased. Studies comparing free-flowing particles and cohesive powders concluded that the amount of shear is more important when mixing cohesive powders than free-flowing particles [18]. This consideration must be taken into account when scaling-up/down powder mixing.

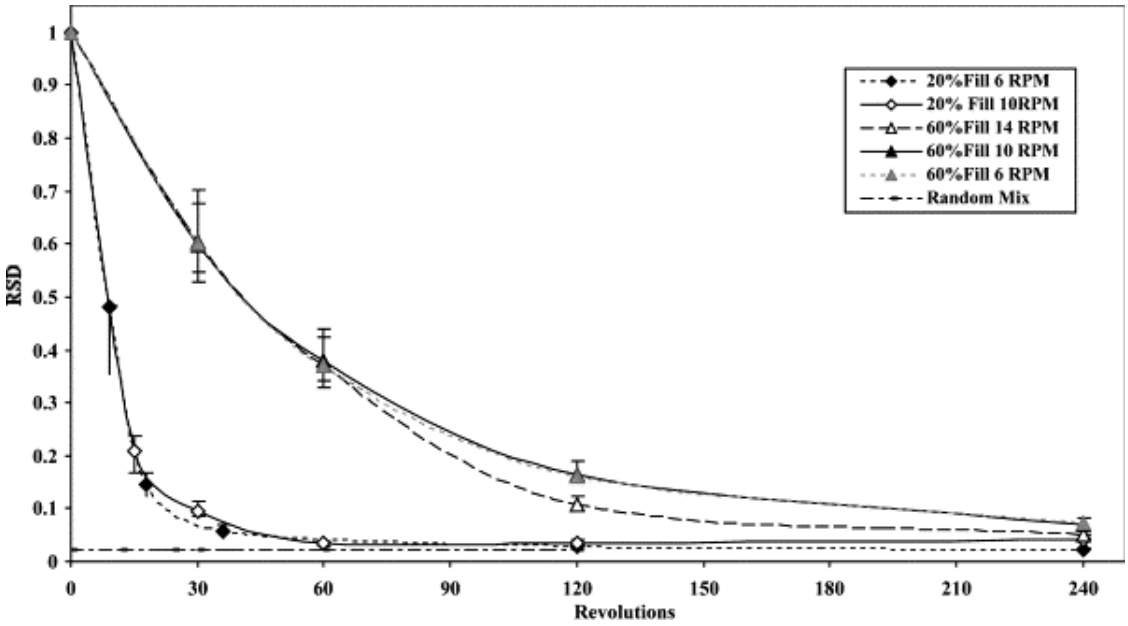

Figure 2-4. Measured mixing curves showing the difference in fill level and rotation rate [60].

Extensive studies on specific blenders have been performed. Most of these studies have been summarized using the aforementioned mixing curves. Such studies have been performed on V-blenders [19, 20, 23, 27, 31], bin-blenders [3, 18, 24, 30, 31], double-cone blenders [22, 32] and ribbon blenders [2, 33]. Since most of the studies have been carried out on different blenders using different materials, the mixing curves cannot be directly compared. Overall, the mixing behavior depends on the design and process parameters, the material properties of the raw materials, and the main mixing mechanism of the blender.

In addition, the mixing dynamics of MgSt have also been characterized in the same fashion [2, 24, 61]. Although useful information was obtained from the macro-mixing characterization, most of the phenomena during the interaction of MgSt, API and other excipients occur at the micro-scale. The small particle size of MgSt (mean particle size = 10 μm) and its low melting point facilitate its coating onto other particles. This is known

to improve the powder flow properties of the blends while serving as a lubricant during compression and ejection of tablets.

In the work presented in this dissertation, the macro-mixing characterization of resonant acoustic mixing was performed using a low concentration of a cohesive API and lubricant. The RAM was characterized as a function of fill level, blending time and acceleration (mixing intensity). Typical mixing curves were measured for both the API and MgSt. As for the bin-blending micro-mixing characterization, the results are compared to typical mixing curves obtained in these types of blenders.

2.2.4 Micro-mixing Characterization

Important advances in understanding the bulk (macro) mixing behavior of pharmaceutical powders have been made within the last few decades. While powder mixing also involves micro-mixing processes, these have been studied substantially less. Micro-mixing is the process that describes how particles from the same and different materials interact with each other to form a blend and to impart it with important properties such as degree of agglomeration [62, 63], cohesion [15], hydrophobicity [16], and electric conductivity [17]. Thus, its proper scale of scrutiny is as small as a particle, and sometimes smaller.

Intuitively, while macro-mixing correlates to total process strain, the phenomena governing micro-mixing should be dependent on both strain and shear rate and therefore should be dependent upon the system scale. Recent research has shown that the mixing order of materials changes the way particles interact with each other at the micro-scale, affecting final blend and tablet bulk properties such as hydrophobicity and dissolution

profiles, respectively [36]. The lack of understanding of how powder blending at the micro-scale works, how particles interact, and how the final arrangement of particles affects subsequent unit operations and final product performance calls for investigations of the micro-mixing of APIs as well as excipients [26, 36]. The micro-mixing characterization of powder blending adds substantial new knowledge and understanding of this process. This is useful both for new product and process development, and to overcome issues that often arise with existing processes.

While the micro-mixing state (i.e. spatial distribution or agglomeration of critical components) of final blends has been characterized in some cases by digital image analysis [64-67] and magnetic resonance imaging [26, 68], these techniques present challenges that have prevented them from becoming common tools in pharmaceutical blending process design. Their “poor” resolution and required color contrast (doping in the case of MRI) to be detectable are limiting factors when studying pharmaceutical powder blends. Most pharmaceutical powders are very similar in color (i.e. white). Scanning electron microscopy (SEM) has also been used to examine single particles; however, this technique is time-consuming, destructive, and may not be representative of the most relevant scales [36]. Thus, a novel technique with high resolution, fast analysis, and ability to examine the concentration and spatial distribution of ingredients in blends and finished product is needed.

In recent years, near-infrared chemical imaging (NIR-CI) has been used to study several pharmaceutical processes and dosage forms. NIR-CI shares all the benefits of NIR (e.g. fast, non-destructive and able to distinguish almost any chemical compound) with the additional insights provided by digital imaging processing. Several articles

explain in detail the principles of NIR spectroscopy and make specific references to its use in the pharmaceutical industry, along with the application of chemometrics to facilitate extraction of relevant information [5, 69-72].

NIR-CI has been used to characterize the distribution of API agglomerates in pharmaceutical blends. The focus of these studies has been in understanding the technique itself, and the chemometric and the univariate or multivariate analysis required [73, 74]. Not much emphasis has been put into understanding powder mixing as a process. NIR-CI was used to characterize the distribution of API agglomerates in pharmaceutical powder blends in small vials [28, 29]. Ma *et al.* compared the mixing curve obtained using NIR-CI and wet chemistry (UV) analysis [29]. Typical and similar mixing behavior was obtained when comparing the results from both techniques. This study also considered the API domain distributions. The frequency of the API domain was measured as a function of aggregate size. El-Hagrasy *et al.* used NIR-CI to monitor mixing in a V-blender [75]. The API quantification using NIR-CI was compared with the results of conventional NIR, but the degree of dispersion of the API (domain size or aggregate size) of the components was not reported. Šašić *et al.* used NIR-CI to study the effect of milling a powder blend before lubrication and compression [76]. The results showed significant agglomeration in blends and tablets from the un-milled process. So far, this has been the only reported study that quantifies the effect of powder mixing on the final blends.

NIR-CI has been used substantially in characterizing the micro-mixing state of pharmaceutical tablets [73, 76-79]. The focus of these studies has also been understanding the chemometric and multivariate analysis [72, 80]. NIR-CI has also been

used to study pellets [81] and films [82]. All of these studies have focused on quantifying the distribution of the API and excipients. All of these studies demonstrate that NIR-CI is a feasible method to study pharmaceutical processing and dosage forms. However, NIR-CI has not been used much to understand powder mixing as a process itself.

The work presented in this dissertation describes studies on the micro-mixing state of pharmaceutical powder blends obtained from a resonant acoustic mixing process using NIR-CI. In addition, the micro-mixing dynamics of three cohesive APIs, varying in flow properties from very cohesive to cohesive to slightly cohesive, were characterized in a bin-blending process using *in situ* NIR-CI, which can be considered a process analytical tool (PAT). The micro-mixing characterization presented here expands the knowledge on powder mixing, both in general, and for the particular processes considered here.

2.3 Material Properties of Powders

Powders exhibit a variety of complex, non-uniform flow patterns [83]. Their state and behavior differ even within the same process. Powders can exhibit gas-like, liquid-like and solid-like behavior depending on the amount of shear and pressure, and particle-to-particle interactions [84]. These complexities are clearly noticeable when mixing different materials with different properties to make a uniform blend. Powder mixing can be as “ideal” as blending 2 identically sized ingredients made of spherical particles, and as “complex” as mixing 20 or more ingredients with a wide range of compositions, particle sizes, and particle shapes. Even the ideal case of mixing two materials can be challenging. While this binary component scenario is unusual in most industrial applications, it is widely used in scientific studies to understand the fundamentals of powder mixing.

Powders have a variety of complex material properties, most notably powder flow. Several powder characterization techniques have been used to understand the material properties of powders and powder mixtures, and to predict and control the performance of mixing processes as well as consecutive processing. Common material properties used to characterize pure powders and powder blends include particle size distribution (PSD) [85], particle shape [86], particle surface properties [87], particle density [88], electrostatic behavior [89] and hydrophobicity (caused by lubricant shearing and smearing during mixing, roller compaction, capsule filling, and compression) [90, 91]. Material properties related to powder cohesion include bulk and tapped density [92], the angle of repose [93], the angle of internal friction [94], compressibility, dilation, flow indexes and flow functions [15, 17, 95].

Powder cohesion significantly affects powder flow. Cohesion has been correlated to the mixing performance of several mixers. For example, in tumbling mixers, large differences are observed between free-flowing materials [18-23] and cohesive materials [24-27]. Free-flowing materials tend to segregate in tumbling mixers, whereas cohesive materials in low concentration tend to agglomerate. It is important to understand that a single material property can seldom describe or predict the behavior of powders in a process; therefore, it is useful to characterize powders using a variety of these material properties throughout processing. Recent work by Vasilenko *et al.* studied and compared various powder flow properties, such as bulk density, compressibility, and flow index, concluding that there are strong correlations among them [95-97]. These correlations are important to choose between powder characterization techniques that measure the “same” property, in most cases cohesion. Understanding how material properties are correlated

and how they change through processing is important to be able to predict and control mixing performance. Although a mixture might be prepared from the "same" materials, lot-to-lot differences in raw materials and processing histories (such as feeding, conveying, delumping and, logically, mixing) [11] often affect final blend properties.

Shear rate (which is proportional to the energy input rate per unit mass) and total strain (which is proportional to the total energy input per unit mass) experienced during blending have been shown to affect the final properties of powder blends [16, 91]. The extent of shear during blending and lubrication often affects powder flow properties. These may vary due to the amount of agglomeration, segregation, dispersion, and/or attrition of the critical ingredients (i.e. API) as well as the smearing of the hydrophobic lubricant and the acquisition of triboelectric charge. Furthermore, the performance of unit operations after blending and the properties of the finished products are also dependent on the rate and extent of mechanical energy dissipation during the blending process. Tableting [36, 91, 98] and capsule filling [99, 100] performance have been shown to be dependent on the powder flow properties of the final blends. In these cases, the variability of tablet or capsule weight is larger for more cohesive powder mixtures. Tablet hardness and dissolution are also affected due to processing variations during blending [36, 91, 101]. Blend hydrophobicity has been back-correlated to the amount of shear rate and total strain experienced, and forward-correlated to longer disintegration and dissolution times in pharmaceutical tablets.

Therefore, understanding the effects of material properties on mixing and the effects of mixing parameters on material properties of blends and finished product is critical. Such studies can be used to effectively design, characterize, and model the blending

process and product performance. For instance, tablets need to have good content uniformity and low weight variability in order to ensure that the dose delivered is the same every time. Content uniformity is a direct indicator of the blending process performance. Weight variability is mainly a function of the powder blend flow properties [98]. Cohesive powder blends tend to yield higher weight variability, although free-flowing blends might present other challenges such as over-flooding and/or segregation, causing deviations in target weight, increases in weight variability and variations in the final dose [102].

Most previous macro-mixing studies have focused on characterizing the mixing dynamics and performance of various blenders for one set of materials with just one model API or powder. In a few cases, the macro-mixing dynamics of materials with different material properties, categorized as cohesive or free-flowing, were compared [9]. These studies have only considered the macro-mixing dynamics of powders with very distinct material properties, but have not compared very cohesive to slightly cohesive powders that are frequently blended in pharmaceutical applications. Most APIs are cohesive in nature and tend to form agglomerates in powder blends. Agglomerates can have a significant effect on product content uniformity, especially at low concentrations ($\leq$ 3% by weight), making it more difficult to obtain an adequately dispersed mixture [11, 12]. On the other hand, as the concentration of the cohesive API is increased, the powder mixing dynamics are governed by the API's flow properties. Hence, in any blending scenario, it is important to consider and understand the effects of the material properties of cohesive APIs.

In the work presented in this dissertation, the API material properties are considered for the studies on resonant acoustic mixing as well as bin-blending. APIs with varying material properties (PSD and cohesion) are considered. The RAM characterization contemplated: 1) three APIs varying in cohesion for blends with low, medium, and medium-high concentrations and 2) one cohesive API in blends with low concentration. The bin-blending characterization considered three cohesive APIs with varying degree of cohesion categorized as very cohesive, cohesive and slightly cohesive in blends with low, medium and medium-high concentrations.

I conclude this chapter by remarking that much progress has been made in recent years in characterizing the macro-mixing state of powder mixtures. The rate of macro-mixing using mixing curves and blend uniformity has been greatly studied. We understand that free-flowing particles are prone to segregation, while cohesive powders are prone to agglomeration. Since segregation occurs in large particle systems, these have been studied using simple imaging techniques [14, 19-21, 68, 103, 104]. Nevertheless, segregation is a metric of the macro-mixing state in which the arrangement of particles or groups of particles determines the blend quality. On the other hand, agglomeration is a metric of the micro-mixing state of the blend that is difficult to study using simple techniques because the particle size is an order of magnitude smaller.

Therefore, to further understand any powder mixing process, the micro-mixing state must be investigated. In addition, the use of ideas from the QbD initiative such as design of experiments and the use of off-line and in-line process analytical technologies (PAT) are advantageous when studying powder mixing. For example, several experimental designs were considered to study the effect of RAM mixing parameters on the final

powder blend uniformity (macro-mixing) and aggregation (micro-mixing) as well as the material properties of the final blends. Since powder blends are not likely to be the final product, the effect of resonant acoustic mixing on tablet properties were also characterized. In addition, the micro-mixing dynamics of cohesive APIs in bin-blending was studied using *in situ* in-line NIR, which could be used as a PAT tool.

Chapter 3 Evaluation of Resonant Acoustic Mixing Performance

3.1 Summary

New technologies that can improve mixing efficiency and performance are of significant interest, in particular for processes that involve cohesive and/or highly potent ingredients [11]. Moreover, for pharmaceutical applications, it is also important to consider the blender's potential for over-lubrication [16, 36], which is usually the result of long mixing times for lubricated blends.

In this chapter, the goal was to evaluate the mixing performance of a new mixer, the Resonant Acoustic Mixer (RAM). This mixer works on a different principle than those commonly used for pharmaceutical processing, using resonant vibration to induce fast motion and homogenization of powders. No work on the RAM had been reported in previous peer-reviewed literature for any type of application. The experimental evaluation carried out in this chapter was divided in two main components. In the first part, the RAM mixing performance was studied as a function of API particle size, fill level, mixing intensity (acceleration) and blending time, using a fractional factorial design of experiments to determine the RAM main effects. The second part was a more detailed study to define the mixing dynamics of both API (acetaminophen, APAP) and lubricant (magnesium stearate, MgSt) as a function of blending time, acceleration, and fill level. The blend uniformity was quantified by estimating the relative standard deviation (RSD) for low concentration of API (APAP, 3% w/w) and lubricant (MgSt, 1% w/w) blend.

It was found that better mixing performance is obtained at higher accelerations and longer mixing times. The fill level for all mixing parameters and materials used did not

show significant effects on the mixing performance. Overall, the RAM is capable of mixing low concentrations of API and lubricant in as little as 30 seconds and 10 seconds, respectively. Longer mixing times at higher accelerations significantly increased the temperature of the powder bed without necessarily improving performance. Resonant acoustic mixing can significantly reduce processing steps and blending time for cohesive APIs, making it a good candidate for improving the efficiency of powder mixing processes.

3.2 Materials and Methods

3.2.1 Materials

The materials used in the first set of experiments reported here were the following: micronized acetaminophen (Mallinckrodt, Raleigh, North Carolina, USA), granulated acetaminophen (Compap-L, Mallinckrodt, Raleigh, North Carolina, USA), caffeine (CSPC Innovation Pharmaceutical Co., LTD., China). Microcrystalline cellulose (Avicel PH 200, FMC Biopolymer, Newark, Delaware, USA) was used as the main excipient. The materials used in the second set of experiments were the following: semi-fine acetaminophen (Mallinckrodt, Raleigh, North Carolina, USA), silicified microcrystalline cellulose (Prosolv HD90, JRS Pharma, Germany), and magnesium stearate (non-Bovine, Tyco Healthcare / Mallinckrodt, St. Louis, Missouri, USA). The nominal particle sizes of the materials used are listed in Table 3-1.

Table 3-1. Materials used for both experimental designs in Chapter 3 with their respective mean particle size.

Material	Mean Particle Size (μm)
Experimental Design 1	
Micronized acetaminophen	18
Caffeine	54
Granulated acetaminophen	195
Avicel PH200	220
Experimental Design 2	
Semi-fine acetaminophen	45
Prosolv HD90	110
Magnesium stearate	10

3.2.2 Resonant Acoustic Mixing

The experimental studies described here were used to characterize the mixing performance of a ResonantAcoutic® Mixer (Resodyn Acoustic Mixers, Butte, Montana, USA). The specific mixer used in the studies was the laboratory scale RAM, or LabRAM (Figure 3-1). The RAM is a new mixing technology that works on the application of low frequency, high intensity acoustic field facilitating the movement of the loose powder mass to induce mixing.

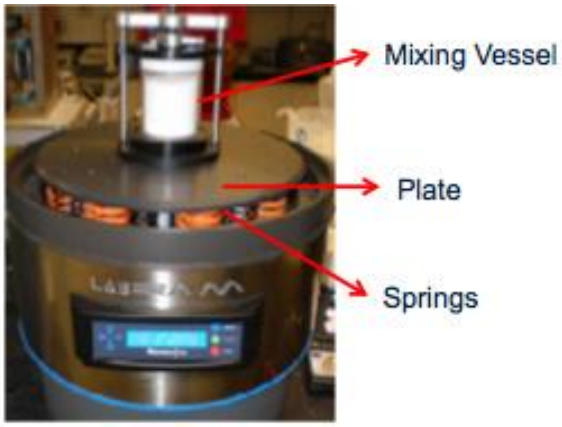

Figure 3-1. Laboratory scale resonant acoustic mixer (LabRAM) with 236-mL mixing vessel used in all experimental studies.

The acoustic mixing principle works on the creation of micro-mixing zones throughout the entire vessel while facilitating bulk movement of the materials (Figure 3-2). The RAM is designed to operate at mechanical resonance, transferring almost all of the mechanical energy created by the mixer to the loose mass in the vessel by the propagation of an acoustic pressure wave. The RAM operates around 60 Hz, defined as the resonant frequency, at which the potential energy stored in the springs can be efficiently transferred to the plates. The principles by which the RAM works are explained in more detail elsewhere [37, 105]. The resonant frequency automatically adjusts by fluctuating constantly around 60 – 61 Hz. The only controllable parameter in the LabRAM is the mixing intensity (0-100%) which determines the amplitude of the mechanical vibration, translating into acceleration values (0-100 g's) depending on the load mass. Therefore in all the experimental work presented here, the acceleration is used (instead of the intensity) for comparison purposes between experiments.

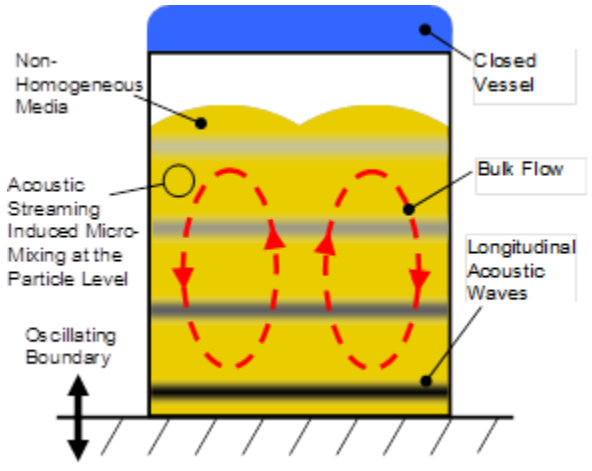

Figure 3-2. RAM mixing mechanisms.

3.2.3 Blending

All experiments were conducted using a 236-mL mixing vessel. Fresh powder and a new mixing vessel were used for each experimental condition. The two experimental designs, along with the blending method used are described next.

3.2.3.1 Experimental Design 1

In order to determine the critical mixing parameters and overall efficiency of the RAM, various concentrations of APIs with varying particle sizes were blended in a common excipient. A 3-level fractional factorial experimental design with 5 factors was used to determine the main effects of mixing parameters in the RAM. A 1/9 fractional factorial design was chosen to decrease the number of experiments from 243 (3^5) to 27 [106]. The process parameters varied were the vessel fill level (25%, 50%, and 75%) and acceleration (30 g's, 60 g's, and 90 g's). The particle size of the APIs (shown in Table 3-1 – Experimental Design 1) was treated as an experimental factor. The API concentration, also treated as an experimental factor, was 3%, 10%, and 30% w/w. Finally the total mixing time (1, 2, and 4 min) was also included in the experimental design. The three APIs used were micronized acetaminophen (APAP), caffeine, and granulated APAP. The excipient used was Avicel PH 200. The final fractional factorial experimental design is shown in Table 3-2. For all experiments here, the API was loaded first (bottom) and the excipient was loaded second (top) into the mixing vessel. This was done to avoid sticking of cohesive API to the top walls of the mixing vessel. RAM accelerates rapidly to its maximum acceleration in a fraction of a second. To avoid

agglomeration, the cohesive APIs (micronized APAP and caffeine) were delumped by passing them through a 20 mesh screen prior to blending.

Table 3-2. Experimental Design 1. A fractional factorial experimental design was used to determine the main effects when blending in the resonant acoustic mixer. Note: Experimental order was randomized.

Fill level (%)	Acceleration (g's)	API	API Conc. (%)	t (min)
25	30	micronized APAP	3	1
50	30	micronized APAP	3	2
75	30	micronized APAP	3	4
25	90	micronized APAP	10	2
50	90	micronized APAP	10	4
75	90	micronized APAP	10	1
25	60	micronized APAP	30	4
50	60	micronized APAP	30	1
75	60	micronized APAP	30	2
25	60	caffeine	3	2
50	60	caffeine	3	4
75	60	caffeine	3	1
25	30	caffeine	10	4
50	30	caffeine	10	1
75	30	caffeine	10	2
25	90	caffeine	30	1
50	90	caffeine	30	2
75	90	caffeine	30	4
25	90	granulated APAP	3	4
50	90	granulated APAP	3	1
75	90	granulated APAP	3	2
25	60	granulated APAP	10	1
50	60	granulated APAP	10	2
75	60	granulated APAP	10	4
25	30	granulated APAP	30	2
50	30	granulated APAP	30	4
75	30	granulated APAP	30	1

3.2.3.2 Experimental Design 2

The mixing performance of the RAM was further evaluated for low concentrations of moderately cohesive API (semi-fine acetaminophen, APAP) and lubricant (magnesium stearate, MgSt). Processing parameters (fill level and acceleration) and total blending time were studied. The blend used in this part of the study was composed of Prosolv

HD90, semi-fine APAP, and MgSt (96%, 3% and 1% w/w, respectively). The experimental design for this part of the study is described in Table 3-3. The blending times were chosen to be able to describe mixing dynamics. This was done using "mixing curves" that describe the evolution of the blend RSD from an initial, completely unmixed state, to the final state where homogeneity is asymptotically maximized. Examination of the blending performance as a function of acceleration was performed for 1 and 2 minutes of blending time to further study this effect. For all experiments here, APAP was loaded first, MgSt was loaded second, and Prosolv was loaded last. This was done to avoid sticking of the APAP and MgSt to the top walls of the mixing vessel. To avoid agglomeration of the cohesive ingredients, APAP and MgSt, were passed through a 20 mesh screen prior to blending.

Table 3-3. Experimental Design 2.

Blending time (min)	Fill level (%)	Acceleration (g's)
0.167	30	20
0.5	60	40
1	90	70
2		
4		
8		
Blending time (min)	Fill level (%)	Acceleration (g's)
1	30	30
2	60	50
	90	80

3.2.4 Sampling

In order to characterize mixing performance, a 1-mL disposable powder thief was used (Sampling Systems, Warwickshire, UK). Ten samples were extracted from the mixing vessel and transferred to scintillation vials (Fisher Scientific, volume: 20 ml,

diameter: 2.5 cm, height: 6 cm). The thief was carefully inserted into the powder bed at each sampling location to minimize perturbations. Since the volume of the mixing vessel was small, each experimental run was started from a fresh blend. This would have prevented any perturbation caused by stopping the blending process and from the excessive sampling. The ten samples were taken from the powder bed in the following manner: around the vessel (8 samples), in the middle (1 sample), and between the wall and the middle (1 sample) as depicted in Figure 3-3.

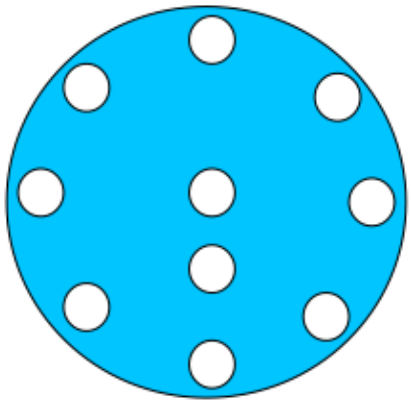

Figure 3-3. Sampling Protocol. Samples were extracted from the powder bed at each location as shown in the top-view schematic of the vessel (picture not to scale).

3.2.5 Near Infrared Spectroscopy

Near-infrared (NIR) spectroscopy was used to quantify the concentration of the API and, where appropriate, MgSt in the samples taken from every experimental condition. In this case, a Nicolet Antaris Fourier Transform Near-Infrared (FT-NIR) spectrometer (Thermo Scientific) was used. The instrument measured the spectrum in the range of 4,000 cm^{-1} to 10,000 cm^{-1} wave numbers. Spectral data, using the diffuse reflectance module, was collected using the software "Omnic" for calibration and experimental

samples in scintillation vials (Fisher), suitable for NIR analysis. The software "TQ Analyst" was used for calibration model development and quantification. The calibration samples were prepared by weighing 500 mg of mixture into the scintillation vials using an Ohaus Explorer analytical balance with an accuracy of ± 0.01 mg (Ohaus, Parsippany, NJ). In all cases, partial least square (PLS) regression methods were used. Different calibration models were developed for the various materials and concentrations used. The PLS models were optimized as to give low errors of predictions and excellent agreement between the calibrated and predicted values ($R^2 \approx 1$). All spectra for all calibration models were mathematically pretreated with a second derivate to minimize particle size and density effects. The descriptions of each model used can be found in Table 3-4. An example calibration model to measure the concentration of semi-fine APAP in the range of 0-7% w/w is shown in Figure 3-4. All other calibration model linear fits were omitted for sake of brevity.

Table 3-4. NIR calibration models description. Root mean squared error of calibration (RMSEC) and prediction (RMSEP) are used as measures for the accuracy of each calibration. Standard normal variate (SNV) and Savitzky-Golay (SG) filtering were used as indicated.

API	Target Concentration (%)	R^2	RMSEC	RMSEP	Concentration Range (%)	Filter	Points
Experimental Design 1							
Micronized APAP	3, 10	0.981	0.361	0.536	0-15	SNV	9, 3
Micronized APAP	30	0.967	0.476	0.650	27-33	SG	7, 3
Caffeine	3, 10	0.996	0.207	0.203	0-15	SG	9, 3
Caffeine	30	0.994	0.218	0.215	27-33	SNV	7, 3
Granulated APAP	3, 10	0.975	0.358	0.596	0-15	SNV	11, 3
Granulated APAP	30	0.986	0.285	0.384	27-33	SG	11, 3
Experimental Design 2							
semi-fine APAP	3	0.992	0.350	0.420	0-7	SG	7, 3
MgSt	1	0.997	0.033	0.088	0-4	SG	7, 3

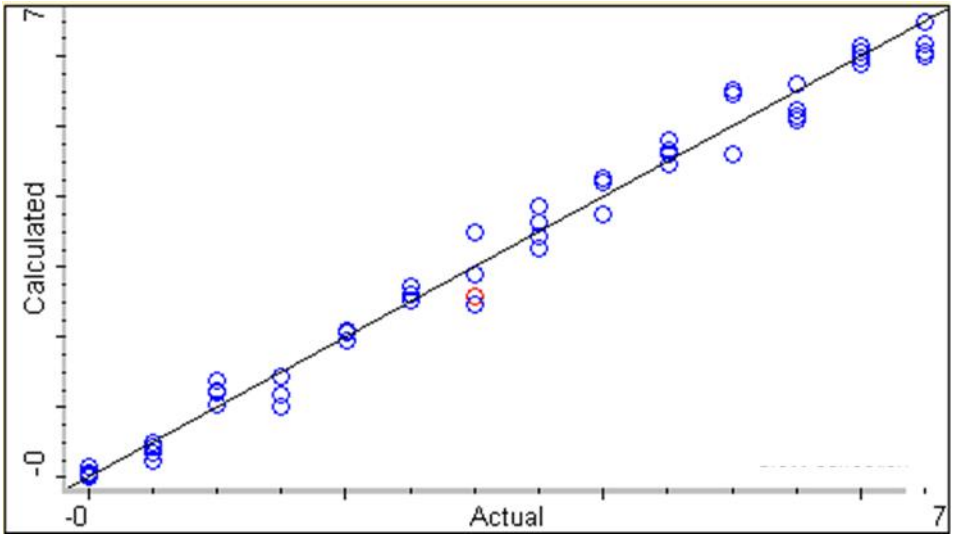

Figure 3-4. Sample NIR calibration for 0-7% w/w semi-fine acetaminophen used in experimental design 2. All other NIR calibration model descriptions are given in Table 3-4. All other calibration model linear fits were omitted for sake of brevity. All calibration linear fits will look very similar to this example.

3.2.6 Mixing performance

The mixing performance was evaluated by measuring the mean concentration of the final blend and the blend uniformity, which was estimated by the relative standard deviation (RSD) of the material of interest. The RSD (eq. 3-1) is defined as

$$RSD = \frac{s}{\bar{C}}, \text{ for } s = \sqrt{\frac{\sum_{i=1}^{N}(C_i - \bar{C})^2}{N-1}} \qquad (3\text{-}1)$$

In the equation above, s is the estimated sample standard deviation of the samples, $\bar{C}$ is the sample mean concentration, C_i is the concentration of sample *i*, and N is the total number of samples. The RSD for each of the experimental runs was calculated from the measured concentration of 10 samples obtained. Since the normalized variance (RSD^2) can be averaged, it was used for the analysis of variance (ANOVA), instead of the RSD, to determine statistically significant processing parameters effects.

3.2.7 Blend Temperature

Preliminary experiments indicated that there was a temperature change when mixing in the RAM. Thus the temperature was measured in the middle of the powder bed using a digital thermocouple (6802II, Shenzhen Handsome Technology Co.) right after each experimental run for "Experimental Design 1".

3.2.8 Energy per unit mass

The total power that goes into the power blend (P_{mix}) is calculated from equation 3-2. This equation was derived empirically by Resodyn Acoustic Mixers and it has a 10% error associated with it [105].

$$P_{mix} = 0.707 F_{rms} \left(\Delta P / 100\right) \left(a_{peak} \cdot G / 2\pi f \right) \tag{3-2}$$

In the equation above, ΔP represents the difference in power intensity from the loaded to the unloaded masses in a typical mixing vessel, F_{rms} is the machine force constant (70 N ± 4 N), G is the gravitational constant, a_{peak} is the peak acceleration experienced at the specific power intensity and f is the frequency (61 Hz) at which the resonant acoustic mixing operates. The force constant (F_{rms}) was empirically derived by the equipment manufacturer by using multiple LabRAM mixers, mixing materials and calorimetry (using energy balance). This value was determined as the root mean square (rms) for the LabRAM mixers and, since it is a machine variable, it does not vary when different materials are mixed [105]. The value of 0.707 is the correction factor from peak to rms.

The total energy that goes into the powder blend per unit mass (E_{mix}) was calculated using the relationship in equation 3-3.

$$E_{mix} = {P_{mix} \cdot t_{mix}}/{m} \quad (3\text{-}3)$$

In the equation above, t_{mix} is the total blending time and *m* is the total mass of the powder blend. The total mass varies depending on the fill level used in the studies performed here. The total energy to the blend per unit mass was calculated and correlated to the mixing performance (blend uniformity of both APAP and MgSt) of the RAM.

3.3 Results and Discussion

3.3.1 Characterization of Resonant Acoustic Mixing Main Effects – Experimental Design 1

The main effects and analysis of variance (ANOVA) of the mixing parameters on mean concentration, blend uniformity (normalized variance – RSD^2) and temperature of the powder bed were analyzed using Minitab 16. The main observations are described next.

3.3.1.1 Blend Uniformity

To measure the main effects on mixing performance (blend uniformity), the normalized variance was used as the blend uniformity indicator instead of the RSD. The variance can be averaged while RSD cannot. Examination of the main effects on the normalized variance (Figure 3-5) shows that the highest variability was obtained when blending caffeine. The variance was the lowest for granulated APAP and a bit higher for

micronized APAP. Granulated APAP is the least cohesive of the three APIs, while caffeine is less cohesive than micronized APAP (which is the most cohesive). This difference in cohesion is the most likely cause of the observed differences in blend homogeneity. Since granulated APAP and Avicel PH200 are similar in particle size and both have good flow properties, a well-mixed blend was obtained from these two materials. The RAM seemed to be mixing the micronized APAP well. A large amount of of energy is transferred during the mixing process, enabling APAP to disperse in the excipient matrix. Caffeine is slightly cohesive, with intermediate flow properties; therefore the difference in particle size from caffeine and Avicel PH200 might be causing some segregation, leading to higher variability. The API type, differing in particle size and cohesion, led to significant differences in the normalized variance ($p = 0.021$).

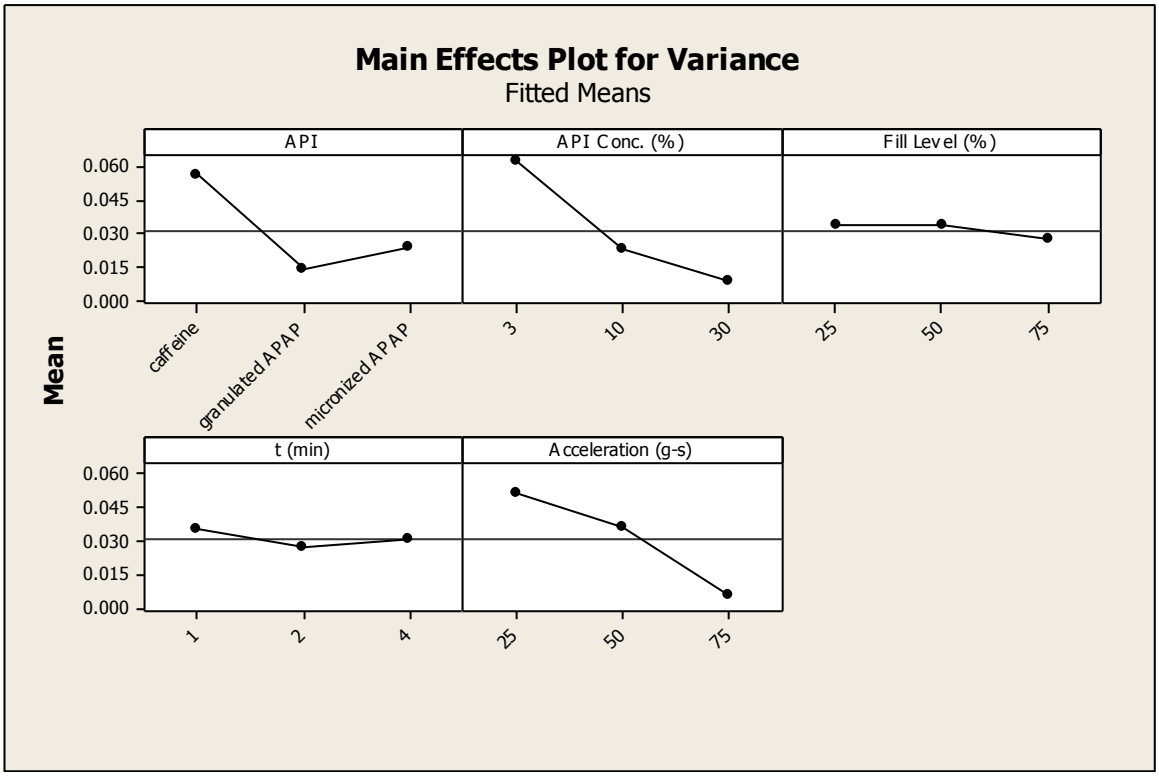

Figure 3-5. Main effects plots on blend uniformity using the normalized variance (Experimental Design 1).

The normalized variance significantly decreased with increasing API concentration ($p = 0.004$). The higher variability for lower concentration of API is a well-known effect that is most likely caused by agglomeration of the more cohesive APIs (micronized APAP and caffeine) and by possible segregation of the free-flowing API (granulated APAP). It is more challenging to disperse homogeneously small amounts of APIs than large amount of APIs in an excipient matrix. The results also indicated that better mixing was achieved at higher blender accelerations ($p = 0.009$). Higher acceleration means that more energy per unit time is dissipated into the mixture. Contrary to what is often observed for both tumblers and convective blenders, no significant differences on the normalized variance were obtained for the different fill levels ($p = 0.825$). The mixing time did not show any significant effect on the normalized variance ($p = 0.829$). In this case, 1 minute of mixing time was sufficient to achieve comparable blend homogeneity for the materials and process parameters used. A complete description of the analysis of variance is given in Table 3-5.

Table 3-5. Analysis of variance for API blend uniformity using the normalized variance for experimental design 1.

Analysis of Variance for Normalized Variance, using Adjusted SS for Tests

Source	DF	Seq SS	Adj SS	Adj MS	F	P
API	2	0.0061738	0.0075322	0.0037661	5.07	0.021
API Conc. (%)	2	0.0121731	0.0120737	0.0060368	8.12	0.004
Fill Level (%)	2	0.0002341	0.0002405	0.0001202	0.16	0.852
t (min)	2	0.0003406	0.0002820	0.0001410	0.19	0.829
Acceleration (g’s)	2	0.0098323	0.0098323	0.0049162	6.62	0.009
Error	15	0.0111471	0.0111471	0.0007431		
Total	25	0.0399011				

S = 0.0272606 R-Sq = 72.06% R-Sq(adj) = 53.44%

3.3.1.2 Blend Temperature

The main effects of process parameters on temperature changes in the powder bed during resonant acoustic mixing were also considered (Figure 3-6). The API type ($p = 0.472$), API concentration ($p = 0.824$) and fill level ($p = 0.206$) did not yield significant differences in the final powder bed temperature. Only changes in the total mixing time ($p = 0.004$) and acceleration ($p \approx 0.000$) caused significant differences in the powder bed temperature. The mean temperature increased with increasing acceleration and longer blending time. Temperature changes must be considered when mixing sensitive materials in the RAM at higher accelerations and longer mixing times. The complete analysis of variance for the temperature of the powder bed after blending is given in Table 3-6.

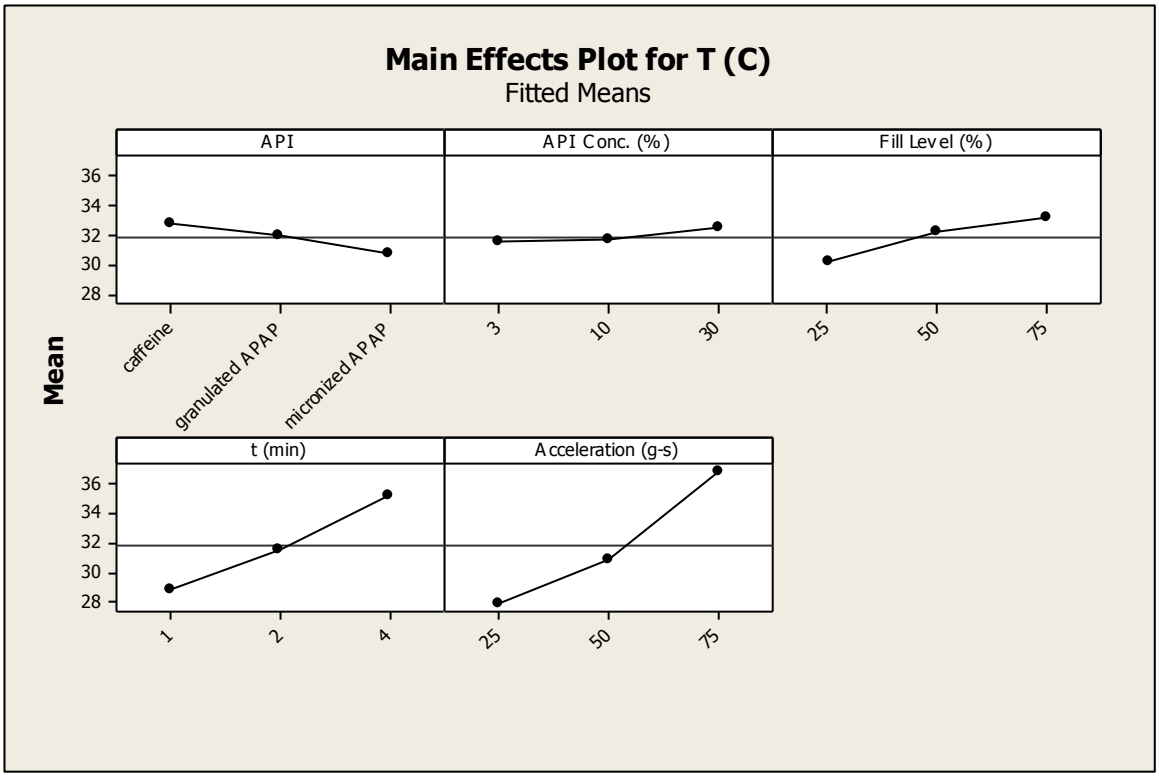

Figure 3-6. Main effects on powder bed temperature after blending (Experimental Design 1).

Table 3-6. Analysis of variance for the powder bed temperature after blending for experimental design 1.

Analysis of Variance for T (°C), using Adjusted SS for Tests

Source	DF	Seq SS	Adj SS	Adj MS	F	P
API	2	25.91	17.74	8.87	0.79	0.472
API Conc. (%)	2	2.85	4.41	2.20	0.20	0.824
Fill Level (%)	2	35.05	39.52	19.76	1.76	0.206
t (min)	2	187.16	187.72	93.86	8.36	0.004
Acceleration (g's)	2	377.52	377.52	188.76	16.81	0.000
Error	15	168.48	168.48	11.23		
Total	25	796.96				

S = 3.35141 R-Sq = 78.86% R-Sq(adj) = 64.77%

3.3.2 Blending profiles – Experimental Design 2

3.3.2.1 Mixing performance as a function of time

In this part of the study, the absolute difference between the target concentration and the measured mean concentration, as well as the blend uniformity (i.e. RSD), of both API and lubricant are summarized. The RAM efficiency as a function of how long it takes to reach the target concentration as well as the final blend uniformity is described. The evolution of the blend mean concentration of the API (semi-fine acetaminophen, APAP) and lubricant (magnesium stearate, MgSt) as a function of time was considered. The mixing curves (RSD vs. time) for the API and lubricant were also studied. Samples were taken at 10 seconds, 30 seconds, and 1, 2, 4 and 8 minutes of blending time to estimate the RSD.

The evolution of the absolute difference between the target concentration and the measured API mean concentration as a function of mixing time for accelerations of 20 g's, 40 g's and 70 g's and 30%, 60% and 90% fill levels is summarized in Figure 3-7. Overall, this difference decreased with increasing mixing time. The measured API composition was significantly dependent on mixing time ($p \approx 0$), as expected. A full

analysis of variance is shown in Table 3-7. The target API concentration is quickly achieved in the resonant acoustic mixer. The time it takes to reach the target concentration is dependent on the mixing time and acceleration. A blending time as low as 10 seconds at higher accelerations was sufficient to reach the target concentration. A higher variability in the measured API concentration was obtained at shorter mixing times.

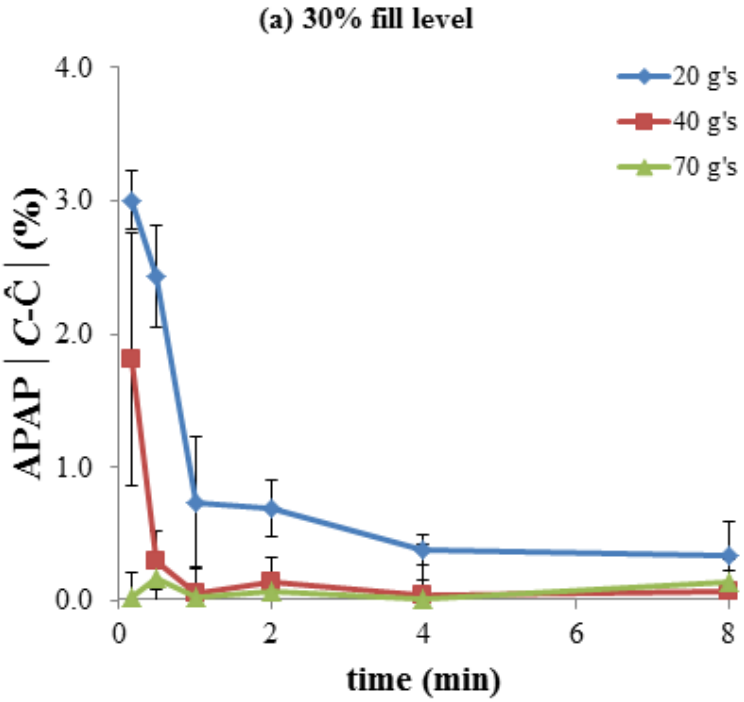

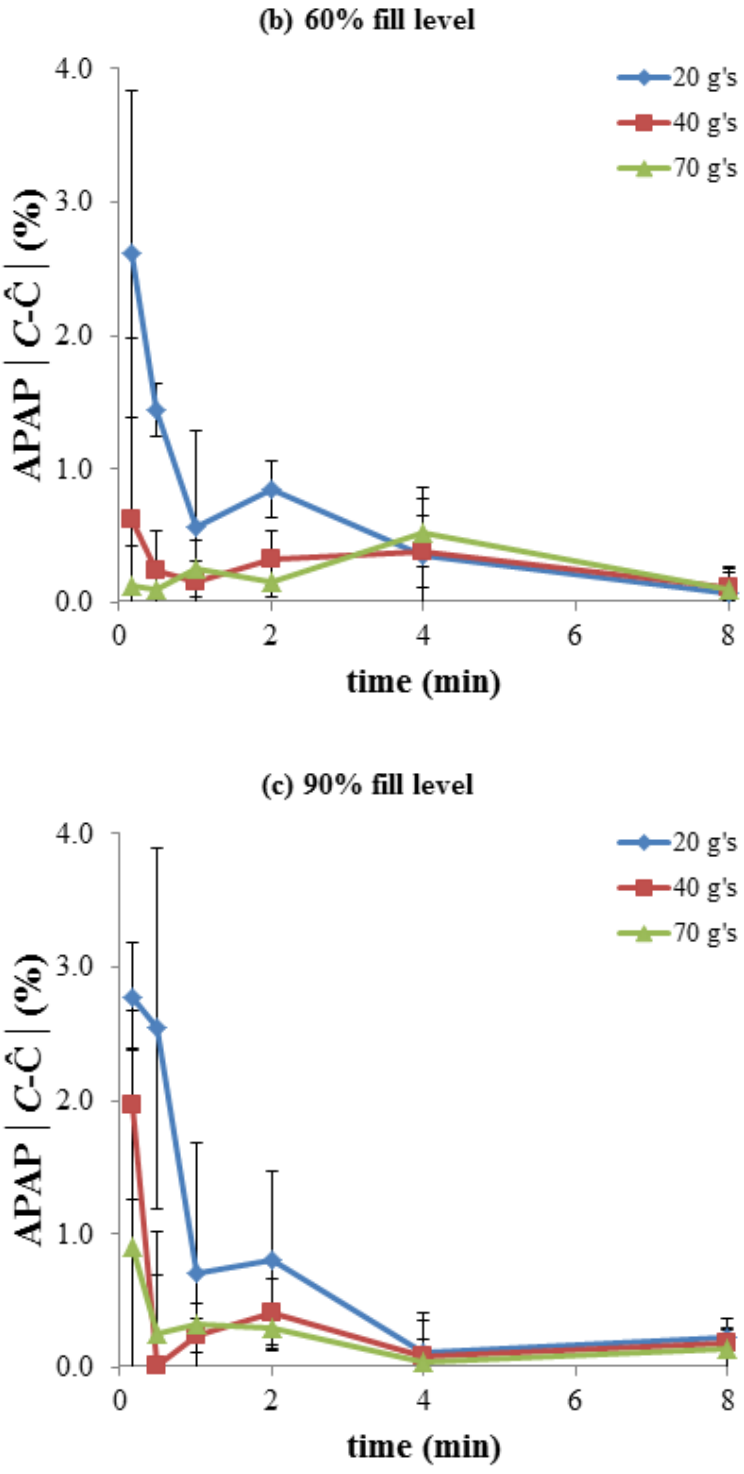

Figure 3-7. Absolute difference between the target concentration (C) and the measured mean concentration (Ĉ) of acetaminophen as a function of time for (a) 30 %, (b) 60% and (c) 90% fill levels for accelerations of 20 g's, 40 g's and 70 g's. Error bars were determined by calculating the uncertainty of the mean concentration of acetaminophen measured at each time point.

Table 3-7. Analysis of variance for the mean API (APAP) concentration for experimental design.

Analysis of Variance for APAP (%), using Adjusted SS for Tests

Source	DF	Seq SS	Adj SS	Adj MS	F	P
t (min)	5	13.1445	13.0839	2.6168	6.52	0.000
Fill level (%)	2	0.0028	0.0030	0.0015	0.00	0.996
Acceleration (g-s)	3	9.1431	9.1431	3.0477	7.60	0.000
Error	44	17.6476	17.6476	0.4011		
Total	54	39.9380				

S = 0.633310 R-Sq = 55.81% R-Sq(adj) = 45.77%

The APAP RSD as a function of mixing time for accelerations of 20 g's, 40 g's and 70 g's and 30%, 60% and 90% fill levels is summarized in Figure 3-8. A complete analysis of variance for the blend uniformity using the normalized variance (RSD^2) is summarized in Table 3-8. For 30% fill level, the APAP RSD decreased with increasing mixing time (Figure 3-8a). A similar trend was obtained for 20 g's and 40 g's; the RSD greatly decreased with increasing blending time. For 70 g's, the changes were not as pronounced indicating that blending at higher accelerations yielded faster homogenization of the API. The RSD results as a function of acceleration are discussed in the following subsection. In some cases, there seemed to be a slight increase in the RSD after longer blending times. Semi-fine APAP is a moderately cohesive API and depending on the initial level of agglomeration, different results can be obtained. Each experiment performed was a new fresh blend every time, thus differences in initial loading can be contributing to the difference in results. Extreme care was used when loading the ingredients for each new experiment to minimize such error. The analysis of variance indicated that blending time ($p = 0.011$) had a significant effect on the blend uniformity, which is captured by the overall trends in the mixing curves.

For the 60% fill level (Figure 3.8b), similar trends were obtained as those for 30% fill level. The RSD decreased with increasing blending time for 20 g's and 40 g's, while for 70 g's it did not change much. Faster mixing was achieved at higher accelerations. For the 90% fill level, the APAP RSD decreased as mixing time increased (Figure 3.8c). For 20 g's, the RSD did not seem to have reached a minimum value, indicating that more homogenization can be obtained if blending for longer time. For 40 g's and 70 g's, a similar trend as for the other fill levels was observed. Physical sampling is limited to a small number of measurements (10 samples), particularly for a small blend size such as the one used here. Thus, individual results might be subjected to experimental error. However, the trends are clear from the multiple conditions examined. Overall, the APAP RSD decreased with increasing mixing time for all fill levels and accelerations studied. Higher accelerations induced faster mixing. The RSD results as a function of acceleration are explained in more detailed in the next subsection.

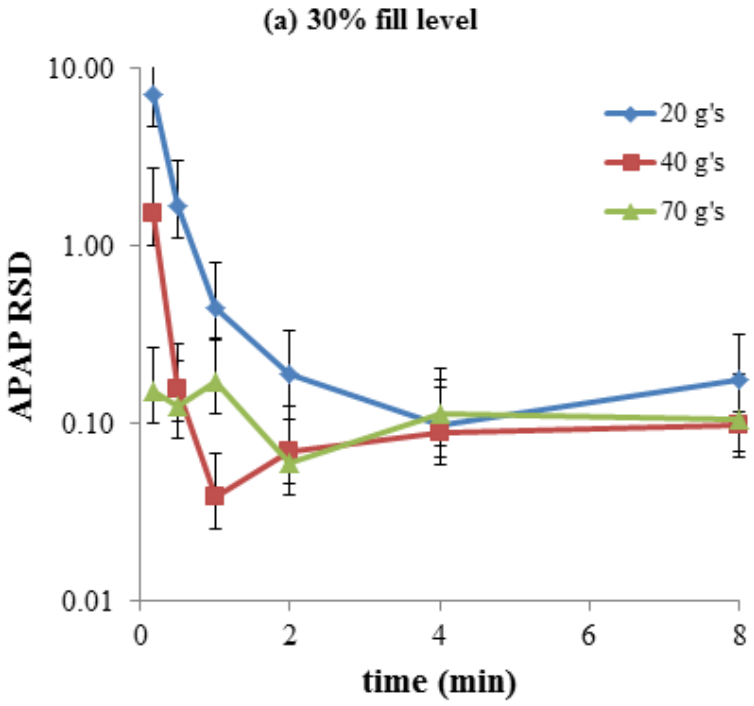

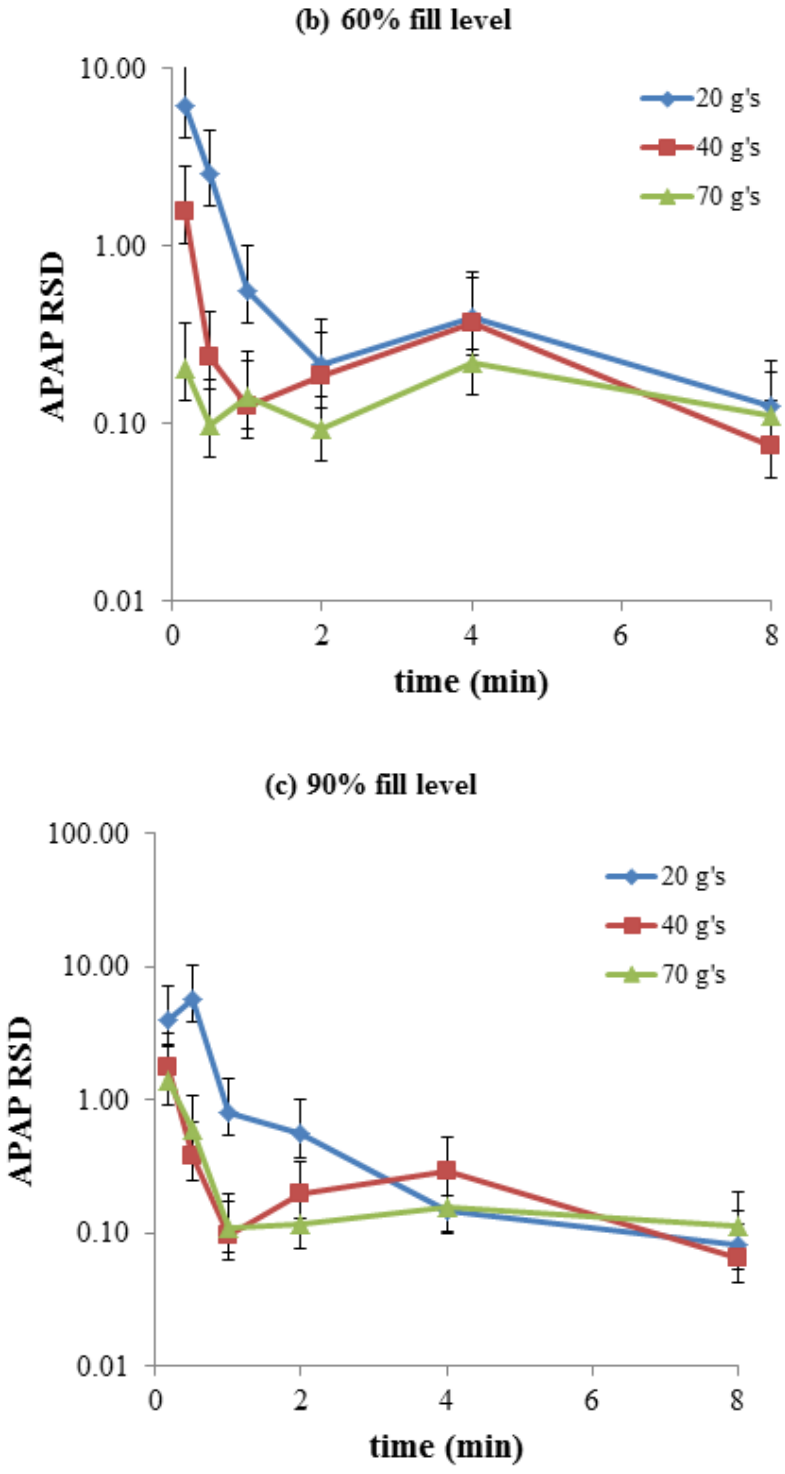

Figure 3-8. Effect of blending time on APAP RSD for (a) 30%, (b) 60%, and (c) 90% fill levels for accelerations of 20 g's, 40 g's and 70 g's. Error bars were determined using the recommendations by Gao et al. to determine the confidence interval of the RSD for a number of samples (N) equals to 10 [54]. Confidence interval used 95% ($\alpha = 0.05$).

Table 3-8. Analysis of variance for API blend uniformity using the normalized variance (RSD^2) for experimental design 2.

Analysis of Variance for RSD² APAP, using Adjusted SS for Tests

Source	DF	Seq SS	Adj SS	Adj MS	F	P
t (min)	5	1253.06	1244.15	248.83	3.43	0.011
Fill level (%)	2	2.70	2.73	1.37	0.02	0.981
Acceleration (g-s)	3	792.16	792.16	264.05	3.64	0.020
Error	44	3191.90	3191.90	72.54		
Total	54	5239.82				

S = 8.51723 R-Sq = 39.08% R-Sq(adj) = 25.24%

The mixing curves obtained are comparable to what is typically obtained using other types of blenders. Lower RSD (better mixing) results were also obtained in the RAM than those when blending the same APAP grade and concentration in similar excipients in other blenders. The mixing curves followed the trend obtained in all powder mixing performance studies considered in all the references presented. Overall the mixing curve (RSD vs. time) has a fast decaying convective mixing stage followed by a slower dispersive mixing stage in which the RSD asymptotically fluctuates around the "possible minimum" value. Such mixing curves were obtained by Mehotra and Muzzio when comparing the mixing performance of uniaxial and biaxial bin-blenders for the same APAP grade and concentration [3]. The results obtained from the reference studies showed that the minimum APAP RSD obtained was above 10% using a similar NIR method to quantify the APAP concentration with a higher number of measurements by extracting approximately 35 samples with a groove sampler. Mixing in the RAM yielded RSDs lower than 10%. This shows that the RAM is a more efficient mixer, when compared to other batch blenders, requiring less mixing time to reach better blend homogeneity.

To illustrate the evolution of lubricant mixing in these experiments, the absolute difference between the target concentration and the measured concentration of MgSt as a function of blending time is shown in Figure 3-9. The target lubricant concentration (1% w/w) was quickly reached in the resonant acoustic mixer. When all the mixing times are considered as part of the same experimental set, the mixing time did not have a significant effect on how fast the target mean concentration was achieved ($p = 0.644$). The analysis of variance for the mean MgSt concentration is summarized in Table 3-9. Overall, the mixing of lubricant in the RAM is a fast process.

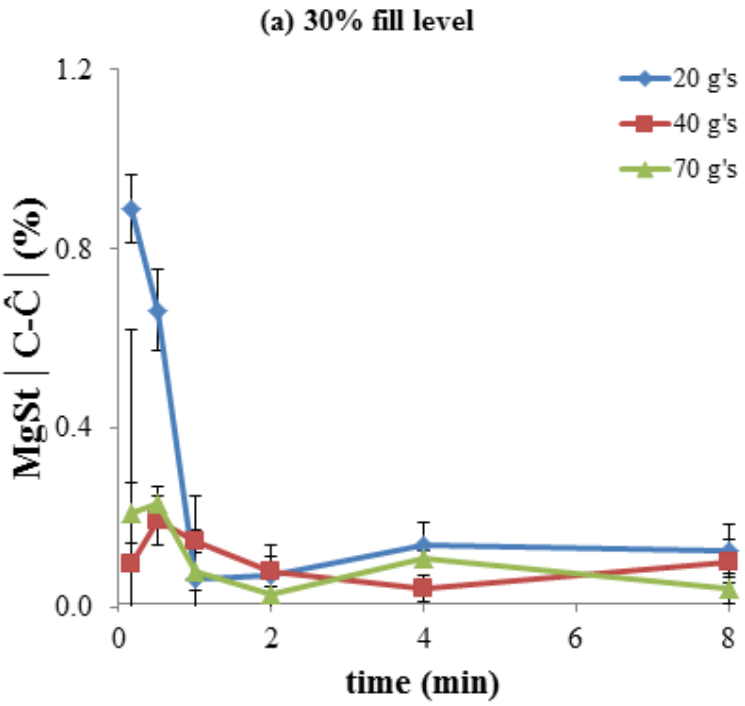

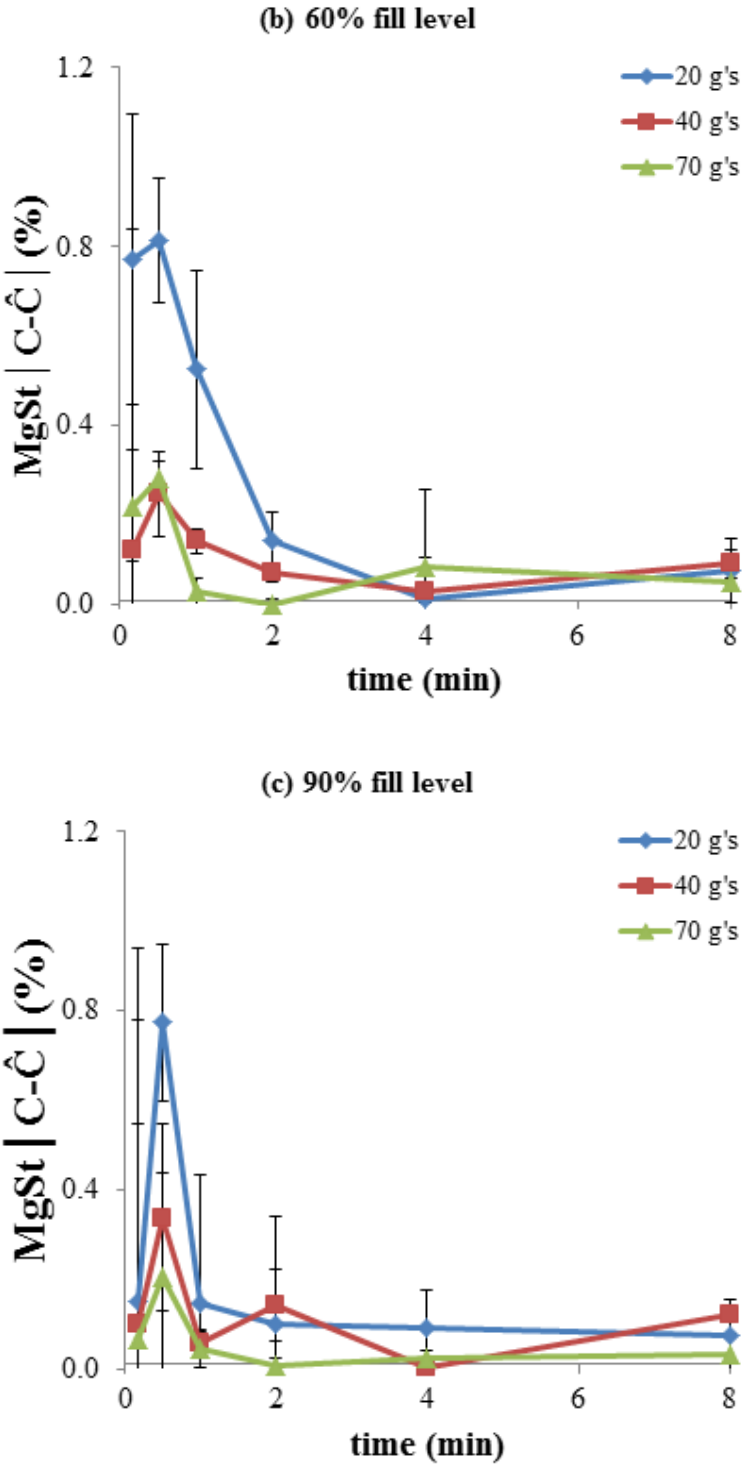

Figure 3-9. Absolute difference between the target concentration (*C*) and the measured mean concentration (Ĉ) of MgSt as a function of time for (a) 30 %, (b) 60% and (c) 90% fill levels for accelerations of 20 g's, 40 g's and 70 g's. Error bars were determined by calculating the uncertainty of the mean concentration of magnesium stearate measured at each time point.

Table 3-9. Analysis of variance for the mean lubricant (MgSt) concentration for experimental design 2.

Analysis of Variance for MgSt (%), using Adjusted SS for Tests

Source	DF	Seq SS	Adj SS	Adj MS	F	P
Time (min)	5	0.21478	0.21018	0.04204	0.68	0.644
Fill level (%)	2	0.02059	0.01819	0.00909	0.15	0.864
Acceleration (g-s)	3	1.08954	1.08954	0.36318	5.84	0.002
Error	44	2.73613	2.73613	0.06218		
Total	54	4.06103				

S = 0.249369 R-Sq = 32.62% R-Sq(adj) = 17.31%

The blend uniformity of MgSt was also considered as a function of time. At 30% fill level (Figure 3-10a), the MgSt RSD decreased with increasing mixing time for all accelerations studied, although it seemed to slightly increase after 8 minutes of blending. Similar behavior is obtained for 60% fill level (Figure 3.10b) and 90% fill level (Figure 3.10c). The RSD decreased with increasing blending time for all three accelerations studied. The analysis of variance for the MgSt blend uniformity using the normalized variance (RSD^2) is summarized in Table 3-10. The mixing time yielded significant differences in the MgSt blend uniformity, confirming the differences in the mixing curves results ($p \approx 0.000$). The MgSt RSD was estimated to understand the mixing profiles when blending the most common used lubricant (MgSt) in pharmaceutical formulations. Although a 5% RSD is indicated for APIs, an expected value for MgSt is not established. In practice, the MgSt RSD of 8-12% is typically sufficient to achieve the purpose of lubricating a blend. A lower MgSt RSD might be an indication of over-lubrication and can affect the final properties of the blends (e.g. flowability) and the tablets (i.e. hardness and dissolution) [91].

(a) 30% fill level

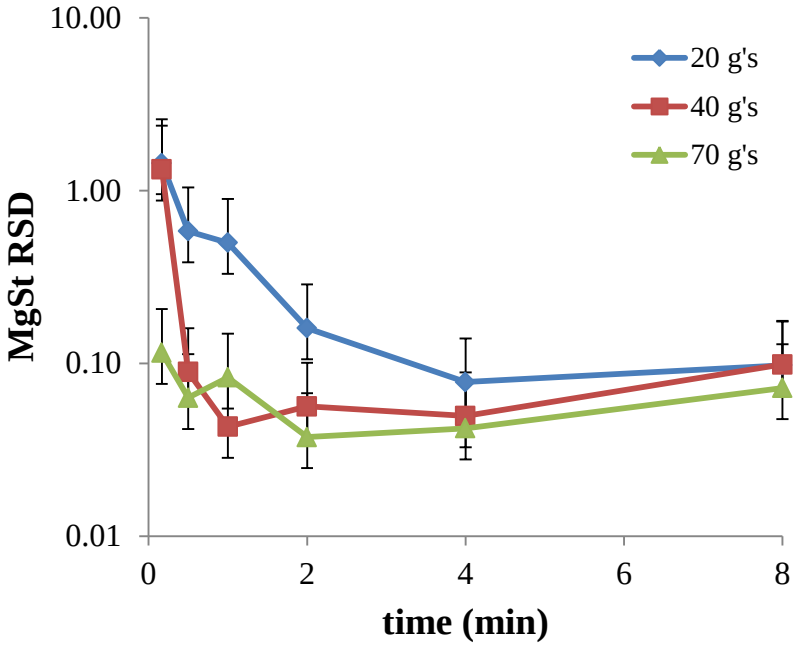

(b) 60% fill level

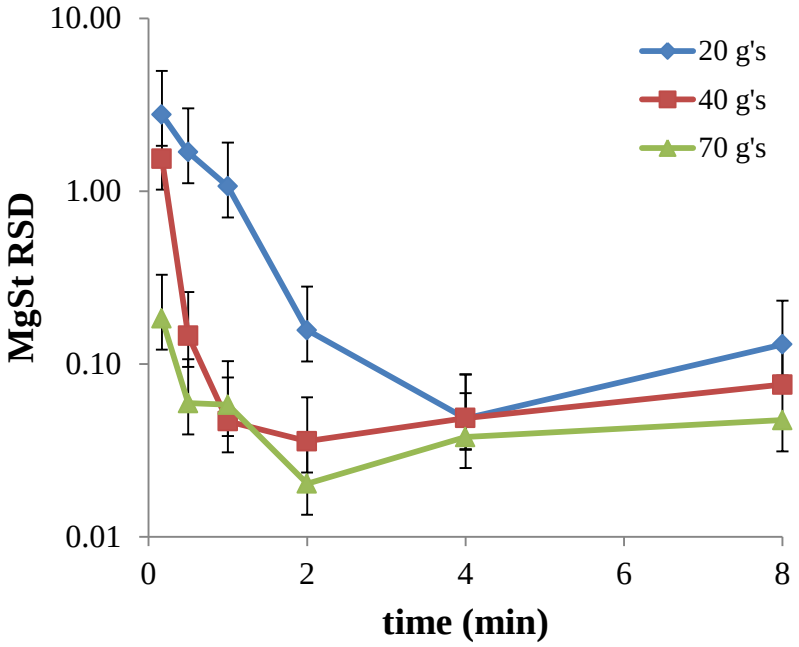

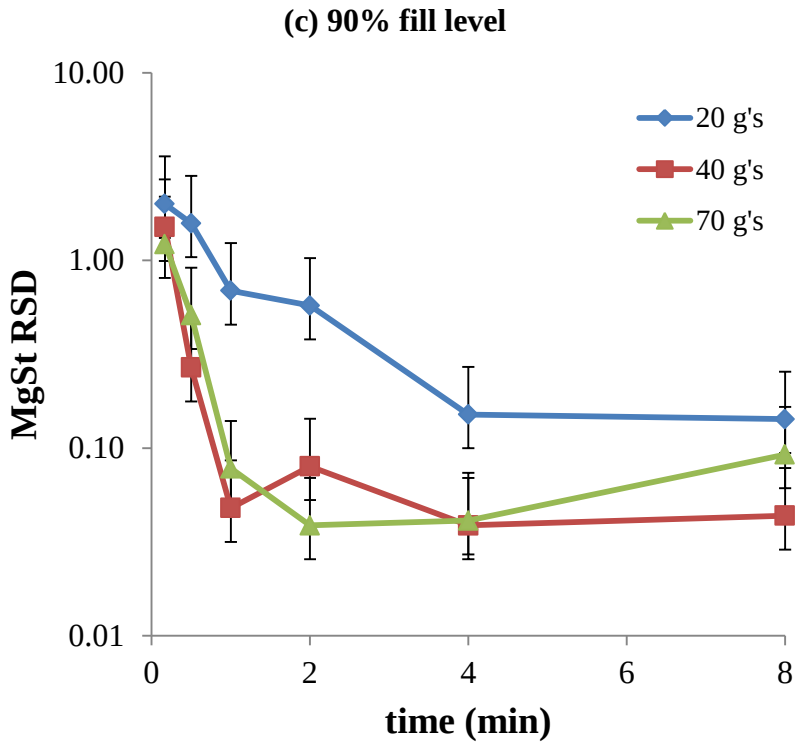

Figure 3-10. Effect of blending time on MgSt RSD for (A) 30%, (B) 60%, and (C) 90% fill levels for accelerations of 20 g's, 40 g's and 70 g's. Error bars were determined using the recommendations by Gao et al. to determine the confidence interval of the RSD for a number of samples (N) equals to 10 [54]. Confidence interval user 95% ($\alpha = 0.05$).

Table 3-10. Analysis of variance for blend uniformity of lubricant using the normalized variance (RSD^2) for experimental design 2.

Analysis of Variance for RSD^2 MgSt, using Adjusted SS for Tests

Source	DF	Seq SS	Adj SS	Adj MS	F	P
t (min)	5	40.4032	40.1368	8.0274	8.78	0.000
Fill level (%)	2	2.7282	2.7608	1.3804	1.51	0.232
Acceleration (g's)	3	12.1199	12.1199	4.0400	4.42	0.008
Error	44	40.2173	40.2173	0.9140		
Total	54	95.4686				

S = 0.956049 R-Sq = 57.87% R-Sq(adj) = 48.30%

The MgSt RSDs obtained in the RAM are comparable to previous studies that have characterized MgSt mixing in different batch blenders. In some cases, the RAM exhibited

better mixing (lower RSD) than observed in other blenders. For example, Muzzio *et al.* studied the mixing performance of a ribbon blender (convective blender) using 0.4% (w/w) MgSt in a blend with microcrystalline cellulose and lactose [2]. The minimum RSD obtained for any of the cases when blending MgSt in this convective blender was around 10% RSD. In another study, Perrault *et al.* evaluated the mixing curves of MgSt in a V-blender [27]. In these studies a concentration of 0.15% MgSt was used. The minimum MgSt RSDs obtained were also around 10%. The main difference is the amount of time that it takes in other blenders to reach comparable RSD values. In the RAM it can take as low as 10 seconds to reach values of ~ 10% RSD, depending on the mixing parameters. This comparison is just for representative purposes since the concentration of MgSt was higher and the RAM vessel used here was much smaller than the blenders just described. In addition, the amount of energy dissipated into the blend per unit mass is quite different. The blending performance of larger RAM blenders has not been yet described in the peer-reviewed literature. However, it is important to remark that the need to achieve effective and reproducible blending performance in laboratory settings, in particular for very small batch sizes, is an ongoing and unmet need in product development. In this respect, the labRAM blender could fill an important gap in the pharmaceutical scientist toolbox.

3.3.2.2 Mixing performance as a function of blender acceleration

The effect of acceleration on the absolute difference between the API target concentration and the measured mean concentration is shown in Figure 3-7. It was previously concluded that this difference was approached minimum value (~ 0) as the mixing time increased. This was true for all three fill levels considered. When the effect

of acceleration is considered, it is clearly observed that higher accelerations led to faster mixing, with this absolute difference approaching its minimum value (~ 0 %) quickly. The effect of acceleration on the API mean concentration was significant ($p \approx 0.000$). The analysis of variance was summarized in Table 3-7. For all fill levels studied, the target concentration was always reached faster by 70 g's followed by 40 g's and 20 g's.

To determine the effect of acceleration on the blend uniformity of APAP, we can refer back to Figure 3-8, where it is shown that faster mixing occurs at higher accelerations for all fill levels studied. This is in accordance with the mean concentration results just described. The difference between 20 g's and 40 g's is greater than the difference between 40 g's and 70 g's. The effect of acceleration on the RSD seems to be an exponential effect at short blending times (10 and 30 seconds). These differences could be caused by the flow patterns formed during mixing which might be similar at higher accelerations, but different at lower accelerations. The amount of total energy transferred to the blend is also greater at higher accelerations. Overall, the acceleration yielded significant differences in the blend uniformity of APAP ($p = 0.020$, Table 3-8). When each mixing time was treated as a different experimental set, the acceleration did not cause significant changes at longer mixing times, as the asymptotic degree of homogeneity is dominated by material properties and appears to depend only slightly, if at all, on acceleration. The p-values from the analysis of variance for each blending time point are summarized in Table 3-11. The analysis of variance indicated that the acceleration had a significant effect on the differences in blend uniformity for 10 seconds ($p = 0.032$), 30 seconds ($p = 0.028$), and 1 minute ($p = 0.010$) of blending time. The

acceleration did no longer have a significant effect on the blend uniformity after 2 minutes (p = 0.234), 4 minutes (p = 0.150), and 8 minutes (p = 0.228) of blending time.

Table 3-11. Summary of probability values (p-values) for fill level and acceleration for both APAP and MgSt blend uniformity using the normalized variance (RSD^2) as an indicator. In this case, each blending time was treated as a separate set of experiments.

	RSD^2 APAP		RSD^2 MgSt	
	Fill level	Acceleration	Fill level	Acceleration
time (min)	P-value	P-value	P-value	P-value
0.17	0.515	0.032	0.395	0.095
0.5	0.431	0.028	0.394	0.067
1	0.432	0.010	0.417	0.020
2	0.306	0.234	0.354	0.324
4	0.078	0.150	0.480	0.282
8	0.331	0.228	0.851	0.115

To further understand the effect of acceleration on the APAP blend uniformity, experiments with extended accelerations were performed for 1 and 2 minutes of blending. The APAP RSD as a function of acceleration for 1 and 2 minutes of blending are shown in Figure 3-11a and 3.11b, respectively. For 1 minute of blending time, the APAP RSD decreased with increasing acceleration (p = 0.010). For 60% and 90% fill levels, it seemed to reach a minimum RSD value at the highest acceleration. For 30% fill level, the RSD seemed to fluctuate more and did not have a defined trend. For 2 minutes of blending time, the acceleration seemed to have less of an effect on the RSD which was no longer statistically significant (p = 0.234). Overall, the RSD decreased with increasing acceleration.

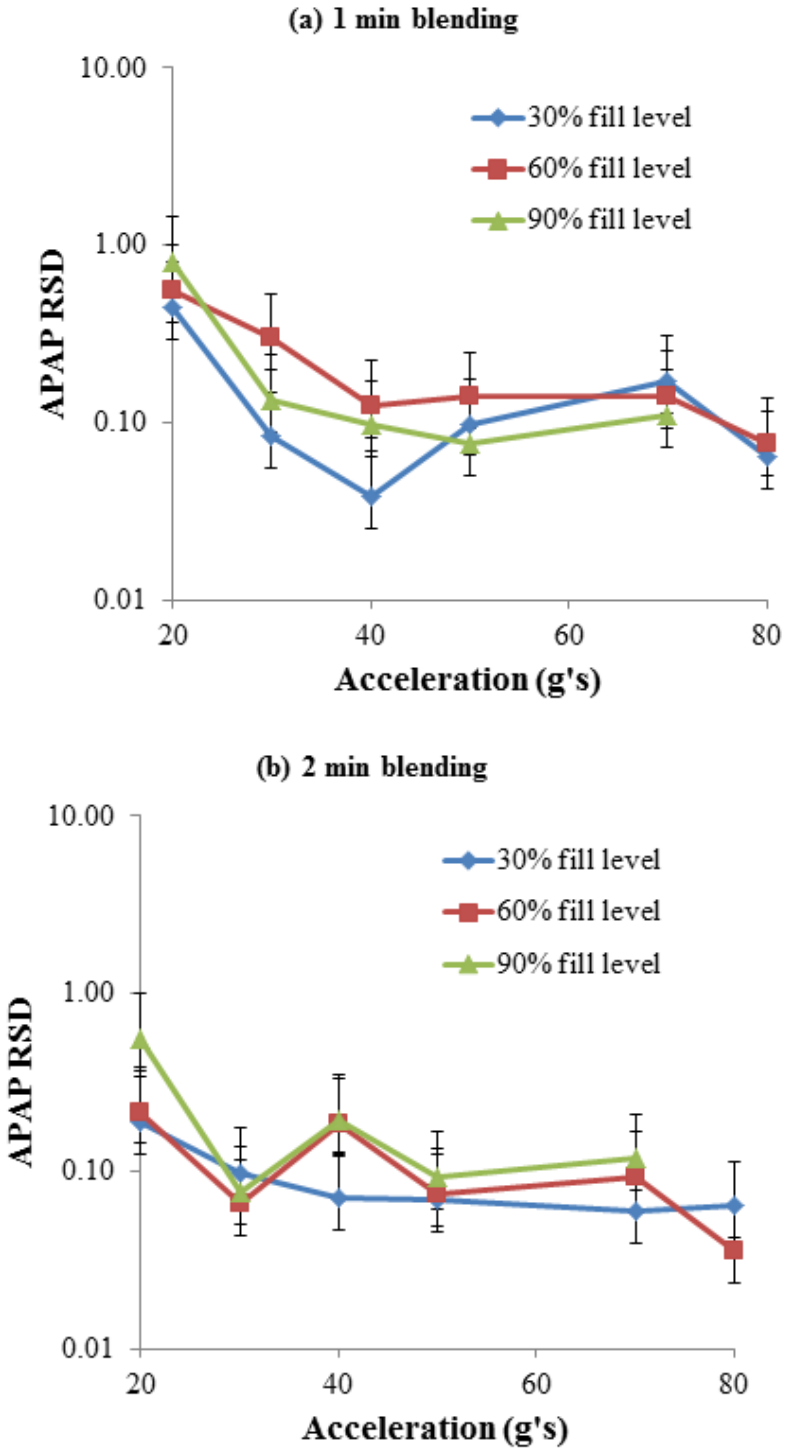

Figure 3-11. Effect of acceleration on APAP RSD for (A) 1 minute and (B) 2 minutes of blending time for 30%, 60%, and 90% fill levels. Error bars were determined using the recommendations by Gao et al. to determine the confidence interval of the RSD for a number of samples (N) equals to 10 [54]. Confidence interval used 95% ($\alpha = 0.05$).

The effect of acceleration on the absolute difference between the MgSt target concentration and the measured mean concentration can be clearly seen in Figure 3-9. Overall, this difference approached its minimum value (~ 0 %) quickly at higher accelerations (40 g's and 70 g's). For 20 g's, it took longer to reach the target MgSt concentration. This is true for all fill levels studied. The acceleration had a significant effect on the MgSt RSD ($p = 0.008$). The analysis of variance was summarized in Table 3-9.

When the MgSt RSD as a function of acceleration is considered, similar results to those just described on the APAP RSD were obtained. Faster mixing occurs at higher accelerations for all fill levels studied (Figure 3-10). The difference between 20 g's is much greater than the difference between 40 g's and 70 g's. Overall, the acceleration has a significant effect on the blend uniformity of MgSt ($p = 0.008$, Table 3-8). The MgSt RSD decreased with increasing acceleration for short mixing times. When each mixing time is treated as a different experimental set, the acceleration did not yield significant changes at longer mixing times. The p-values from the analysis of variance for each blending time point are summarized in Table 3-11. The ANOVA indicated that the acceleration had a significant effect on the differences in blend uniformity for 10 seconds ($p = 0.095$), 30 seconds ($p = 0.067$) and 1 minute ($p = 0.020$) of blending. The acceleration did no longer have a significant effect on the blend uniformity after 2 minutes ($p = 0.324$), 4 minutes ($p = 0.282$), and 8 minutes ($p = 0.115$) of blending.

The MgSt RSD was also considered for extended accelerations for 1 and 2 minutes of blending. The MgSt RSD decreased with increasing acceleration for 1 minute of blending (Figure 3-12a). For 2 minutes of blending time (Figure 3.12b), the MgSt RSD

decreased with increasing acceleration until it seemed to reach a minimum value. The RAM reached "typical" MgSt blend homogeneity either by mixing at high acceleration (e.g. 70 g's) for short blending times (e.g. 10-30 seconds) or low accelerations (20 g's) for longer mixing times (i.e. 1 minute). Longer mixing times and higher accelerations might not be beneficial when blending MgSt because it might cause over-lubrication of the blends, which might lead to slower dissolution rates and weak tablets (low hardness) [16, 36].

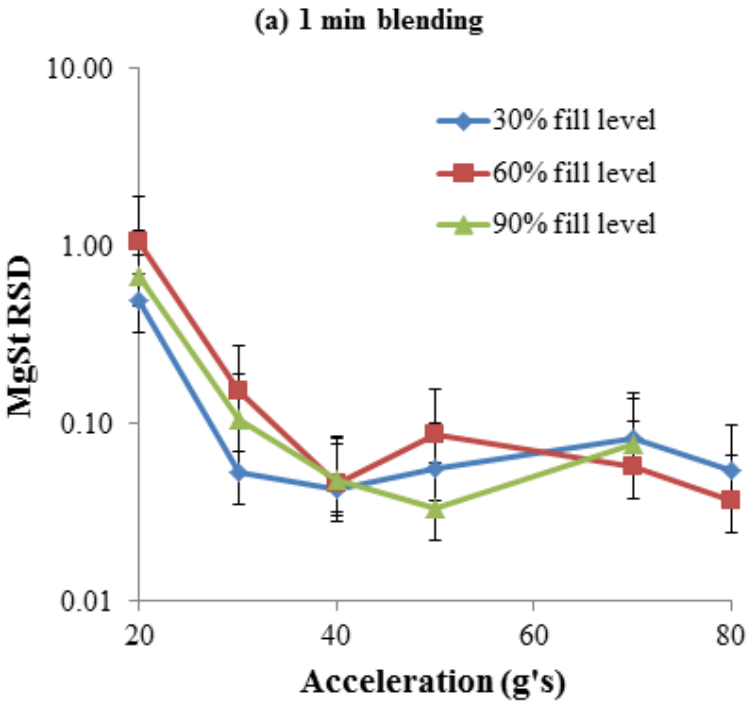

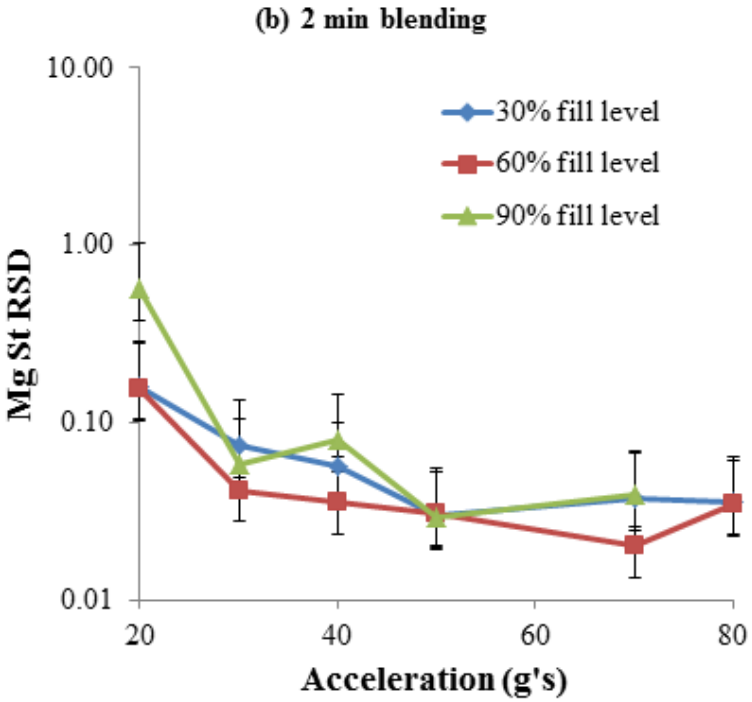

Figure 3-12. Effect of acceleration on MgSt RSD for (A) 1 minute blending time and (B) 2 minutes blending time. Error bars were determined using the recommendations by Gao et al. to determine the confidence interval of the RSD for a number of samples (N) equals to 10 [54]. Confidence interval used 95% (α = 0.05).

Overall, when the APAP RSD and MgSt RSD results are compared, it appears that APAP should be mixed for longer time and at high accelerations before adding the MgSt. The lubricant should be mixed at high accelerations for a short period or a low accelerations for longer blending times. This ensures that there is better homogeneity of the APAP in the final blend while the blend does not become over-lubricated. This routine is commonly used in other batch blending processes to avoid over-lubrication. In these studies, the blend uniformity of APAP and MgSt as a function of resonant acoustic mixing parameters and blending time were considered. Further experiments studying the overall effect of lubrication in the labRAM were performed and are summarized in Chapter 4.

3.3.2.3 Mixing performance as a function of fill level

Although the APAP RSD and the MgSt RSD may seem to depend on the fill level in some experimental results, the fill level did not yield any statistically significant differences on the mean concentration of the components studied or their blend uniformity. The analyses of variance are summarized in Tables 3-7 to 3-11. The APAP RSD and MgSt RSD for 20 g's of acceleration are shown in Figure 3-13 and 3-14, respectively. The results obtained in experimental design 1 were confirmed. Thus it can be concluded that the fill level does not significantly affect the RSD for the mixing parameters and vessel size used. Similar results were also obtained for higher accelerations (40 g's and 70 g's).

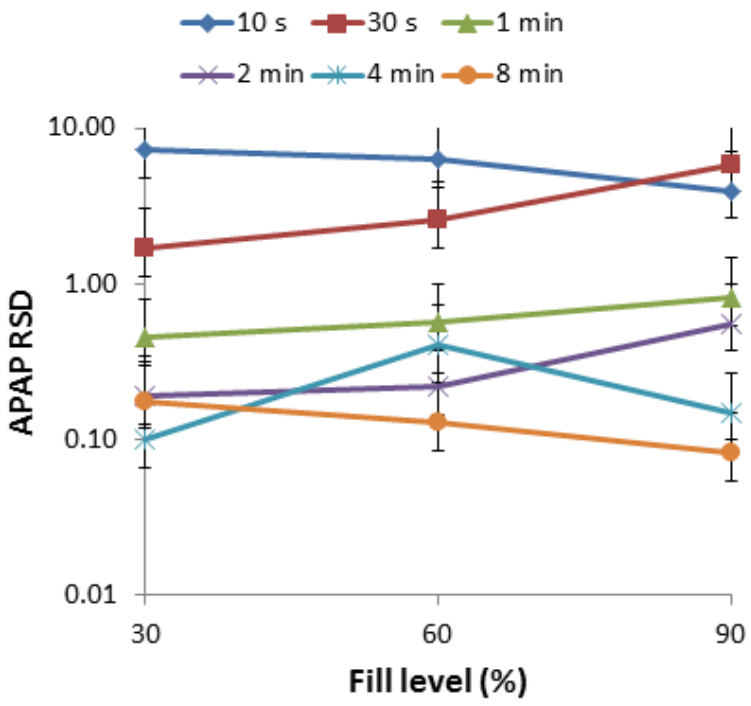

Figure 3-13. Effect of fill level on APAP RSD for 20 g's of acceleration. Error bars were determined using the recommendations by Gao et al. to determine the confidence interval of the RSD for a number of samples (N) equals to 10 [54]. Confidence interval used 95% ($\alpha = 0.05$).

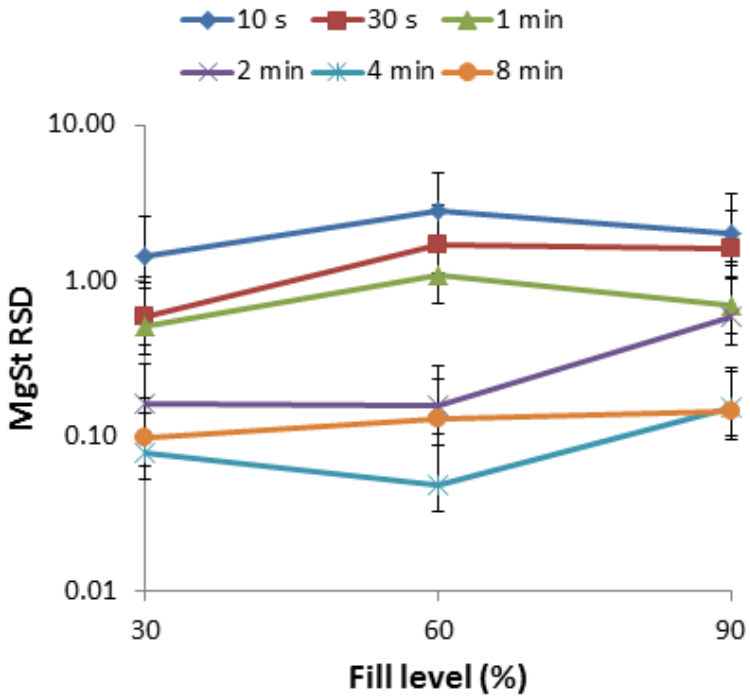

Figure 3-14. Effect of fill level on MgSt RSD for 20 g's of acceleration. Error bars were determined using the recommendations by Gao et al. to determine the confidence interval of the RSD for a number of samples (N) equals to 10 [54]. Confidence interval used 95% (α = 0.05).

3.3.2.4 Mixing performance as a function of total energy to the blend

The amount of total energy per unit mass transferred to each blend in the RAM was calculated using equations 3-2 and 3-3. The mixing performance (i.e. RSD) of both the API and lubricant was correlated to the total energy per unit mass (Figures 3-15 and 3-16, respectively). The mixing performance increased (decreasing RSD) with increasing total energy input, as expected. A negative power law was obtained for both the APAP and MgSt mixing performance. The RSD decreased exponentially as the total energy input increased, and then it seemed to reach a plateau. The total energy to the blend per unit mass is a function of the acceleration, the mixing time and the powder blend mass (i.e. fill level in this case). Although there was substantial variability within the RSD

measurements obtained, the trend is clear. Therefore, the total energy per unit mass is recommended to be used as the input parameter to control the blend uniformity in the RAM.

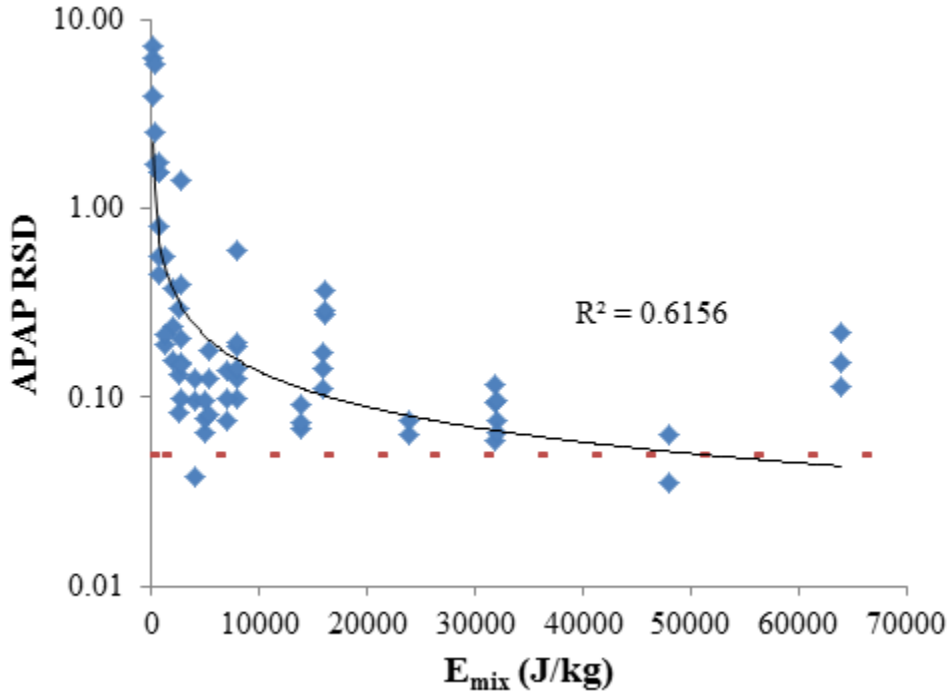

Figure 3-15. Effect of total energy to the blend per unit mass on the blend uniformity of APAP.

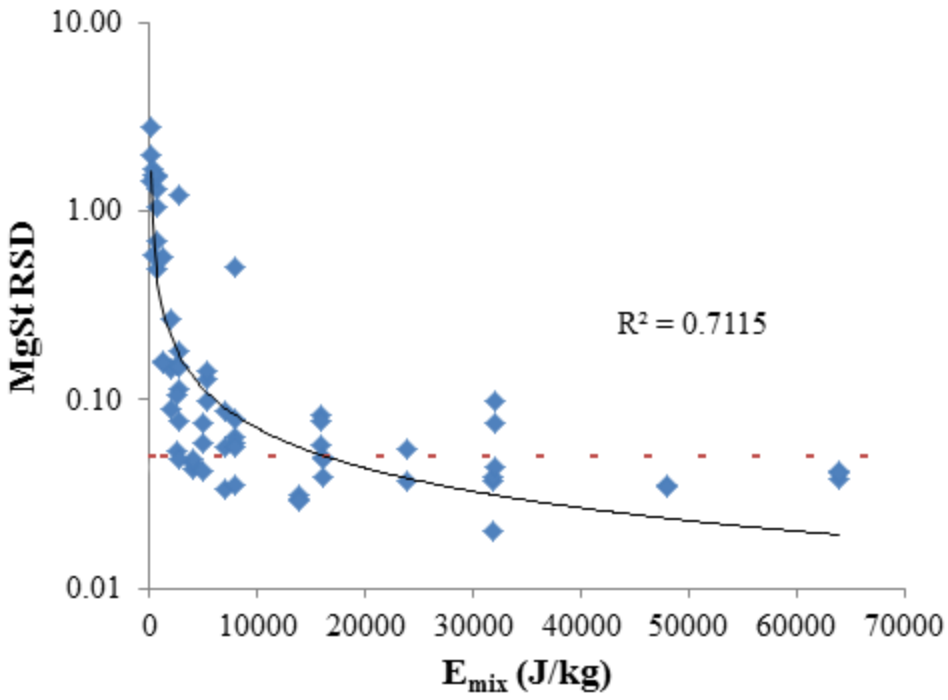

Figure 3-16. Effect of total energy to the blend per unit mass on the blend uniformity of MgSt.

3.4 Conclusions

The main observation for the results described here is that better mixing performance in the resonant acoustic mixer is achieved when blending at higher accelerations. The fill level and blending time for the parameters used in experimental design 1 did not significantly affect blend homogeneity, showing that 1 minute of blending time is enough to reach comparable blend uniformities for the materials, process parameters, and API concentrations used. The average temperature of the powder blends increased at higher accelerations for longer mixing times.

The first fractional factorial design of experiments illustrated the critical mixing parameters in the RAM. An expanded study to determine the blending profiles (mixing curves) of a low concentration cohesive API (semi-fine acetaminophen) and lubricant

(magnesium stearate) blend was performed and described in experimental design 2. The second study described within this chapter examined the mixing curves as a function of mixing time and acceleration for the mixing parameters used. Overall the APAP and MgSt blend uniformity, as measured by the RSD, significantly decreased with increasing mixing time and acceleration. It was found that up to 1 minute of mixing time, the acceleration had a significant effect on both the APAP and MgSt blend uniformity. After 2 minutes of blending, the acceleration did no longer have a significant effect on the RSDs. Mixing performance was found to be independent of fill level which is not the case in different blender types (e.g. tumbling mixers or shear mixers).

Overall, resonant acoustic mixing was able to blend APAP and MgSt efficiently. Care must be taken when blending MgSt in the RAM since the low RSDs obtained indicate that there might be over-lubrication when mixing at higher accelerations and longer blending times. It is also recommended to use lower concentrations of MgSt (< 1 % w/w) in the labRAM. The RAM was also able to blend a moderately cohesive API (semi-fine APAP) although fluctuations in the RSD results might indicate agglomerations for some mixing parameters. The effect of total energy to the blend per unit mass on the blend uniformity was studied. A negative power law trend was obtained. It is recommended that the energy to the blend per unit mass to be used as the input parameter to predict and control the blend uniformity in the RAM.

These studies have laid out the ground work for understanding powder blending in a resonant acoustic mixer. Further investigations to determine the effects of resonant acoustic mixing on blends and tablet properties have been performed. Final blends obtained using “Experimental Design 2” were characterized using different techniques to

determine mixing effects on particle size, cohesion and lubrication. Tablets were also compressed and characterized for weight, hardness and dissolution. These studies are critical to increasing the understanding of RAM powder blending and are summarized in the next chapter.

Chapter 4 Effect of Resonant Acoustic Mixing on Pharmaceutical Powder Blends and Tablets

4.1 Summary

In this chapter, the characterization of resonant acoustic mixing was continued. The blending performance (mixing curves) of a laboratory-scale resonant acoustic mixer (RAM) was described as a function of the mixing parameters in Chapter 3. It was shown that the RAM is a good candidate for mixing pharmaceutical powders, especially during the formulation stage where the amount of API is limited [107]. In those studies, changes in the final bulk density were visually detected after blending. Therefore, it was suspected that the material properties of the blend were affected by the blending process. To confirm the visual observations, further investigations were conducted.

The main objective of this study was to investigate the effect of the resonant acoustic mixing parameters on the material properties of final blends and tablet performance. A common formulation was used while varying the intensity of mixing (acceleration) and total blending time. The following material properties of the final blends were measured and correlated to the mixing parameters: particle size, bulk and tapped density (Carr's compressibility index), compressibility, and hydrophobicity. Tablets were compressed using a tablet press simulator due to the small quantity of powder available from each blend. The tableting compression force and the weight, hardness and dissolution of the tablets were measured and correlated to the mixing parameters. The main findings of these investigations are presented in this chapter. Results indicated that the powder blend material properties and tablet characteristics were significantly affected by the

acceleration (mixing intensity) and the blending time. RAM is a good choice for blending low concentrations of cohesive APIs, but care must be taken when blending hydrophobic lubricants because the high energy input can adversely affect the final tablet properties such as hardness and dissolution.

4.2 Materials and Methods

4.2.1 Materials

The materials used in all experiments were as follows: semi-fine acetaminophen (Mallinckrodt, Raleigh, North Carolina, USA), silicified microcrystalline cellulose (Prosolv HD90, JRS Pharma, Germany), and magnesium stearate (MgSt, non-Bovine, Tyco Healthcare / Mallinckrodt, St. Louis, Missouri, USA). The nominal particle sizes of the materials used are listed in Table 4-1.

Table 4-1. Concentrations and mean particle size of materials in blend.

Concentration (%)	Material	Mean Particle Size (μm)
3	Semi-fine acetaminophen	45
96	Prosolv HD90	110
1	Magnesium stearate	10

4.2.2 Resonant Acoustic Mixing and Blending

The formulation for each powder blend consisted of 3% semi-fine APAP, 1% MgSt and 96% Prosolv HD90. All powder blends were prepared in a laboratory scale ResonantAcoutic® Mixer (RAM, Resodyn Acoustic Mixers, Butte, Montana, USA) shown in Figure 4-1. The principles by which the RAM works are explained in more detail in Chapter 3 and elsewhere [37]. In this study, each blend was made with a different combination of acceleration and mixing time. For the blend characterization, the

experimental design used is shown in Table 4-2a. The experimental design was slightly changed for the tablet characterization study and is shown in Table 4-2b. A 236-mL vessel, filled up to 60% by volume, was used for all the experimental work shown here.

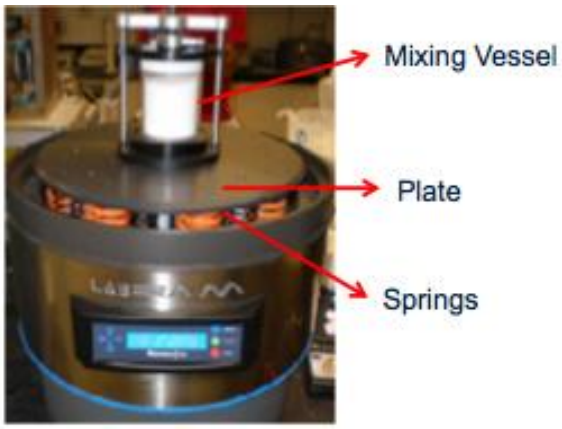

Figure 4-1. LabRAM with 236-mL mixing vessel.

Table 4-2. Experimental design used to study the effect of resonant acoustic mixing on (a) pharmaceutical powder blends and (b) tablets.

(a)

time (min)	acceleration (g's)
0.5	20
1	40
2	70
4	
8	
Additional acceleration	
1	80
2	

(b)

time (min)	acceleration (g's)
0.5	20
1	40
2	70
4	80

4.2.3 Blend Characterization

4.2.3.1 Particle Size

The particle size distribution of the finals blends was determined using a laser-diffraction (LS-13 320) analyzer with a Tornado Dry Powder System (Beckmann-Coulter, Brea, California, USA).

4.2.3.2 Bulk and Tapped Density

Bulk density measurements were performed by pouring the powder blends slowly into a 75-mL graduated cylinder. The graduated cylinder was filled up to approximately 50 mL and the mass was weighed. Once the weight was recorded, an automatic tapping machine (Model No. AT.4.110.60, Quantachrome Instruments, Boynton Beach, Florida, USA) was used to tap the material 1000 times and the new volume was recorded to obtain the tapped density.

4.2.3.3 Compressibility

A commercially available powder testing system (FT4, Freeman Technology Ltd. Gloucestershire, UK) was used to measure the compressibility of the final powder blends. The compressibility of a powder is a measure of how density changes as a function of applied normal stress. A 48-mm cylinder was used for these tests. The compressibility is the percentage change in volume after compaction at a specific normal stress. Cohesive powders show a large change in volume, while non-cohesive powders show little change in volume. The FT4 compresses the powder from 0-15 kPa with increasing steps of 0.5 kPa. The compressibility values used for comparison were obtained at a normal stress of 15 kPa. More details on compressibility measurements and correlations to other powder flow properties can be found elsewhere [15, 97].

4.2.3.4 Hydrophobicity

The Washburn technique has been previously demonstrated to be able to measure the "hydrophobicity" of powder blends [16]. The hydrophobicity, in this case, is the rate at which a liquid permeates a powder bed through capillary forces. Thus, when a blend is hydrophobic, the liquid permeates slowly, if at all, through the powder bed. The hydrophobicity of the final powder blends was measured with this technique using a saturated water solution of all the soluble components in the blends. A more hydrophobic blend (powder) is produced by higher dispersion and/or smearing of magnesium stearate (hydrophobic lubricant) in the blend caused by different levels of shearing during blending. Thus, the hydrophobicity is a direct measurement of the extent of dispersion of lubricants in a powder blend after experiencing shear. The hydrophobicity was measured for selected blends to examine the effect of acceleration and blending time in the RAM. In this case, the times were 0.5, 1, 4, and 8 minutes for accelerations of 20, 40 and 70 g's.

4.2.4 Tableting

Tablets were compacted from each powder blend using a single-station, linear, mechanical compaction simulator (Presster™ 252, Metropolitan Computing Corporation, East Hanover, NJ). The tableting conditions (i.e. die volume) for all the blends were maintained constant as the main aim was to investigate the effects of the resonant acoustic mixing parameters on compression and tablet properties. A Kikusui Libra 2 (36 stations at a linear speed of 0.4 m/s, corresponding to a turret speed of 20 rpm or a tableting speed of 43,200 tablets/hour and a dwell time of 22.1 ms) was simulated using the Presster™. The punch used was a 10 mm round, flat-faced EU-B tablet compression tooling. The formed tablets were characterized for weight, hardness and dissolution. The

tableting compression force obtained for each powder blend was also considered as part of the results.

4.2.5 Tablet Characterization

4.2.5.1 Weight and Hardness

The weight of 10 tablets from each blend was measured using a precision balance (Adventurer Pro-AV 64 C, OHAUS Corporation). After the tablets were weighed, the hardness was measured using a tablet hardness tester (Model 6D Tablet Tester, Dr. Schleuniger, Pharmatron).

4.2.5.2 Dissolution

Tablet dissolution test was conducted for tablets of each powder blend in a USP-II apparatus (Varian VK 7010 Dissolution Apparatus, Varian Inc.) [108]. Pre-weighed tablets from each batch were tested separately in dissolution vessels consisting of 900 ml of USP buffer solution of pH 5.8. The temperature of the buffer solution (the dissolution medium) was maintained at 37°C. The paddle rotation speed was set at 50 rpm. The overall process was run for 90 minutes. Aliquots of the dissolution medium were collected at intervals of 3 minutes through 35 micron full flow filters (Agilent Dissolution filter) by a peristaltic pump and their absorbance was measured by a UV spectrophotometer (Cary 50 Bio UV-Visible spectrophotometer, Varian) at 243 nm. The collected samples were then returned to the vessel to keep the vessel volume constant. Absorbance values from the spectrophotometer were used to calculate a dissolution

release profile, based on the calibration equation developed by Pingali *et al.* [91]. The whole process was monitored by Varian UV Dissolution Software (Version 4.20 (466)).

4.2.6 Energy per unit mass

The total power that goes into the power blend (P_{mix}) is calculated from equation 4-1. This equation was derived empirically by Resodyn Acoustic Mixers and it has a 10% error associated with it [105].

$$P_{mix} = 0.707 F_{rms} \left({}^{\Delta P}/_{100}\right) \left({}^{a_{peak} \cdot G}/_{2\pi f} \right) \tag{4-1}$$

In the equation above, ΔP represents the difference in power intensity ($P-P_o$) from the loaded (P) to the unloaded (P_o) masses (Figure 4-2), F_{rms} is the machine force constant (70 N ± 4 N), G is the gravitational constant, a_{peak} is the peak acceleration experienced at the specific power intensity and f is the frequency (61 Hz) at which the resonant acoustic mixing operates. The force constant (F_{rms}) was empirically derived by the equipment manufacturer by using multiple LabRAM mixers, mixing materials and calorimetry (using energy balance). This value was determined as the root mean square (rms) for the LabRAM mixers and, since it is a machine variable, it does not vary when different materials are mixed [105]. The value of 0.707 is the correction factor from peak to rms.

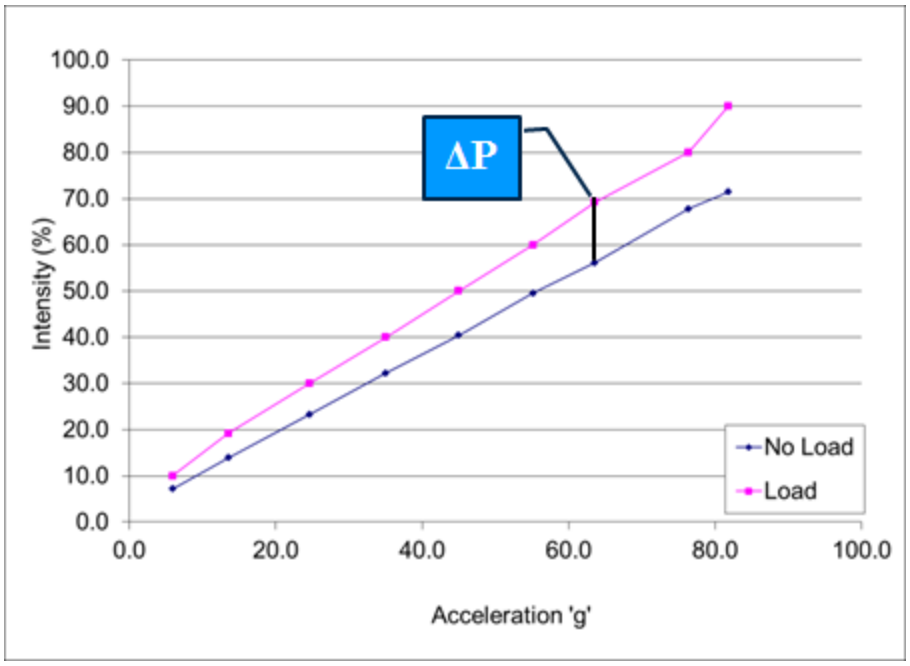

Figure 4-2. Intensity (%) of mixing showing the difference in power intensity from loaded to un-loaded masses in the RAM. Courtesy of Resodyn Acoustic Mixers [17].

The total energy that goes into the powder blend per unit mass (E_{mix}) was calculated using the relationship in equation 4-2.

$$E_{mix} = {P_{mix} \cdot t_{mix}}/{m} \tag{4.2}$$

In the equation above, t_{mix} is the total blending time and m is the total mass of the powder blend. In all experiments, a total mass of 70 g was used. The total energy to the blend per unit mass was calculated and correlated to the measured material properties of the blends, and the tableting and tablet properties.

4.3 Results and Discussion

The experimental results discussed in this chapter are from blends produced in the RAM, and tablets made from those blends. The acceleration, which can be treated as the

shear rate, and the total blending time were used as the mixing parameter variables. The combination of these two parameters yield a specific amount of energy to the blend, which is calculated as described in equations 4-1 and 4-2. The effect of acceleration, blending time and, thus, total energy to the blend per unit mass on the powder blend material properties are described as part of the results in this chapter. Although the acceleration, blending time and total amount of energy affects the material properties of the blend, these indirectly affect the final tableting and tablet properties. The indirect effects of acceleration, blending time and total energy to the blend per unit mass on tableting and tablet properties are also described as part of the results (Figure 4-3).

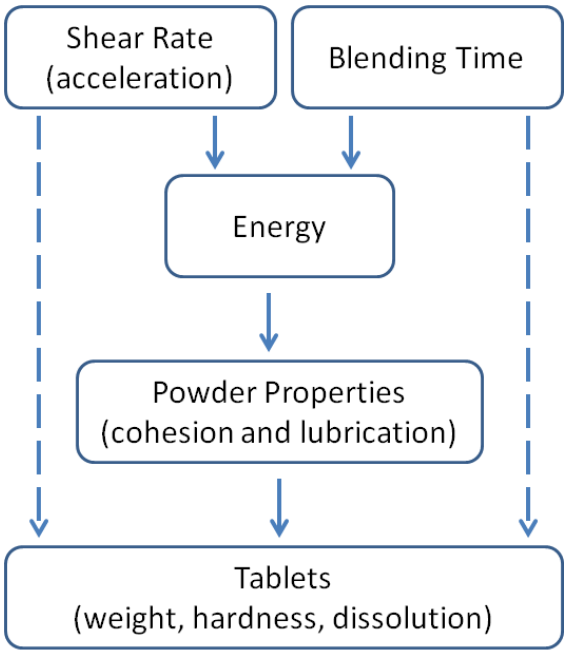

Figure 4-3. Schematic of resonant acoustic mixing on the material properties of blends and, consequently, tablets.

4.3.1 Blend Properties

Material properties of the final blends were characterized using various metrics, namely the particle size, the bulk density, the tapped density, and the compressibility. From the bulk density and tapped density, the Carr's index was also calculated and used in the results. The effect of power intensity (acceleration), blending time, and total energy to the blend per unit mass was correlated to the measured material properties and are presented next.

4.3.1.1 Particle Size

Particle size characteristics, d_{10}, d_{50} and d_{90}, were calculated and correlated to the acceleration and blending time. The d_{10} changed significantly due to acceleration ($p = 0.001$) and total blending time ($p << 0.05$). The d_{50} and d_{90} showed significant differences due to acceleration ($p << 0.05$ and $p = 0.006$, for d_{50} and d_{90} respectively) and due to blending time ($p << 0.05$ for both d_{50} and d_{90}). To illustrate the correlations found, d_{10} is shown in Figure 4-4 as a function of acceleration, blending time and total energy to the blend per unit mass.

(a)

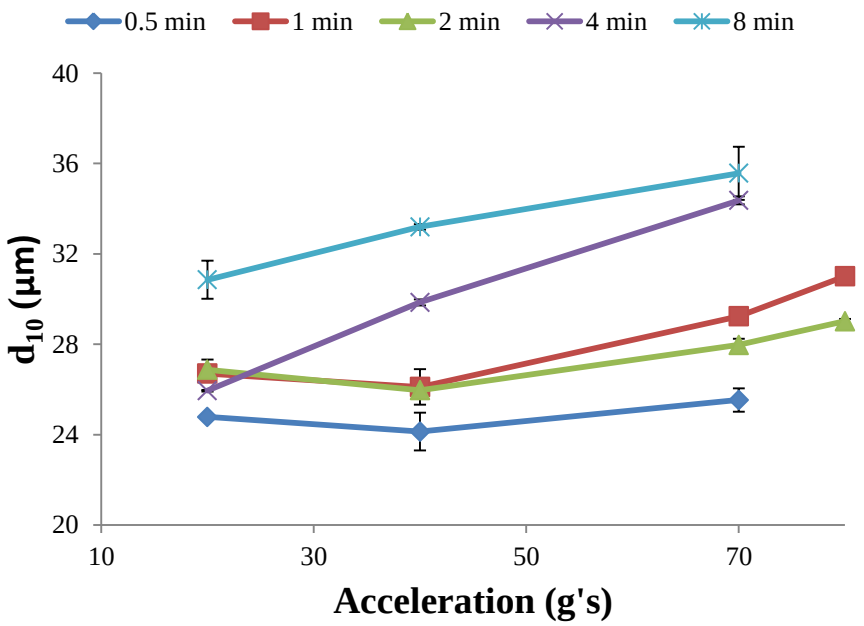
0.5 min
1 min
2 min
4 min
8 min
40
36
32
28
24
20
10
30
50
70
d10 (µm)
Acceleration (g's)

(b)

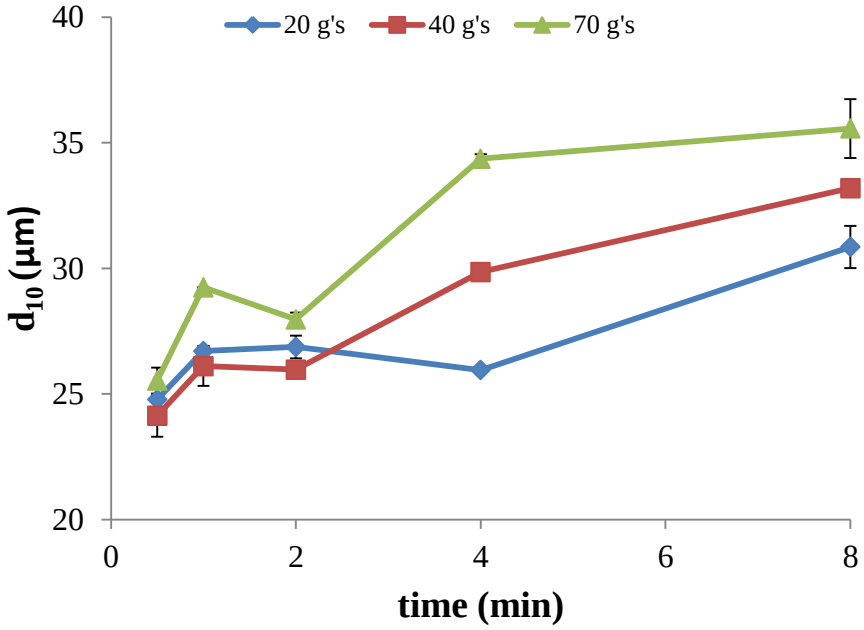
20 g's
40 g's
70 g's
40
35
30
25
20
0
2
4
6
8
d10 (µm)
time (min)

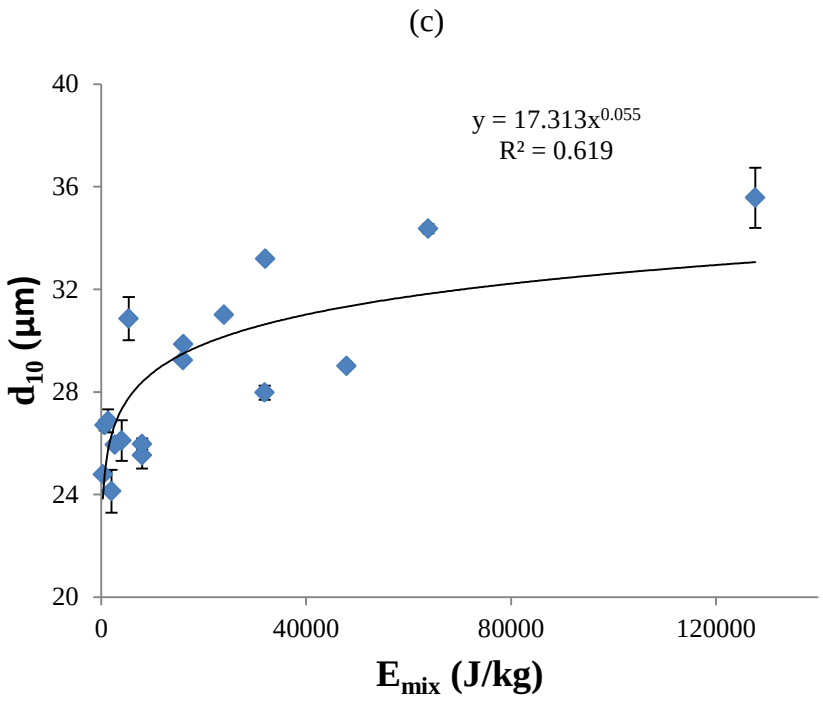

Figure 4-4. Effect of (a) acceleration, (b) blending time and (c) total energy to the blend per unit mass on particle size (d10).

The observed value of d_{10} increased with increasing acceleration (Figure 4-4a) and blending time (Figure 4-4b). No defined trends were obtained for any of the other particle size measurements (mean, d_{50} and d_{90}) considered. Differences in d_{10} due to acceleration are more significant at longer blending times. The maximum d_{10} increase was obtained at higher accelerations (70 g's). An increase in the d_{10} particle size fraction can be an indication that agglomerates of the main excipient (Avicel) or of APAP, cohesive in nature, are being formed in the blend. Another indication might be that the minor components (MgSt and APAP fines) are smearing and coating onto the surface of the major excipient (Prosolv); this might have led to an increase in particle size. The agglomeration, and the smearing and coating of APAP and, mainly, MgSt lead to an overall increase in the d_{10} fraction of the particle size. This increase in the d_{10} fraction of

the particle size should lead to an improvement in "flowability" of the blends. The d_{10} as a function of total energy to the blend per unit mass is shown in Figure 4-4c. This correlation resulted in a power law showing that the energy per unit mass can be used as an input variable to determine (or predict) the change in particle size during resonant acoustic mixing. The correlation for d_{10}, as well as the other properties of blends and tablets, is summarized in Table 4-3.

Table 4-3. Material properties of blends, and tableting and tablet properties correlations to the total energy to the blend per unit mass (shown as 'x' in the equations above).

Measured Property	Correlation	R^2
d10 (µm)	$17.313x^{0.055}$	0.619
bulk density (g/mL)	$0.3636x^{0.0421}$	0.852
tapped density (g/mL)	$0.4653x^{0.0337}$	0.880
Carr's Index	$23.567x^{-0.045}$	0.540
Hydrophobicity (min/g^2)	$0.2419\exp^{65.05x}$	0.812
Compression Force (kN)	$2.0067x^{0.1159}$	0.930
Tablet Weight (mg)	$317.81x^{0.0348}$	0.941
Tablet Hardness (N)	$1148.9x^{-0.296}$	0.886

The absence of a definite trend for mean, d_{50} and d_{90} can be explained by the action of two opposing mechanisms on large particles. Due to the coating of large particles by the smaller APAP and MgSt particles, the size of the larger particles might have increased. However, due to the application of shear and strain during mixing, these particles could also break down into smaller particles. Hence depending on the dominating mechanism at those particular blending parameters, the size of the large particles either increase or decrease; thus the lack of a clear trend.

4.3.1.2 Bulk and tapped density

The effect of acceleration on bulk density and tapped density was studied. The bulk density ($p << 0.05$) and tapped density ($p << 0.05$) increased with increasing acceleration (Figure 4-5a and 4-5b, respectively). Carr's compressibility index (CI) was calculated from the bulk and tapped density [92]. The CI changed significantly ($p = 0.028$) and generally decreased with increasing acceleration (Figure 4-5c). Overall, an increase in acceleration improved the powder flow properties of the final blends.

(a)

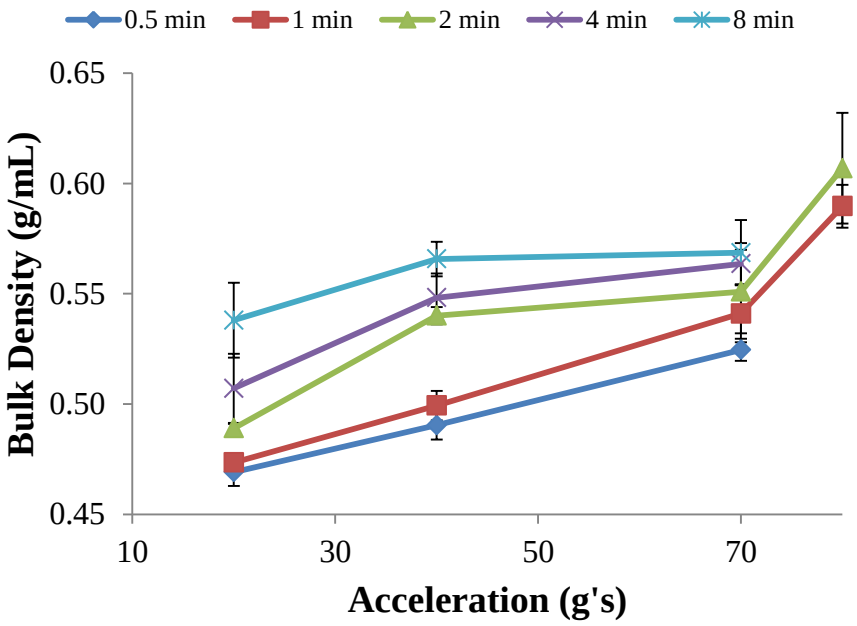

(b)

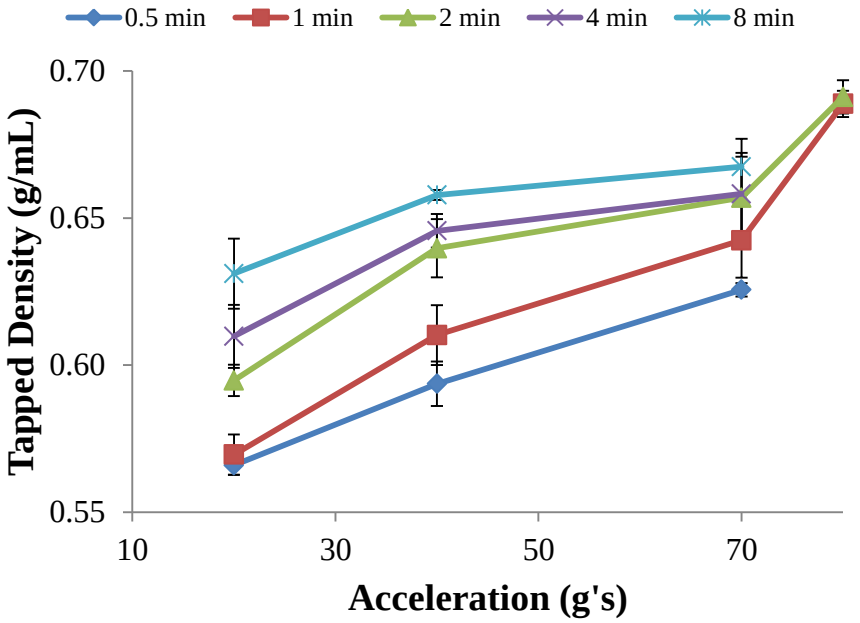

(c)

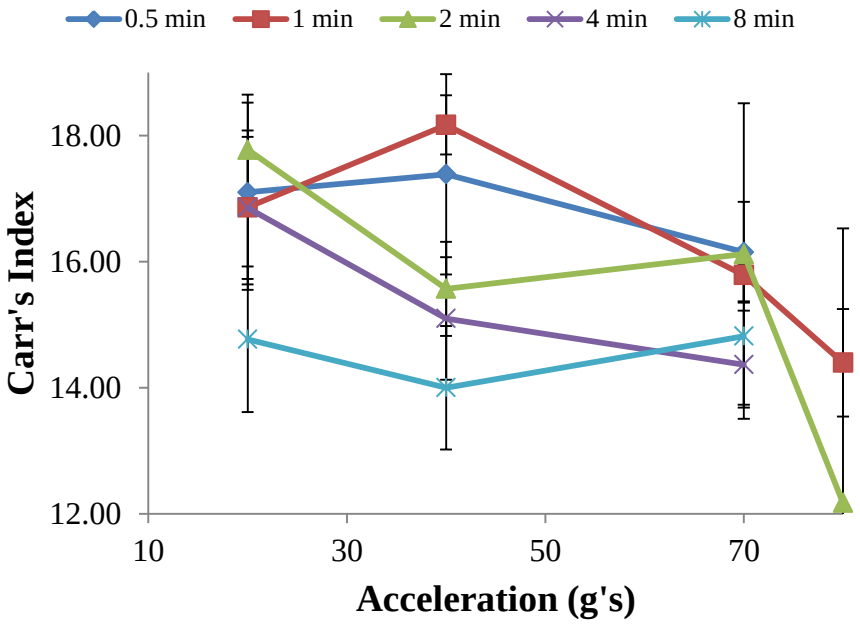

Figure 4-5. Effect of acceleration on (a) bulk density, (b) tapped density and (c) Carr's Index.

The effect of blending time on the bulk density, tapped density and, consequently, on the CI was also studied. The bulk density ($p << 0.05$) and tapped density ($p << 0.05$) increased with increasing blending time (Figure 4-6a and 4-6b, respectively). The CI ($p << 0.05$) decreased with increasing blending time (Figure 4-6c). Therefore, increasing acceleration as well as blending time led to "better" powder flow properties of the final blends. This is in agreement with the results obtained from the particle size measurements when the change in the d_{10} fraction is considered.

(a)

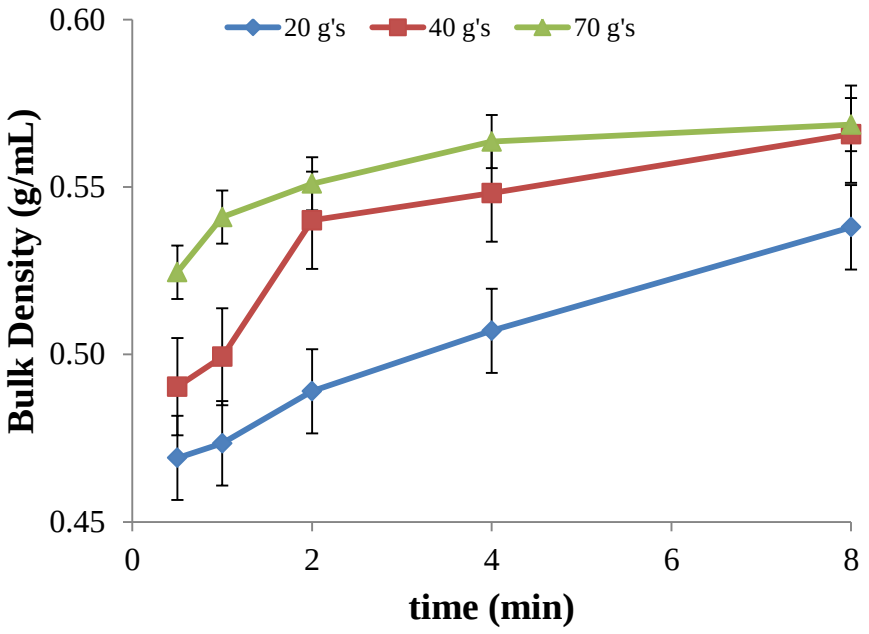

(b)

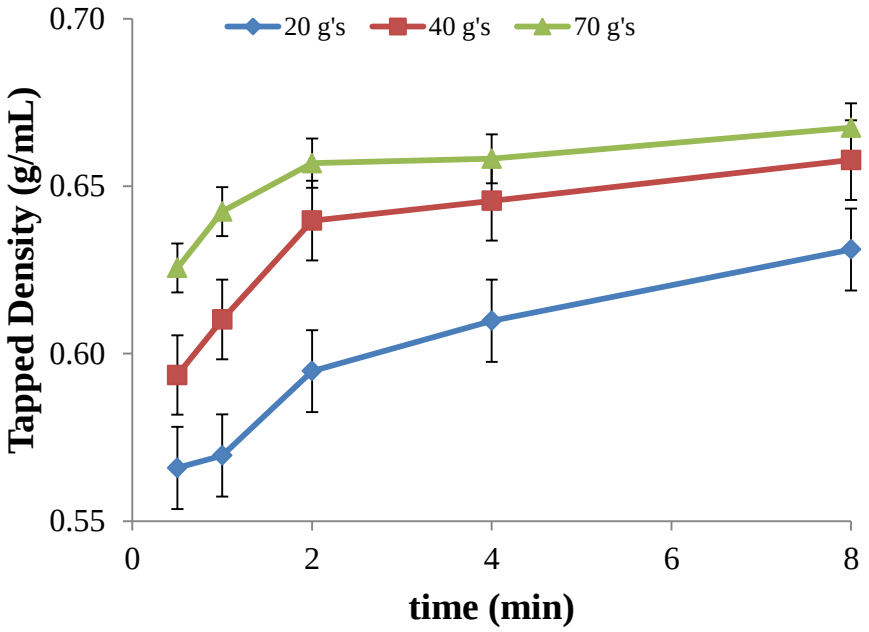

(c)

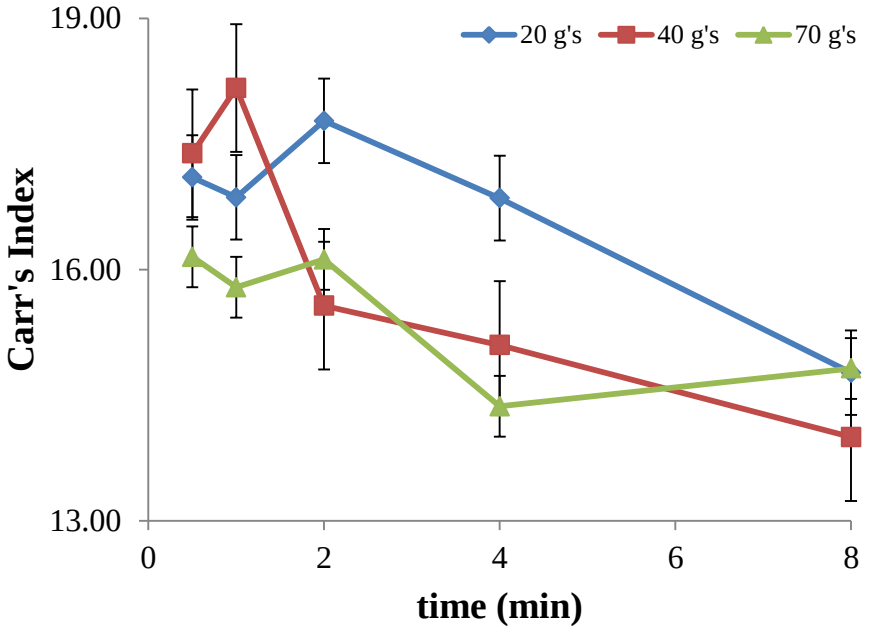

Figure 4-6. Effect of blending time on (a) bulk density, (b) tapped density and (c) Carr's Index.

Many hypotheses can explain the changes in flow properties. For example, the MgSt in the blend might be smearing onto other particles at higher acceleration and longer blending times, improving the powder flow properties by disrupting capillary cohesion. MgSt is commonly used as a glidant and known to improve the powder flow properties of blends. Mehrotra *et al.* studied the effect of shear intensity and total shear using a shearing device on blends with and without MgSt [47]. An increase in bulk density was observed with increasing total strain for the blends with MgSt.

Another hypothesis is that the silicon dioxide in the Prosolv (SiO_2 + microcrystalline cellulose) might be further mixing and coating the API as well as the microcrystalline cellulose particles changing the flow properties of the final blends. Pingali *et al.* demonstrated that the mixing order of silicon dioxide and MgSt affected the final properties of the blends [36]. In our case, the silicon dioxide was pre-mixed with the microcrystalline cellulose, thus added prior to MgSt. This combination had the greatest effect on changing the properties of blends, as demonstrated by Pingali's work. Therefore in the case of the resonant acoustic mixing, higher acceleration (intensity) and/or longer blending time dissipate more energy onto the blend, possibly creating similar effects to those previously obtained in a shearing device.

The bulk density, tapped density and Carr's Index were correlated to the total energy to the blend per unit mass (Figure 4-7). All numerical correlations (fits) to the material properties measured as a function of total energy to the blend per unit mass are described in Table 4-3. The bulk density (Figure 4-7a) and tapped density (Figure 4-7b) increased with increasing energy per unit mass following a power law relationship. The correlations

of the bulk density and tapped density are very good with $R^2 > 0.85$. The Carr's Index decreased with increasing energy per unit mass, also following a power law (Figure 4-7c). The correlation of the CI to the energy per unit mass is not as good as for the bulk density and tapped density due to the large variability obtained from these measurements, even though it is calculated from the bulk and tapped densities.

(a)

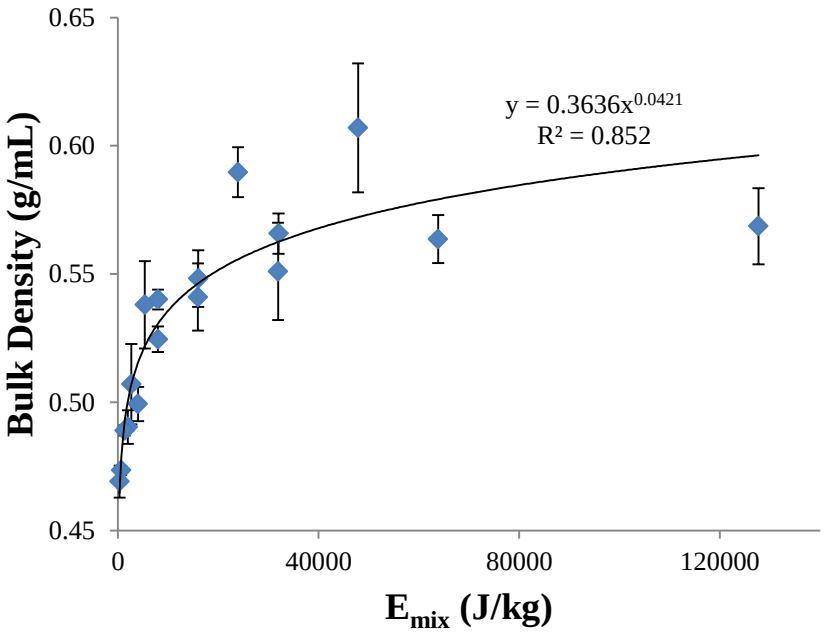

(b)

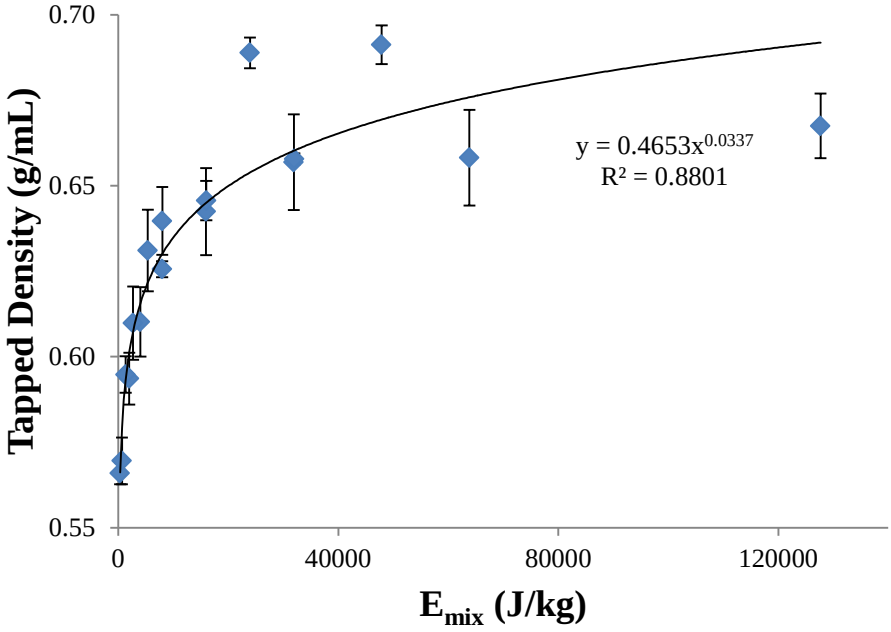

(c)

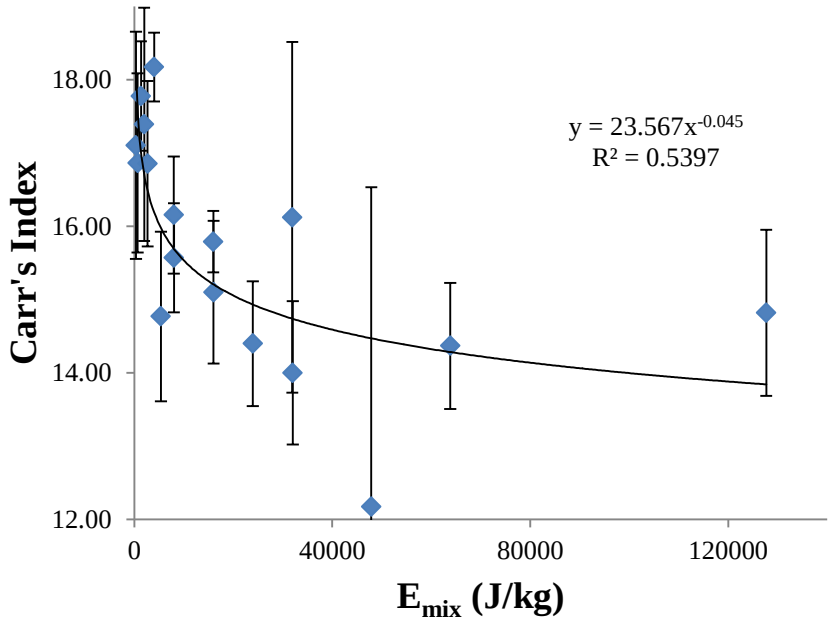

Figure 4-7. Effect of total energy to the blend per unit mass on (a) bulk density, (b) tapped density and (c) Carr's Index.

4.3.1.3 Compressibility

The effect of acceleration and blending time on compressibility was also determined. The difference in compressibility of the final blends caused by the acceleration was significant ($p = 0.064$), but no clear trend was obtained. The difference in compressibility caused by blending time was also significant ($p << 0.05$). The compressibility slightly decreased with increasing blending time especially at lower accelerations (Figure 4-8). Lower compressibility is also an indication of "better" flowability confirming the results obtained from the bulk and tapped densities just described.

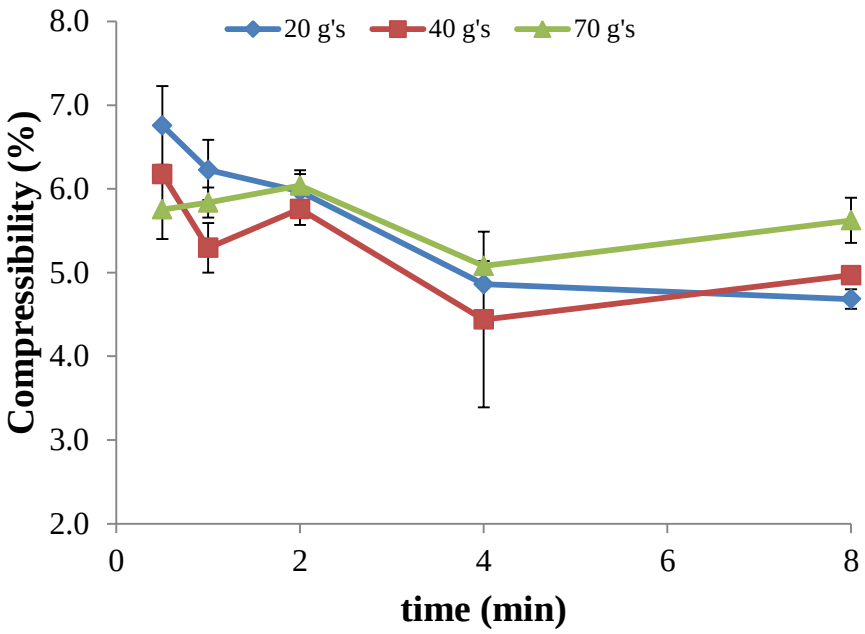

Figure 4-8. Effect of blending time on compressibility.

4.3.1.4 Hydrophobicity

The hydrophobicity of the blends was measured and correlated to acceleration (Figure 4-9a), blending time (Figure 4-9b) and total energy to the blend per unit mass (Figure 4-9c). The hydrophobicity increased with increasing acceleration, especially when blended for longer blending times. The hydrophobicity changed only slightly with increasing blending time at the lower acceleration (20 g's), but increased substantially at higher accelerations (40 g's and 70 g's). The increase in hydrophobicity is more evident for 70 g's. Blends mixed at 70 g's after 4 minutes became considerably hydrophobic. The hydrophobicity increased exponentially as a function of the energy to the blend per unit mass. This correlation was different from those obtained for all other measurements (e.g. bulk density and tapped density) in this study. All other measurements followed a power law when correlated to the energy per unit mass meaning that eventually they should reach maximum (or minimum) value, while the hydrophobicity should keep increasing exponentially.

(a)

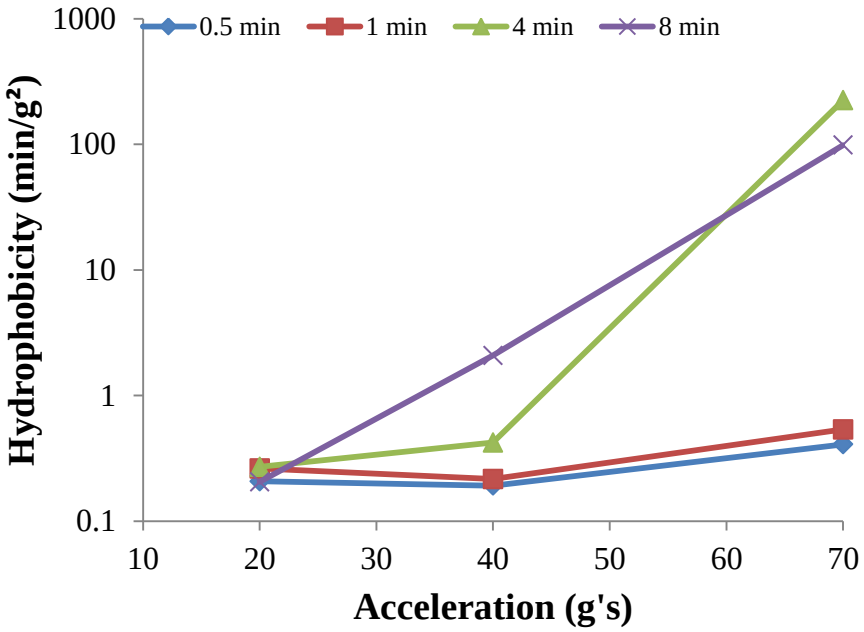
1000
100
10
1
0.1
0.5 min
1 min
4 min
8 min
Hydrophobicity (min/g²)
10
20
30
40
50
60
70
Acceleration (g's)

(b)

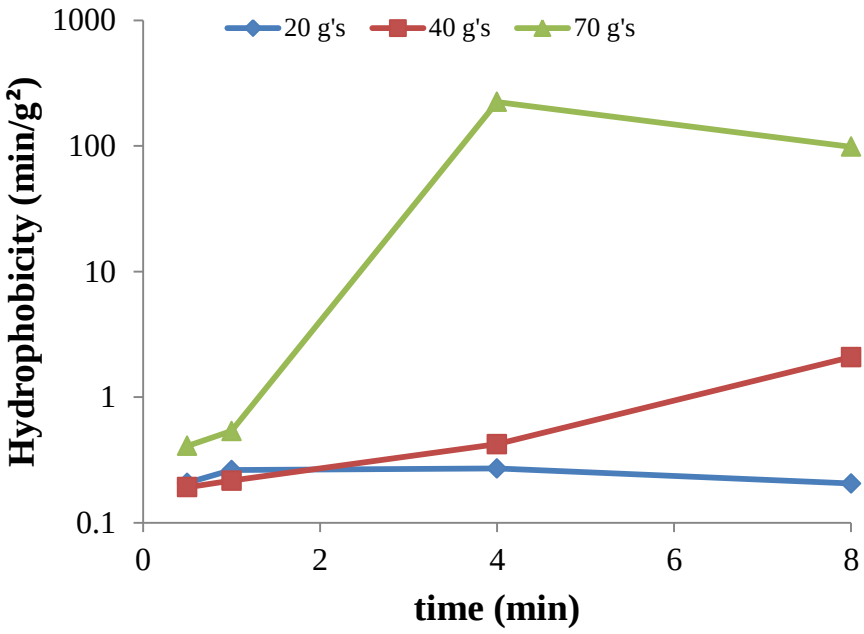
1000
100
10
1
0.1
20 g's
40 g's
70 g's
Hydrophobicity (min/g²)
0
2
4
6
8
time (min)

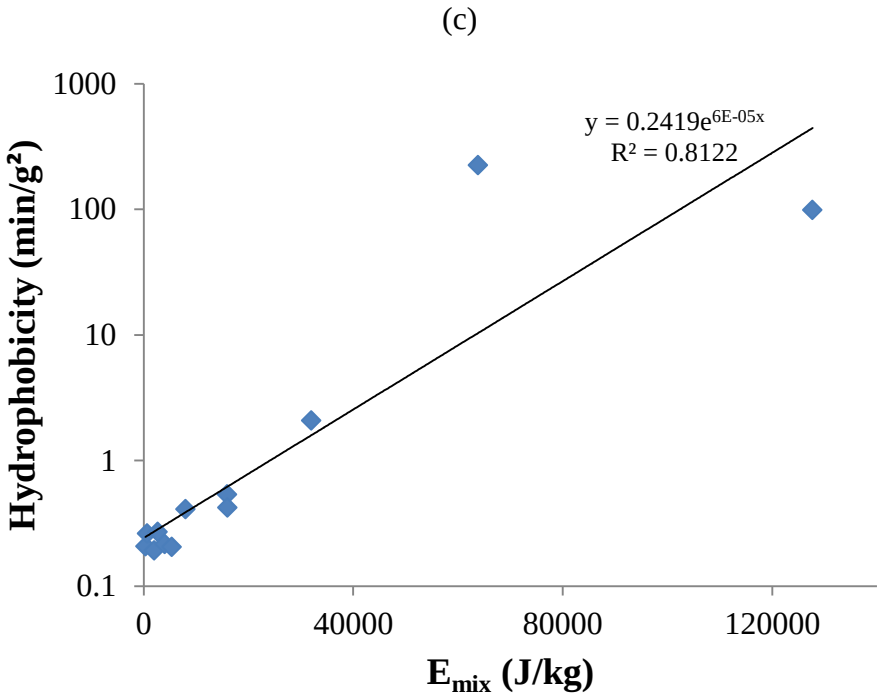

Figure 4-9. Effect of (a) acceleration, (b) blending time and (c) total energy to the blend per unit mass on hydrophobicity.

Hydrophobicity results are analogous to those obtained in previous work by Llusa and Pingali [16, 91], respectively, for other blenders. The hydrophobicity increased with both shearing intensity and total shear. These results indicate that the final blend properties indeed change when mixing in a RAM. In previous work by other members of our group, the hydrophobicity was correlated to the rate of drug dissolved. It was shown that higher hydrophobicity correlated to, and possibly caused, a lower amount of drug going into solution when compared at a specific dissolution time [91]. Since pharmaceutical powder blends are not the final dosage form, tablets, which are the most common dosage form, were compressed and characterized. The results from the tableting and tablet characterization are shown in the next subsection.

4.3.2 Tableting and Tablet Properties

4.3.2.1 Tableting Compression Force

Tablets were made using the same fill volume and same thickness in order to determine the effects of mixing parameters (material properties of blends) on the tableting process and the resulting tablets under conditions similar to those enacted in commercial tablet presses. The tableting mean compression force was calculated from the compression force for all 60 tablets made for each blend. The effect of acceleration during blending on the compression force is shown in Figure 4-10a. The compression force increased with increasing acceleration for all blending times. These differences were significant ($p << 0.05$) demonstrating that the blends are indeed different in density. The compression force as a function of blending time was also considered (Figure 4-10b). The compression force increased ($p << 0.05$) with increasing blending time. A smaller increase was obtained for 20 g's of acceleration once again proving that blending for longer time at 20 g's has a smaller effect on the blend than higher accelerations. The biggest change was for 40 g's of acceleration. While the compression forces required for blends mixed at 70 and 80 g's were higher, the change in compression force due to blending time was less than at 40 g's. A strong interaction between blending time and acceleration was obtained, affecting the compression force significantly ($p << 0.05$). The increase in the measured compression force can be attributed to the increasing density of the blend. More energy (pressure) is needed to compress a denser powder than a less dense powder into the same tablet dimensions.

The tableting compression force was also correlated to the total energy to the blend per unit mass (Figure 4-10c). Since there was a strong interaction between the blending time and acceleration on the compression force, the same behavior was expected for the energy per unit mass (i.e. function of blending time and acceleration as described in equation 4-2). The compression force increased with increasing energy per unit mass following a power law with a very good fit (R^2 = 0.9299). This demonstrates again that using the energy per unit mass as a resonant acoustic mixing variable is a better choice than choosing variations of accelerations and blending times.

(a)

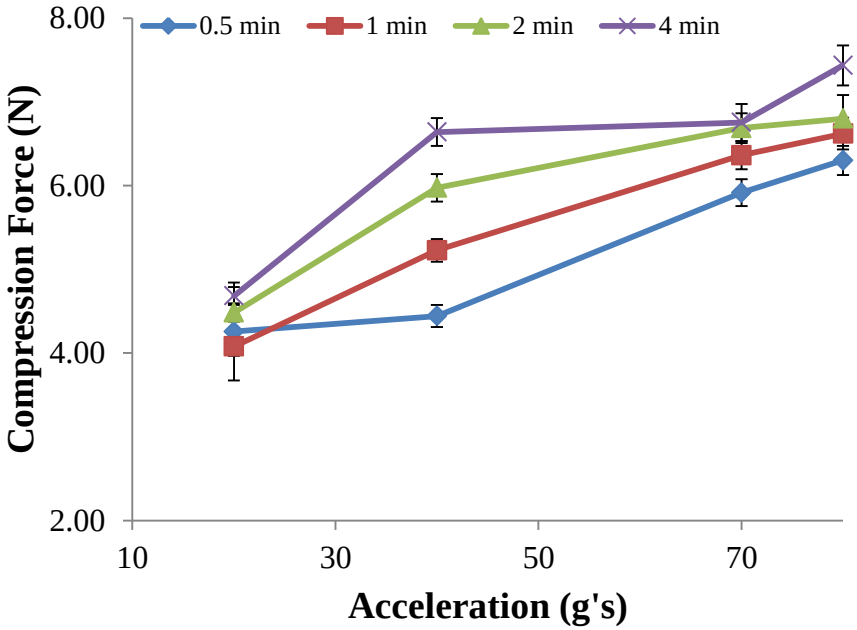

(b)

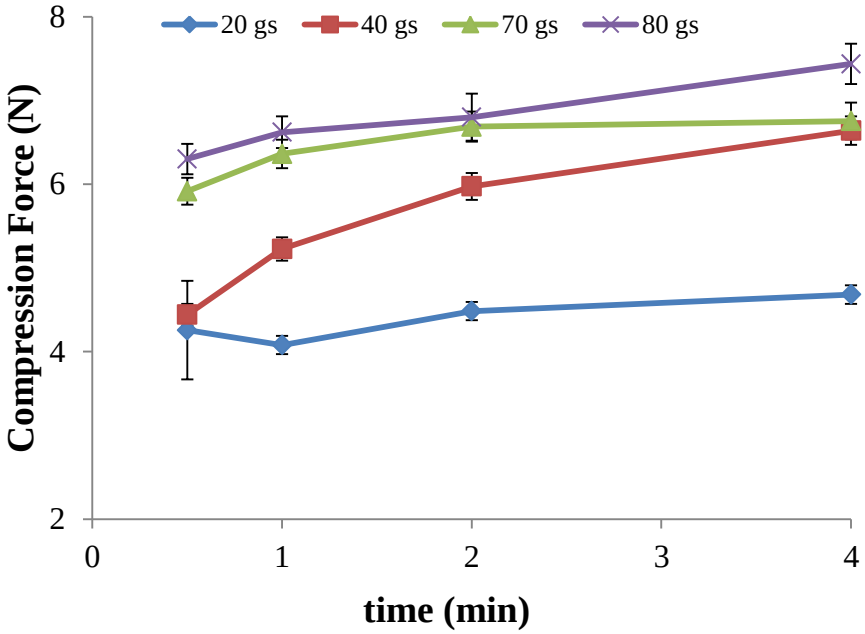

(c)

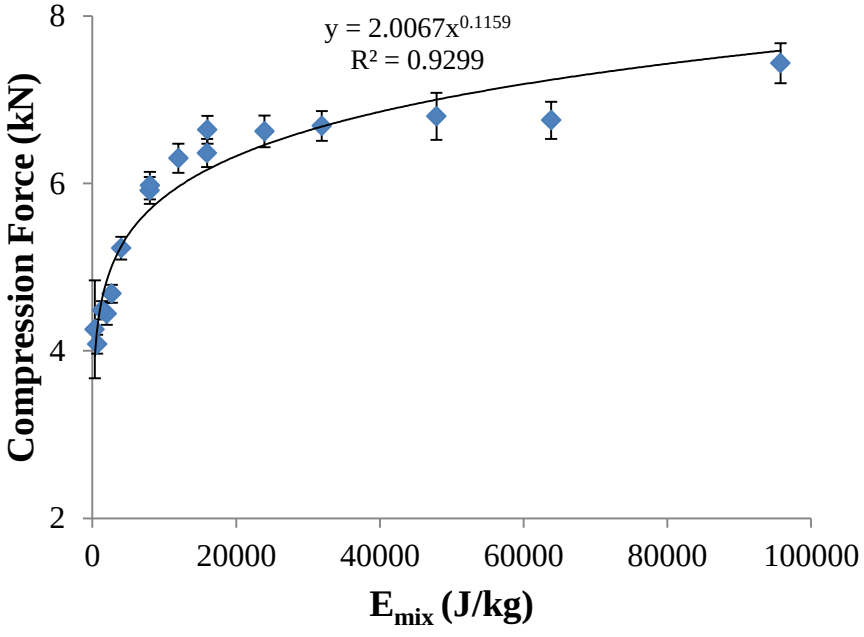

Figure 4-10. Effect of (a) acceleration, (b) blending time and (c) total energy to the blend per unit mass on tableting compression force.

4.3.2.2 Tablet Weight

The effect of acceleration and blending time on tablet weight was also considered. The mean tablet weight significantly increased ($p << 0.05$) with increasing acceleration (Figure 4-11a). The tablet weight also increased ($p << 0.05$) with increasing blending time (Figure 4-11b). This increase in tablet weight at constant fill volume, as an indirect result of increase in blending time and acceleration, can be explained by the rise in bulk density. The tablet mean weight increase was the least for blends mixed at 20 g's. Blends mixed at 40 g's had the greatest change in tablet weight as a function of blending time. Tablet weights were similar at 70 and 80 g's and the rate at which the tablet weight increased as a function of blending time was also similar for both values of acceleration.

(a)

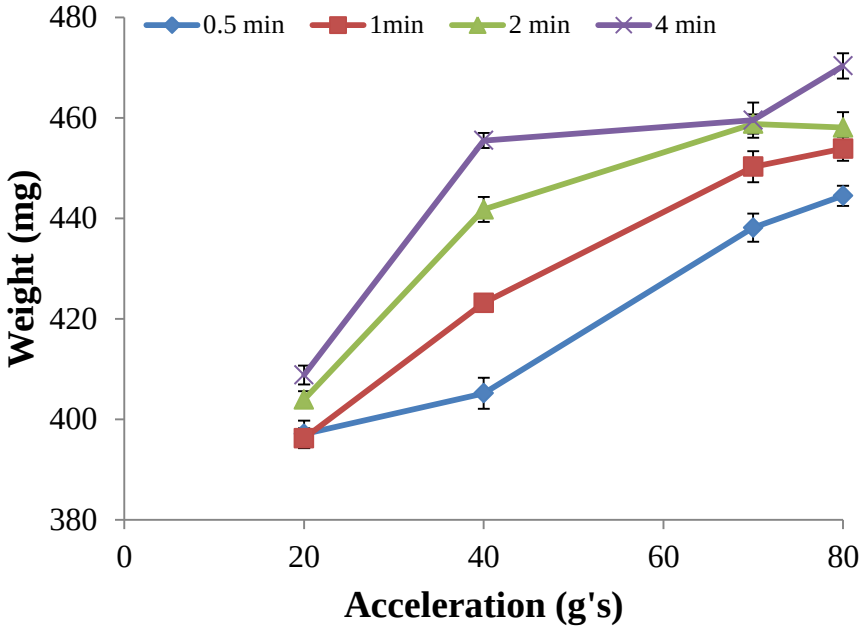

(b)

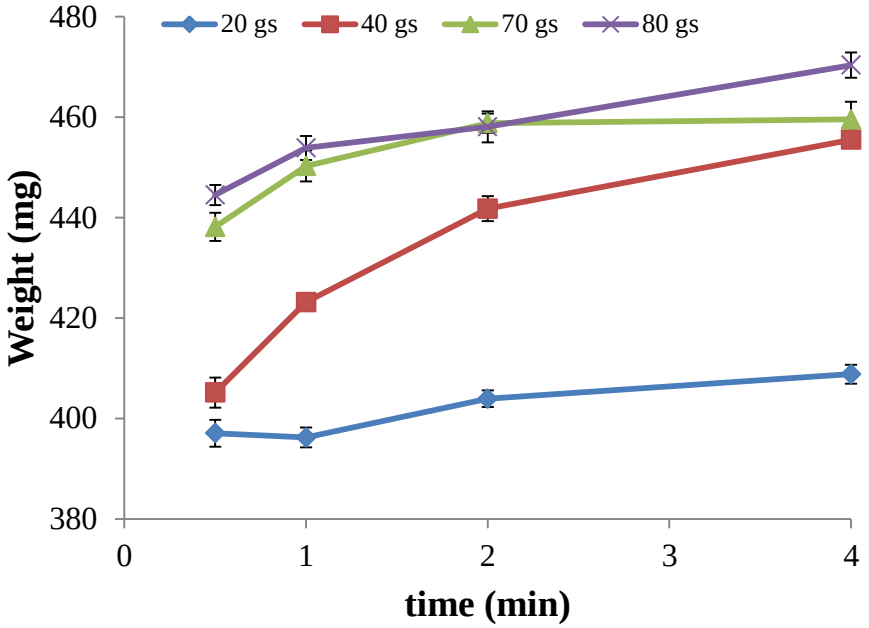

Figure 4-11. Effect of (a) acceleration and (b) blending time on tablet weight.

To confirm that the tableting compression force increases with an increase in density of the blends (translated into the tablet weight) using the same fill volume, the compression force as a function of the mean tablet weight was plotted in Figure 4-12. Indeed, the tablet weight increased with increasing compression force, showing a linear relationship. The tablet weight as a function of total energy per unit mass is shown in Figure 4-13. The tablet weight increased with an increase in energy per unit mass following a power law (R^2 = 0.9406). The energy per unit mass can also be used to predict the final tablet weight of lubricated blends mixed using resonant acoustic mixing.

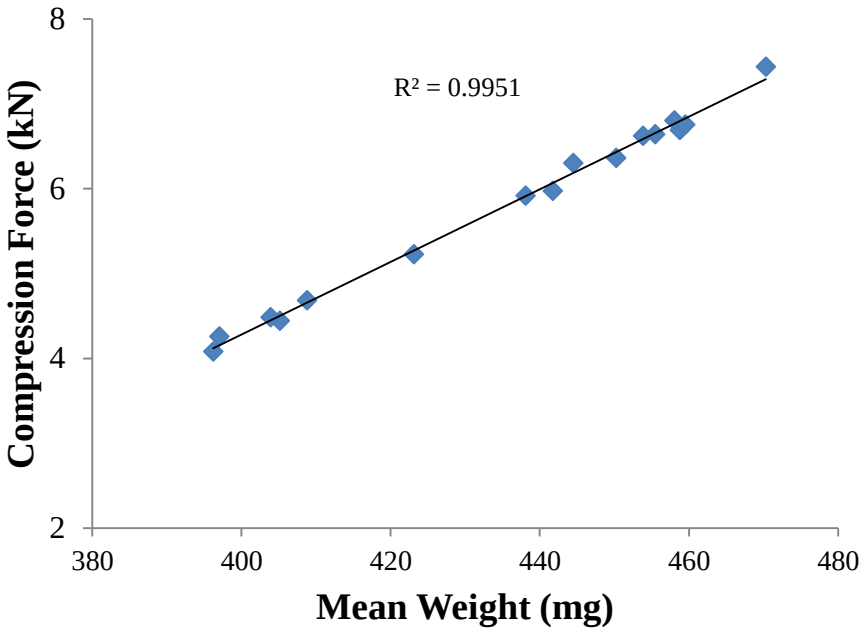

Figure 4-12. Compression force as a function of tablet mean weight.

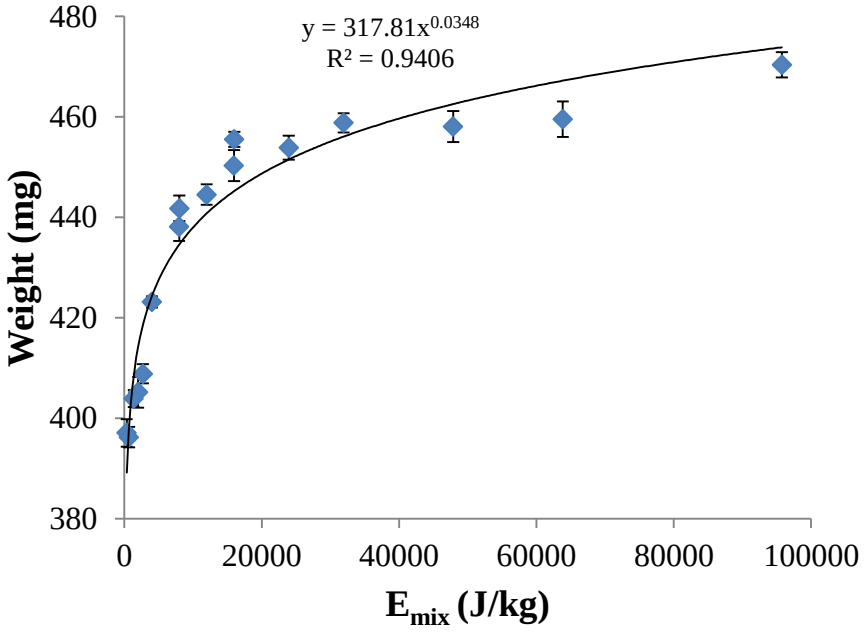

Figure 4-13. Tablet weight as a function of total energy to the blend per unit mass.

4.3.2.3 Tablet Hardness

The tablet hardness was studied as a function of acceleration and total blending time. The hardness decreased with increasing acceleration ($p << 0.05$) as shown in Figure 4-14a. The hardness also decreased with increasing blending time (Figure 4-14b). These changes were more evident at lower accelerations (20 g's and 40 g's). A gradual change was seen for 40 g's while for 70 g's and 80 g's the tablet hardness seemed to have reached a plateau after 1 and 2 minutes of blending, respectively.

(a)

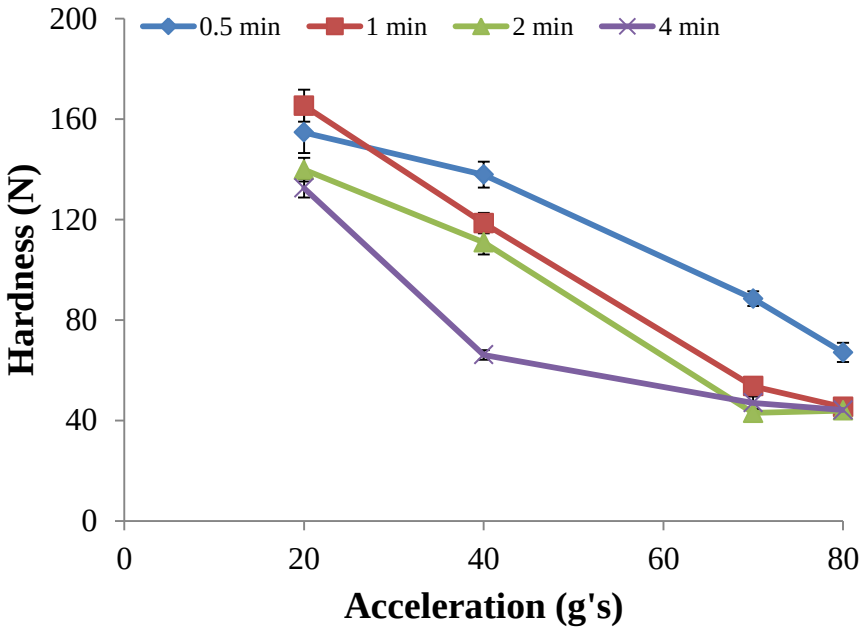

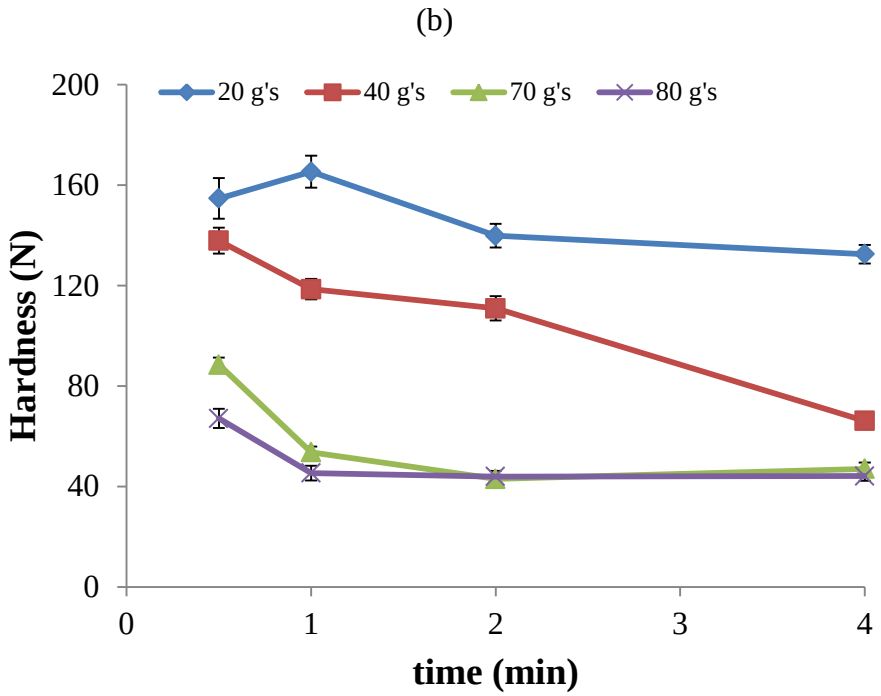

Figure 4-14. Effect of (a) acceleration and (b) blending time on hardness. Error bars were calculated from the standard deviation of the hardness from 10 tablets.

The hardness as a function of compression force is shown in Figure 4-15, where hardness decreased with increasing compression force. As mentioned, the density of the powder blend, as measured by the bulk and tapped density, increased with increasing acceleration and blending time, making the powder more compact. However, this also made the blend more hydrophobic. As the powder blend was more extensively lubricated, the tablet hardness decreased, while the required compression force needed was higher due to the increase in density. The tablet hardness was correlated to the total energy to the blend per unit mass (Figure 4-16). The tablet hardness decreased with increasing energy per unit mass following a power law (R^2 = 0.8862). This demonstrated once again that the energy per unit mas can be used as an input variable for resonant acoustic mixing.

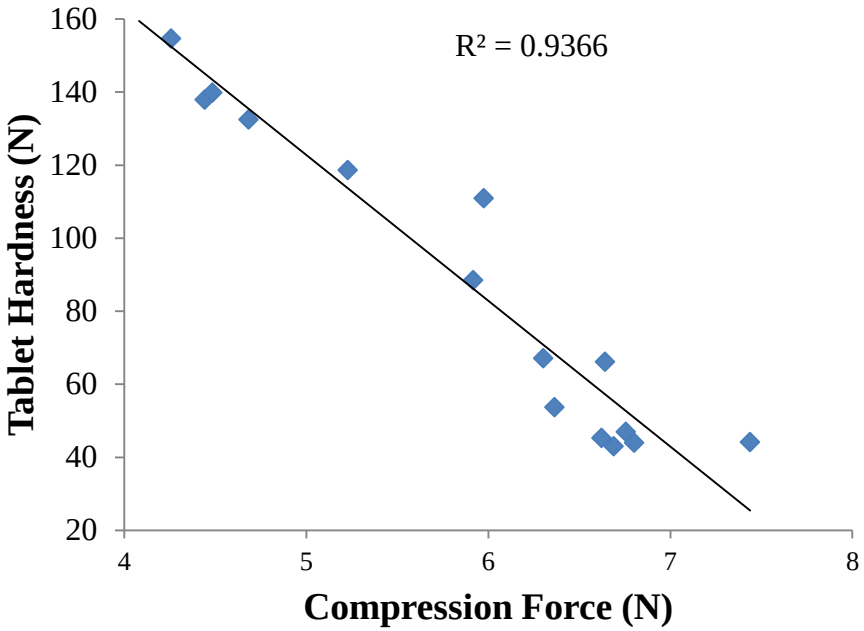

Figure 4-15. Tablet hardness as a function of compression force.

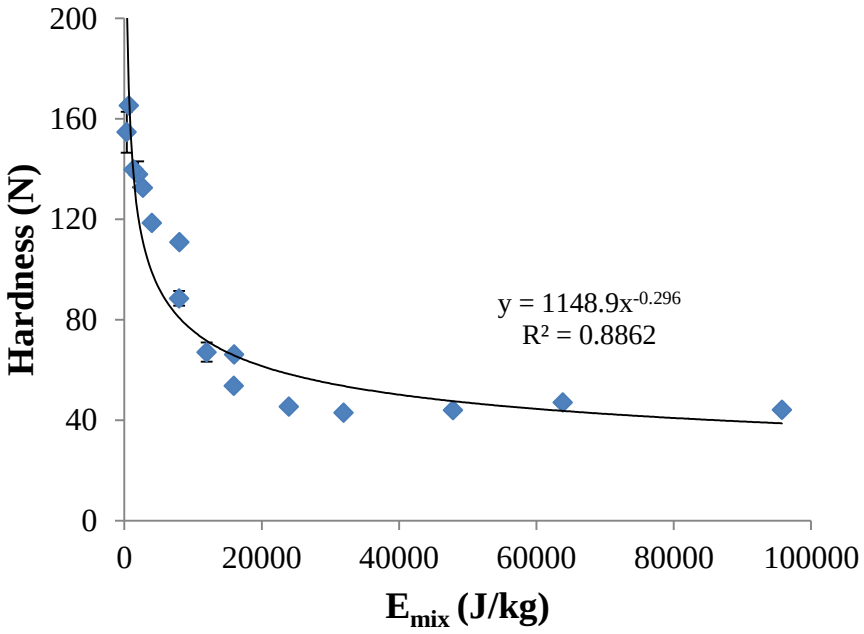

Figure 4-16. Tablet hardness as a function of total energy to the blend per unit mass.

4.3.2.4 Tablet Dissolution

Tablet dissolution is often one of the most important parameters in tablet characterization. Previous studies have shown that tablet dissolution is affected by shearing intensity and total shear during lubrication [91]. The dissolution profiles for blends with the same blending time at various accelerations mixed in the RAM were compared here. The dissolution profiles for 0.5 minutes of blending are shown in Figure 4-17. The dissolution profiles for 20 and 40 g's (Figure 4-17a) indicate large variations in the amount of drug dissolved. The variability in dissolution rate was higher for 20 g's than for 40 g's. The total amount of drug dissolved was only about 80% of the nominal 3% w/w APAP. These results might be an indication that the blend was not well mixed after 0.5 minute of blending at lower accelerations. This is shown by the large variations in the percentage amount of drug found in the tablets at 0.5 minutes for 20 g's and 40 g's. The dissolution profiles for 70 and 80 g's after 0.5 minute of blending (Figure 4-17b) indicate that the blend homogeneity was better with less variability than the results obtained from 20 and 40 g's. The amount of drug dissolved is close to 100% of the nominal amount of drug in the blend. A slight decrease in the amount of drug dissolved due to an increase in acceleration (from 70 g's to 80 g's) was also observed.

(a)

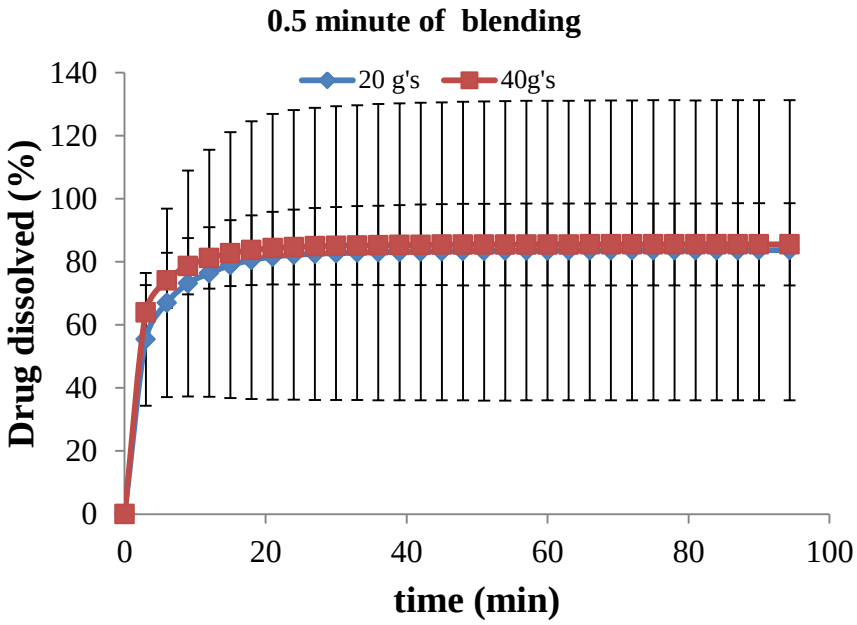

(b)

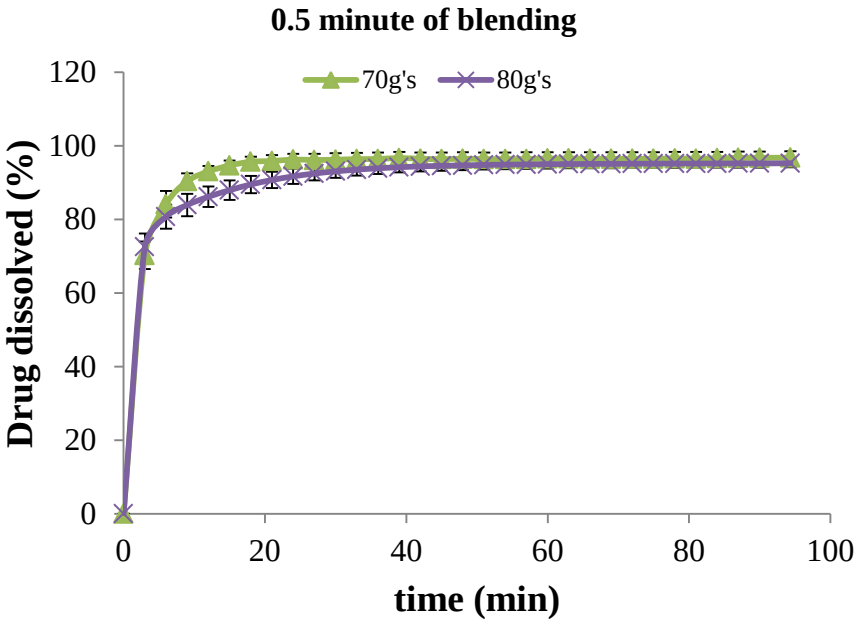

Figure 4-17. Dissolution profiles for tablets made with blends after for 0.5 minutes of resonant acoustic mixing at (a) 20 and 40 g's and (b) 70 and 80 g's of acceleration.

The dissolution profiles for blending times of 1, 2 and 4 minutes are shown in Figure 18. The dissolution profiles for 1 minute of blending time (Figure 4-18a) shows the differences between accelerations. At higher acceleration, less drug goes into solution. These results are in agreement with previous results that indicated that an increase in hydrophobicity (caused by an increase in acceleration in our case) is correlated to a decrease in the amount of drug dissolved [10]. Similar trends were seen for 2 minutes of blending (Figure 4-18b) as well as 4 minutes of blending (Figure 4-18c). The difference in amount of drug dissolved at higher accelerations is less after longer blending times.

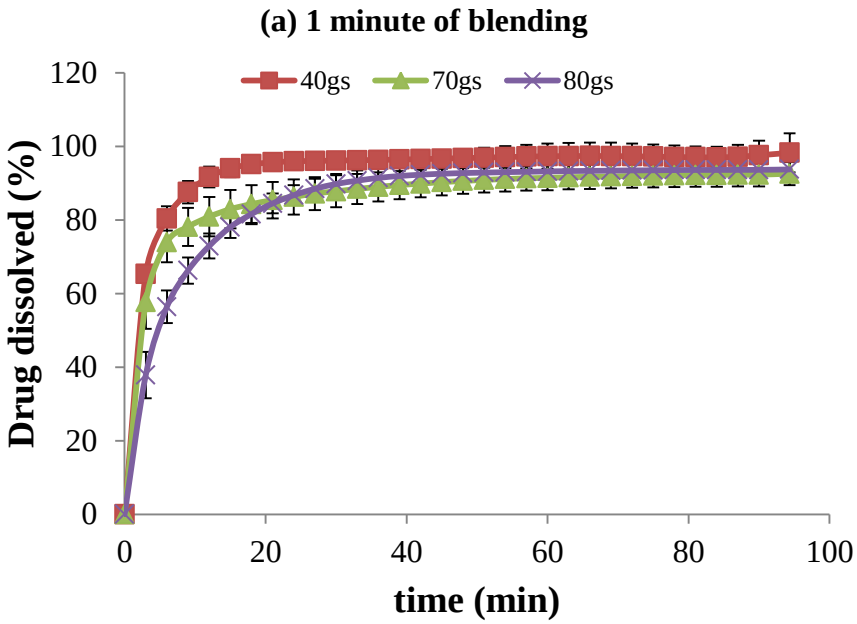

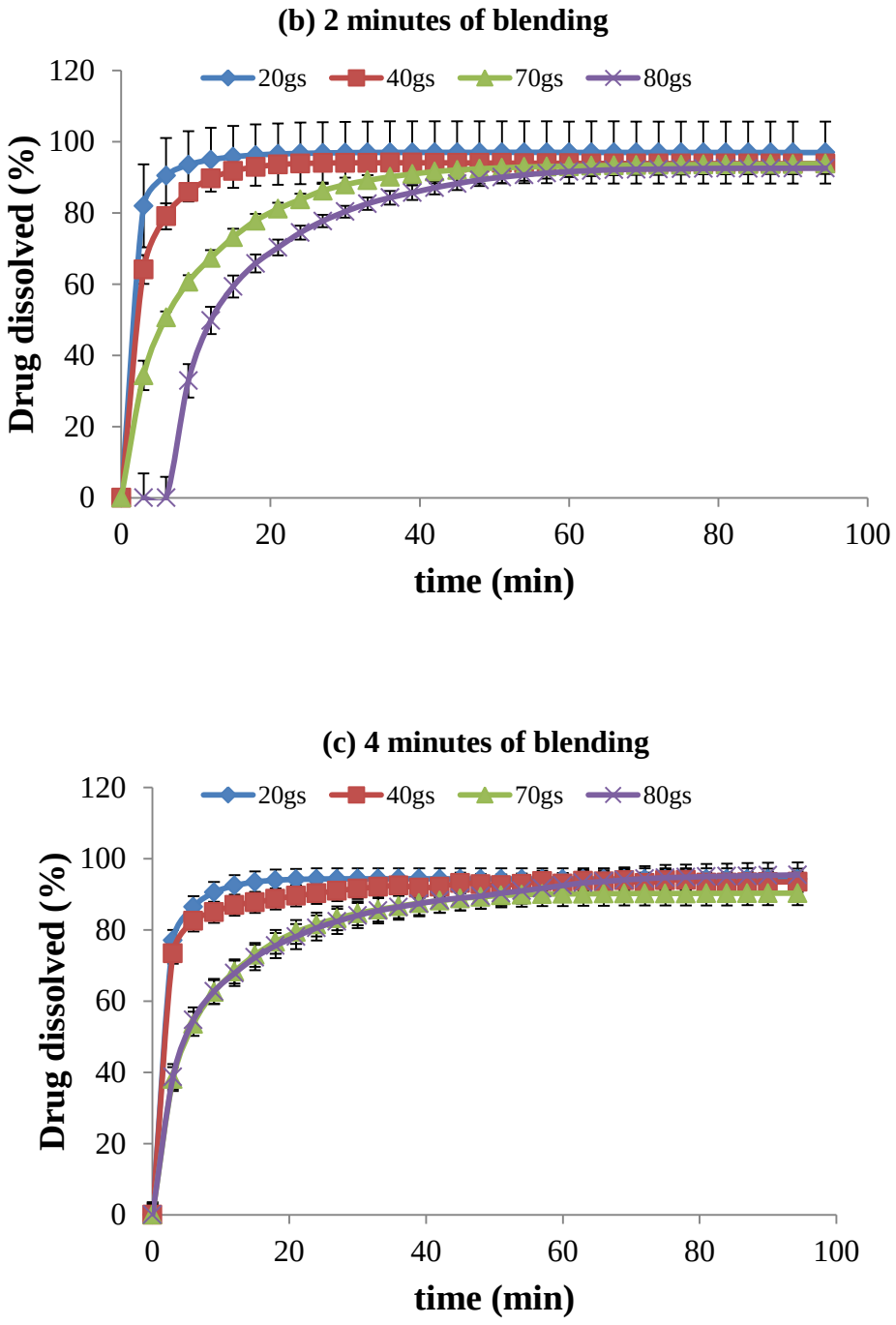

Figure 4-18. Dissolution profiles for tablets made with blends after (a) 1, (b) 2 and (c) 4 minutes of resonant acoustic mixing.

In order to examine the effects of acceleration and blending time on the amount of drug dissolved, the amount of APAP dissolved after 6 minutes of dissolution time was

considered. The effect of acceleration on the amount of APAP dissolved is shown in Figure 4-19a. For 0.5 minute of blending, the amount of APAP dissolved after 6 minutes increased with increasing acceleration. This might be due to the fact that a more homogeneous blend is obtained at higher accelerations when mixing for short periods of time, increasing the chance that the nominal concentration of the API under investigation was reached. An opposite trend was observed for 1, 2 and 4 minutes of blending where the amount of APAP dissolved after 6 minutes of dissolution decreased with increasing acceleration. This observation can be explained by the higher lubrication (hydrophobicity) obtained when mixing for longer mixing times at higher accelerations.

The amount of APAP dissolved after 6 minutes of dissolution time was also considered as a function of blending time for the various accelerations used (Figure 4-19b). For lower accelerations (20 and 40 g's), the amount of APAP dissolved increased as a function of blending time. The variation in amount of APAP dissolved for 20 g's indicated that the variation in the drug concentration in the measured tablets is large. At 40 g's, the amount of APAP dissolved did not seem to change much. The trends obtained for 70 and 80 g's were the same as those obtained with increasing acceleration. The amount of APAP dissolved decreased with increasing blending time due to increase in hydrophobicity of the powder blend. Overall, there is an increase in dissolution with increasing mixing time at low accelerations and a decrease in dissolution with increasing mixing time at higher accelerations.

(a)

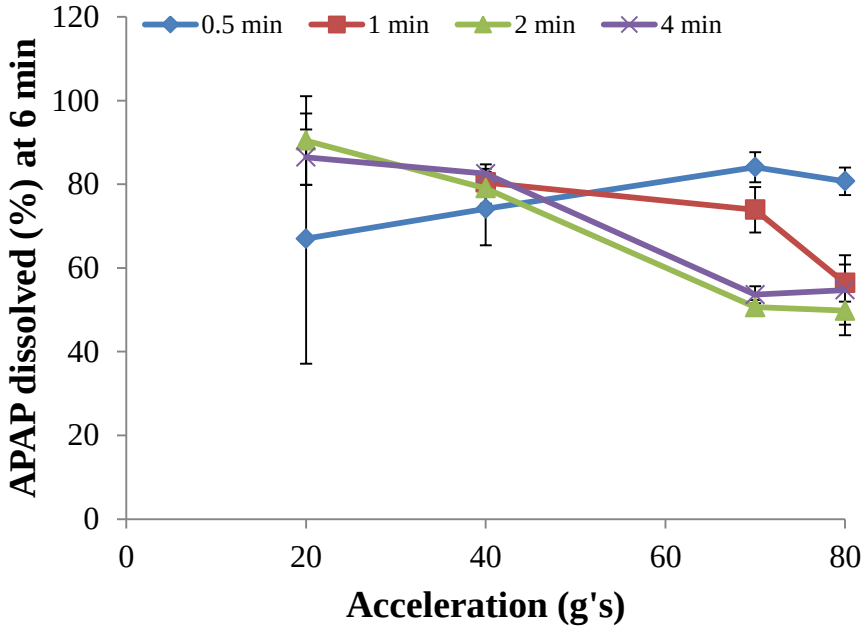

(b)

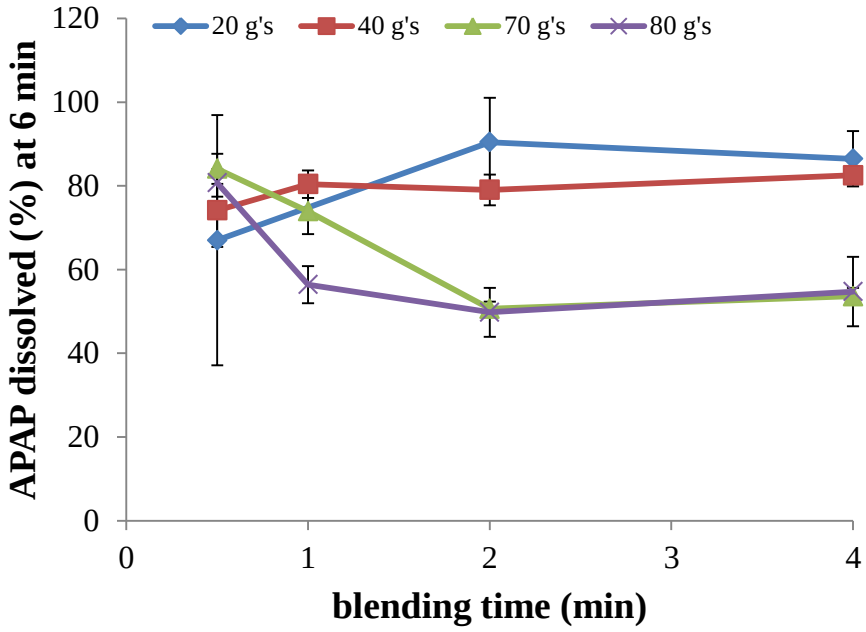

Figure 4-19. Amount of APAP dissolved after 6 minutes of dissolution time as a function of (a) acceleration and (b) blending time.

4.4 Conclusions

This chapter continued the characterization of a laboratory scale resonant acoustic mixer used for pharmaceutical powder blending. Lubricated blends were considered. The effects of acceleration, blending time and total energy to the blend per unit mass on the blend material properties and tablet characteristics were assessed. The particle size, the bulk density, the tapped density and the compressibility were considered as the material properties of the blends studied. For the tablets compressed, the tableting compression force and tablet hardness, weight and dissolution were considered. Overall, powder blend material properties and tablet characteristics were affected by changes in blending parameters during resonant acoustic mixing.

The particle size significantly changed due to acceleration and blending time. An increase in the d_{10} fraction was found with increasing acceleration and blending time. The same trend was also observed for bulk density and tapped density of the powder blends. The compressibility of the powder blends decreased with increasing blending time. These differences can be attributed to the effect of shear and strain during the rapid movement of the particles caused by the high input energy going to the blend during resonant acoustic mixing. An improvement in flowability of the blend was obtained with increase in acceleration and blending time. Owing to higher shear and shearing intensity, an increase in blend hydrophobicity was observed with increase in acceleration and mixing time.

The increase in hydrophobicity is suspected to have accounted for a subsequent decrease in tablet hardness. At constant fill volume and tablet thickness, the tableting compression force and tablet weight significantly increased with increasing acceleration

and blending time. These results were caused by the higher blend density obtained. The dissolution of the tablets indicated some interesting results. At lower accelerations and mixing time of 0.5 minutes, large variations in the amount of drug dissolved were observed. Variations decreased and the amount of drug dissolved reached the nominal blend concentration at higher accelerations at the same mixing time. However, for blending times of 1 minute or greater, the amount and rate of drug dissolution was found to decrease with increasing acceleration.

Higher accelerations and longer blending time increased the density of the powder blends. However, it also increased the blend hydrophobicity which lowers the tablet hardness and dissolution. Hence, optimum blending parameters depending on the formulation requirements need to be considered. A mixing time of one or two minutes at acceleration of 40 g's seems to fulfill these criteria. All the material properties of the blend, and the tableting and tablet properties were also correlated to the total energy to the blend per unit mass. All measured properties, except hydrophobicity, yielded a power law when correlated to the energy per unit mass. The total energy to the blend per unit mass should be used as the input variable for resonant acoustic mixing instead of the acceleration and total blending time.

Chapter 5 Micro Characterization of Resonant Acoustic Mixing Using Near-Infrared Chemical Imaging

5.1 Summary

In this chapter, the characterization of a resonant acoustic mixer (RAM), which has been shown to efficiently mix pharmaceutical powders with low concentrations of cohesive APIs, is continued. The mixing performance of the RAM and the effects of resonant acoustic mixing on powder blends and tablets properties were characterized in Chapters 4 and 4, respectively. It was found that the RAM is capable of mixing cohesive APIs in as low as 30 seconds while the amount of energy input can be used to control the materials properties of lubricated blends as well as the properties of final product (i.e. tablets).

The main objective of this chapter was to investigate the main effects of process parameters, acceleration (mixing intensity) and blending time, on the micro-mixing properties of pharmaceutical powder blends produced in a laboratory RAM. NIR-CI was used to measure the micro-mixing properties presented in this study. Qualitative (i.e. chemical images) and quantitative analyses (e.g. mean diameter of aggregates) were performed. Larger aggregates of API were found at lower accelerations and shorter mixing times. The micro-mixing results obtained in this study corroborate previous findings on the mixing performance of this blender (Chapter 3). Overall, the resonant acoustic mixing performance increased with increasing acceleration and mixing time. Mixing in the RAM efficiently reduced the overall aggregate size of the cohesive API (semi-fine APAP) used.

5.2 Materials and Methods

5.2.1 Materials

The materials used in all experiments were semi-fine acetaminophen (Mallinckrodt, Raleigh, North Carolina, USA), magnesium stearate (MgSt, non-Bovine, Tyco Healthcare / Mallinckrodt, St. Louis, Missouri, USA) and silicified microcrystalline cellulose (Prosolv HD90, JRS Pharma, Germany). The mean particle size of each material used is listed in Table 5-1. The particle size was measured using a Beckman Coulter laser diffraction particle size analyzer.

Table 5-1. Particle size of materials used.

Material	Mean Particle Size (μm)
Semi-fine acetaminophen	45
Magnesium stearate	10
Prosolv HD90	110

5.2.2 Resonant Acoustic Mixing

A laboratory resonant acoustic mixer (LabRAM, Resodyn, Butte, MT, USA), shown in Figure 5-1, was used to make all the powder blends examined in this study. The RAM is a new type of mixer that works on the application of low frequency, high intensity acoustic field facilitating the movement of the loose powder mass to induce mixing. The acoustic mixing principle works on the creation of micro-mixing zones throughout the entire vessel while facilitating bulk movement of the materials. The principles by which the RAM works are explained in more detail elsewhere [26].

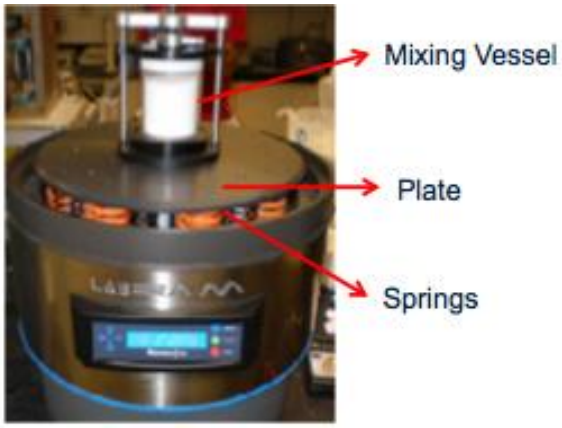

Figure 5-1. Laboratory scale resonant acoustic mixer with a 236-mL mixing vessel used in all experimental studies.

A preliminary study was performed to develop the near-infrared chemical imaging method used in all experiments here. The mixing parameters are specified in Table 5-2. The APAP concentration used in this case was 10% w/w. A commonly used concentration of MgSt (0.75% w/w) was used in two of the blends. Two blending parameters, acceleration (shear rate) and total blending time (total strain) were used. The first combination of blending parameters was 20 g's of acceleration for 2 minutes for blends 1 and 2. The second combination of blending parameters was 70 g's of acceleration for 4 minutes for blends 3 and 4. These two sets, based on what was previously learned for the RAM [24, 25], yielded distinctive blends, which could be categorized as "poorly mixed" (blends 1 and 2) and "well mixed" (blends 3 and 4). This preliminary study was performed to confirm that the technique was indeed measuring the materials of interest.

Table 5-2. Preliminary study to determine the feasibility of the near-infrared chemical imaging analytical method. A higher concentration of API (10% w/w) was used.

Blend	APAP (%)	MgSt (%)	Blending Parameters	"Mixing Extent"	Aggregate Mean Area (mm^2)
1	10	0.75	20 g's - 2 min	Poorly	0.219
2	10	0	20 g's - 2 min	Poorly	0.219
3	10	0.75	70 g's - 4 min	Well	0.211
4	10	0	70 g's - 4 min	Well	0.199

A second set of blends was used to characterize the effects of resonant acoustic mixing on the degree of agglomeration of the cohesive API at a lower concentration (3% w/w) and of the lubricant (MgSt, 1% w/w). Nine conditions (three mixing times by three accelerations) were explored (Table 5-3). A 236-mL vessel, filled up to 60% by volume, was used for all the experimental work presented here.

Table 5-3. Conditions Studied. Lower API concentration with 3% w/w API + 1% w/w MgSt + 96% w/w Prosolv.

time (min)	acceleration (g's)
0.5	20
1	40
4	80

5.2.3 Sampling

Since the objective for the first set of blends was to characterize the near-infrared chemical imaging method, only one sample from each blend was examined. For the second set of experiments, ten samples were extracted from the mixing vessel and transferred to 10-mL Ziploc bags. A 1-mL disposable powder thief (Sampling Systems, Warwickshire, UK) was used to extract the samples from each powder blend. The thief was carefully inserted into the powder bed at each sampling location to minimize powder bed perturbations. Since the volume of the mixing vessel was small, each experimental

run was performed with fresh powder in order to minimize perturbations caused by stopping repeatedly the blending process and by excessive sampling. Ten samples were taken from the powder bed in the following manner: near the wall at the perimeter of the vessel (8 samples), in the center (1 sample), and half way between the wall and the center (1 sample), as shown in Figure 5-2. The samples were carefully transferred to the Ziploc bags and the air was removed to prevent any movement of the mixed powder. The samples were carefully removed from the Ziploc bags onto sampling trays for chemical imaging analysis.

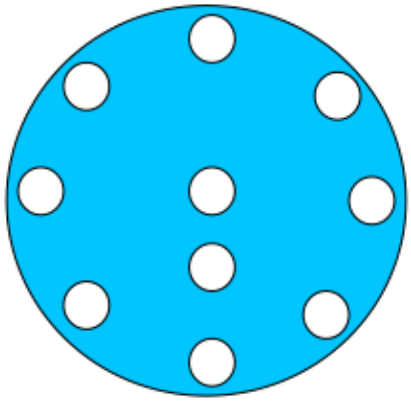

Figure 5-2. Sampling Procedure. Samples were extracted from the powder bed at each location as shown in the top-view schematic of the vessel (picture not to scale).

5.2.4 Near-infrared Chemical Imaging

Near Infrared Chemical Imaging (NIR-CI) was used to study the micro-mixing properties (spatial information) of the components in the powder blends obtained. A Spectral Dimension SyNIRgy chemical imaging spectrometer equipped with a Stirling cooled InGaAs focal plane array detector, a liquid crystal tunable filter, a microscope stage and computer-controlled illumination was used (Malvern Instruments, Worcestershire, UK). The chemical image data were collected in the diffuse reflectance

mode and consisted of 320 x 256 pixels, with a spectral range of 1300 to 2300 nm (10-nm spectral spacing), forming the spectral hypercube. A 40-µm objective (field of view) measuring an area of 13 mm x 10 mm was used.

Chemical image pre-processing, pretreatment and analysis were performed with the "ISys 5.0" cross-platform chemical imaging analysis software (Malvern Instruments, Worcestershire, UK). The first step was to background-correct each chemical image. Dark and background references were obtained using identical settings as for the chemical images. The background correction converted the spectral data into absorbance units, normalizing the signal from each chemical image taken. Once the background correction was performed, the spectral data for each chemical image was smoothed using a low pass triangle squared spectral Fourier filter. Another step in the pre-processing was a "bad pixel" correction, which used the white reference to determine the few spatial and spectral pixels that were outliers (bad pixels) due to camera imperfections. These bad pixels were removed and replaced with the average pixel number of their non-outlier neighbors for each chemical image collected [27].

5.3 Chemical Imaging Analysis

5.3.1 Chemical Images

Near infrared (NIR) spectra of acetaminophen (APAP), magnesium stearate (MgSt) and silicified microcrystalline cellulose (Prosolv) were obtained to develop the method. The spectra of the APAP, MgSt and a sample blend are shown in Figure 5-3. The spectra were pre-treated using the standard normal variate (SNV) and a Savitzky-Golay second derivative with a filter length of 11 and filter order of 3. The wavelengths that showed the

greatest differences in the spectra were observed at 1660 nm for APAP and 1730 nm for MgSt (Figure 5-3). All the chemical images analyzed in this paper were produced using a univariate analysis approach. The pre-treatments minimized the differences obtained from physical differences, such as particle size and density.

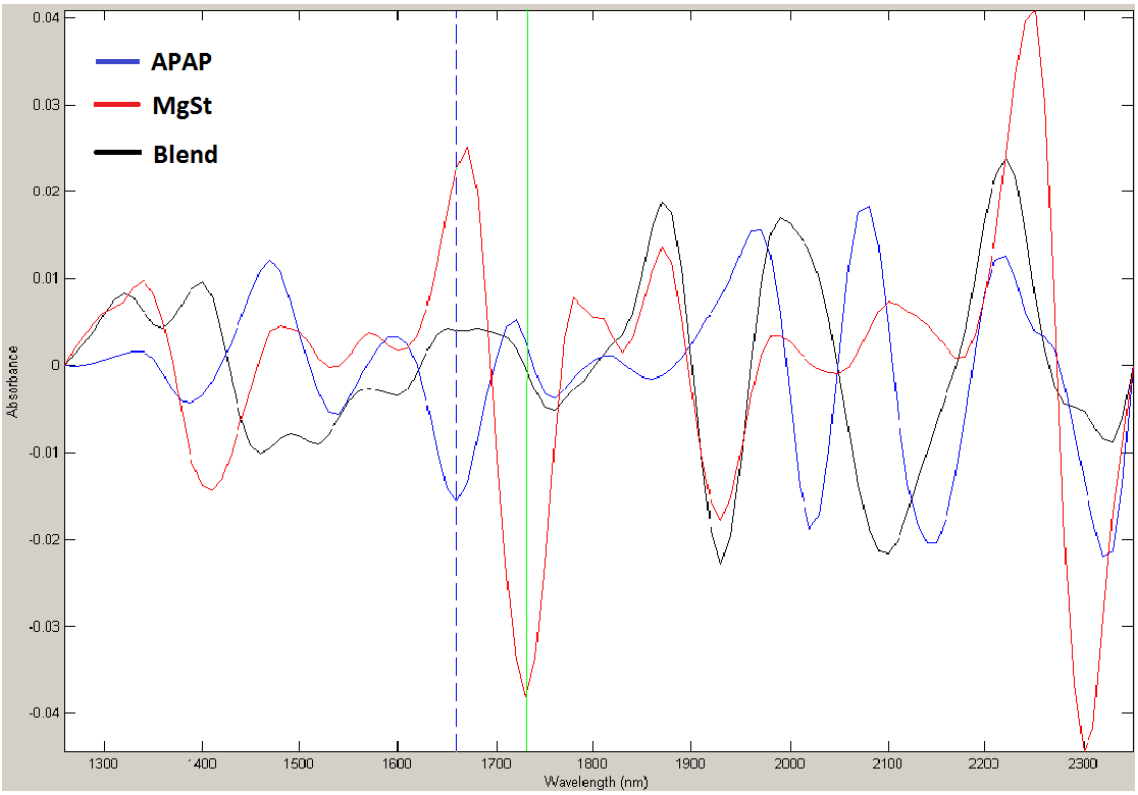

Figure 5-3. Spectra of API (APAP), lubricant (MgSt) and blend. The spectra here showed large differences at 1660 nm for APAP and 1730 for MgSt.

5.3.2 Intensity images

Measured intensity images for both APAP and MgSt were obtained after pre-treatment. These images show the intensity, in absorbance units, of all the pixels in each sample blend. Each image allows the user to visually estimate the aggregate size of the components of interest. This analysis is purely qualitative and is only useful when large

aggregates of the ingredient of interest are present. To obtain quantitative results for this type of experiments, binary images within a predefined threshold were analyzed.

5.3.3 Determination of aggregate size

Since the wavelengths that showed the most difference for APAP and MgSt had negative intensity (absorbance) values, the thresholds used to obtain the binary images and identify aggregates were chosen as follows: the minimum intensity value was used as lower threshold and the value of the $[\text{mean} - 2 * \text{StdDev}]$ as the upper threshold, as shown in Figure 5-4. The mean and standard deviation (StdDev) were the values obtained from the second derivative intensity pixel distribution of the chemical image at each specified wavelength, depending on the ingredient under investigation. A binary image was created by assigning 1 to all pixels between the upper and lower thresholds and 0 to all other pixels. Once a binary image was obtained, it was treated with morphological filters to reduce threshold noise artifacts and artificial features. The morphological filters used were "clean" and "majority" as referred to in the chemical image analysis software. The clean filter removed isolated pixels in the binary image. The majority filter set a pixel to 1 in the binary image if a majority of pixels in its 3-by-3 neighborhood were 1's. After the morphological filtering, the aggregate statistical analysis was performed.

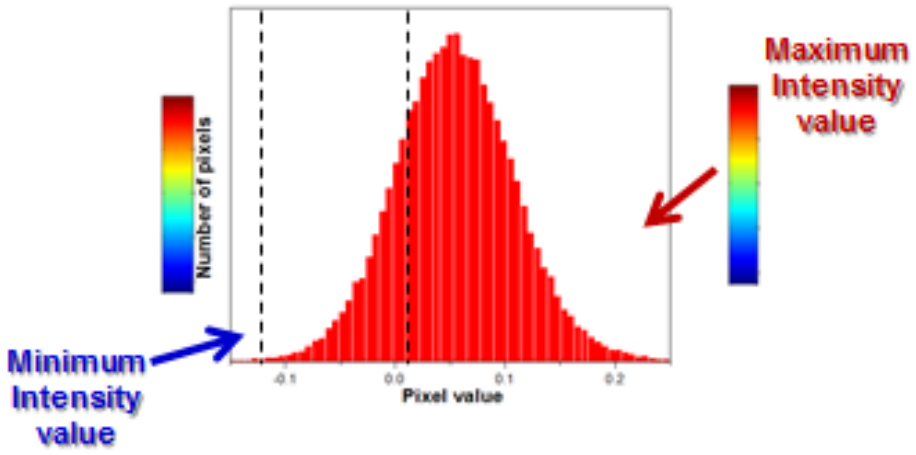

Figure 5-4. Minimum intensity value (lower threshold) and the [mean − 2 ∗ StdDev] (upper threshold) used to obtain binary images from the intensity images.

An aggregate was defined as a group of 9 (3-by-3) or more connecting pixels, all within the predetermined intensity thresholds. Aggregate statistical analysis was performed on the binary images obtained. The metrics obtained from the binary image statistics shown in this article were the API mean aggregate area, the standard deviation of the aggregate area and the percentage of area covered in each binary image by the API aggregates. .

The API mean aggregate area and the standard deviation of the aggregate area were calculated by approximating the area of each aggregate as a circle and averaging the area of all aggregates in each binary image. The percentage of area covered is the portion of each whole binary image covered by API aggregates. The area of each binary image obtained was approximately 10 mm by 12 mm. The effect of mixing time and acceleration on each of the metrics described are summarized and explained in this article.

5.4 Results and Discussion

5.4.1 Preliminary Study

The intensity and binary images for APAP for the preliminary studies are shown in Figure 5-5. The aggregates of APAP in the intensity images are composed of pixels with the lowest intensities (blue) and in the binary images are the pixels in black. Blends at lower acceleration (20 g's) and shorter mixing time (2 minutes) contained large aggregates of APAP. These APAP aggregates are larger than those found in blends processed at higher acceleration (70 g's) and longer mixing time (4 minutes) as shown in Table 5-2. These results were as expected since a higher acceleration and longer mixing time provide higher energy input into the blend, decreasing the degree of aggregation of the cohesive API [24].

(a)

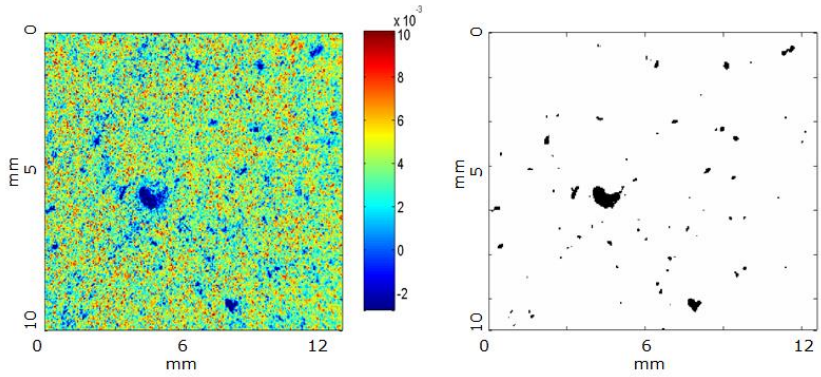

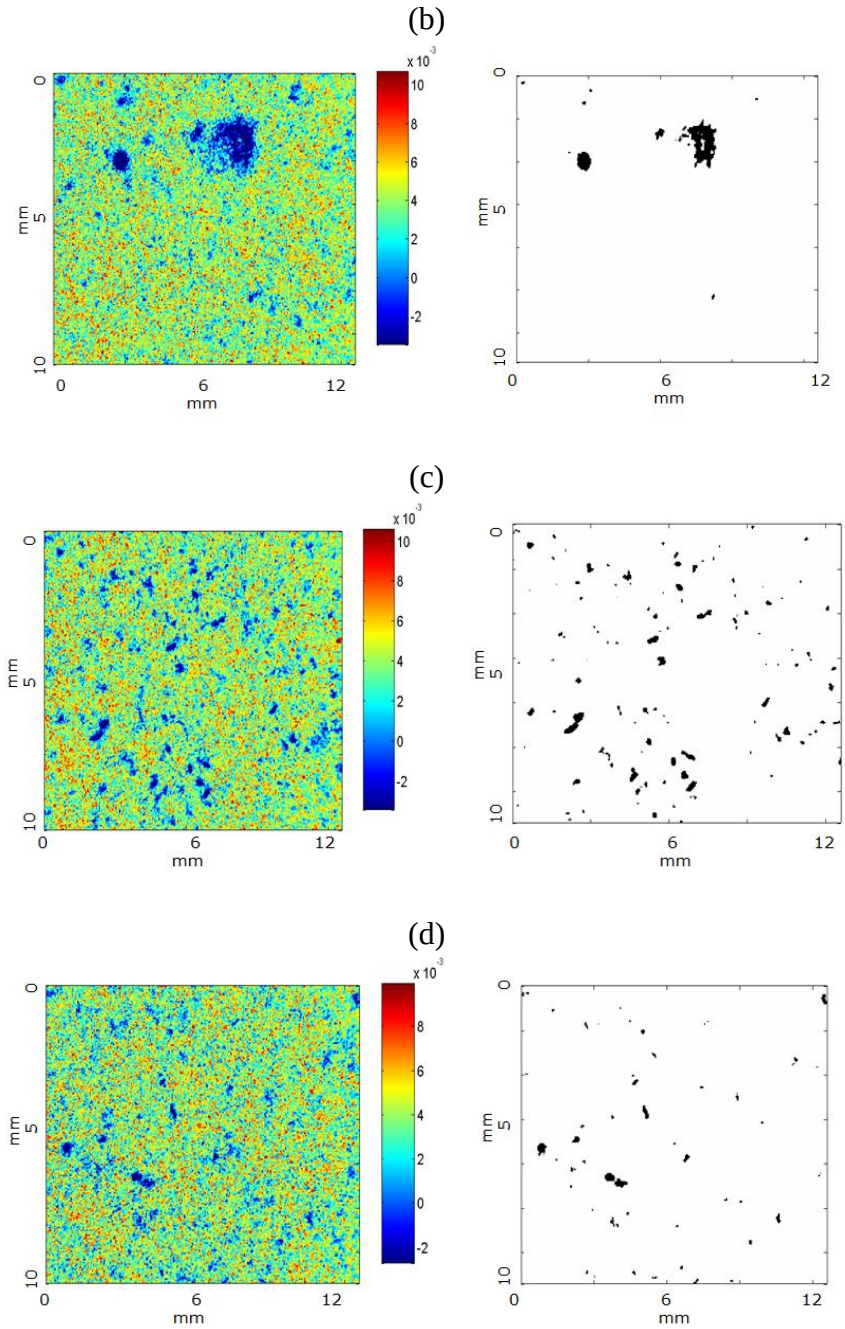

Figure 5-5. Intensity images at 1660 nm (left) and binary images (right) of APAP for (a) blend 1 (b) blend 2 (c) blend 3 and (d) blend 4. Blends are described in Table 2.

This preliminary study was also performed to corroborate that the NIR-CI technique worked to detect MgSt at the wavelength specified (1730 nm) and whether MgSt agglomerates could be detected using the described threshold. Intensity and binary

images for MgSt are shown in Figure 5-6. There was no noticeable difference in the results obtained for MgSt for the different mixing parameters. No large aggregates were detected using the lower and upper thresholds described. This means that the MgSt was well dispersed throughout the blend, confirming previous studies where MgSt mixed rapidly [24]. In all experiments here, a 40-μm objective (field of view) measuring an area of 13 mm x 10 mm was used. NIR-CI is not a good technique to identify single particles of MgSt. Although MgSt is considered a cohesive material, it is known to coat other particles within a blend and its final particle size after blending is well below 40 μm [17]. To detect MgSt using this technique, either the field of view or the threshold would have to be changed. The threshold used to detect MgSt was changed in the next subsection to qualitatively show the dispersion of MgSt onto the blends.

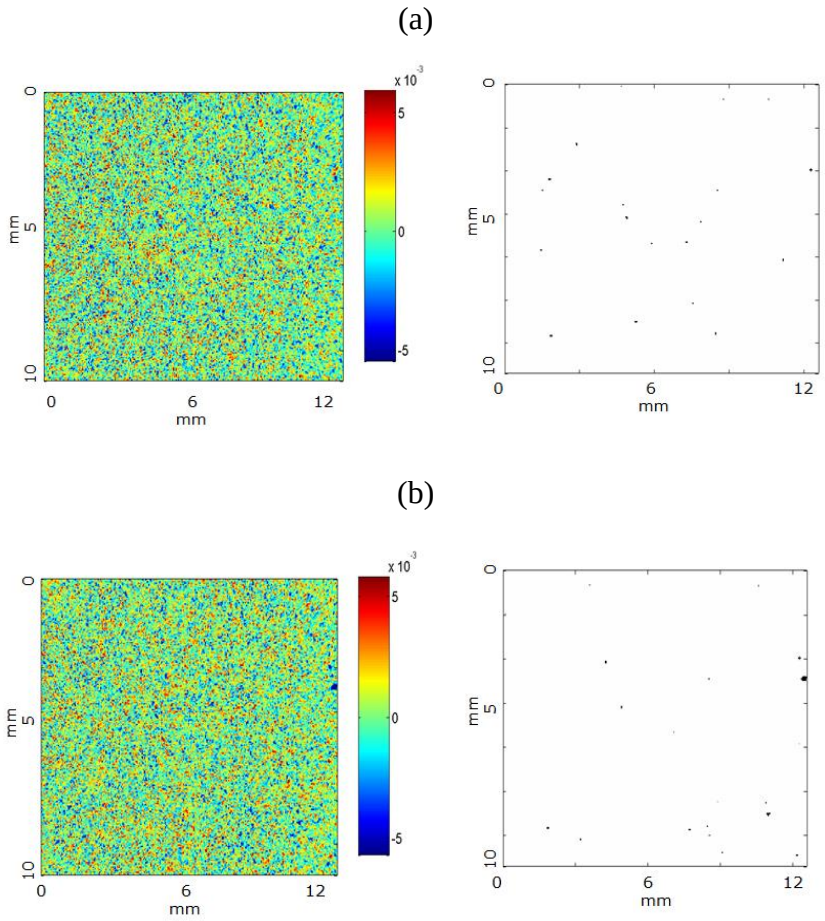

Figure 5-6. Intensity images at 1730 nm (left) and binary images (right) of MgSt for (a) blend 1 and (b) blend 3. Blends are described in Table 2.

5.4.2 Micro-mixing performance

A second set of conditions with a common blend was examined to describe the effect of the mixing parameters on the micro-mixing performance in the RAM. The aggregation and dispersion of APAP (3% w/w) and MgSt (1% w/w) in a common excipient (Prosolv) was studied. The acceleration and total blending time were varied as described in Table 5-3. Sample intensity and binary images of the API for this second set of experiments are shown in Figures 5-7 and 5-8. Blends mixed for 0.5 minutes at 20 g's (Figure 5-7) and 40 g's (Figure 5-8) are shown to describe the evident effect of acceleration on aggregation of

the API used. In this case, 5 images areas of 10 mm x 13 mm were concatenated to show several samples side-by-side.

(a)

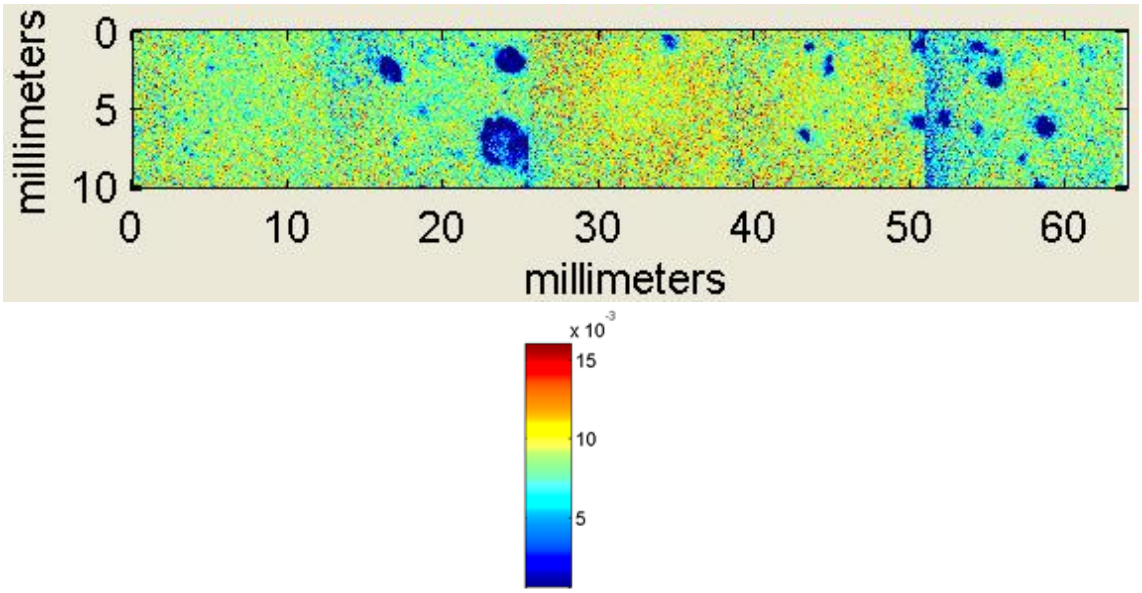

(b)

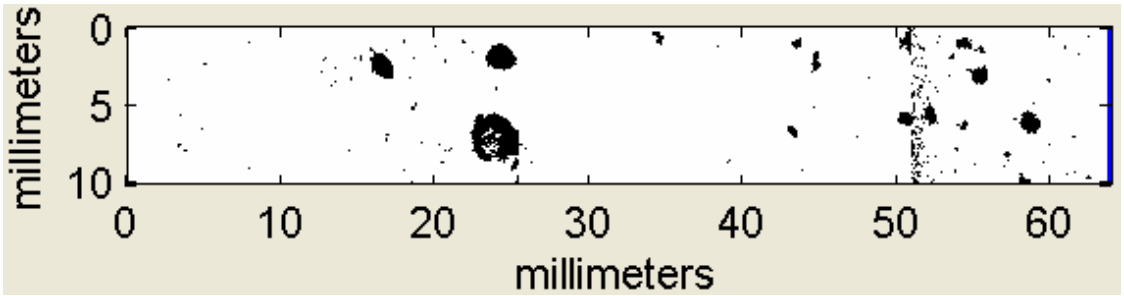

Figure 5-7. (a) Intensity and (b) binary images for APAP blended at 20 g's for 0.5 minutes. The blend studied here was composed of 3% APAP + 1% MgSt + 96% Prosolv.

(a)

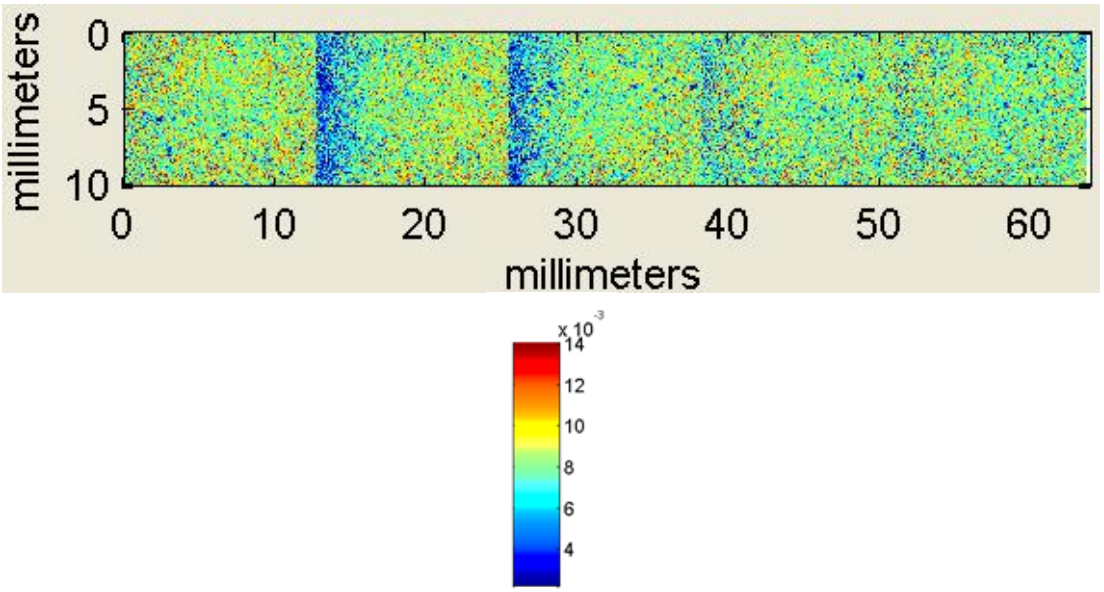

(b)

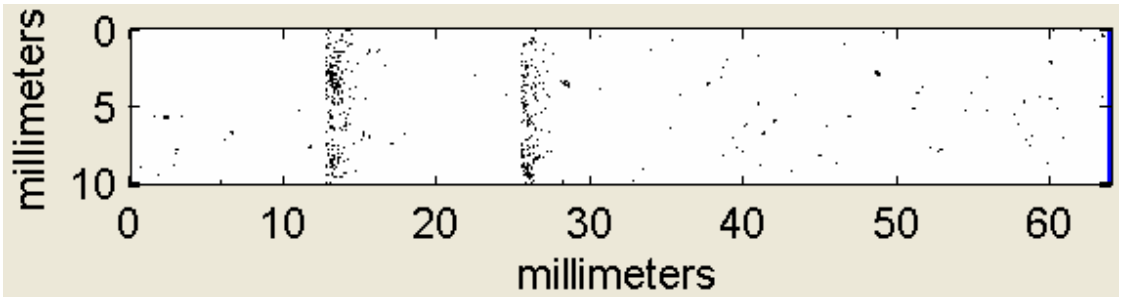

Figure 5-8. (a) intensity image and (b) binary image for APAP at 40 g's for 0.5 minutes. The blend studied here was composed of 3% APAP + 1% MgSt + 96% Prosolv.

Large APAP aggregates were detected using this technique at lower acceleration (20 g's - Figure 5-7) when compared to blends at higher acceleration (40 g's - Figure 5-8) for the same amount of mixing time. These results show that APAP is better mixed, showing less aggregation, at 40 g's than at 20 g's. These results are in accordance to the results presented in the previous subsection. This also confirms our previous work that

characterized the mixing behavior by quantifying the blend homogeneity of powder samples and tablets [24, 25]. Similar qualitative results to the 40 g's blended for 0.5 minutes were obtained for all other intensity and binary images for the rest of the conditions studied. Such results cannot be objectively interpreted just by visual examination; thus aggregate statistical analysis was performed on the binary images.

The main effects of the acceleration and total blending time on the API mean aggregate area, the standard deviation of the API aggregate area, and the percentage of area covered by API aggregates were considered as part of the study. The analysis examined the dependence of the global mean of each of these metrics on either acceleration or blending time. The main effects of the acceleration and total blending time on the API mean aggregate area are shown in Figure 5-9. The API mean aggregate area decreased with increasing acceleration and blending time. The API mean aggregate area decayed exponentially for increasing acceleration and total blending time. The overall API mean aggregate area was much larger for blends after 0.5 minutes of blending when compared to those mixed after 1 and 4 minutes. This indicates that most of the reduction in aggregate size (or agglomeration) occurs after 0.5 minutes of mixing in the RAM. A similar trend is seen when the effect of acceleration is considered. The API mean aggregate area is much larger after mixing at 20 g's when compared to those blends mixed at 40 and 70 g's. These phenomena can be explained by the large amount of energy that goes into the blend at 40 and 70 g's than that at 20 g's [24, 25].

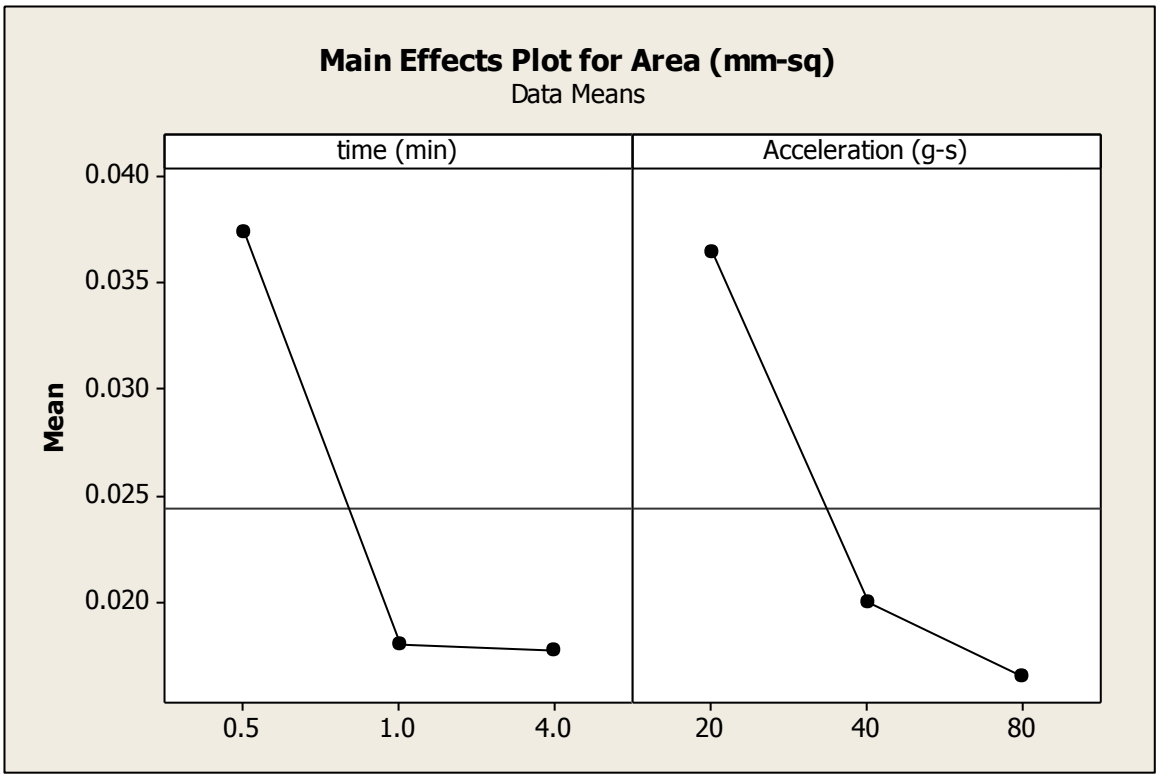

Figure 5-9. API mean aggregate area. The blend studied here was composed of 3% APAP + 1% MgSt + 96% Prosolv.

The main effects of the acceleration and total blending time on the standard deviation of the API aggregate area are shown in Figure 5-10. The standard deviation of the API aggregate area decreased with increasing acceleration and total blending time. This shows that the variability in the aggregate area is reduced with an increase in the acceleration and total blending time. This means that the API aggregates found at higher accelerations and longer mixing times are more similar in size to one another than those aggregates obtained at lower accelerations and shorter mixing times. The standard deviation of the API aggregate area seems to further decrease beyond the accelerations and blending times considered. This is an indication that the variability in the size of the API aggregates can be further reduced yielding better micro-mixing performance.

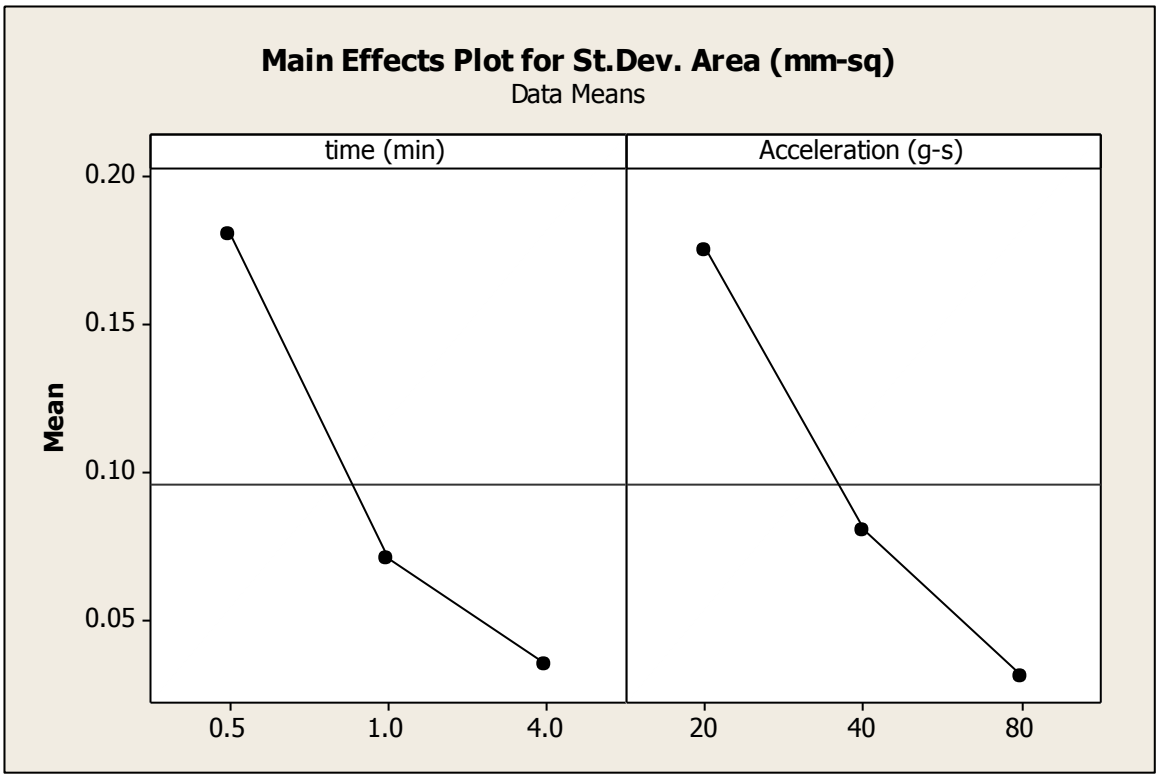

Figure 5-10. API mean aggregate area standard deviation. The blend studied here was composed of 3% APAP + 1% MgSt + 96% Prosolv.

The main effects of the acceleration and total blending time on the percentage of area covered by API aggregates are shown in Figure 5-11. The percentage of area covered by the API aggregates decreased with increasing acceleration and blending time. This means that there is a reduction in the mass fraction and size of the API aggregates with increasing acceleration and blending time. This indirectly confirms the results obtained from the standard deviation of the aggregate size by indicating that fewer aggregates are present at higher acceleration and longer mixing times, and that those present are more similar in size.

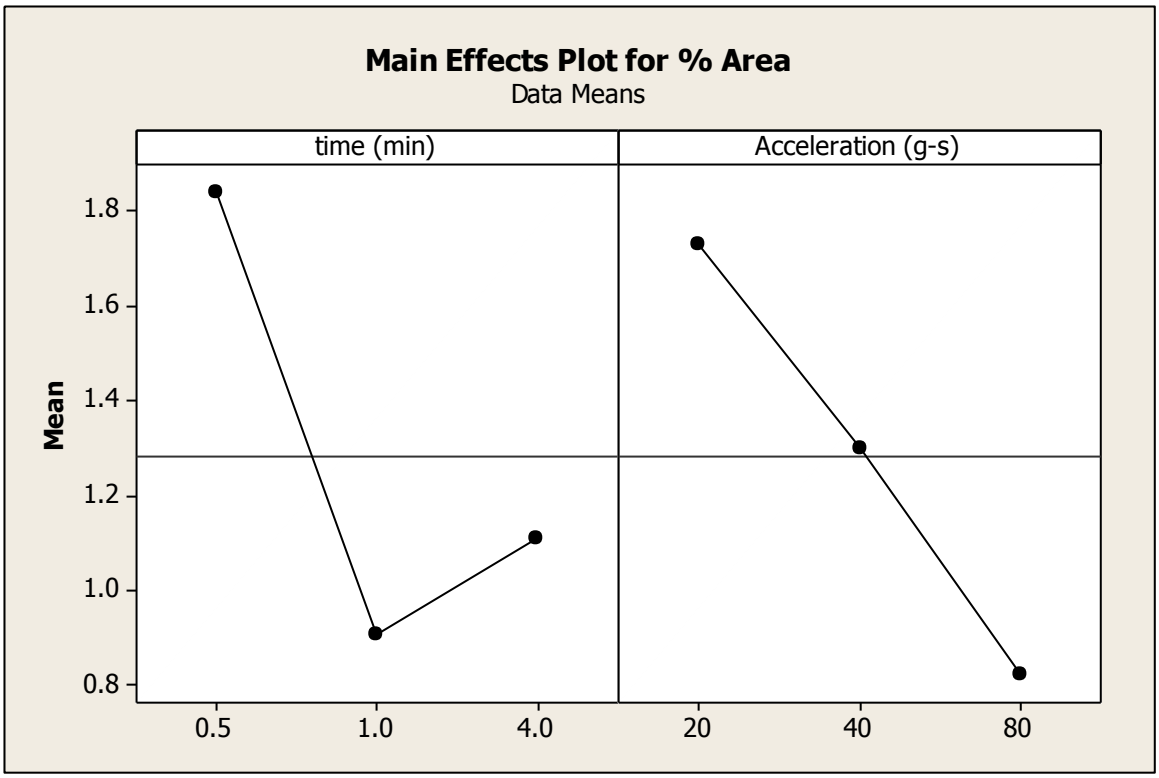

Figure 5-11. Percentage of area covered by API aggregates. The blend studied here was composed of 3% APAP + 1% MgSt + 96% Prosolv.

For illustration purposes, we will assume that the mean API particle size (45 µm) as the diameter of a single particle. This assumption is used for comparison purposes and it is an approximation. This comparison does not take into account that real particles in the aggregates are 3-dimensional, that are not arranged one after another (side-by-side) and that there is scattering of the NIR radiation. With this in mind, the mean API particle area is 0.00159 mm^2. Using this area we can approximate how many API particles are in an aggregate. The number of API particles in an aggregate calculated from the mean aggregate area for all blending times and accelerations studied are described in Tables 5-4 and 5-5, respectively. For example, the number of API particles in an aggregate for 0.5 minutes of blending was 24, while for 1 and 4 minutes was 11. Recall also that the standard deviation of the aggregate area decreased with increasing blending time. Thus,

the variability in the number of particles in an agglomerate is larger at shorter blending times. Similar results were obtained for the accelerations used. For 20 g's, the total number of API particles in the measured aggregates was 23, while for 40 g's and 80 g's was 13 and 11, respectively. The standard deviation of the aggregate area also decreased with increasing acceleration, showing similar results as those obtained for the blending times used. With this illustration, we are able to conclude that the number of API particles in the aggregates was reduced with increasing blending time and acceleration.

Table 5-4. Number of API particles in the aggregate mean area using the API mean particle size as the standard diameter. Results were obtained from the main effect of total blending time.

time (min)	Aggregate mean area (mm^2)	# of API particles
0.5	0.0374	24
1	0.0180	11
4	0.0177	11

Table 5-5. Number of API particles in the aggregate mean area using the API mean particle size as the standard diameter. Results were obtained from the main effect of acceleration.

Acceleration (g's)	Aggregate mean area (mm^2)	# of API particles
20	0.0365	23
40	0.0200	13
80	0.0166	10

In the previous subsection we mentioned that no MgSt aggregates were detected using the common threshold values described. Thus, an alternative way of studying MgSt dispersion in the blends with the same chemical imaging data was developed. All pixels with negative intensities (most negative pixel intensity value to zero intensity pixel value) at 1730 nm were used to create a binary image showing the dispersion of MgSt in the

blend. This method detected all of the MgSt "visible" in the chemical images. To illustrate the results obtained using this method, MgSt intensity and binary images are shown in Figures 5-12 and 5-13. These figures show that MgSt is well mixed throughout all the samples considered. The dark spots in the binary images are the areas where MgSt is present and is detectable as negative values at 1730 nm. It is worth mentioning that the mean particle size of MgSt is around 10 μm. In some cases, where enough energy has gone into the blend, some of the MgSt will be smaller than the detectible limit (due to light scattering) in this technique. Similar behavior was seen for the blends mixed at all other conditions. Most of the MgSt was well dispersed for all the conditions studied as expected. It is important to mention that the areas without MgSt correspond to the areas where APAP was present in considerably large aggregates. No quantitative correlations between the MgSt micro-mixing performance (e.g. mean aggregate area) and the mixing parameters (acceleration and blending time) were found.

(a)

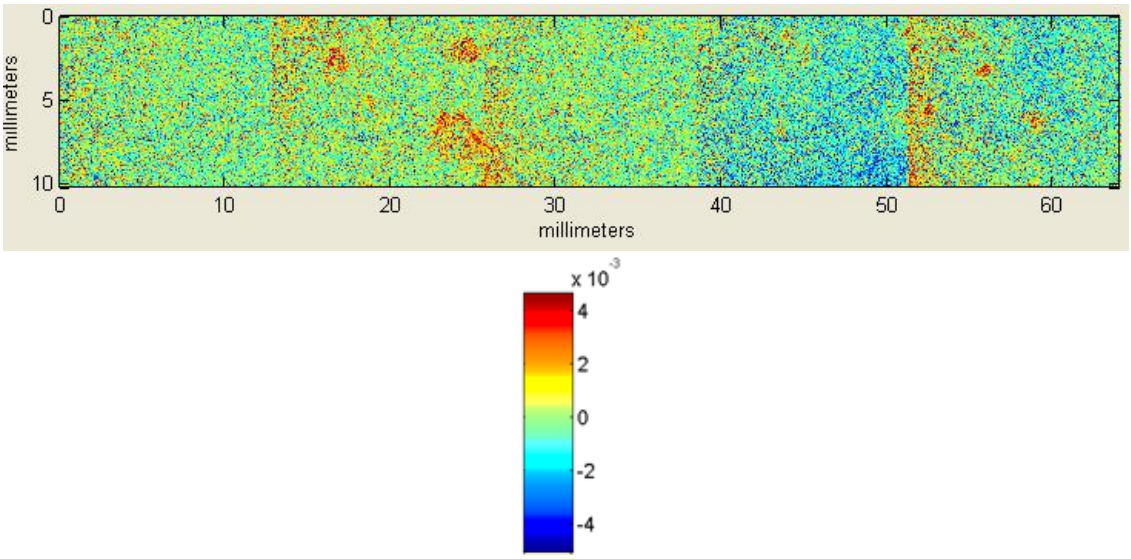

(b)

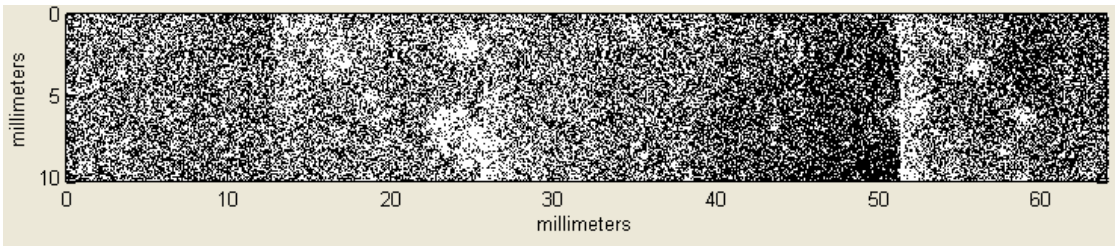

Figure 5-12. (a) intensity image and (b) binary image for MgSt at 20 g's for 0.5 minutes. The blend studied here was composed of 3% APAP + 1% MgSt + 96% Prosolv.

(a)

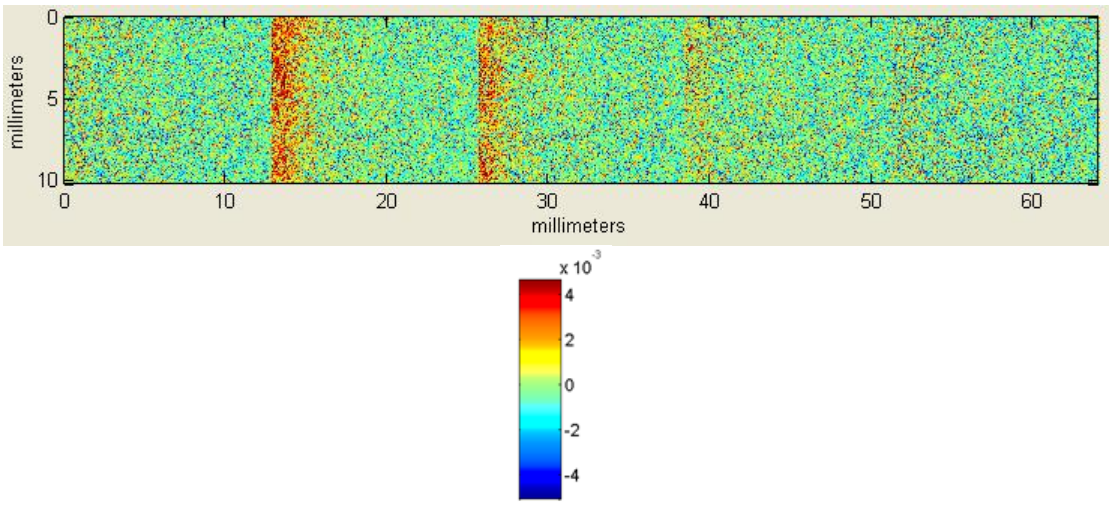

(b)

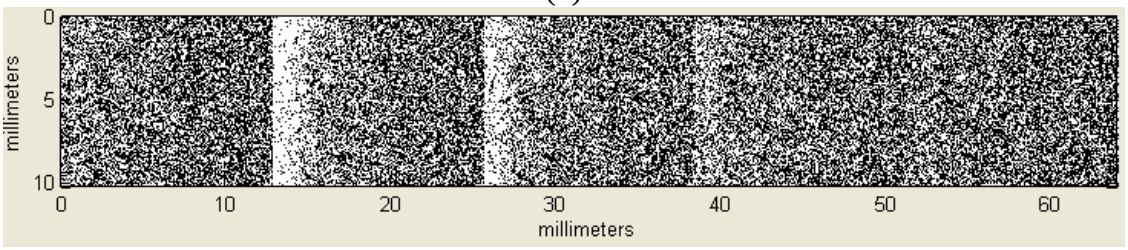

Figure 5-13. (a) intensity image and (b) binary image for MgSt at 40 g's for 0.5 minutes. The blend studied here was composed of 3% APAP + 1% MgSt + 96% Prosolv.

5.5 Conclusions

The micro-mixing state of powder blends produced in a resonant acoustic mixer (RAM) was studied using near-infrared chemical imaging. Both qualitatively (chemical images) and quantitative analysis (e.g. mean API aggregate area) were considered. It was found that APAP showed less aggregation (higher dispersion) at higher accelerations and longer blending times. These results were in accordance with the previous characterization of the RAM mixing performance. The RAM was shown to efficiently

reduced API agglomeration without any other mechanical means. Such results are commonly obtained by using intensifier bars in the mixers or milling the blend after mixing. It was also shown that MgSt was well dispersed throughout the blend for all the conditions explored. The RAM is a good candidate for a variety of applications in which cohesive APIs, or powders in general, must be used. The RAM can be used in the early stages of formulation development where the API quantity is limited.

Chapter 6 Characterization of pharmaceutical powder blends using *in situ* near-infrared chemical imaging

6.1 Summary

This chapter introduces the use of an *in situ* near-infrared chemical imaging technique able to examine the distribution of the materials while being blended. The non-destructive method used here generates thousands of spectra per second, providing a larger amount of compositional information than other conventional methods. This technique allows monitoring micro-mixing as the blending process progresses while eliminating issues encountered with extractive sampling [4, 109-111], and with long and destructive characterization techniques. A Science-Based Calibration (SBC) method [112, 113] which uses pure component spectral data and noise estimates to create a calibration model, was used to create the concentration maps of the blends studied here. The advantage of SBC over partial least squares (PLS) or principal component analysis (PCA) calibration methods is that it does not require a large amount of samples to create a calibration.

The main objectives of the study reported in this chapter were to characterize this NIR-CI analytical technique, to quantify micro-mixing in pharmaceutical blends using statistical analysis of the compositional maps obtained, and to determine the micro-mixing dynamics in a bin-blender as a function of processing parameters. The use of this NIR-CI tool allowed the micro-mixing dynamics studies of various formulations using acetaminophen (APAP) as the model drug. This technique was useful in monitoring the spatial distribution and aggregate sizes of APAP and of excipients in the blends. Using a

1-liter bin-blender, measurements were able to detect changes in the constituents as a function of APAP concentration and blending time. Such measurements can be used to determine the mixing time and shear requirements of blends during product and process development.

6.2 Materials and Methods

6.2.1 Materials

The materials used in all the experiments reported here were as follows: acetaminophen (semi-fine, USP / paracetamol PhEur, Mallinckrodt, Raleigh, North Carolina, USA), microcrystalline cellulose (Avicel PH101, FMC Biopolymer, Newark, Delaware, USA), lactose (monohydrate N.F., crystalline, 310, Regular, Foremost Farms USA, Rothschild, Wisconsin, USA), amorphous fumed silica (Cab-O-Sil M-5P, Cabot Corporation, Tuscola, Illinois, USA), and magnesium stearate N.F. (non-Bovine, Tyco Healthcare / Mallinckrodt, St. Louis, Missouri, USA). The nominal particle sizes of the materials used are listed in Table 6-1.

Table 6-1. Blend constituents and nominal mean particle size.

Material	Mean Particle Size
Acetaminophen (APAP)	45 µm
Avicel 101	50 µm
Regular lactose	180 µm
Cab-O-Sil (SiO_2)	5-20 nm
Magnesium Stearate	10 µm

6.2.2 Hyperspectral Chemical Imaging

The imMix^{TM} system (Middleton Research, Middleton, Wisconsin, USA) was used (Figure 6-1a) in all the experiments presented here. The imMix is a NIR chemical imaging (NIR-CI) tool used to study in-line the micro-mixing blend behavior. The imMix system consists of a push-broom short-wave infrared (SWIR) hyperspectral camera (Specim Spectral Imaging Ltd, Oulu, Finland) with a 1-liter bin-blender attached. The SWIR camera has a wavelength region of 1000-2500 nm and a full frame rate of 100 Hz. The SWIR camera captures images with 320 spatial points by 256 spectral points at a time, with an approximate resolution of 30 μm per pixel. The camera is positioned to scan the blend through a window at the bottom of the rotating blender as shown in Figure 6-1. A computer-controlled motor rotates the blender with the near-infrared camera programmed to scan the blender window on specific rotations. Hyperspectral data is collected throughout the blending process, and composition maps (spatial dispersion) are created for all blend ingredients.

(a)

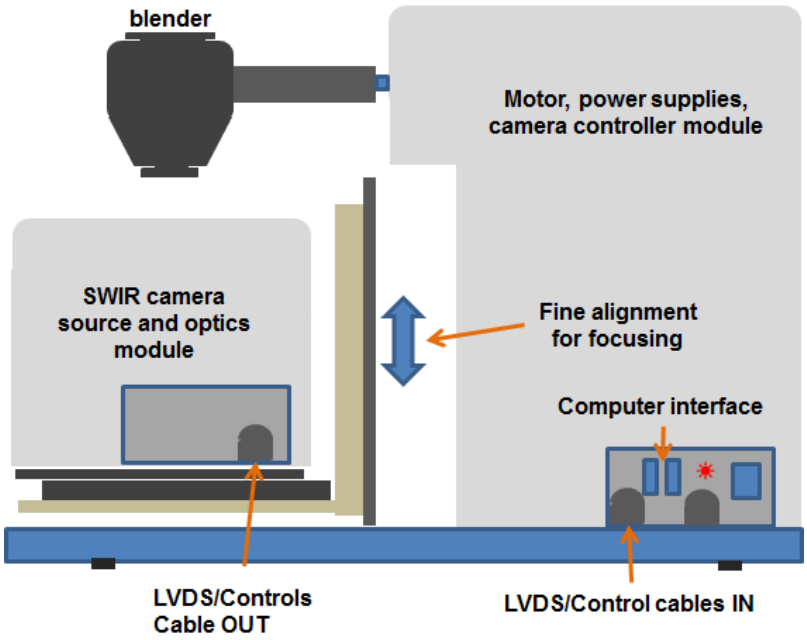

(b)

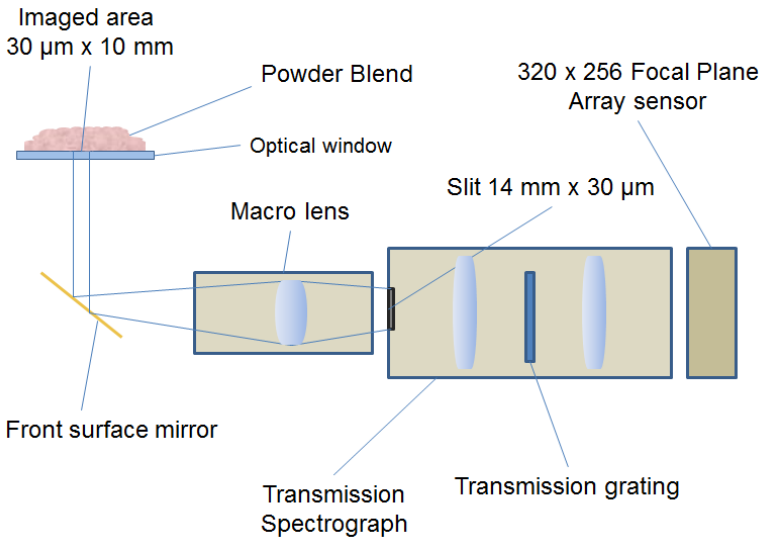

Figure 6-1. imMix System. (a) size-view block diagram with all parts with 1-liter bin-blender used in all experiments and (b) optical block diagram of the imMix system.

The optical block diagram (Figure 6-1b) depicts how the hyperspectral camera works. Light sources (not shown) illuminate the optical window (a borosilicate glass window was used in these experiments) and the powder blend behind it. The light diffusely reflected off the blend is collected by a mirror, which redirects it toward the SWIR macro lens. This macro lens focuses the imaged line on the slit of the NIR spectrograph. The light then passes through the spectrograph optics, including lenses and a transmission grating, before reaching the focal plane array sensor. The blend images were collected for the specified rotations by slowing down the blender and allowing the camera to scan an approximate area of 1 cm by 1 cm, line by line, across the optical window on the blender. The push-broom camera collects all the spectra for a single line on the window at a time. By scanning across the window, a hypercube of data is collected, to form a square image [114]. All the results reported here correspond to an exposure time (integration time) of 1 millisecond and a frame rate of 75 frames per second.

6.2.3 Blending and In-line Monitoring

The imMix was equipped with a 1-liter stainless steel intermediate bulk container bin-blender. Approximately 40% of the total blender volume was used for all experiments discussed here. Three concentrations (3, 10, and 30% by weight) of semi-fine acetaminophen (APAP) were used. The remainder of the blend was composed of 50/50 Avicel PH101 and regular lactose with constant concentrations of 0.5% Cab-O-Sil (SiO_2) and 1.5% Magnesium Stearate (MgSt). Concentrations of materials in each blend are described in Table 6-2. APAP, Cab-O-Sil, and MgSt were sieved using an 80-mesh sieve to break up large agglomerates before use. Components were added through the top of the blender as follows: Avicel PH101 was added first, lactose was added second,

acetaminophen was added third, and Cab-O-Sil was added fourth. After 40 revolutions, the blender was stopped and MgSt was added through the top.

Table 6-2. Nominal concentrations of Materials in blends (% weight by weight).

Material	Concentration (%)		
	Blend 1	Blend 2	Blend 3
Acetaminophen	3	10	30
Avicel 101	47.5	44	34
Regular lactose	47.5	44	34
SiO2	0.5	0.5	0.5
MgSt	1.5	1.5	1.5

The blender was rotated at speeds of 15, 25, and 35 RPM up to 200 revolutions. The experimental design used is described in Table 6-3. Hyperspectral images were taken at 1, 5, 10, 20, 30 and 40 revolutions to quantify the effect of initial blending without significantly disrupting the blending process. After the first 40 revolutions, the blender was stopped and the MgSt was added. Hyperspectral images were taken at turns 41, 45 and 50 to detect any changes in the blends after adding MgSt. Thereafter, hyperspectral images were taken every 10^{th} revolution from 50 to 200. Images were taken while gradually slowing down the blender after every specified turn minimizing disturbances in the blending process.

Table 6-3. Experimental conditions studied.

Experiment #	API (%)	Rotation Rate (RPM)
1	3	15
2	3	25
3	3	35
4	10	15
5	10	25
6	10	35
7	30	15
8	30	25
9	30	35

6.2.4 Hyperspectral Imaging Processing

The Science-Based Calibration (SBC) method [112, 113] was used to quantify all the constituents in the composition maps in each blend at the predetermined rotations. The SBC method only requires spectra of the pure components (Figure 6-2a) previously collected in the same manner with a small sample holder attached to the bottom of the blender. Noise estimates, including the hardware, offset, and slope noises necessary for the SBC method are given in Table 6-4. The hardware noise is an estimate of the variation caused by the instrument from measurement to measurement in absorbance units (Au). A typical 2 mAu noise estimate was used. The most relevant noise input was the spectral shape of the other ingredients in order to minimize arbitrary correlation between components. The offset noise was determined by the baseline variation of the image spectra. Each spectrum may have a unique baseline depending on the reflectivity and light scattering of the particles; the offset noise accounts for this. The slope noise was determined by the variance of the slope of the spectra. The slope of typical solid powder spectra estimated to vary 0.25 Au. This translated to the 0.1667 mAu/nm value used in

the APAP blend prediction for the 1000-2500 nm region such that $\left(0.25\ Au * 1000\frac{mA}{A}\right)/(2500\ nm - 1000\ nm)$. The most relevant noise input is the spectral shape of the other ingredients in order to minimize arbitrary correlation between the components. For each component, the spectra of all other ingredients were automatically used by the software module generating the calibration equations. In addition, the final blend's spectrum (Figure 6-2b), called "operating point" in the SBC method, was used as a bias correction factor for each final blend.

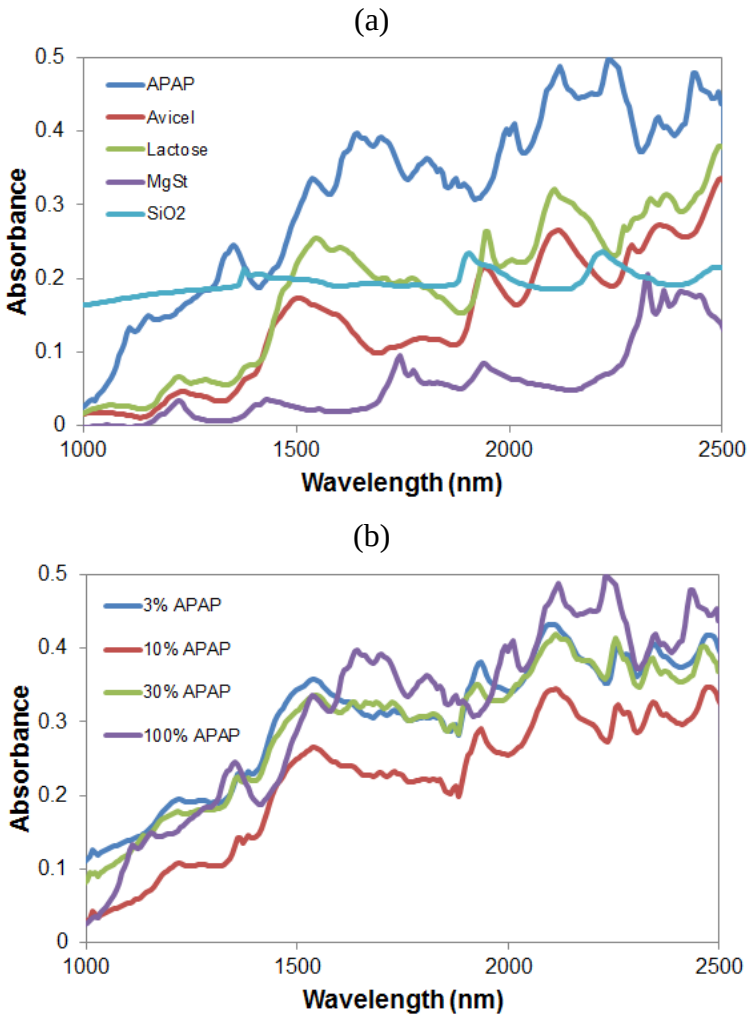

Figure 6-2. (a) Typical pure ingredients' spectra and (b) examples of final blend spectrum ("operating point") for each concentrations of each formulation and pure APAP.

Table 6-4. Noise estimates used in SBC calibration.

Hardware Noise	2 mAu
Off-set Noise	50 mAu
Slope Noise	0.1667 mAu/nm

For the white reference, a blender attachment that contained a highly reflective polytetrafluoroethylene material placed behind an optical window, was fixed to the blender and scanned in the same configuration as all other samples. For the dark reference, the system activated a shutter inside the camera before collecting an image. The white and dark references' spectra were used as the background. Each spectrum, whether it was of the powder blend, the pure components, or the operating point blend, was corrected ("ratioed") with the white and dark references to convert the intensity values into reflectance. To convert the spectra to absorbance, the negative logarithm was applied as shown in equation 6-1.

$$Absorbance = -log_{10}\left(\frac{I_{sample}-I_{dark}}{I_{white}-I_{dark}}\right) \quad (6\text{-}1)$$

A wavelength region of 1,000 to 2,500 nm was specified for the calibration. Another step in the pre-processing was a pixel correction, which looked at the white reference and determined the few spatial and spectral pixels that were outliers due to camera imperfections. These pixels were replaced with the average of their non-outlier neighbors for all images collected. Calibration coefficients (b-vectors) were then calculated for each component and used to predict every pixel of the blend rotat.lion images. The result was a composition map for each rotation specified, for each blend component, which was then

used to estimate concentration averages and other useful parameters. All images collected were processed and analyzed using a Matlab-based chemometric and statistical software.

6.3 Image Analysis

6.3.1 Images

Measured composition images show concentration maps (0-100%) of each component in the blend. Each image allows one to visually estimate the agglomerate sizes of each of the components in the blend and to determine when all the components are adequately dispersed. Further mathematical analysis of each image allows the extraction of parameters that are helpful in the interpretation of the images and in the understanding of the blending process studied.

6.3.2 Concentration Statistics

From each chemical image, the concentration average (mean, μ), the standard deviation (σ) and the relative standard deviation (RSD) were calculated for each analyte at each turn. The average (eq. 6-2) showed the point (rotation number) in blending when the nominal concentration for each analyte was achieved, and the progression in concentration levels toward this point.

$$\mu = \frac{\sum_{p=1}^{P} concentration(p)}{P}, \tag{6-2}$$

where p is the pixel number and P is the total number of pixels in the measured image.

The standard deviation (eq. 6-3) is determined in the same manner and is a measure of the pixel distribution in each image, indicating the composition range in which most of the pixels lie. The relative standard deviation (RSD) is calculated from the ratio of the

standard deviation (σ) and the mean (μ) of each measured image. The RSD is a commonly used tool in the pharmaceutical industry to estimate the uniformity of a component within a blend. The customary RSD description of pharmaceutical blends is based on the calculated variance of API concentration from one unit dose to another. In the case of image analysis, the system was sensing the variation of concentration from pixel to pixel, each covering an approximate area of 30 μm by 30 μm of the blend. Thus, the actual amount of material "sampled" is much smaller, and the RSD measured in these experiments is much higher than the customary unit dose sample RSD.

$$\sigma = \sqrt{\frac{\sum_{p=1}^{P}(p-\mu)^2}{P}} \tag{6-3}$$

6.3.3 Fraction of Pixels Statistics

6.3.3.1 Within Threshold

"Within threshold" is the fraction of pixels that are within a specified concentration threshold. The average concentration does not give an indication of whether there are many pixels above or below this average. Calculating the fraction of pixels within a threshold may be useful, for example, if there is some criteria that the blend must be mixed to a point such that 95% of the blend is within 10% of the nominal composition. The criteria for acceptance depend on the blend formulation requirements, and may be different for each blend and component. The thresholds used for all components are shown in Table 6-5.

Table 6-5. Thresholds used for identification of aggregates, fraction "within threshold", and "above threshold" statistics.

	Lower and Upper Thresholds (nominal ± nominal*factor)			
Blend	Avicel (%)	Lactose (%)	APAP (%)	MgSt (%)
1	30.9 to 64.1	26.1 to 68.9	-6.0 to 12.0	-22.5 to 25.5
2	28.6 to 59.4	24.2 to 63.8	0 to 20.0	-22.5 to 25.5
3	17.0 to 51.0	10.2 to 57.8	21.0 to 39.0	-22.5 to 25.5

In order to calculate this quantity, a baseline value (the nominal composition) was selected to quantify the fraction of the measured image that was within a certain range. A factor was defined to calculate the lower and upper limits of the threshold as specified in Table 6-5. To determine the appropriate threshold levels, the images on a ternary scale were visualized. An example of an image in ternary scale is shown in Figure 6-3. This shows the pixels within the threshold in gray, the pixels above the threshold in white, and the pixels below the threshold in black. This image analysis allows the visual identification of the proper threshold. The image of a better mixed blend (later rotation) showed several small aggregates (groups of white pixels), with most of the image in gray and a few black areas. If the threshold was set too low, a large fraction of the image was colored white. This was not a realistic size for aggregates and the threshold was increased. For very low concentration components, such as magnesium stearate, the threshold was set to the nominal concentration ± 16x the nominal concentration; for low to mid-range concentration components, a lower threshold factor is appropriate. For example, for the 10% APAP blend, the threshold was set to the nominal concentration ± 3x the nominal concentration. For higher concentration components (10% to 40% w/w), 0.3x to 1.0x is an appropriate threshold factor. The exact lower and upper thresholds used in this study are given in Table 6-5. In some cases, the lower thresholds are negative.

Even though a negative concentration does not have a physical meaning, the statistical distribution of the prediction values can have a wide range including negative predicted concentrations.

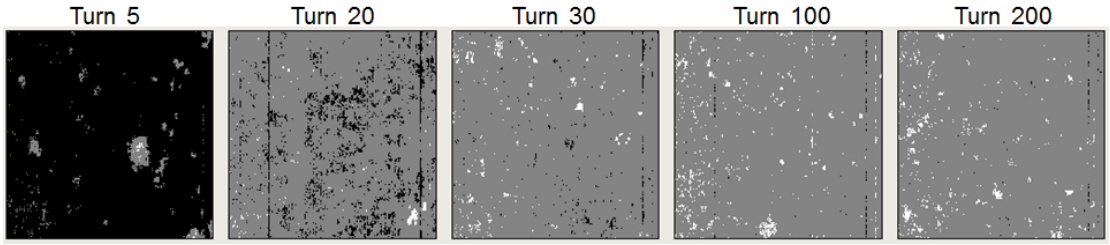

Figure 6-3. "Peaks and Valleys" display: Grey areas are between the upper and lower thresholds (nominal concentration +/- nominal*factor), white areas are higher concentration than the upper threshold; black areas are concentrations less than the lower threshold.

6.3.3.2 Above Threshold

The fraction of pixels above a threshold indicate the presence of agglomerates of pure components. This is important because this can determine whether a blend is homogeneous at the micro-scale. In order to estimate the fraction of the measured image that displays aggregates, the pixels above the thresholds specified in Table 6-5 were determined. A threshold was specified as previously explained. The uniformity of a blend is optimum if the fraction of pixels above the threshold is close to zero. As an example, a criterion that the blend is complete is when less than 10% of the image pixels are high points (above the threshold).

6.3.4 Aggregate Size Statistics (Mean and Maximum of Aggregate Sizes)

In order to determine the mean, median, or maximum aggregate size, the following algorithm was used. A pixel was part of an aggregate if it was above a certain specified

threshold defined in the same way as described above in subsection 6.3.3.1. Aggregates were defined as a group of x or more adjacent pixels all above the predetermined concentration threshold, where the minimum aggregate size x is specified. The size of each aggregate and their statistics were calculated for each composition map for each component. The mean and maximum aggregate sizes were calculated. Other aggregate size statistics can also be useful to characterize the progression of blending, such as the median aggregate sizes or skew and kurtosis. Mathematical descriptions of these additional statistical tools were omitted for sake of brevity.

6.4 Results and Discussion

6.4.1 Image Results

Measured composition images from each ingredient were obtained for all conditions described in the experimental design. The visual inspection of the measured images helped to describe the mixing evolution of all the components. As examples, the composition images of 3%, 10% and 30% APAP blended at 25 RPM are shown in Figure 6-4. These images are on a color scale corresponding to a concentration gradient from 0% to 100%. The images show the mixing evolution of all the components as a function of the number of revolutions. As evidenced by the images, for all blends, Avicel was added first, covering the window, and therefore the corresponding composition images started at 100% and then approached the nominal concentration for Avicel. For 3% APAP (Figure 6-4a), the nominal concentration of Avicel was reached at around turn 45. Lactose was added second, not reaching the window. Its concentration started at 0% and then approached its nominal concentration between 20 and 30 turns. MgSt was added after 40

revolutions, and therefore its concentration indicated 0% until then. After its addition, MgSt was detected as agglomerates but it was mixed efficiently after a few additional revolutions.

Visual inspection did not reveal substantial APAP agglomerates at the 3% concentration level. It seemed that APAP was efficiently mixed after a few revolutions. A few agglomerates of APAP were detected even after 40 rotations for higher concentrations. The agglomerate concentration of SiO_2 was higher in the first few rotations and decreased as the blending process took place, as seen in the images for all concentrations of APAP. Although the concentration of SiO_2 is low and it was sieved before blending, it maintained agglomerates throughout the entire blending process. The detection of agglomerates indicates that the shear inside the mixer is not enough to completely break these agglomerates, which were already present or reformed in the SiO_2 as a raw material before blending. The mean particle size of the SiO_2 used was ~ 10 nm. Forces, such as van der Waals forces, between the SiO_2 particles at this scale are large and easily induce spontaneous agglomeration. Therefore, to improve the blending of SiO_2, a shearing aid (intensifier bar) should be used in such low-shear blender.

Similar blending behavior for Avicel, lactose and APAP was detected for experiments with 10% APAP and 30% APAP (Figures 6-4 b and 6-4c). In these examples, the two main components, Avicel and lactose, determined the blending end-point. Their micro-mixing evolution was seen in the composition images. The mixing of the main components took longer as the APAP concentration increased. The powder flow behavior changed with increasing APAP concentration. Therefore APAP, as a cohesive material, governed the flow of the blend and other components as its concentration increased in the

blends. It is known that as the concentration of a cohesive material is increased in a powder blend, the flow properties of the powder blend worsen (i.e. the powder blend becomes more cohesive) [99]. The higher the concentration of APAP, the longer it took for all the components - in particular Avicel - to become more dispersed (better mixed). One hypothesis for this phenomenon is that the similarity in particle size of Avicel and APAP, with APAP being a more cohesive material, might have a strong influence on the mixing rate of Avicel. In current practice, when a blend is monitored for homogeneity, usually only the API homogeneity is taken into account [115]. However, the homogeneity of other components is also an important indication of when the blend is actually well mixed, and this is particularly important if the other ingredients perform important functional roles. In the case described here, if only APAP was being monitored, then a "homogeneous" blend would have been determined after a few rotations as shown in the images. The use of this in-line NIR-CI technique allows for the monitoring of all ingredients in a blend at once and is able to consider the effects of the important ingredients on the blending behavior.

(a)

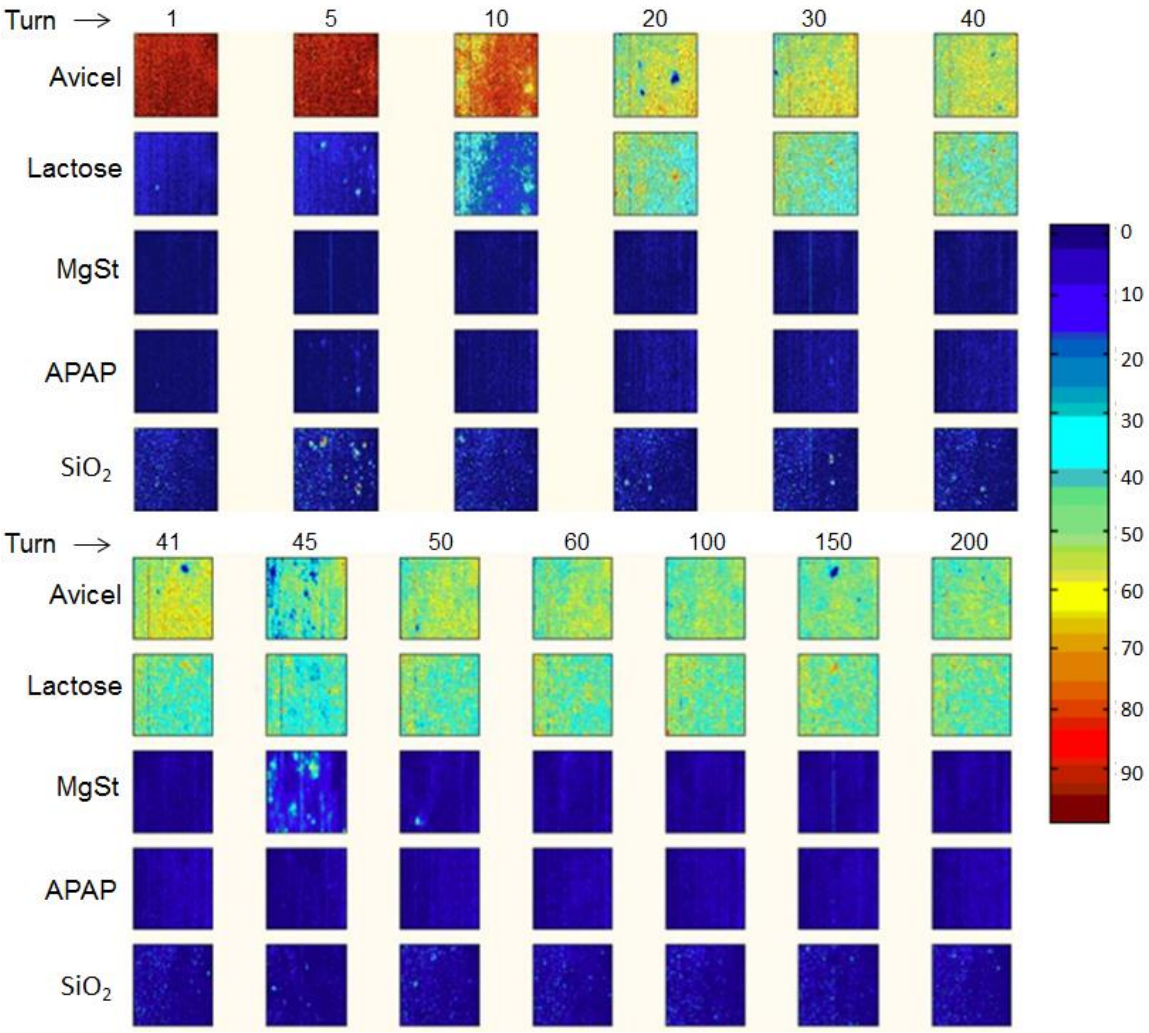
Turn →
1
5
10
20
30
40
Avicel
Lactose
MgSt
APAP
SiO2
Turn →
41
45
50
60
100
150
200
Avicel
Lactose
MgSt
APAP
SiO2
0
10
20
30
40
50
60
70
80
90

(b)

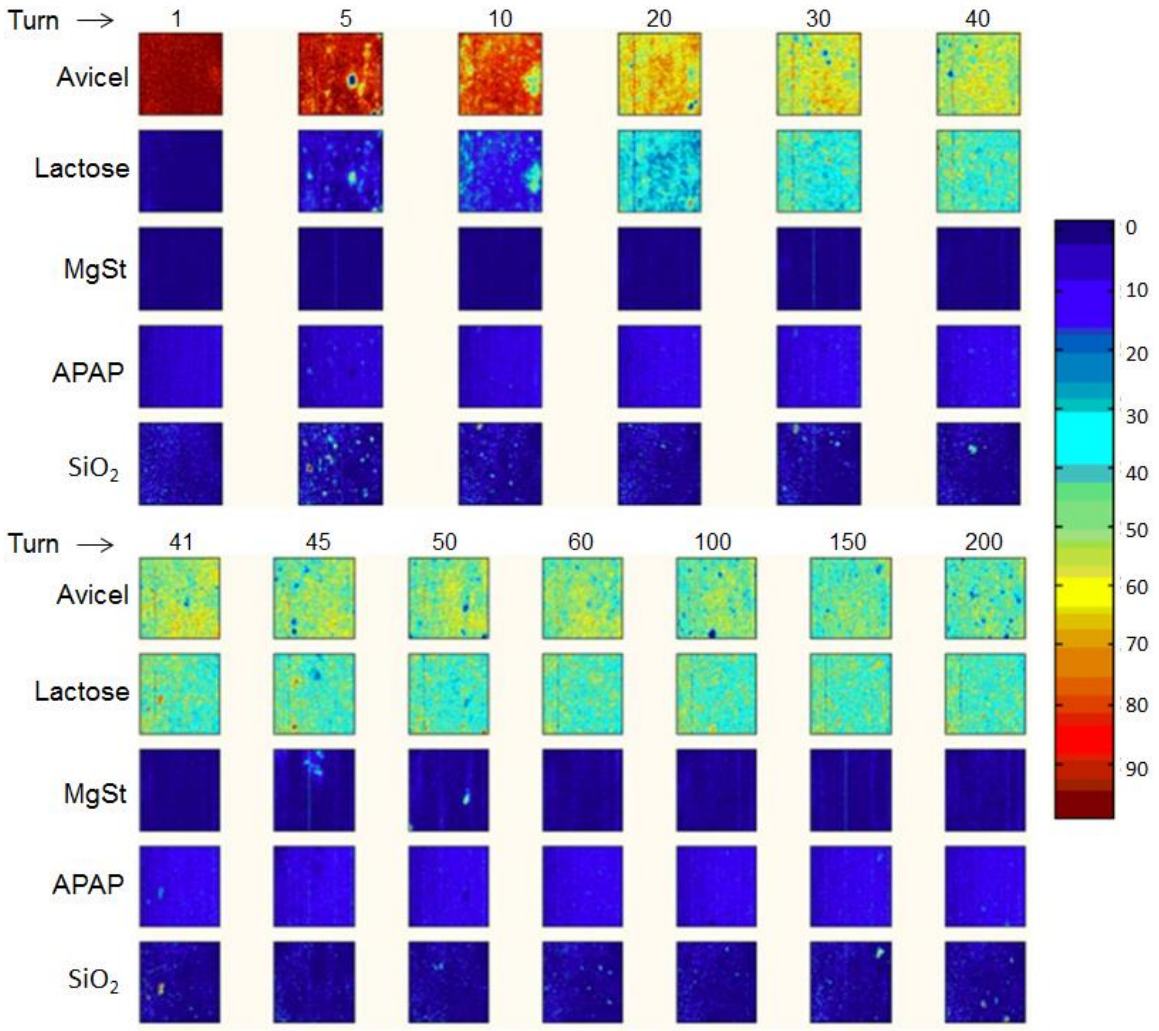
Turn →
1
5
10
20
30
40
Avicel
Lactose
MgSt
APAP
SiO2
Turn →
41
45
50
60
100
150
200
Avicel
Lactose
MgSt
APAP
SiO2
0
10
20
30
40
50
60
70
80
90

(c)

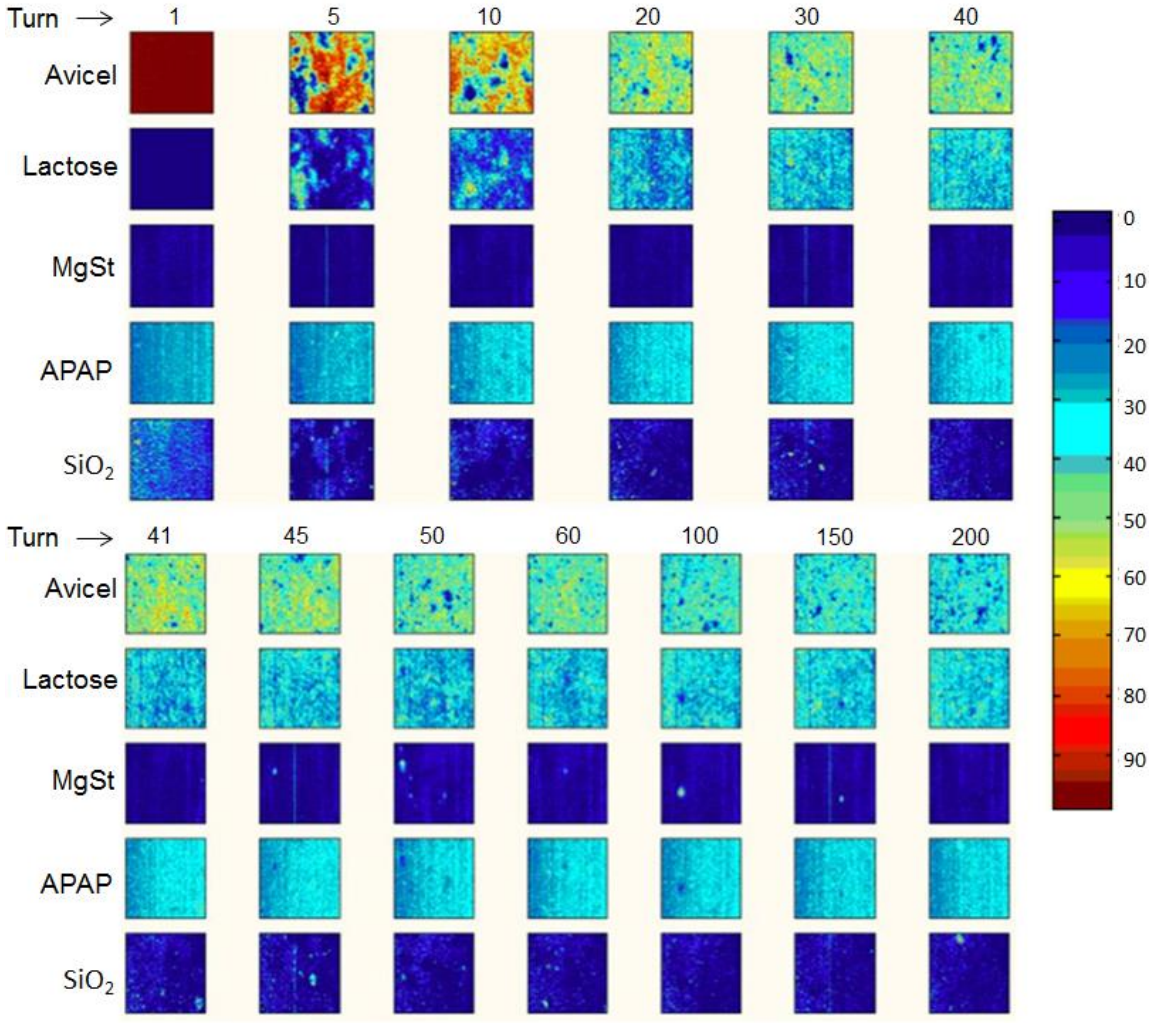

Figure 6-4. Sample Images – (a) 3% APAP, (b) 10% APAP and (c) 30% APAP. Other parameters: blender speed: 25 RPM.

The concentration maps as measured by the SBC method and absorbance images at wavelength 1350 nm are shown in Figures 6-5a and 6-5b for experiment 1, respectively. The SBC concentration images show the red spots where APAP agglomerates were detected by this calibration method. The single wavelength (univariate) images at 1350 nm show the spots where APAP has the most intensity in absorbance as indicated by the color bar. This serves as a brief comparison and "validation" showing that the SBC

method actually detects APAP agglomerates and is able to measure the overall concentration of APAP as well as the other ingredients in each chemical image.

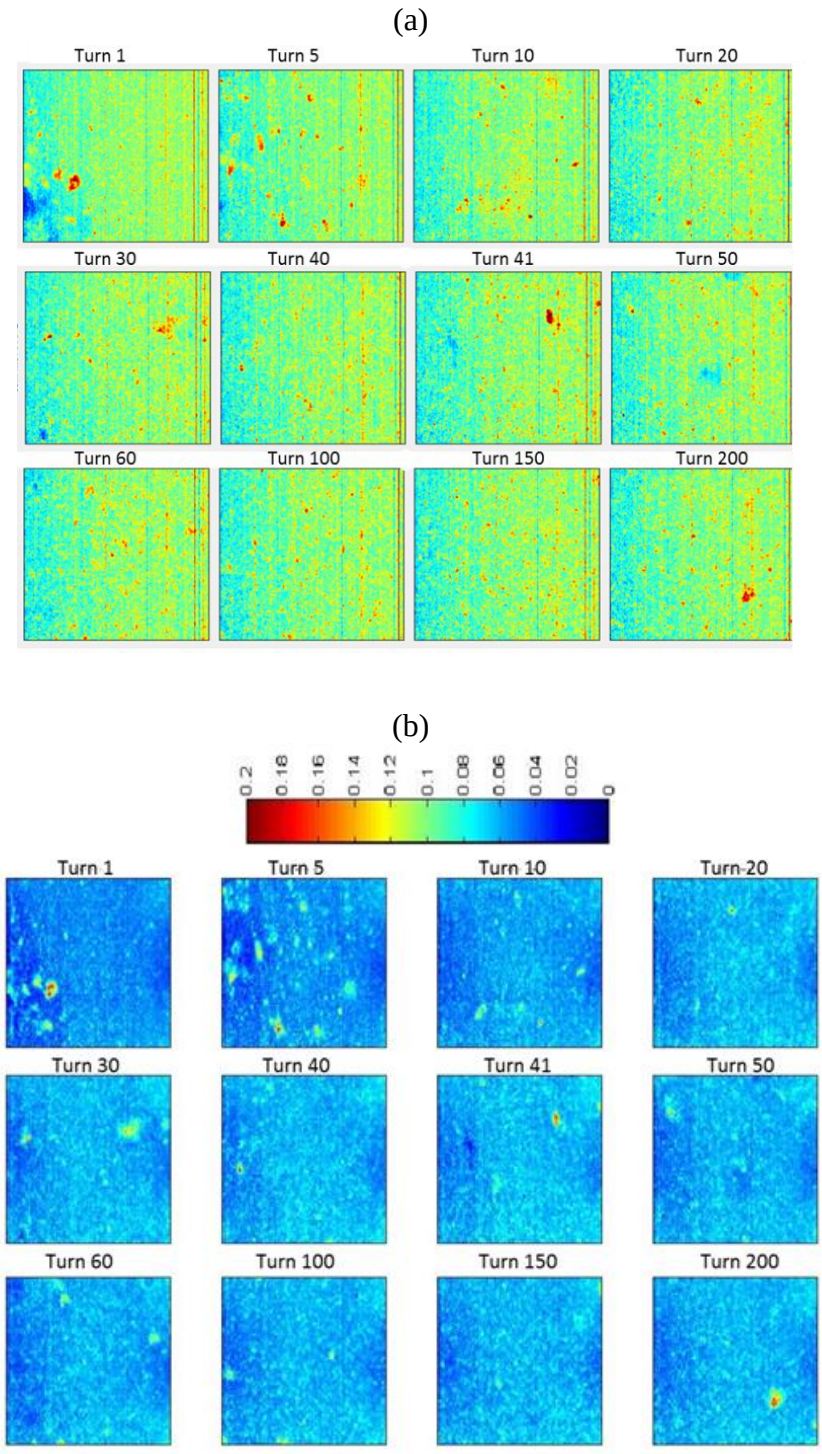

Figure 6-5. Comparison images for experiment 1 (a) Scientific Based Calibration (SBC) and (b) single wavelength at 1350 nm (color scale in absorbance units).

6.4.2 Concentration Statistics

6.4.2.1 Average Concentration

The calculated average concentrations of the main components as a function of the rotation number for the 25-RPM experiments are shown in Figure 6-6. The time it took for a blend to reach stable nominal composition increased with the increase in APAP concentration. APAP reached nominal concentrations rather quickly, but the addition of MgSt caused a disturbance in the average concentration when detected. For these concentrations, APAP seemed to have reached its nominal concentration value even before the addition of MgSt (Figure 6-6a). After the addition of MgSt, APAP reached its nominal value around 50 revolutions into the blending process for all levels of concentration. Avicel reached its nominal composition at around 45 revolutions for 3% APAP, 80 revolutions for 10% APAP, and 180 revolutions for 30% APAP (Figure 6-6b). Thus, it can be seen that Avicel did indeed take longer to blend as the concentration of APAP was increased. Lactose reached its nominal composition at around 20 revolutions for 3% APAP, and 40 revolutions for both 10% and 30% APAP (Figure 6-6c). Measurements were also obtained at 15 and 35 RPM. The blender rotation rate did not significantly affect the blending profiles for any of the materials used ($p << 0.05$). It seems that at this level of shear rate, the rotation speed has negligible effect for these ingredients and concentrations (with comparisons performed at the same number of rotations, which roughly correspond to an equivalent amount of strain). For this reason, only the curves for 25 RPM are shown here.

(a)

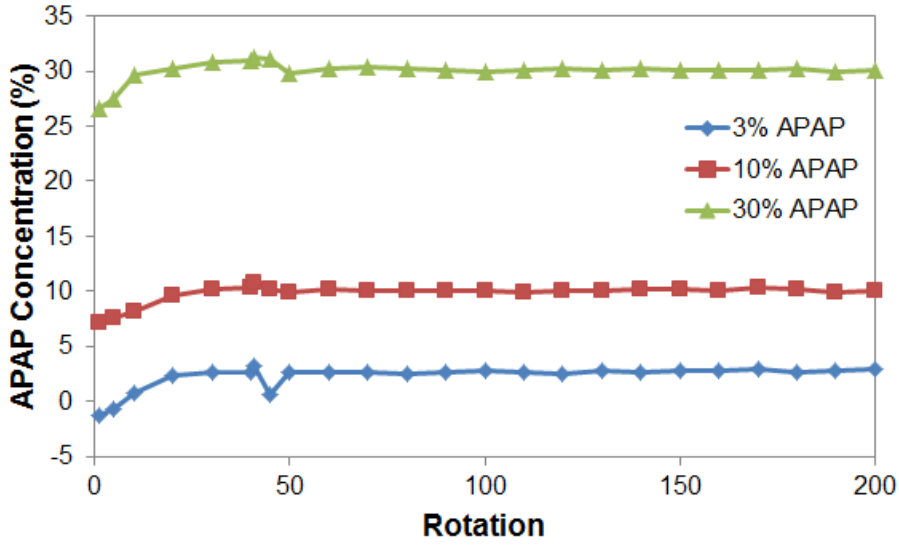
APAP Concentration (%)
35
30
25
20
15
10
5
0
-5
0
50
100
150
200
Rotation
3% APAP
10% APAP
30% APAP

(b)

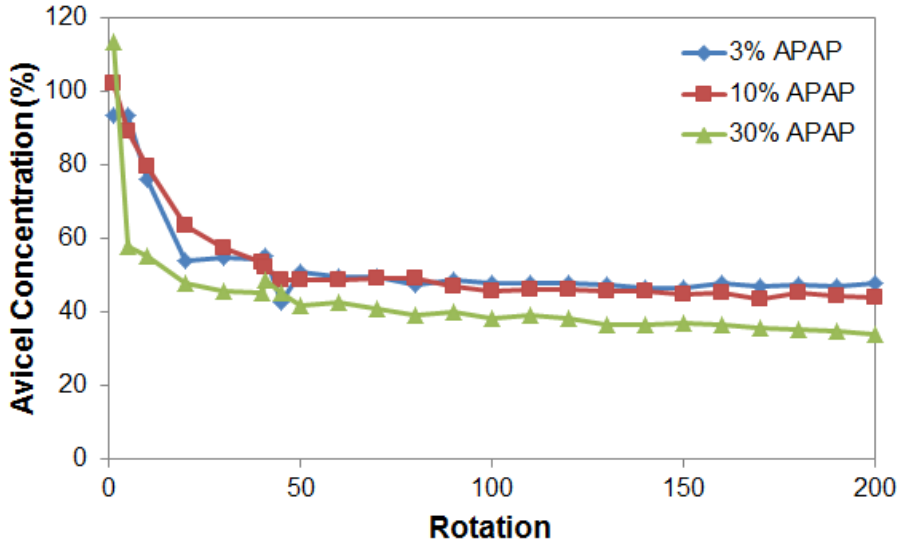
Avicel Concentration (%)
120
100
80
60
40
20
0
0
50
100
150
200
Rotation
3% APAP
10% APAP
30% APAP

(c)

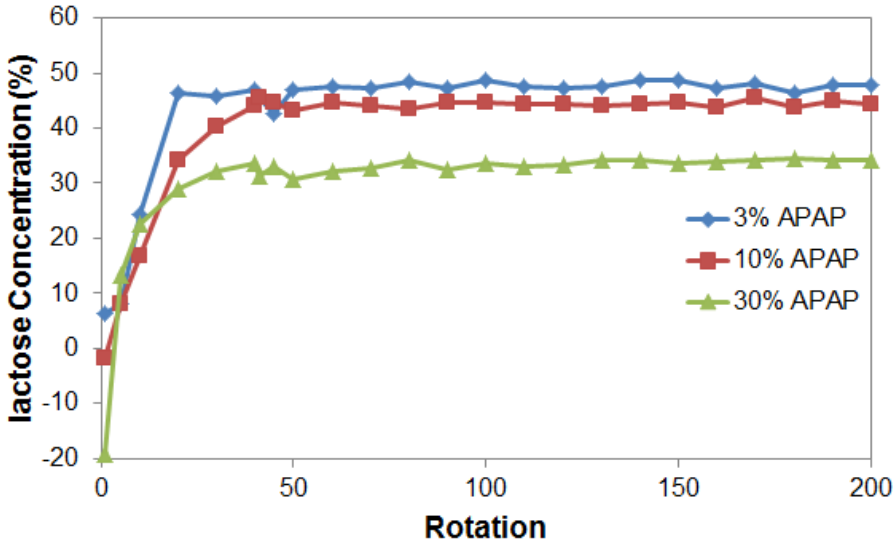

Figure 6-6. Sample average concentrations for (a) APAP, (b) Avicel, and (c) lactose. For Avicel and lactose, the nominal concentration at 3% APAP was 47.5%, at 10% APAP was 44%, and at 30% APAP was 34%. Other parameters: blender speed at 25 RPM. Figures shown in different scales to point out differences in results.

6.4.2.2 Relative Standard Deviation

The relative standard deviation (RSD) of each composition image as a function of time was calculated for all the experiments to study their blending profiles. A higher concentration of APAP (Figure 6-7a) yielded a lower RSD. These results are common, and are due to the natural tendency for this type of cohesive APAP to stay in aggregates, especially at low concentrations. The rotation rate did not have a significant impact on the RSD for the blends used, but the number of revolutions did affect the RSD. This result is in agreement with previous results published by Muzzio's group [3]. At the beginning of blending for 3% APAP, small RSD differences were observed for the various rotation rates. The difference in RSDs became less as the number of rotations increased. In this case, the RSDs also seemed to continue decreasing even at the final

rotations. This means that APAP might become even more evenly dispersed after 200 rotations; therefore more rotations should be used. For 10% APAP, a decrease in RSD was obtained up to 30 revolutions. The RSDs then reached a plateau. For 30% APAP, the lowest RSD was reached after a few revolutions with no clear trend. The rotation rate did not yield significant differences in the RSD measurements for 10% and 30% APAP blends. The mixing curves for APAP were not well defined as it has been shown in previous work when measuring the bulk concentration of this API [3].

The Avicel RSD results did not to follow any particular trend (Figure 6-7b). Nonetheless, the RSD results were higher for blends with higher concentration of APAP - especially for 30% APAP. The RSDs were also slightly higher for 10% APAP when compared to 3% APAP blends. This is in agreement with the previous results shown here that a higher concentration of APAP affected the manner in which Avicel was blending. For lactose, on the other hand, the RSD decreased with increasing number of revolutions (Figure 6-7c). The RSD values were higher for the 30% APAP blends. The presence of higher APAP concentration made it more difficult for Avicel and lactose to form a highly uniform blend. Lactose followed typical mixing curves showing both regimes usually encountered in powder mixing. The first regime is driven by convection, wherein most of the bulk (macro-) mixing occurs, and the second regime is driven by dispersion of particles, where most micro-mixing occurs. Lactose reached a minimum RSD with most of its mixing obtained by convection [30].

(a)

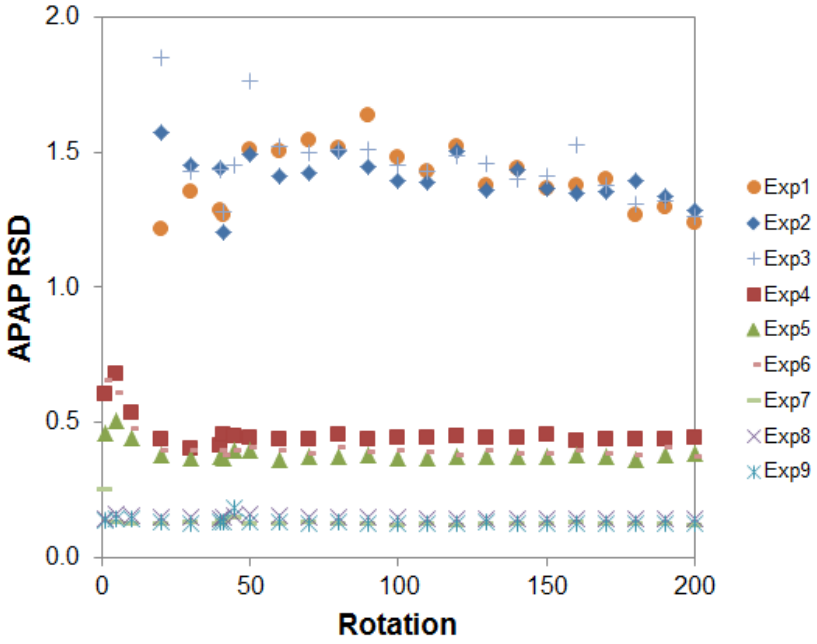
APAP RSD
Rotation
2.0
1.5
1.0
0.5
0.0
0
50
100
150
200
Exp1
Exp2
Exp3
Exp4
Exp5
Exp6
Exp7
Exp8
Exp9

(b)

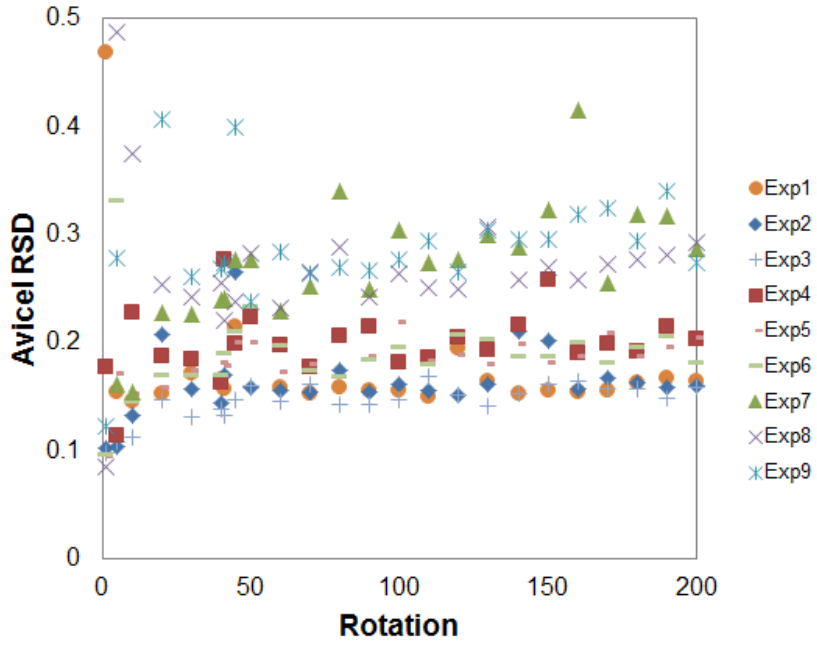
Avicel RSD
Rotation
0.5
0.4
0.3
0.2
0.1
0
0
50
100
150
200
Exp1
Exp2
Exp3
Exp4
Exp5
Exp6
Exp7
Exp8
Exp9

(c)

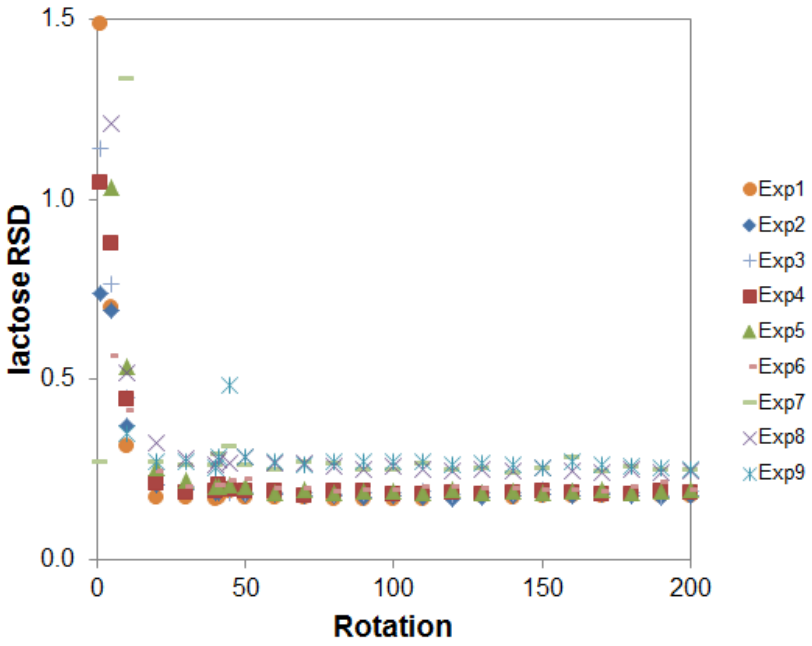

Figure 6-7. Relative Standard Deviation (RSD) of (a) APAP, (b) Avicel and (c) lactose. 3%, 10%, and 30% represent the nominal concentration of APAP in the blends. Figures shown in different scales to point out differences in results.

Further analysis of the RSD of 3% and 10% API blends at 25 RPM, as a function of image size (sample size) was carried out to demonstrate their correlation (Figure 6-8a). The measured RSD decreased as the sample size increased, as expected. The linearization using the natural log of the RSD^2 and the image size also yielded the expected trend (Figure 6-8b). This demonstrates that the variability of an ingredient in a blend also decreases with increasing sample size when measured using NIR-CI.

(a)

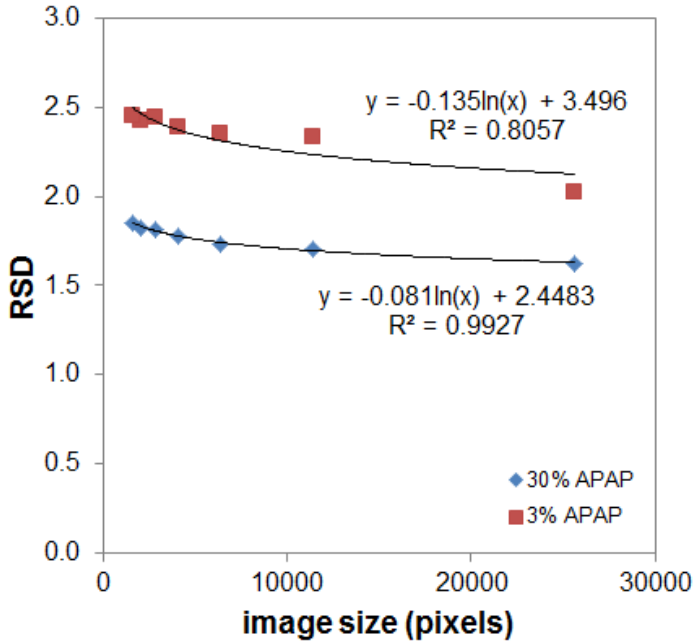

(b)

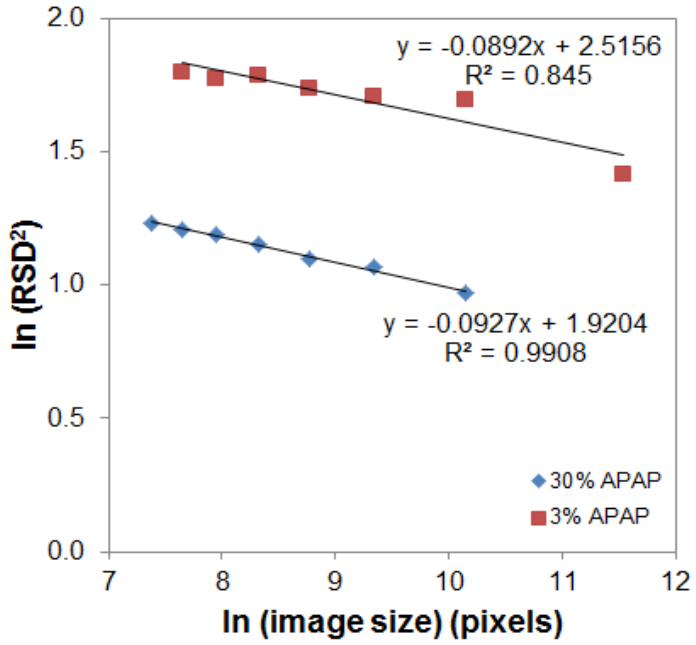

Figure 6-8. (a) RSD as a function of sample size (image size) and (b) linearization of RSD^2 as a function of image size.

6.4.3 Fraction of Pixels Statistics

6.4.3.1 Within Threshold

Concentration thresholds were chosen for each component to calculate the fractions of pixels within the range as defined previously. Thresholds chosen are listed in Table 6-5. The fraction of pixels for APAP at the different concentration levels are plotted in Figure 6-9a. For all concentration levels and rotation speeds, the fraction of pixels within the range reached at least 0.95. This means that APAP has mixed well within the range defined. There is no clear relationship between this fraction and the concentration level of APAP. Overall, the fraction of pixels within range seemed to increase as the number of rotations increased, especially during the first rotations, reaching a maximum quickly. The fraction of pixels within range confirmed that APAP, in all cases studied here, mixed quickly.

The fraction of pixels within range for both Avicel (Figure 6-9b) and lactose (Figure 6-9c) increased with the number of revolutions until it reached a maximum value. Avicel reached a plateau after fewer revolutions when the concentration of APAP was lower. This confirms that there is a strong interaction between APAP and Avicel during blending. The fraction of pixels within range for Avicel were lower for higher concentrations of APAP in the blends. Lactose reached the fraction of pixels within range faster than Avicel even for the blends with 30% APAP. The “good” flow properties (indicated by larger particle size) of lactose promote faster blending of this ingredient in all blends.

(a)

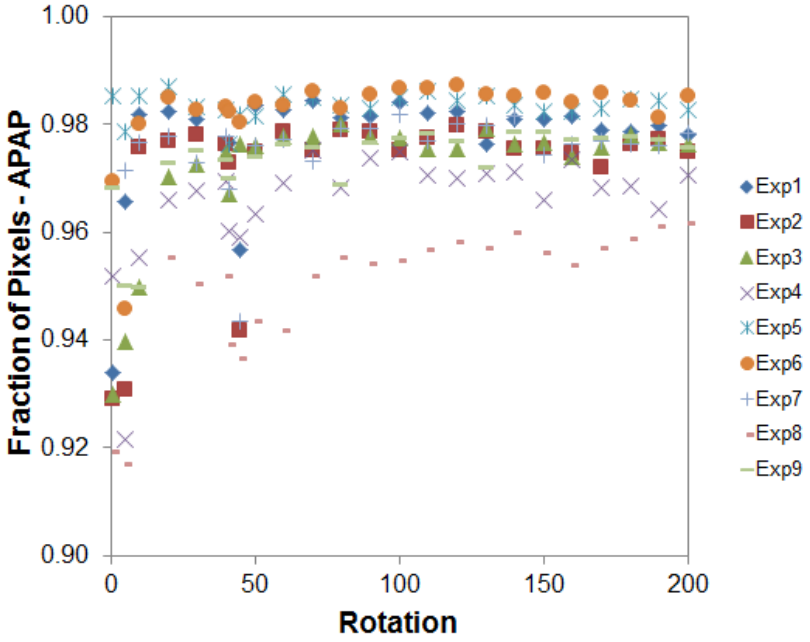
1.00
0.98
0.96
0.94
0.92
0.90
Fraction of Pixels - APAP
0
50
100
150
200
Rotation
Exp1
Exp2
Exp3
Exp4
Exp5
Exp6
Exp7
Exp8
Exp9

(b)

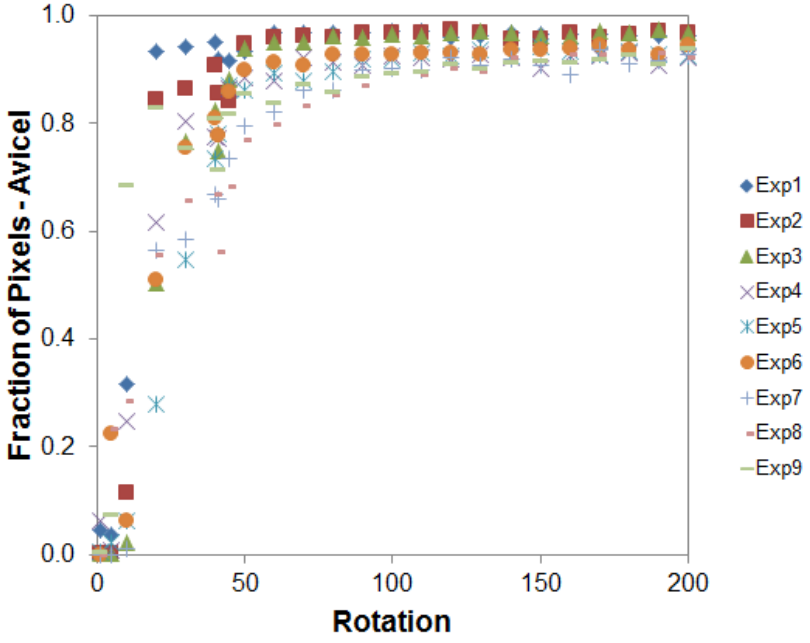
1.0
0.8
0.6
0.4
0.2
0.0
Fraction of Pixels - Avicel
0
50
100
150
200
Rotation
Exp1
Exp2
Exp3
Exp4
Exp5
Exp6
Exp7
Exp8
Exp9

(c)

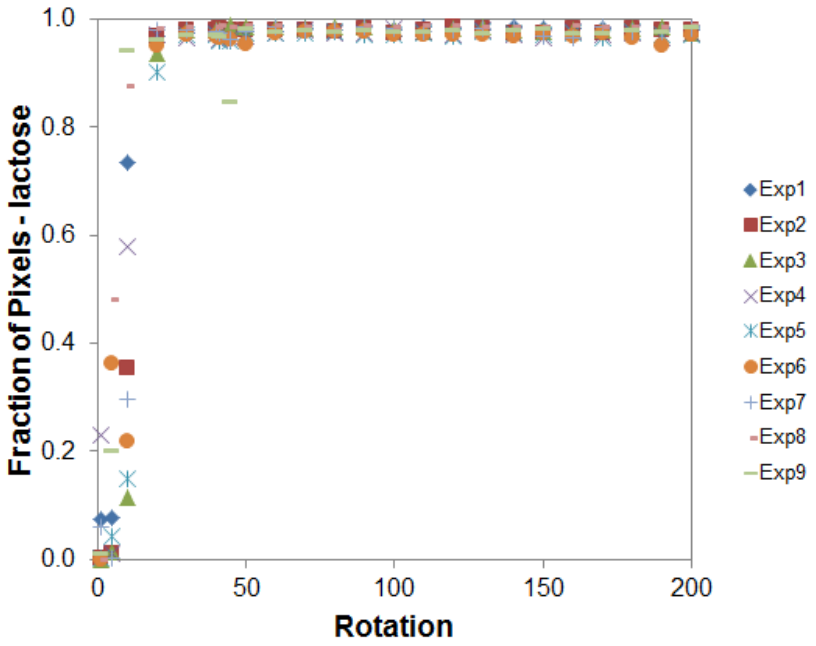

Figure 6-9. Fraction of pixels within range of threshold for (a) APAP, (b) Avicel and (c) lactose.

6.4.3.2 Above Threshold

The concentration thresholds chosen here were the upper thresholds of those used in the "within threshold" calculations. For APAP (Figure 6-10a), the fraction of pixels above the threshold was very low. The fraction of pixels above threshold increased during the first few revolutions, before adding MgSt. Once the MgSt was added (turn 40), the fraction of pixels reached a plateau, although the variability from rotation to rotation was high in some cases. While the fraction of pixels above the threshold were low, the measurements revealed larger possible aggregates even towards the end of the blending process. These results can describe the dispersive mixing of APAP in the blend. Although APAP seemed to have been mixed well, the presence of agglomerates is still evident. The fraction of pixels for Avicel (Figure 6-10b) decreased with increasing rotations and

reached a minimum after 130 rotations. The Avicel results show the typical powder mixing kinetics previously described. Avicel blending experienced fast mixing by convection for the first 50 revolutions. In this phase, the fraction of pixels above threshold was largely reduced. After 50 rotations, Avicel experienced mixing by dispersion which is a much slower process. For lactose (Figure 6-10c), the fraction of pixels above the threshold increased slightly the first 50 rotations, but remained low all throughout blending. Since the fraction of pixels above threshold for lactose was so low, substantial noise was detected. There was no clear trend due to the variation in concentration of lactose in the blends or to rotation rate. Disturbances after the addition of MgSt (turn 40) were also detected in the lactose measurements.

(a)

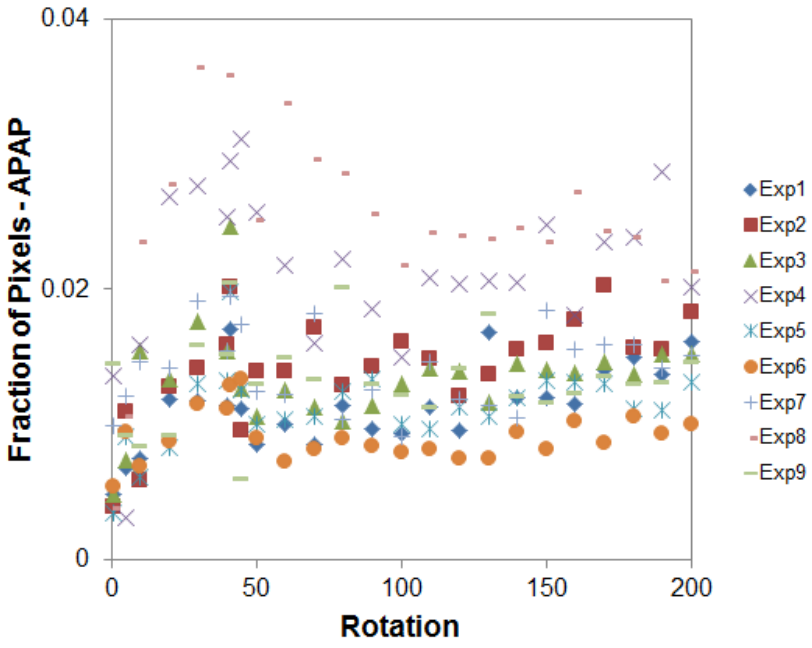

(b)

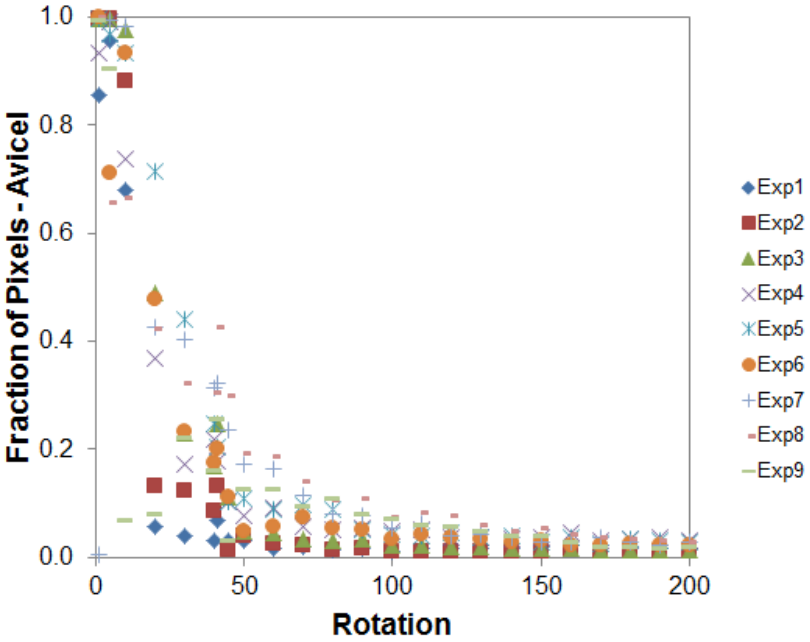

(c)

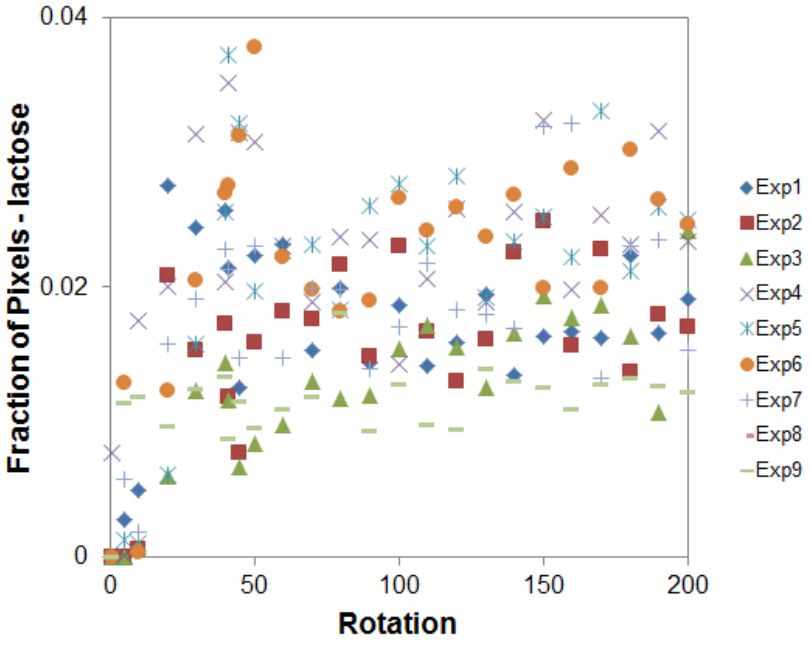

Figure 6-10. Fraction of pixels above threshold for (a) APAP, (b) Avicel and (c) lactose.

6.4.4 Aggregate Size Statistics

6.4.4.1 Mean Aggregate Size

The mean aggregate size was calculated using the same upper thresholds as in Table 6-5. In addition, for a pixel to be considered part of an aggregate, it must be contiguous to a group of at least 9 (3x3) outlier pixels. In the experiments reported here, the mean aggregate size for APAP (Figure 6-11a) slightly decreased in the first few rotations. The APAP mean aggregate size reached a minimum quickly. There was not a clear correlation between APAP concentration and aggregate size in this case. These results are in accordance with all the previous results shown. If the mean particle size diameter of APAP (45 μm) is used to calculate the mean area of APAP particles, then a mean particle area of 1590 μm^2 is obtained. Using this analogy, APAP is always in aggregates throughout the blending process. The mean aggregate size for Avicel (Figure 6-11b) was high in the first few turns as Avicel was being mixed with the other components. The aggregate size decreased substantially by turn 20. For the remainder of the blending process, the blends with a larger concentration of APAP (and less Avicel) had larger aggregates of Avicel. The mean aggregate size of lactose (Figure 6-11c) started high like that of Avicel, but since lactose was the larger component and mixed faster, the mean lactose aggregate size reached a minimum quickly.

(a)

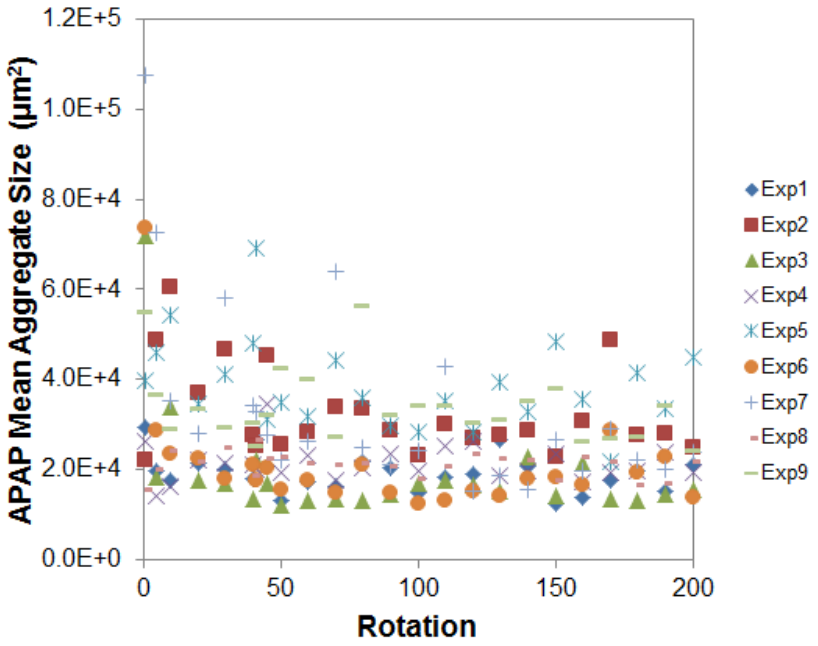
APAP Mean Aggregate Size (µm²)
1.2E+5
1.0E+5
8.0E+4
6.0E+4
4.0E+4
2.0E+4
0.0E+0
0
50
100
150
200
Rotation
Exp1
Exp2
Exp3
Exp4
Exp5
Exp6
Exp7
Exp8
Exp9

(b)

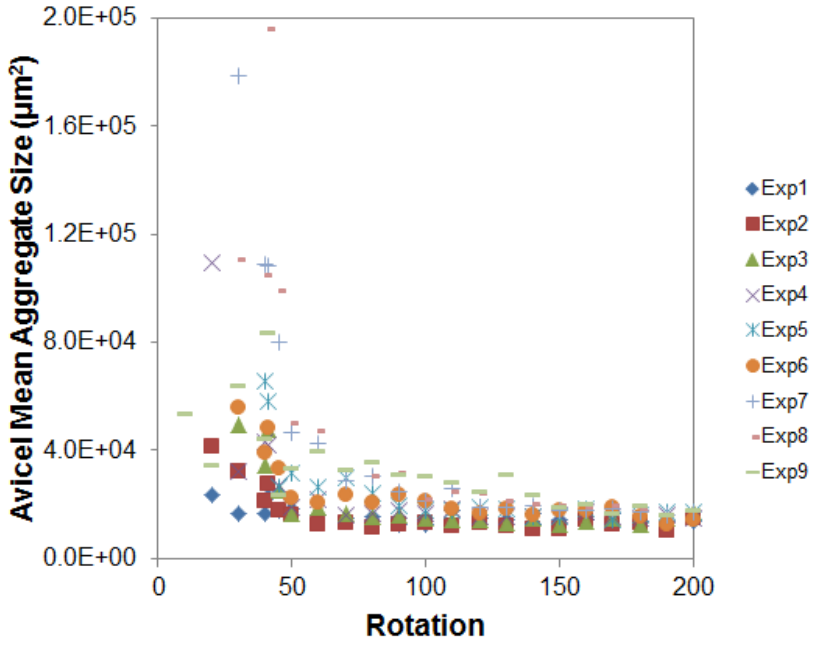
Avicel Mean Aggregate Size (µm²)
2.0E+05
1.6E+05
1.2E+05
8.0E+04
4.0E+04
0.0E+00
0
50
100
150
200
Rotation
Exp1
Exp2
Exp3
Exp4
Exp5
Exp6
Exp7
Exp8
Exp9

(c)

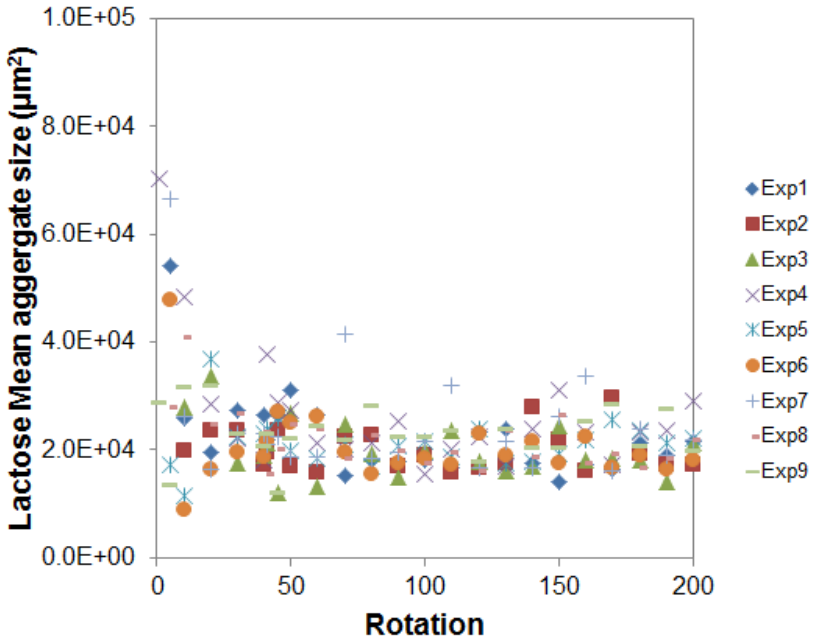

Figure 6-11. Mean aggregate size for (a) APAP, (b) Avicel, and (c) lactose.

6.4.4.2 Maximum Aggregate Size

The maximum aggregate size, indicating remaining unbroken large aggregates, as a function of rotation rate for APAP and Avicel, is shown in Figure 6-12. The detection of large aggregates is important especially when blending potent APIs. When large aggregates are detected, the blending process must often be modified to improve blending. In the case of APAP, there was no clear trend between APAP concentration or blend rotation speed and maximum aggregate size (Figure 6-12a). Large aggregates of APAP (15.5x larger than the mean particle area of APAP particles) were detected even at the end of the blending process for 3% APAP blends. If this were the case of a potent API, the blending process would have to be modified to reduce such large aggregates.

For Avicel, the maximum aggregate size followed the same trend as the mean aggregate size. The maximum size was larger for lower concentrations of Avicel, and decreased quickly with more revolutions (Figure 6-12b). In some experiments, the first few rotations showed large aggregates of lactose, but after a couple turns of the blender there was not a clear trend for the maximum aggregate size (Figure 6-12c). It is interesting to note that the two main ingredients, lactose and Avicel, act quite differently in the blend. The large Avicel aggregates continue to be broken down gradually as blending progresses, but large lactose aggregates remain, even at later turns, as evidenced by the outliers in the plot. Having large aggregates of high concentration excipients is not as critical, although these should also be well mixed to ensure the right dispersion of the API and other components.

(a)

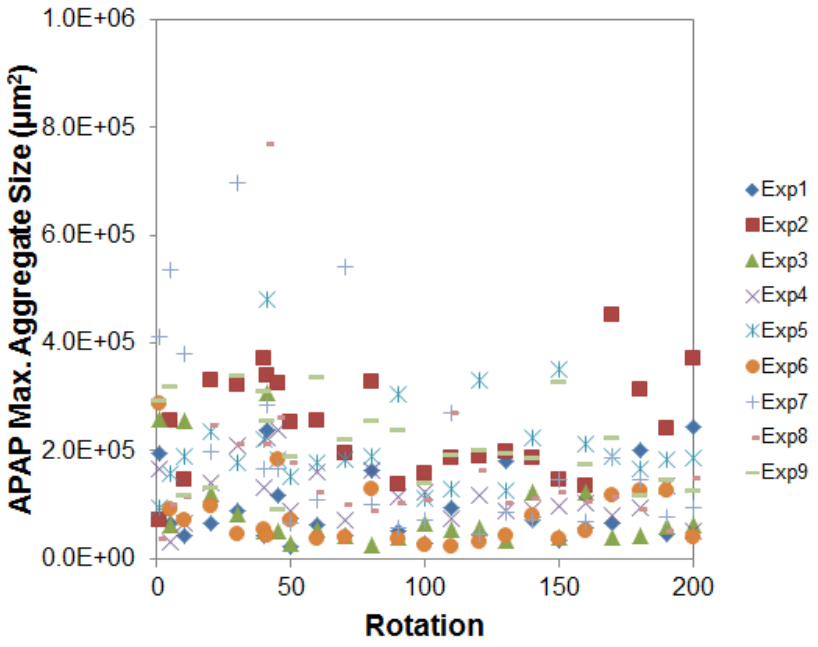

(b)

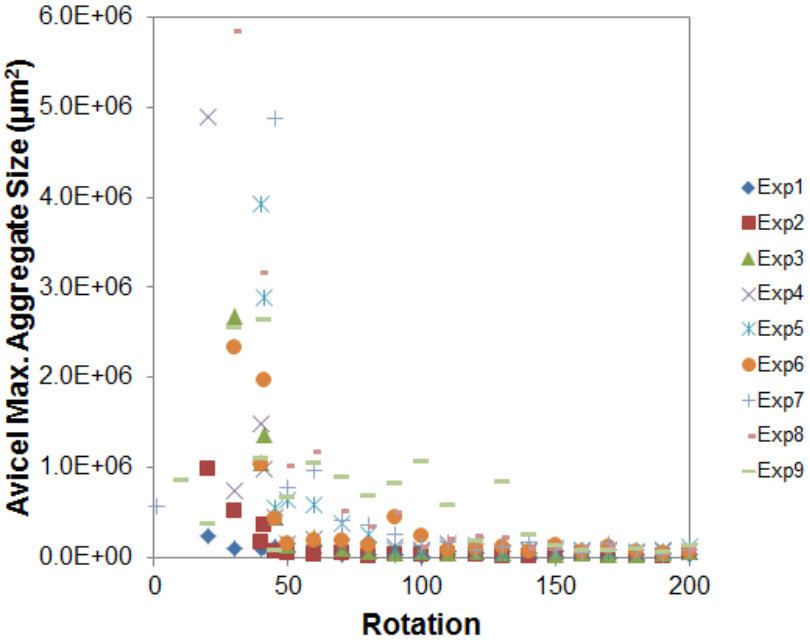

(c)

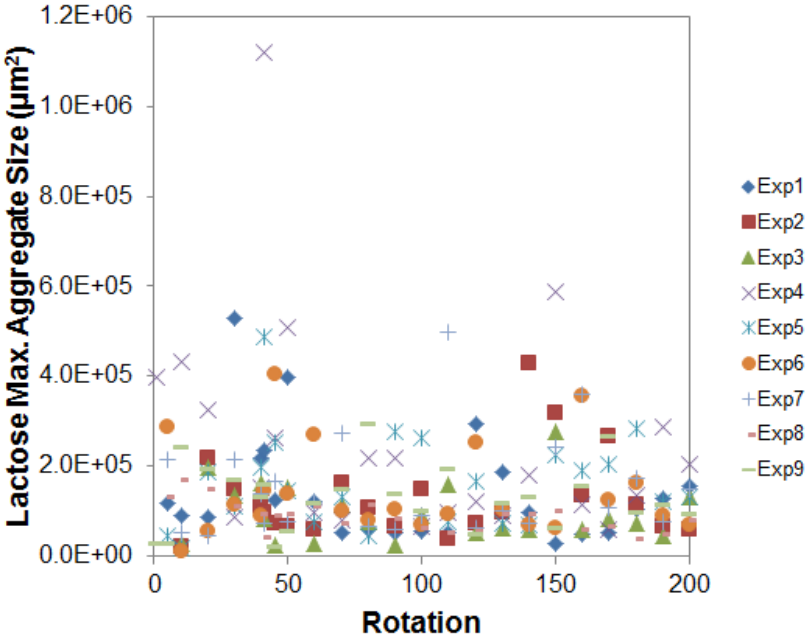

Figure 6-12. Maximum aggregate size for (a) APAP, (b) Avicel and (c) lactose.

For SiO_2, the maximum aggregate size did not show any correlation with APAP concentration or rotation speed, but in a few experiments, large aggregates remained even at later turns. For such low concentration ingredients, imaging was able to capture the statistically small occurrence of remaining relatively large aggregates. For MgSt, aggregates were only detected immediately after its addition. This concludes that MgSt was mixed quickly after a few rotations of blending and aggregates could no longer be detected

6.5 Conclusions

A new *in situ* near-infrared chemical imaging technique (imMix™) designed to characterize micro-mixing in pharmaceutical powder blends was introduced in this chapter. This technique used non-contact monitoring of the blending process, eliminating the bias introduced when using typical extractive sampling techniques. The spectral data was analyzed using the Science-Based Calibration (SBC) method to obtain concentration images of the ingredients in nine different blends in this experimental model. Each image allowed the estimation of the size of agglomerates and was used as a visual tool to help determine a suitable mixing time when all the components have formed a well-mixed blend. The mean concentration and RSD as a function of blending time was obtained from all images to further characterize the blending process. The time required for a blend to reach the nominal composition increased with the increase in APAP concentration. This was mainly due to the interaction of APAP and Avicel. It was concluded that the rotation rate, using the 1-liter bin-blender did not have an impact on the RSD, but the number of revolutions affected the blend homogeneity (RSD) of the main components.

Statistical analysis of each image was used to obtain detailed information about the blending progression of each of the components in the blends. The number of pixels above a predetermined concentration threshold and the fraction of pixels within a specified range of the nominal composition were used to characterize the blending progression. The fraction of pixels within threshold for APAP was independent of its concentration. The fraction of pixels within the threshold and above the threshold indicated that Avicel blended at a significantly slower rate than lactose. Avicel blended in fewer revolutions when the concentration of APAP was lower. The mean aggregate size statistics also supported the finding that Avicel blended at a slower rate than lactose. The maximum aggregate size analysis of the near-infrared chemical images provided a sensitive tool to detect aggregates of low-dose active materials that could pose a hazard if they remained unblended. Large APAP aggregates were detected in some blends even at later rotations. This was an indication that APAP was still present in the blend in form of agglomerates.

The imMix system showed to be useful in characterizing the distribution of aggregate sizes of the model API and excipients used for this study. The hyperspectral imaging-based blend monitoring can help in the development of pharmaceutical powder blend formulations. Further studies have been performed using various APIs with different particle size distributions, shapes and cohesion properties to understand these effects on micro-mixing, and are summarized in the next chapter.

Chapter 7 Effect of API Cohesion on the Micro-Mixing Dynamics of Pharmaceutical Powders

7.1 Summary

This chapter summarizes the micro-mixing dynamics studies of three cohesive APIs differing in material properties blended in a common excipient. Commonly, cohesive APIs are blended in a high shear mixer to overcome the forces that make them form or remain as agglomerates. In this case, the APIs were mixed in a 1-liter bin-blender (low shear) to study the effect of cohesion on micro-mixing dynamics and outcomes. The studies presented here were conducted using an *in-situ* NIR chemical imaging technique previously characterized [116]. The main objective of this work was to understand and compare how APIs varying in cohesion mixed at the micro-scale as a function of API concentration and process parameters. The study used three APIs that ranged from very cohesive (chlorpheniramine maleate), to moderately cohesive (acetaminophen) and to slightly cohesive (caffeine). The main results showed that chlorpheniramine, the most cohesive API, remained in large aggregates throughout the blending process. Overall, chlorpheniramine required a longer blending time (number of rotations) for other ingredients (e.g. Avicel) to become well dispersed, as evidenced by the aggregate size measurements. The effect of cohesion on the micro-mixing state of blends as measured by NIR-CI was demonstrated here. The most cohesive API followed the expected trend (i.e. higher RSDs and larger aggregate sizes) for all concentrations and rotation rates, while the trends for APAP and caffeine were dependent on their concentrations.

7.2 Materials and Methods

7.2.1 Materials

The materials and suppliers used in all the experiments reported here were the following. The three active pharmaceutical ingredients (APIs) used were chlorpheniramine maleate (USP, Spectrum Chemical MFG. Corp., New Brunswick New Jersey, USA), acetaminophen (semi-fine, USP, paracetamol PhEur, Mallinckrodt, Raleigh, North Carolina, USA) and caffeine (anhydrous, USP, CSPC Innovation Pharmaceutical Co., LTD., China).

The measured material properties, including particle size, of the APIs used are listed in Table 7-1. The excipients in all blends were microcrystalline cellulose (Avicel PH101, FMC Biopolymer, Newark, Delaware, USA), lactose (monohydrate N.F., crystalline, 310, Regular, Foremost Farms USA, Rothschild, Wisconsin, USA), amorphous fumed silica (Cab-O-Sil M-5P, Cabot Corporation, Tuscola, Illinois, USA), and magnesium stearate N.F. (non-Bovine, Tyco Healthcare / Mallinckrodt, St. Louis, Missouri, USA). The nominal particle sizes of all excipients used are listed in Table 7-2.

Table 7-1. Material Properties of active pharmaceutical ingredients studied. Compressibility value obtained at 15 kPa.

Material	Mean particle size (µm)	d10 (µm)	d50 (µm)	d90 (µm)	Bulk density (g/mL)	Compressibility (%)
Chlorpheniramine	7.1	1.4	6.2	13.3	0.23	45.5
Acetaminophen	47.2	5.5	29.8	116.4	0.39	34.9
Caffeine	54.0	4.8	34.7	135.8	0.54	19.2

Table 7-2. Nominal particle size of excipients used.

Material	Mean Particle Size (μm)
Avicel 101	50.0
Regular lactose	180.0
Cab-O-Sil (SiO_2)	0.005-0.02
Magnesium Stearate	10.0

7.2.2 Material properties of APIs

Material properties of the APIs were characterized by three metrics: the particle size, the conditioned bulk density, and the compressibility.

7.2.2.1 Particle size

The particle size distribution of each API used was determined using a laser-diffraction (LS-13 320) analyzer with a Tornado Dry Powder System (Beckmann-Coulter, Brea, California, USA). The APIs were chosen based on their difference in particle size. The mean particle size, and d_{10}, d_{50} and d_{90} fractions of each API are recorded in Table 7-1.

7.2.2.2 Conditioned bulk density

The conditioned bulk density of the APIs was measured using a powder rheometer system (FT4, Freeman Technology Ltd. Gloucestershire, UK) using a 48-mm cylinder. The conditioned bulk density is the density after the powder has gone through the conditioning cycle which was performed before each compressibility test in the FT4 rheometer. This ensures that the state of each powder was "reproducible" [117]. Thus

before each compressibility measurement, the conditioned bulk density for each API was obtained. The values are recorded in Table 7-1 and are referred as to "bulk density".

7.2.2.3 Compressibility

The compressibility of the APIs was measured using the same powder rheometer system (FT4) used to measure the conditioned bulk density. The compressibility of a powder is a measure of the change in density as a function of applied normal stress. In this case, the compressibility is the percentage change in volume after compaction at a specific normal stress. The FT4 compresses the powder from 0 to 15 kPa with increasing steps of 0.5 kPa. Cohesive powders show a large change in volume, while non-cohesive powders show little change in volume. The compressibility profiles for the APIs used are shown in Figure 7-1. The compressibility values used for comparison were obtained at a normal stress of 15 kPa and are recorded in Table 7-1.

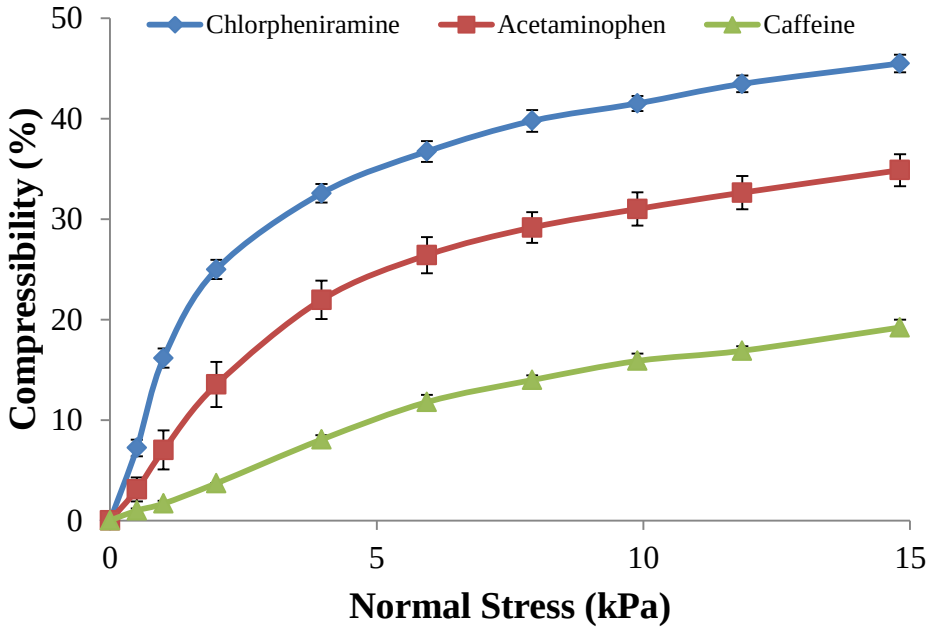

Figure 7-1. Compressibility profiles of APIs used.

7.2.3 Blending and in-line monitoring

Blending was performed in a 1-liter stainless steel bin blender. Approximately 40% of the total blender volume was used in all experiments here. Three concentrations (3%, 10%, and 30% by weight) of each API were used in this study. The blend concentrations for the APIs and excipients are given in Table 7-3. The blender was loaded through the top in the following manner: Avicel PH101 was loaded first, lactose was added second, the API was added third and Cab-O-Sil (SiO_2) was added fourth. The order and the filling technique was kept the same throughout the set of blend experiments to avoid any effects other than the composition, rotation speed and the type of API studied. The blender was stopped after 40 revolutions and magnesium stearate (MgSt) was added through the top. Three rotational speeds (15, 25, and 35 RPM) were used in the experiments for each blend and each API.

Table 7-3. Blend concentrations.

	Blend 1	Blend 2	Blend 3
API (%)	3.0	10.0	30.0
Avicel 101 (%)	47.5	44.0	34.0
Lactose (%)	47.5	44.0	34.0
SiO_2 (%)	0.5	0.5	0.5
MgSt (%)	1.5	1.5	1.5

Hyperspectral images were taken throughout the blending process at specified numbers of rotations. Hyperspectral images were taken at 1, 5, 10, 20, 30 and 40 revolutions to study the initial mixing progression. The blender was stopped after 40 revolutions to add MgSt. Once the MgSt was added, hyperspectral images were taken at 41, 45, and 50 revolutions to study the effect of MgSt addition. After the 50^{th} turn,

hyperspectral images were taken every 10^{th} revolution up to 200 revolutions. Potential mechanical disturbances were minimized by gradually slowing the blender to scan the sample, and thus avoiding any unwanted jarring of the powder in the blender.

7.2.4 Near infrared chemical imaging

7.2.4.1 Hyperspectral imaging

Hyperspectral images of the blends were taken using an imMix system (Middleton Research, Middleton, Wisconsin, USA). The imMix system consists of a push-broom short-wave infrared (SWIR) hyperspectral camera (Specim Spectral Ltd, Oulu, Finland) with a 1-liter bin-blender attached (Figure 7-2). The SWIR camera has a wavelength region of 1000-2500 nm and a full frame rate of 100 Hz. The SWIR camera measures 320 spatial points by 256 spectral points with an approximate resolution of 30 μm per pixel. Hyperspectral images were taken throughout the blending process at specified rotations through a borosilicate glass window on the bottom of the blender. Light sources illuminate the glass window and the powder inside the blender that is in contact with the window. The diffusely reflected light off the blend is then redirected by a mirror towards the SWIR macro lens. A hyperspectral cube is formed line by line across the window creating a chemical image of the blend with an approximate area of 1 cm x 1 cm. More details on how the imMix system [116] and the push-broom SWIR camera [114] operate can be found elsewhere. In all the experiments here, an integration time of 1 millisecond and a frame rate of 75 frames per second were used.

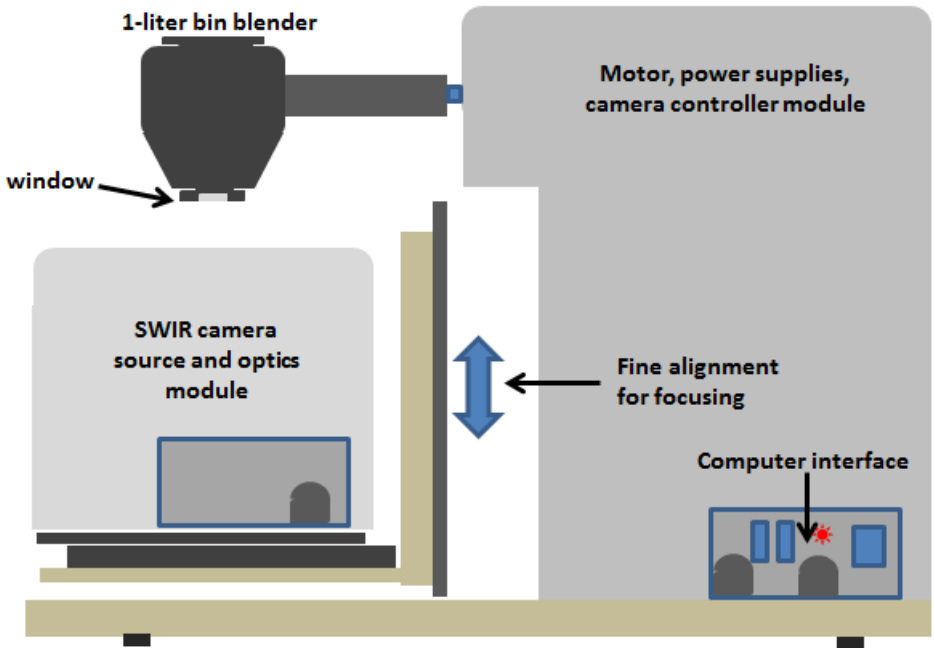

Figure 7-2. imMix System diagram.

7.2.4.2 Image processing

A Matlab-based chemometric and statistical software (Middleton Research, Middleton, Wisconsin, USA) was used to create calibrations and analyze the images. The Science-Based Calibration (SBC) method [112, 113] was chosen to analyze and quantify all the blend ingredients in the chemical images obtained. The SBC method only required the input of the pure components' spectra, which were collected in the same manner using a small sample holder attached to the bottom of the blender. For the SBC method, we used noise estimates for the hardware (2 mAU), offset (50 mAU) and slope (0.1667 mAU/nm). The final blend's spectrum, called the "operating point" in the SBC method, was used as a bias correction factor for each blend. In addition, white and dark references were also collected and used to correct all hyperspectral images taken. This correction transforms the intensity values into absorbance as shown in equation 7-1.

$$Absorbance = -log\left(\frac{I_{sample} - I_{dark}}{I_{white} - I_{dark}}\right) \quad (7\text{-}1)$$

Calibration coefficients (b-vectors) were calculated for each pure component and used to predict the composition of every pixel of the blend chemical images. The result was a composition map for each rotation specified, for each blend component, which was then used to further characterize the blend progression.

7.2.5 Image analysis

7.2.5.1 Composition images

Composition images obtained show concentration maps (0-100%) of each ingredient in a region of the blends. The images are useful to visually detect large aggregates of APIs and their intensity in concentration, and to monitor the blending progression. Although the images are useful, they create large amounts of data and deriving quantitative conclusions from them is difficult. Therefore, statistical analysis of each image was necessary to extract parameters that were helpful in the interpretation of the images and to understand the effects of API material properties on the micro-mixing behavior throughout blending. Various statistical measures - such as average concentration, the fraction of pixels within concentration thresholds, and aggregate sizes - were extracted and analyzed from each of the chemical images. These measures were described in detail in Chapter 6, which characterized the use of this NIR-CI method [116]. To follow the results in this chapter, a brief description of each measurement is presented here.

7.2.5.2 Concentration

Concentration statistics, including the mean concentration ($\bar{C}$) and the relative standard deviation (RSD) of the pixel-by-pixel concentration of each component in each chemical image, were considered. The RSD was calculated as shown in equation 7.2.

$$RSD = \frac{\sigma}{\bar{C}} = \frac{standard\ deviation}{average\ concentration}, where\ \sigma = \sqrt{\frac{\sum_{p=1}^{P}[c(p)-\bar{C}]^2}{P}} \quad (7.2)$$

In the equation above, *c* is the concentration, *p* is the pixel number and *P* is the total number of pixels in the measured image. The average concentration ($\bar{C}$) is the mean concentration of all the pixels measured in the chemical image. The RSD measured from the chemical images differs from the common RSD measured from sample to sample to characterize bulk mixing. The scale of scrutiny here is a pixel, while for the typical RSD it is the size of a unit dose (e.g. tablet).

7.2.5.3 Fraction of pixels

Fraction of pixels statistics, including the fraction of pixels within an upper and lower threshold, and above a threshold were considered. Thresholds were specified for each ingredient relative to its nominal composition (Table 7-4). Due to the fluctuations in the pixel-to-pixel composition values, some thresholds were set at negative values although the negative concentration has no physical meaning. The fraction of pixels within the range indicated the amount of the blend that was well-mixed and close to the nominal composition for a given component. This metric can be used as a quality measurement requiring all the ingredients to be above a specific fraction depending on the formulation. On the other hand, the fraction of pixels above the threshold indicated the amount of the

blend for which that component remained above the nominal concentration, possibly in aggregates. The fraction of pixels above the threshold can be related to the aggregate size statistics described next.

Table 7-4. Thresholds used for identification of aggregates, fraction "within threshold", and "above threshold" statistics - Lower and upper thresholds (nominal ± nominal*factor).

Chlorpheniramine blends			
API (%)	Chlor (%)	Avicel (%)	Lactose (%)
3	-12.0 to 18.0	38.0 to 57.0	28.5 to 66.5
10	-15.0 to 35.0	30.8 to 57.2	17.6 to 70.4
30	6.0 to 54.0	17.0 to 51.0	10.2 to 57.8
Acetaminophen blends			
API (%)	APAP (%)	Avicel (%)	Lactose (%)
3	-6.0 to 12.0	30.9 to 64.1	26.1 to 68.9
10	0 to 20.0	28.6 to 59.4	24.2 to 63.8
30	21.0 to 39.0	17.0 to 51.0	10.2 to 57.8
Caffeine blends			
API (%)	Caffeine (%)	Avicel (%)	Lactose (%)
3	-12.0 to 18.0	38.0 to 57.0	28.5 to 66.5
10	-15.0 to 35.0	33.0 to 55.0	19.8 to 68.2
30	12.0 to 48.0	20.4 to 47.6	11.9 to 56.1

7.2.5.4 Aggregate size

The aggregate size statistics, including the mean aggregate size and the maximum aggregate size of each ingredient at each measured rotation of the blends, were calculated from the chemical images. A pixel was considered to be a part of an aggregate if its concentration value was above the specified thresholds (shown in Table 7-4.) and if there were 9 or more connected pixels (e.g. a square region of 3x3 pixels) in a group.

7.3 Results and Discussion

The results and discussion section is divided into two parts. The first part (section 3.1) covers the main results and observations of the measurements on the API micro-mixing. The second part (section 3.2) covers the main results and observations of the measurements of the main excipients, lactose and Avicel, and some observations about the minor excipients (MgSt and Cab-O-Sil).

7.3.1 Active Pharmaceutical Ingredients

7.3.1.1 Material properties of APIs

Three APIs, known to be cohesive, were used in these studies. Since the main objective of the work here was to understand and compare how the APIs, varying in cohesion, blended at the micro-scale as a function of API concentration and processing parameters, some of their material properties were measured to confirm that the APIs were in fact different from each other. In this case, the particle size, conditioned bulk density and compressibility of the APIs were measured. The numerical values from all measurements performed (Table 7-1) indicated that the APIs were different from each other, yet all three were still considered cohesive.

Chlorpheniramine had the smallest particle sizes with a d_{10}, d_{50} and d_{90} of 1.4 µm, 6.2 µm and 13.3 µm, respectively. Acetaminophen (also referred as "APAP" in this paper) had intermediate particle sizes with a d_{10}, d_{50} and d_{90} of 5.5 µm, 29.8 µm and 116.4 µm, respectively. Finally, caffeine had the larger particle sizes with d_{10}, d_{50} and d_{90} of 4.8 µm, 34.7 µm and 135.8 µm, respectively. It is worth noting that the d_{10} fraction of APAP is slightly larger than that of caffeine. Also, the differences in particle size between the

latter two are smaller than their difference with chlorpheniramine. The mean particle size of chlorpheniramine, APAP, and caffeine were 7.1 µm, 47.2 µm, 54.0 µm, respectively. Although particle size is not a direct measure of powder cohesion (as is the case for most measurements), it has a strong influence on cohesion (i.e. powder flow) [118, 119].

The conditioned bulk density results indicated that chlorpheniramine had the lowest bulk density (0.23 g/mL) followed by APAP and caffeine (0.39 g/mL and 0.54 g/mL, respectively). In general, the bulk density of organic materials has been used as a powder flow property itself and it has been correlated to other powder flow properties [119]. A higher bulk density is an indication of better flowability (lower cohesion).

The compressibility of the three APIs was also measured. The compressibility and its counterpart, the dilation coefficient, have both been correlated to powder flow properties (e.g. flow index) [15]. The compressibility as a function of normal stress is shown in Figure 7-1. In order to have a single numerical value, the compressibility at a normal pressure of 15 kPa was used as the compressibility value. A higher compressibility is an indication of worse flowability (higher cohesion). As expected, the compressibility of chlorpheniramine was the highest (45.5%) followed by APAP (34.9%) and caffeine (19.2%). The meaning of these values, in simple vernacular terms, is that caffeine would be considered to "flow relatively well", while APAP and chlorpheniramine would be considered to "flow poorly" (APAP) and "very poorly" (chlorpheniramine). Thus, with these results in mind, the APIs used were categorized as very cohesive (chlorpheniramine), cohesive (APAP), and slightly cohesive (caffeine). Subsequently, the effect of API material properties (i.e. API cohesion) on the micro-mixing dynamics as a function of blending parameters and API concentration was examined.

7.3.1.2 Chemical Images

Chemical images were obtained for all experiments at the specified number of rotations. Representative examples of chemical images of the APIs from blends at 25 RPM for all three concentrations used are shown in Figure 7-3. For 3% API blends (Figure 7-3a), the chlorpheniramine images showed large aggregates with high intensity (80-100% API). Although APAP aggregates could not be identified using this scale and the naked eye, some areas in which the concentration is much higher than 3% were detected. Caffeine images showed smaller and less intense, yet significant, aggregates than those of chlorpheniramine. As the API concentration increased, more aggregates were seen in the chemical images. For example, at 10% API (Figure 7-3b), the chlorpheniramine images showed several aggregates larger than those in the 3% API images. Some APAP aggregates were detected at this concentration level, and caffeine presented more aggregates at this level as well. For 30% API (Figure 7-3c), larger, high intensity aggregates of chlorpheniramine were detected. The APAP chemical images showed that APAP was well dispersed throughout. The caffeine chemical images showed that caffeine was also well dispersed, although a few large aggregates were detected.

(a)

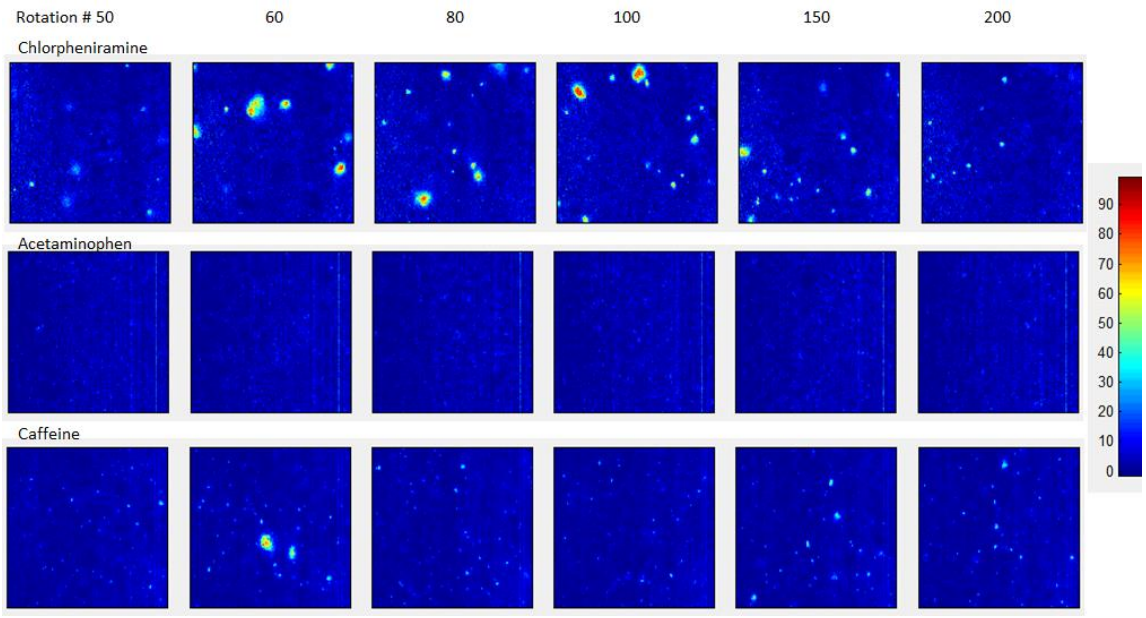
Rotation # 50
60
80
100
150
200
Chlorpheniramine
Acetaminophen
Caffeine
90
80
70
60
50
40
30
20
10
0

(b)

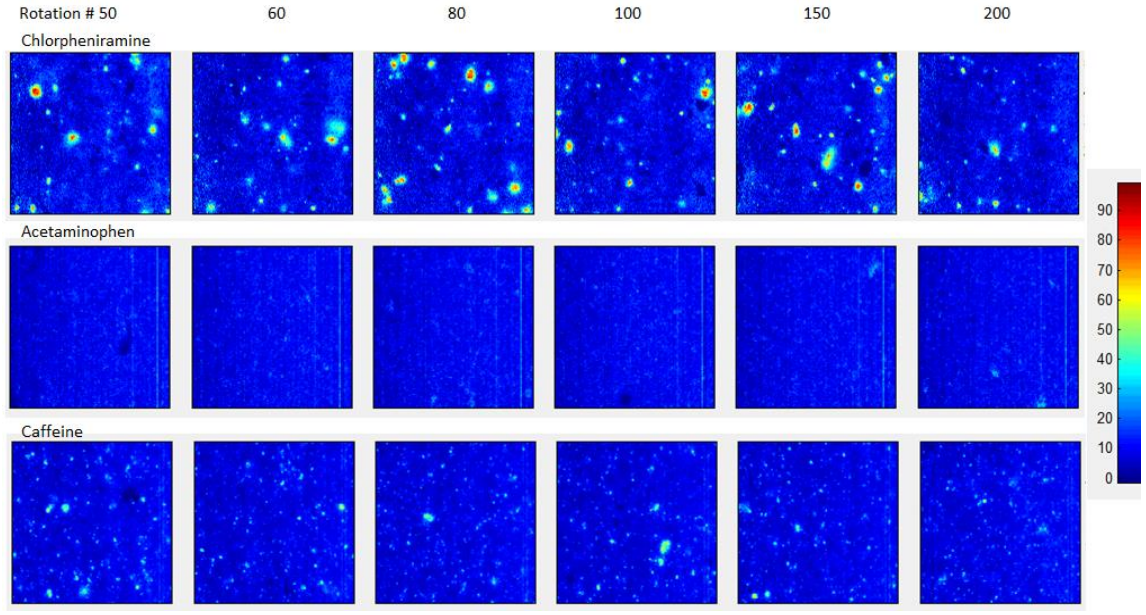
Rotation # 50
60
80
100
150
200
Chlorpheniramine
Acetaminophen
Caffeine
90
80
70
60
50
40
30
20
10
0

(c)

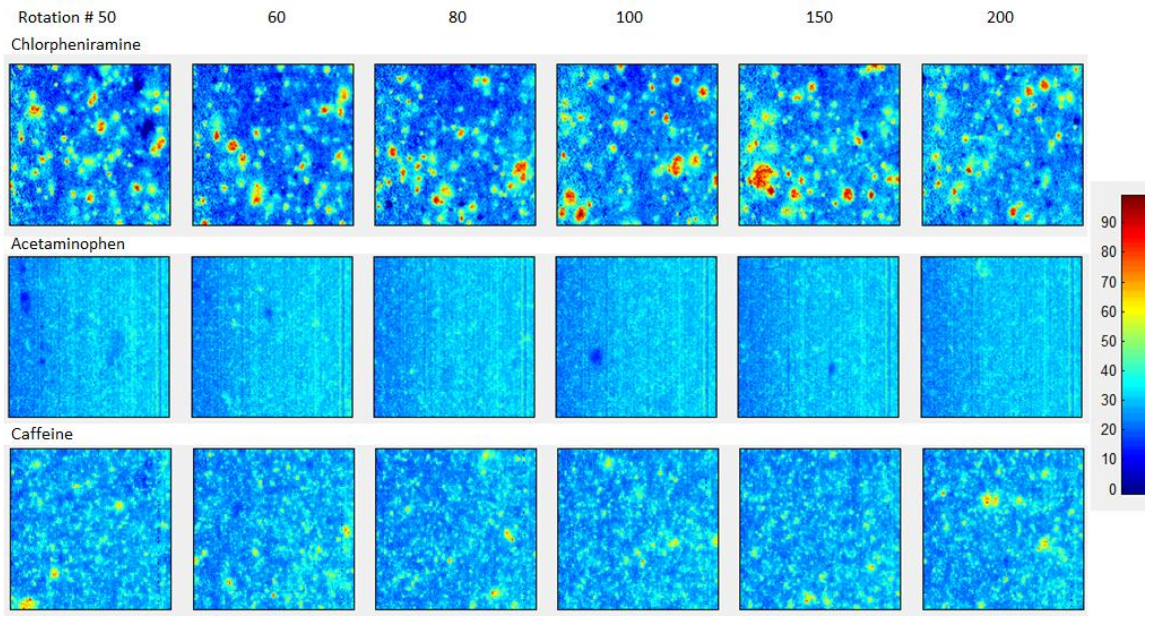

Figure 7-3. Example of chemical images for (a) 3%, (b) 10%, and (c) 30% API at 25 RPM. Concentration bar indicates the concentration within each graph from 0 to 100% API.

The results indicated that the most cohesive API, chlorpheniramine, was present through the blending process for all concentrations in larger aggregates than the other two APIs. Caffeine also had several high intensity (higher concentration) aggregates, but they were smaller than those of chlorpheniramine. Some APAP aggregates were still present with less intensity than those of caffeine. Although the results from the chemical images were useful in monitoring large aggregates, most of the time large visible aggregates such as those present in chlorpheniramine will not be observed. For example, APAP did not show "obvious" large aggregates in the image, but this did not mean that there were no APAP aggregates within the blend. This meant that we were not able to detect them using plain sight with this color scale. A narrower color scale may provide more contrast and show the APAP aggregates. For this reason, statistical analyses of the chemical images should be used to examine the micro-mixing state of the blends more objectively.

7.3.1.3 Concentration statistics

The average concentration of all APIs was calculated for each rotation image. The measured concentration for all three APIs increased with increasing number of rotations until it reached close to the target value, fluctuating around it. To illustrate the effect of API on the concentration, the results at 25 RPM are shown in Figure 7-4 for each API concentration. The results obtained at 15 RPM and 35 RPM showed a similar behavior to those of 25 RPM and were omitted for the sake of brevity. The concentration for chlorpheniramine presented more variability when compared to the other two APIs, for all blend concentrations. These results are an indication of the presence of large variability within the blend even at a larger number of rotations. This indicated the presence of large aggregates as seen in the chemical images. Fluctuations in the concentration of chlorpheniramine decreased with increasing concentration of the API in the blend.

(a)

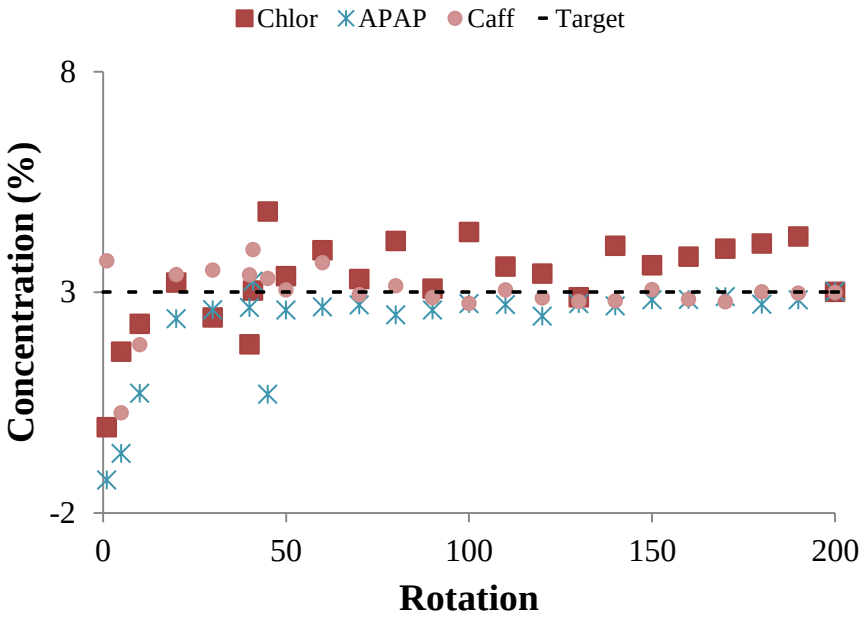

(b)

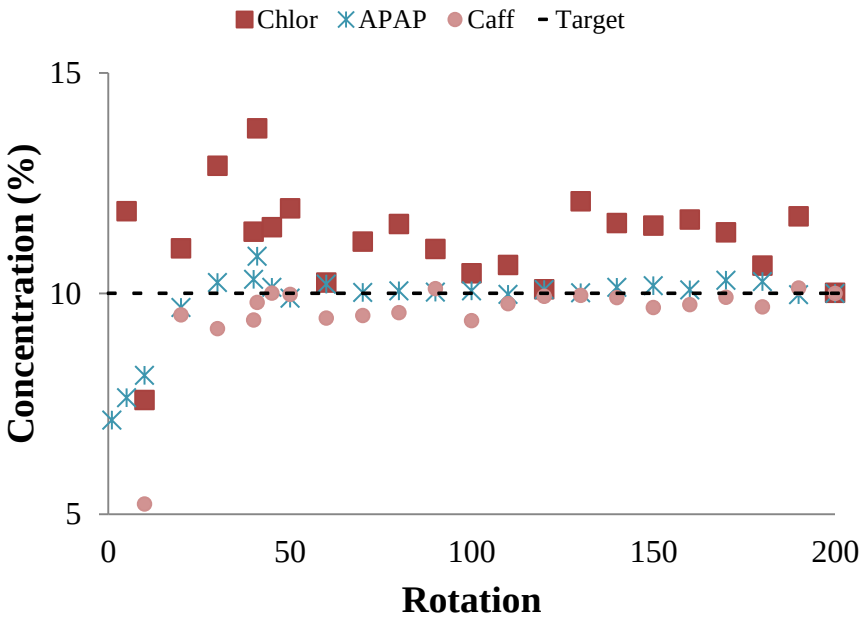

(c)

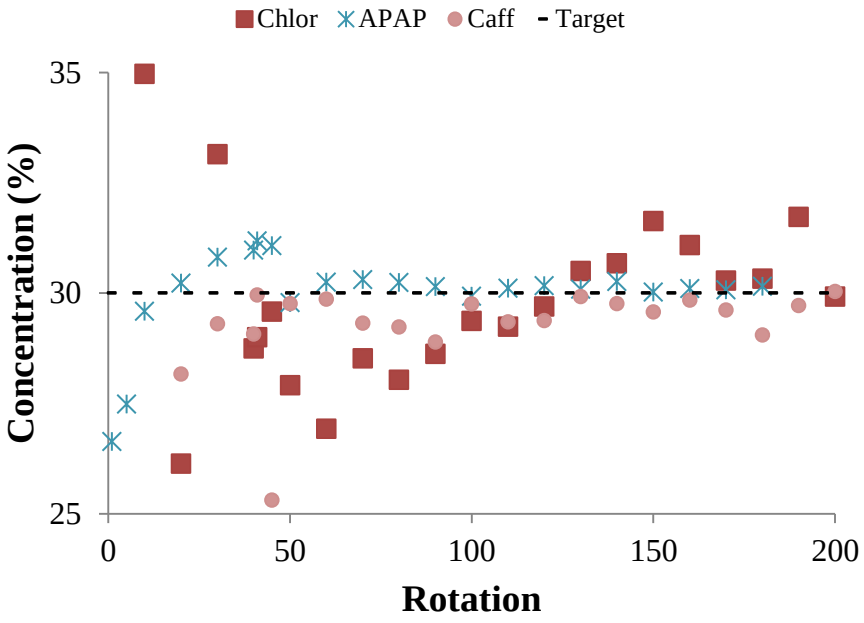

Figure 7-4. Blending profiles for (a) 3%, (b) 10% and (c) 30% API at 25 RPM.

The concentration of APAP and caffeine seemed to reach the target concentration rather quickly. This indicates that their mixing behavior is similar even though they are different in cohesion. We can assume that the aggregates present in APAP and caffeine were being broken and dispersed throughout the matrix of the blend while this process was not as efficient for chlorpheniramine.

The relative standard deviation (RSD) of all APIs was measured as a function of the number of rotations. Overall, the RSD decreased with an increase in the number of rotations (as expected). Let us recall that three mechanisms have been proposed for powder mixing: convection, dispersion and shear [38]. Convective mixing occurs when groups of particles are transported from one location to another by the bulk flow. Dispersive mixing refers to the "diffusion-like" co-mingling of individual particles (micro-mixing) due to velocity fluctuations. Shear mixing, which is also a micro-mixing effect, is caused by slipping planes within the powder bed, driven by the same external forces (e.g. gravity) that drive convective and dispersive mixing. In a typical mixing curve, we will see convective mixing followed by dispersive mixing (as described in Figure 7-5a). For 3% blends (Figure 7-5), the rate of convective mixing was slower for chlorpheniramine than for APAP and caffeine. The difference between the convective mixing rates of APAP and caffeine was less than the difference between both APIs and chlorpheniramine for all 3% API blends at all three rotation rates used. In all cases, the chlorpheniramine RSD was higher, followed by the APAP RSD and the caffeine RSD. This RSD trend is in accordance with what was expected by the material properties of the APIs used. The most cohesive API, chlorpheniramine, was expected to remain more

aggregated, yielding the highest RSD followed by the medium and slightly cohesive APIs (APAP and caffeine, respectively).

(a)

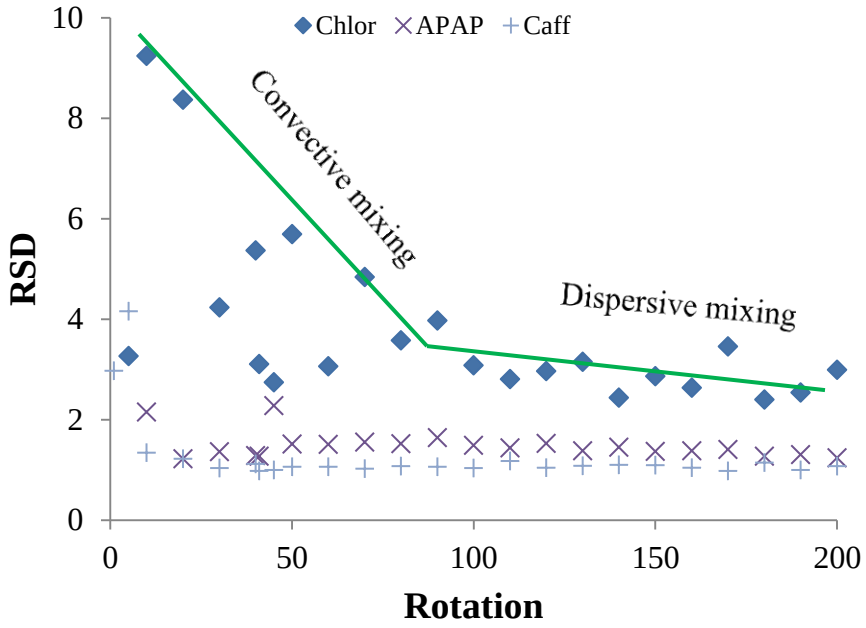

(b)

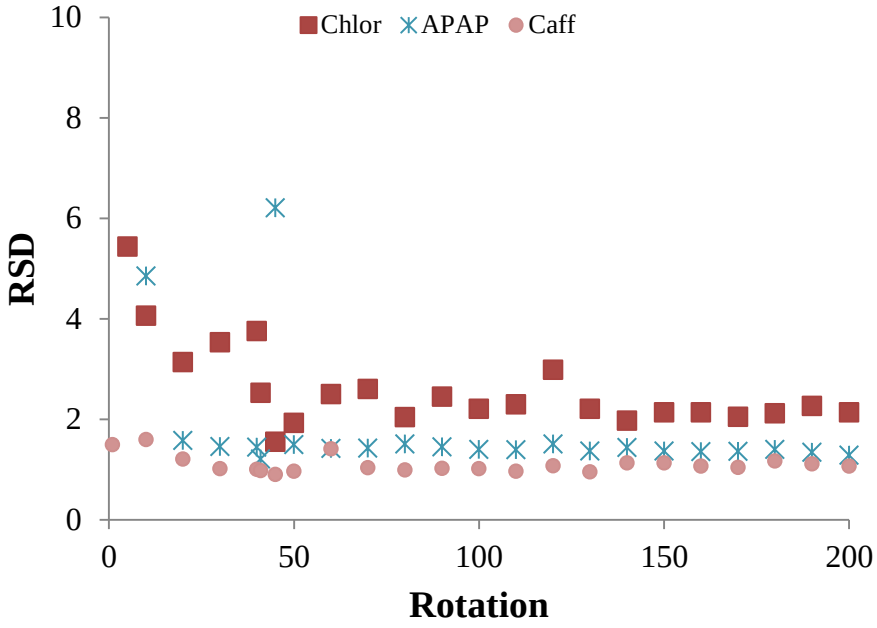

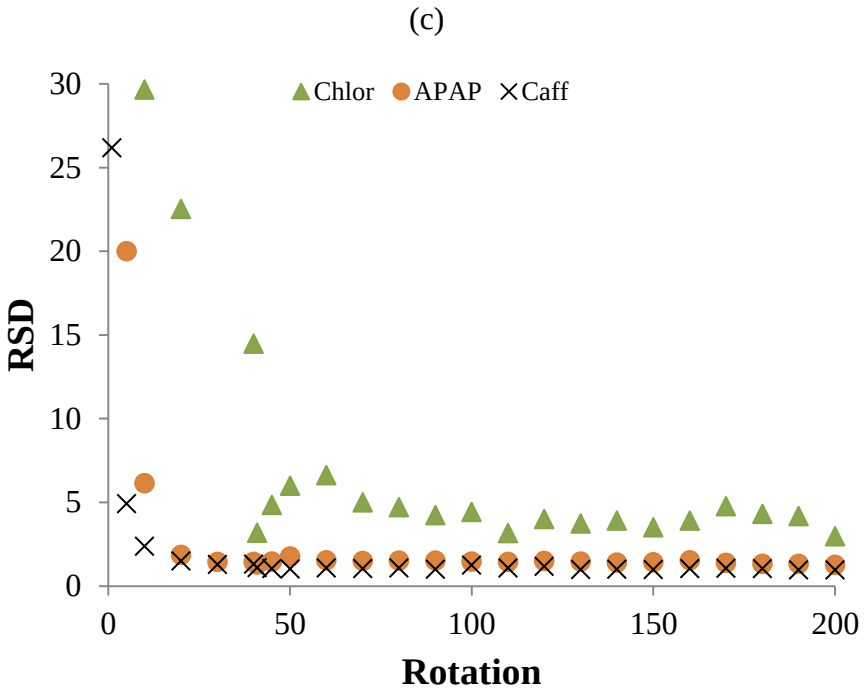

Figure 7-5. RSD profiles for 3% API blends at (a) 15 RPM, (b) 25 RPM and (c) 35 RPM. Scale at 35 RPM different to be able to see the difference in convective mixing rates from all three APIs. In this case, the RSD measurements start much higher.

It is worth noting that for the 3% chlorpheniramine blends, the rotation rate seemed to have an influence on the convective mixing rate (Figure 7-6). For the APAP and caffeine blends, the RSDs were very similar for all rotation rates used. It has been shown previously that the rotation rate did not have a significant effect on the mixing rate [9]. Although this was demonstrated, the RSD results obtained using this method showed differences for a very cohesive API. Very importantly, in considering the observed RSD values, the reader should keep in mind that observed RSD values depend on sample size, i.e., smaller samples always result in larger RSD values. The pixel-to-pixel RSD measured here correspond to samples much smaller than the unit dose-based RSD that is typically measured in most macro-mixing experiments. The RSD calculated by looking at

the pixel-to-pixel concentration of the APIs is a measure of the micro-mixing state variability.

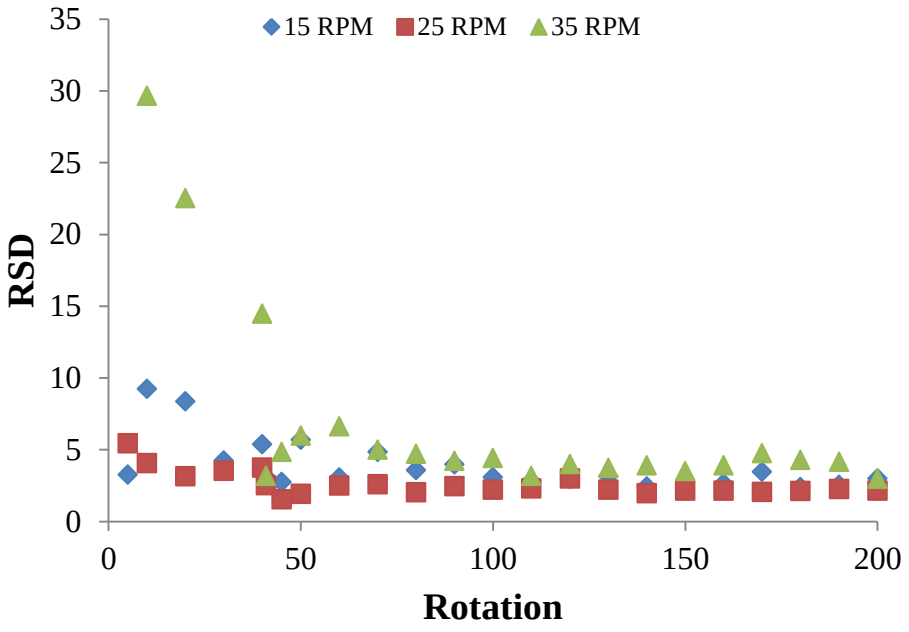

Figure 7-6. RSD as a function of rotation rate for 3% chlorpheniramine blends at 15 RPM, 25 RPM, and 35 RPM.

The RSDs as a function of rotation rate for the 10% API and 30% API blends are shown in Figures 7-7 and 7-8, respectively. The RSD for chlorpheniramine was higher than that of APAP and caffeine for all concentrations. For the 10% API blends, the RSD measurements for APAP and caffeine were very similar, although the APAP RSD was slightly lower for all rotation rates used. For 30% API blends, the difference in RSD between APAP and caffeine was larger than that of the 10% API blends. The RSD for APAP blends was lower in this case. Although the results were as expected at low concentrations (i.e. 3% API), as the concentration of APAP and caffeine increased, their difference in RSD was more noticeable. One explanation for this phenomenon is that since caffeine has a larger particle size, it might be segregating at high concentrations

(10% and 30%). In our previous studies (Chapter 6), we saw a strong interaction between Avicel and APAP, likely due to their similarity in particle size [116]. This similarity might have also caused more mixing at higher concentrations of APAP, while the larger particle size of caffeine may have caused it to segregate.

(a)

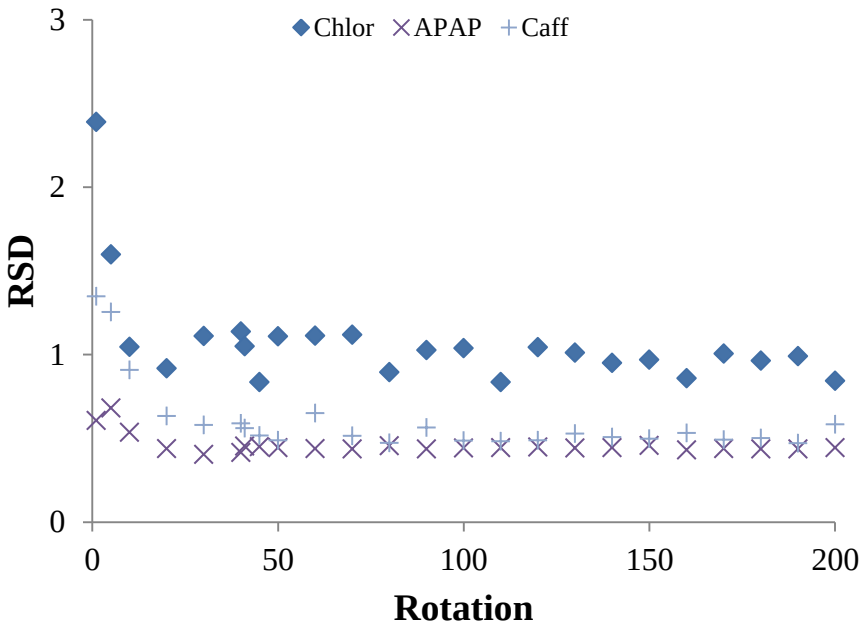

(b)

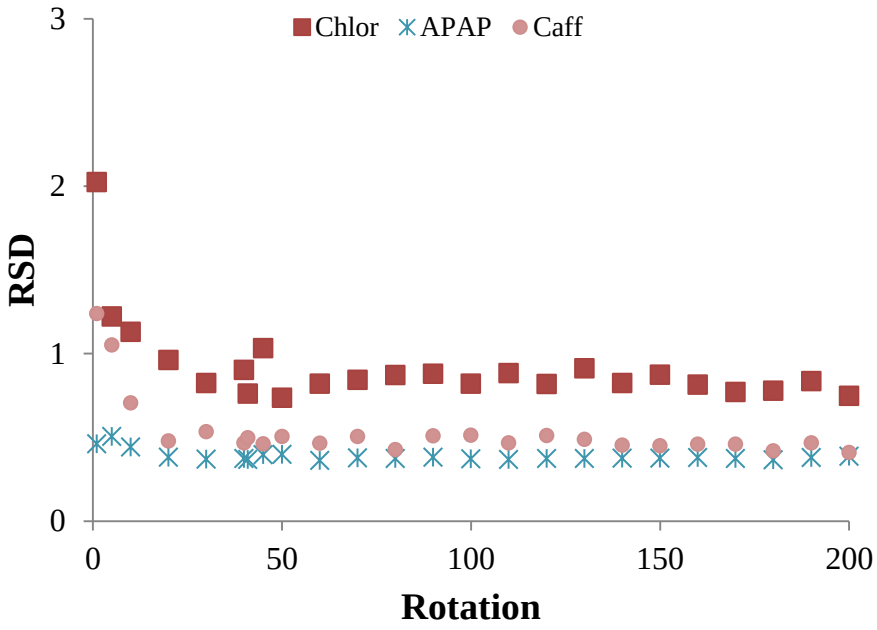

(c)

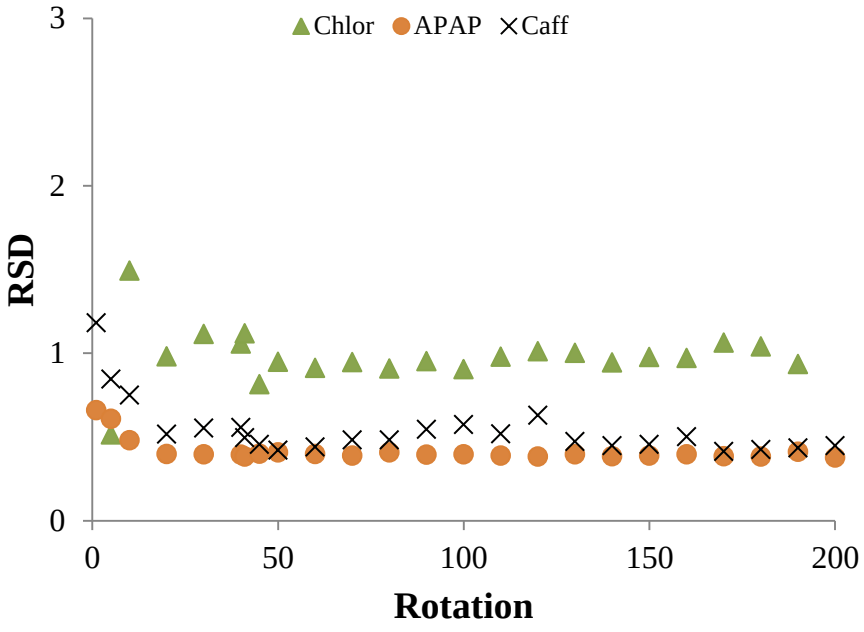

Figure 7-7. RSD profiles for 10% API blends at a) 15 RPM, b) 25 RPM and c) 35 RPM.

(a)

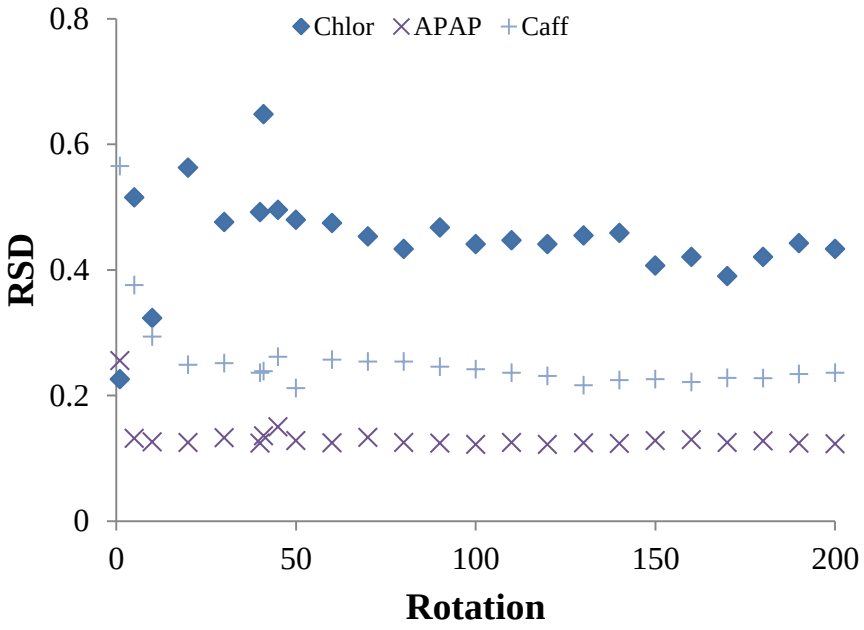
Chlor
APAP
Caff
RSD
Rotation
0.8
0.6
0.4
0.2
0
0
50
100
150
200

(b)

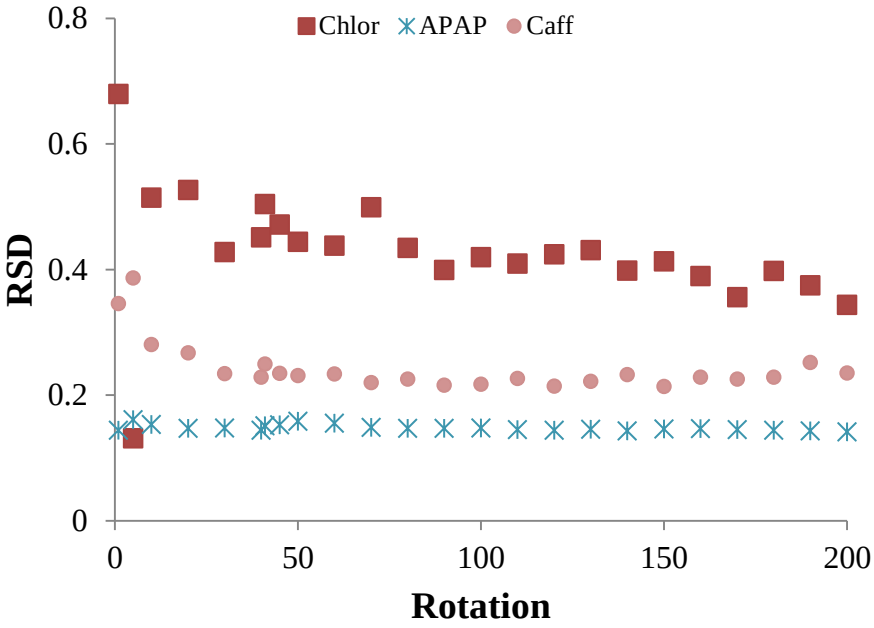
Chlor
APAP
Caff
RSD
Rotation
0.8
0.6
0.4
0.2
0
0
50
100
150
200

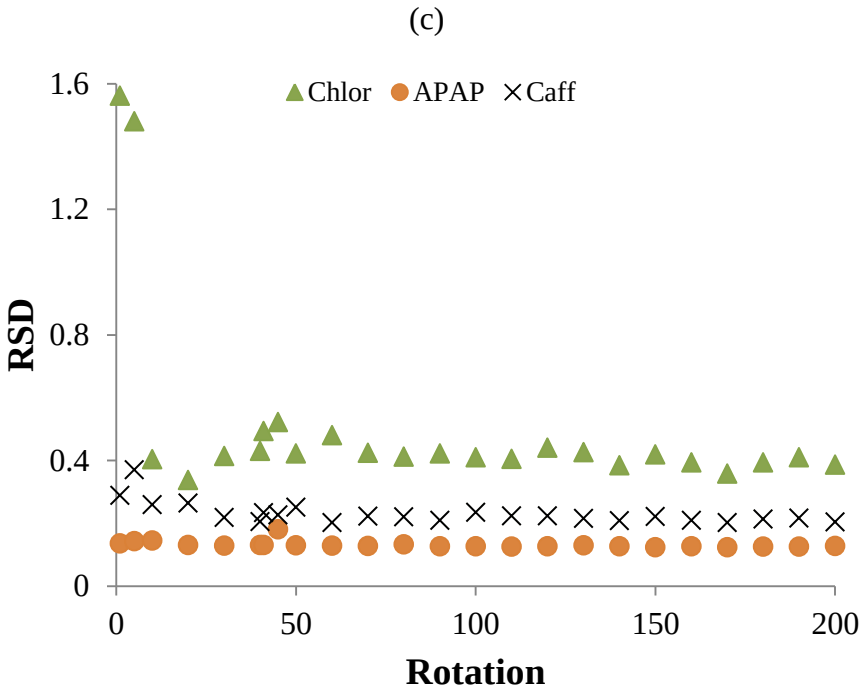

Figure 7-8. RSD profiles for 30% API blends at (a) 15 RPM, (b) 25 RPM and (c) 35 RPM. Scale at 35 RPM different to be able to see the difference in convective mixing rates from all three APIs. In this case, the RSD measured started much higher for chlorpheniramine.

The RSD for the different APIs at all three concentrations used at 25 RPM was plotted in Figure 7-9. The main observation, besides that the RSD was lower with higher concentration levels (expected), is that the difference between the chlorpheniramine RSDs at different concentration levels (Figure 7-9a) was larger than the difference between the RSDs for APAP (Figure 7-9b) and caffeine (Figure 7-9c). The same trend was detected for 15 RPM and 35 RPM.

(a)

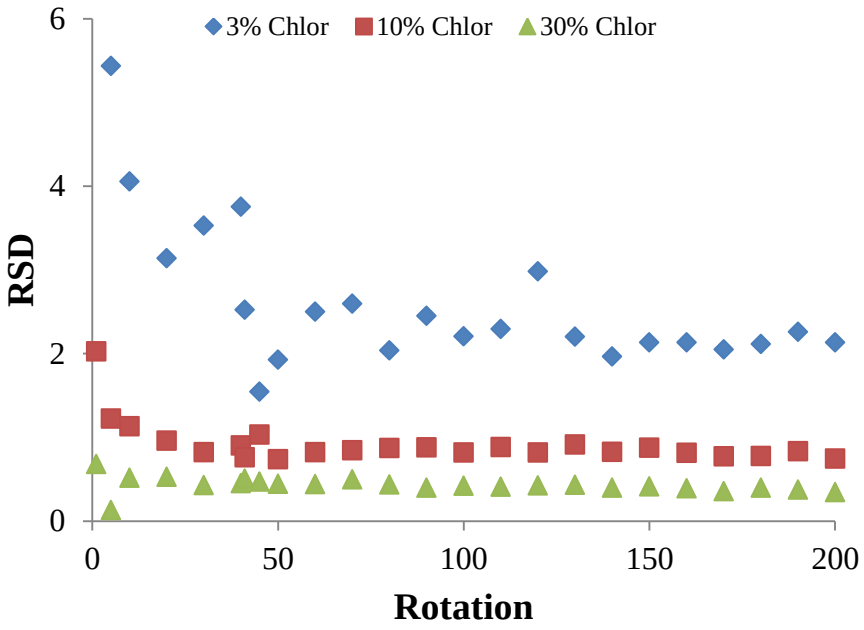
3% Chlor
10% Chlor
30% Chlor
RSD
Rotation
0
2
4
6
0
50
100
150
200

(b)

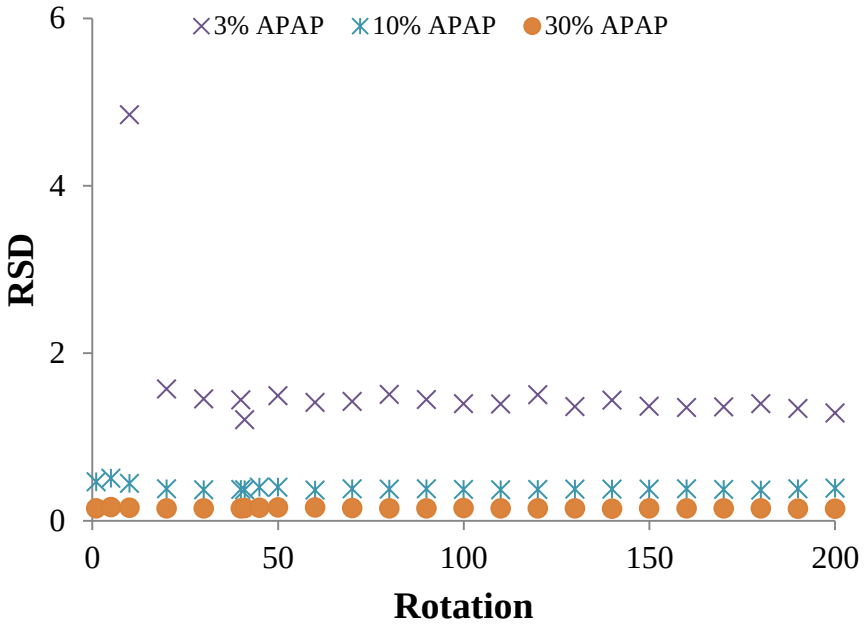
3% APAP
10% APAP
30% APAP
RSD
Rotation
0
2
4
6
0
50
100
150
200

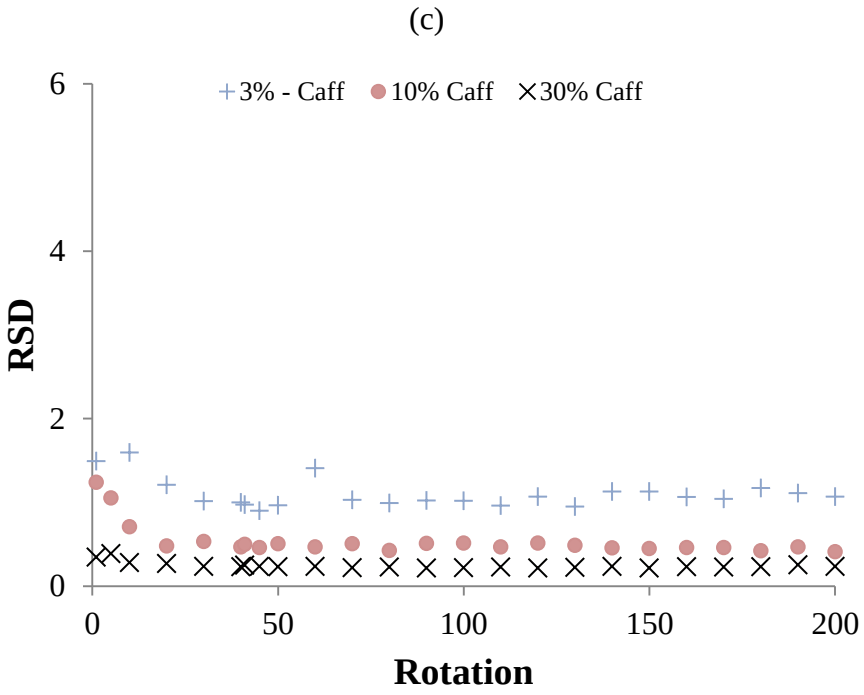

Figure 7-9. RSD profiles as a function of concentration for (a) chlorpheniramine, (b) APAP and (c) caffeine.

7.3.1.4 Fraction of pixels

The fraction of pixels within the threshold as a function of the number of rotations at 25 RPM is shown in Figure 7-10. For the sake of brevity, figures for 15 RPM and 35 RPM, which showed the same trend, were omitted. In most cases, the number of pixels within the threshold increased with increasing number of rotations. In all cases, the fraction of pixels within the threshold for chlorpheniramine did not increase as high as the other APIs and presented the most variability from rotation to rotation. Caffeine reached the highest fraction of pixels within the threshold, followed by APAP. These results are in accordance to what was expected considering the material properties of the three APIs used in these experiments. The differences between caffeine and APAP were smaller at higher concentration levels. The number of pixels within threshold can be used

as a complementary measurement to the average concentration and RSD to determine if a blend is truly uniform when its concentration is measured pixel by pixel.

(a)

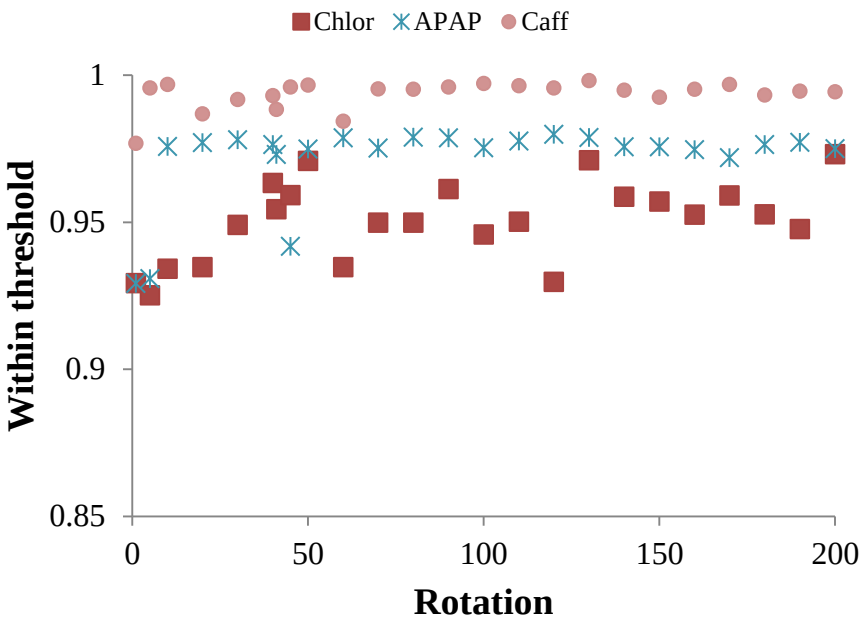

(b)

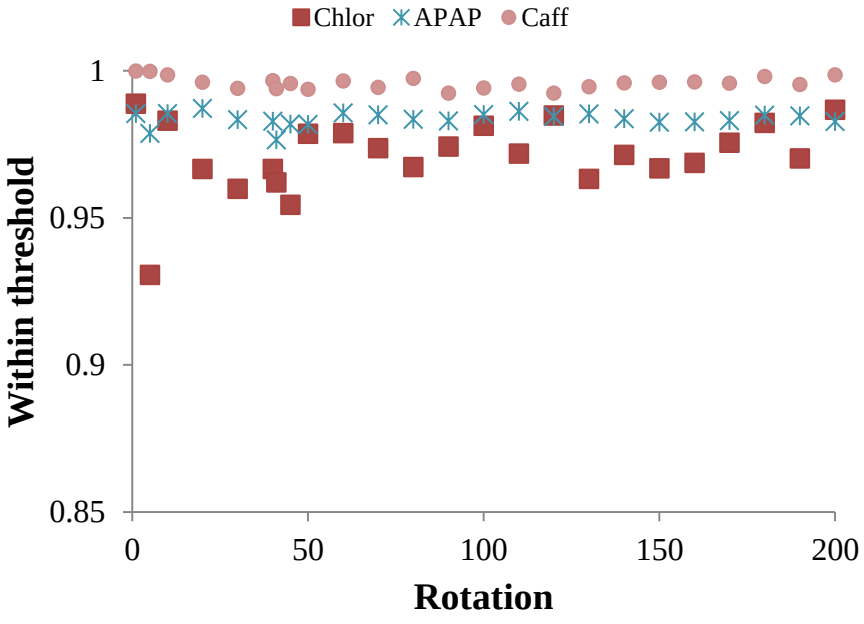

(c)

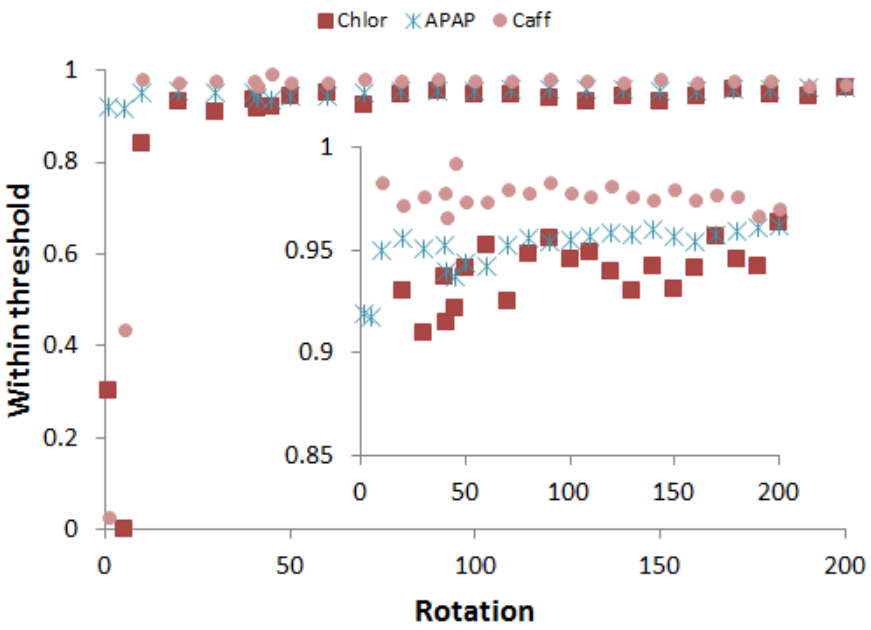

Figure 7-10. Fraction of pixels within threshold for a) 3%, b) 10% and 30% API at 25 RPM.

The fraction of pixels above the thresholds for the APIs (i.e. unbroken pure aggregates and high outlier pixels) as a function of the number of rotations at 25 RPM is shown in Figure 7-11. The fraction of pixels above the thresholds started and remained very low for all experiments, indicating that most of the blend was below or within the specified range of the nominal composition. In all cases studied (rotation rates and concentrations), this fraction was higher for chlorpheniramine. For 3% (Figure 7-11a) and 10% (Figure 7-11b), the fraction of pixels above threshold was higher for APAP than that of caffeine. For 30% API blends (Figure 7-11c), the fraction of pixels of APAP and caffeine were very similar. The fraction of pixels above the threshold can be used as an indication of how well an ingredient has been dispersed throughout the matrix of all other

components. This metric is analogous to the maximum aggregate size measurement, which is discussed in the next section.

(a)

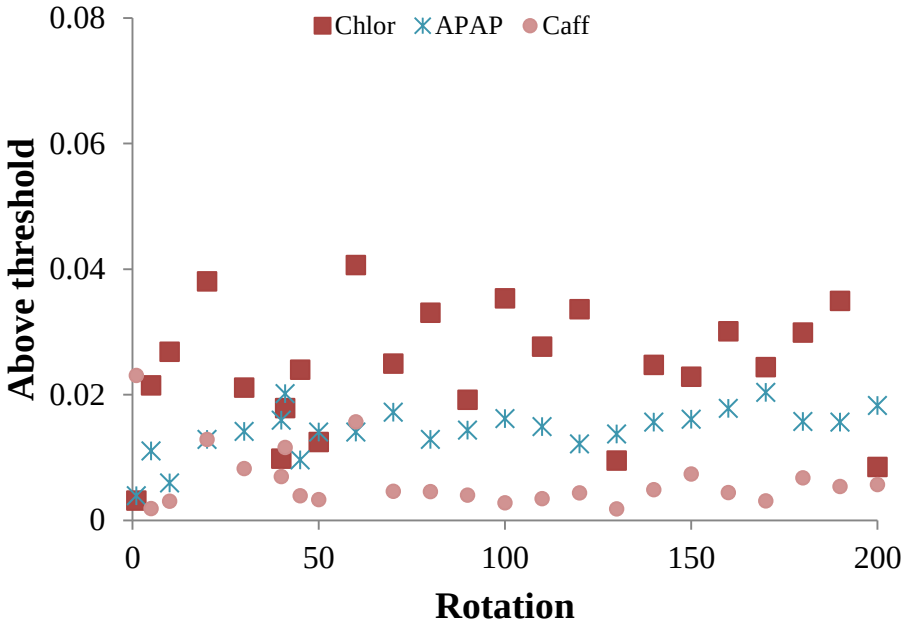

(b)

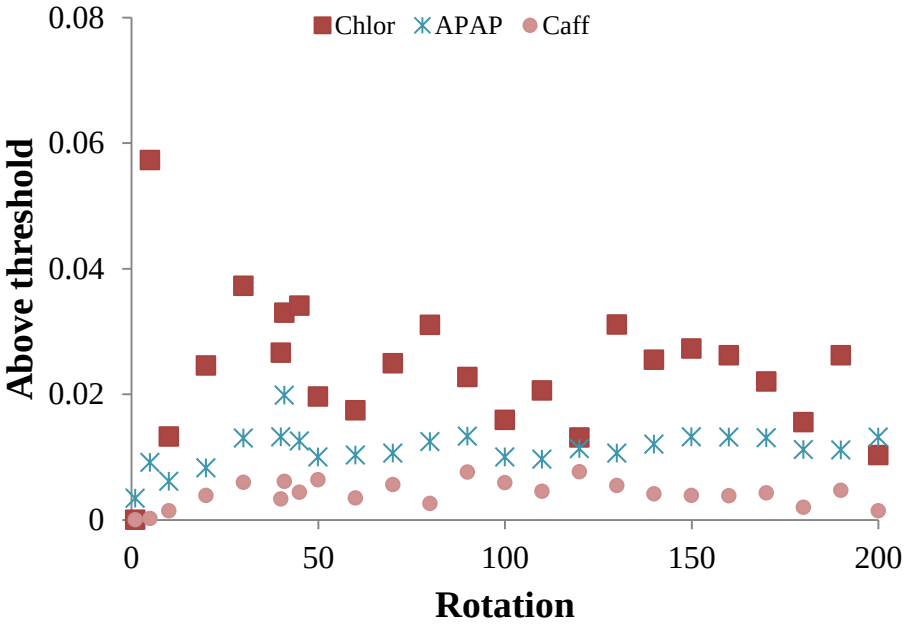

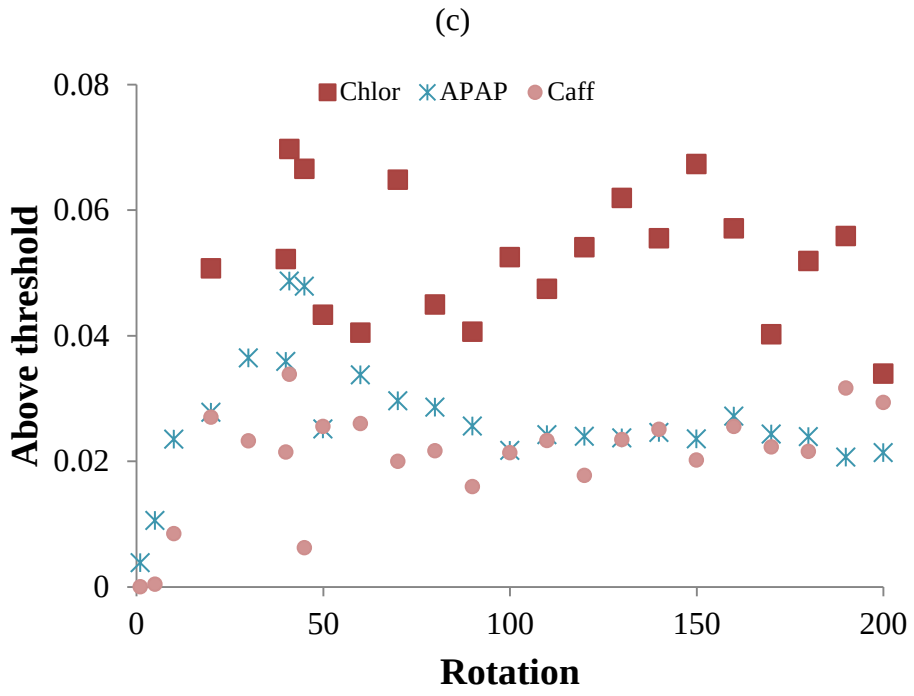

Figure 7-11. Fraction of pixels above threshold for a) 3%, b) 10% and 30% API at 25 RPM.

7.3.1.5 Aggregate size

The mean aggregate size was calculated from the blend images for all experiments reported here. To illustrate the results, the mean aggregate size as a function of the number of rotations for 25 RPM is shown in Figure 7-12 for all three API concentrations. The mean aggregate size did not seem to change much throughout the blending process. No clear relationship between the number of rotations or API concentration and mean aggregate size was seen. This might be an indication that most of the aggregates were dispersed throughout the blend in the first few rotations. Since only a small part of the blend (1 cm x 1 cm) was measured in the specified rotations, only a few aggregates could

have been detected out of the total amount of aggregates in the whole volume of the blend.

(a)

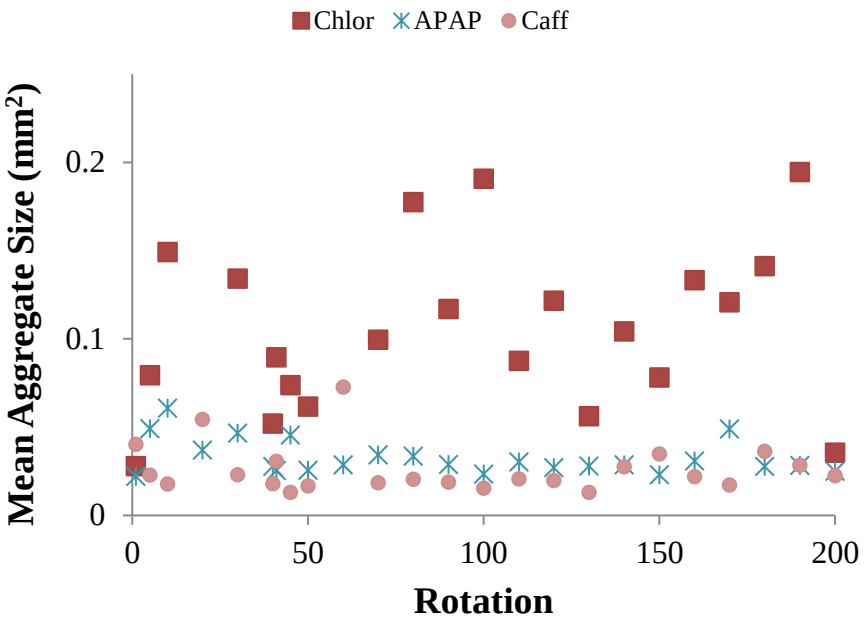

(b)

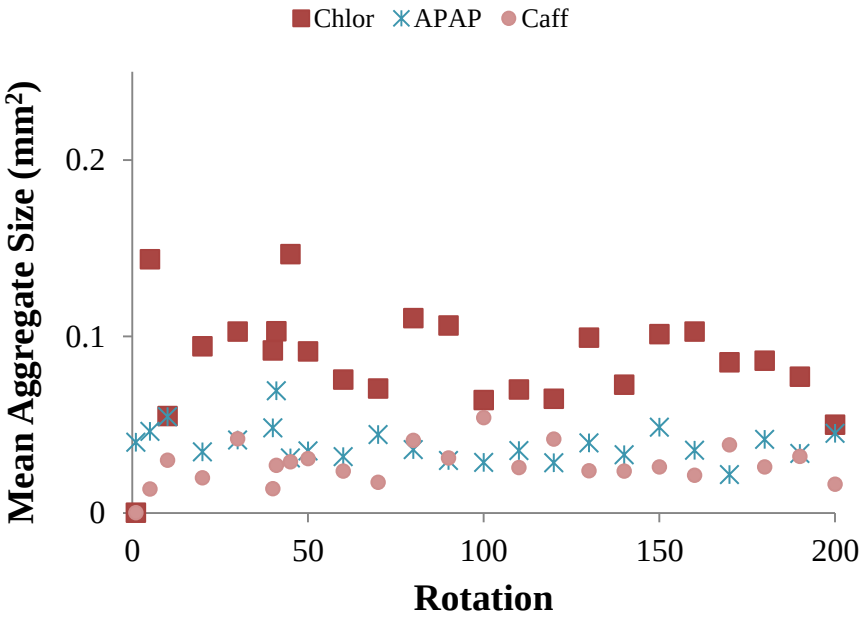

(c)

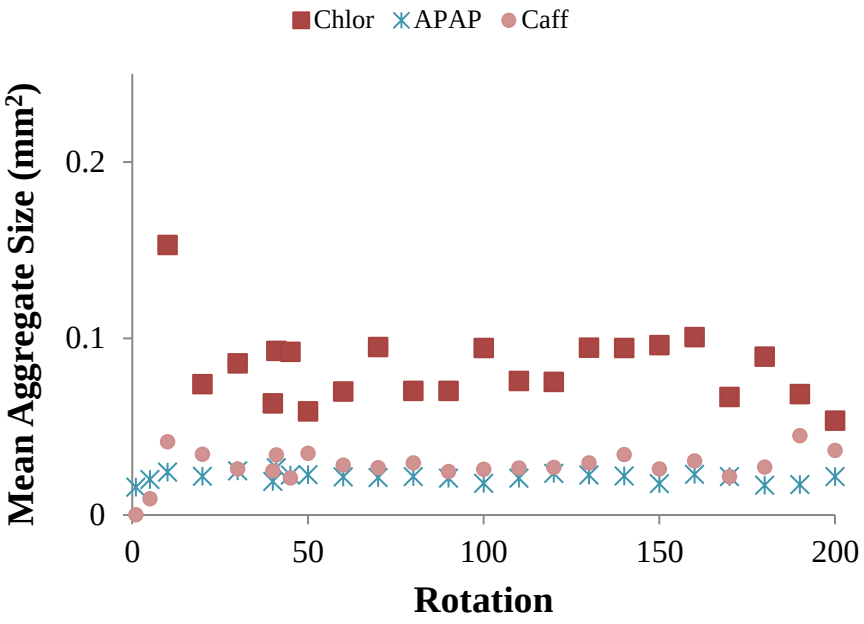

Figure 7-12. Mean aggregate size for (a) 3%, (b) 10% and (c) 30% API at 25 RPM.

Nevertheless, it is important to note that the mean aggregate size for chlorpheniramine was greater in all cases (rotation rates and concentrations). Chlorpheniramine also presented the most fluctuations in the results, indicating that a large variation of aggregates (i.e. unbroken pure chlorpheniramine agglomerates) were present through the whole blend volume. The mean aggregate size for caffeine and APAP were very similar in all cases.

To briefly compare the size of the API particle to the mean aggregate size, their areas were calculated using the mean particle size and the mean aggregate size (measured at the 200th revolution) as the diameter of the particle (Table 7-5). The assumption taken was that all particles were circular. The number of "single" particles that composed an aggregate with the mean size was calculated assuming that the particles are laying side by

side in any direction. This comparison does not indicate that the actual number of particles in the aggregate is the number presented. This analogy is done for comparison purposes and only takes into consideration the mean particle size for all materials. This analogy does not take into account that the chemical images are 2-dimensional while real particles are 3-dimensional, and that particles can be on top of each other rather than side-by-side. This was true for all comparisons using the mean aggregate size and the mean particle size for both the APIs and the excipients. These results showed that chlorpheniramine was still present in large aggregates (high number of particles) at the end of the blending process. Acetaminophen and caffeine had similar results. Overall, the number of particles within an aggregate decreased with increasing concentration. This means that higher concentrations of APIs disperse and mix much more efficiently than APIs at lower concentrations. This phenomenon known as agglomeration was proven using this technique and it was stronger for the most cohesive API (chlorpheniramine).

Table 7-5. API aggregate size and mean particle size comparison. The mean area of each API (using its mean particle size as the diameter) is compared to the mean aggregate size and the maximum aggregate size areas. All areas are calculated using the area of a circle for comparison. The number of particles in each aggregate is the ratio of the mean particle area to the mean or maximum aggregate area.

			Mean aggregate size		Maximum aggregate size	
API	API Conc. (%)	Rotation rate (RPM)	Area (mm^2)	# of particles	Area (mm^2)	# of particles
Chlorpheniramine (mean particle area = 3.96E-05 mm^2)	3	15	0.02081	526	0.96560	24389
	3	25	0.00099	25	0.00662	167
	3	35	0.01347	340	0.32341	8169
	10	15	0.00221	56	0.04468	1128
	10	25	0.00196	50	0.04776	1206
	10	35	0.00714	180	0.15026	3795
	30	15	0.00569	144	0.28729	7256
	30	25	0.00223	56	0.07097	1793
	30	35	0.00508	128	0.13345	3371
Acetaminophen (mean particle area = 0.0017 mm^2)	3	15	0.00035	9	0.04707	1189
	3	25	0.00048	12	0.10851	2741
	3	35	0.00019	5	0.00321	81
	10	15	0.00029	7	0.00207	52
	10	25	0.00159	40	0.02726	689
	10	35	0.00015	4	0.00123	31
	30	15	0.00045	11	0.00701	177
	30	25	0.00037	9	0.01774	448
	30	35	0.00046	12	0.01265	319
Caffeine (mean particle area = 0.0023 mm^2)	3	15	0.00049	12	0.02570	649
	3	25	0.00039	10	0.00994	251
	3	35	0.00022	6	0.00147	37
	10	15	0.00310	78	0.09283	2345
	10	25	0.00021	5	0.00065	16
	10	35	0.00051	13	0.00756	191
	30	15	0.00051	13	0.02177	550
	30	25	0.00104	26	0.28814	7278
	30	35	0.00036	9	0.03976	1004

The maximum aggregate size was also calculated for each blend image. To show the main results, the maximum aggregate sizes at 25 RPM are shown in Figure 7-13. Overall, the maximum aggregate size was higher for chlorpheniramine. Large fluctuations in the maximum aggregate size, especially for chlorpheniramine, were present even at the end

of the blending process. The maximum aggregate sizes for APAP and caffeine were very similar.

Examples of chemical images showing these large aggregates are also shown in Figure 7-13. The chemical images show aggregates which contain large amounts of API. For 3% API blends (Figure 7-13a), the large aggregates of chlorpheniramine were mainly pure drug (60-100% API). The large aggregates of APAP and caffeine had a drug content much lower (~20-30%) than the chlorpheniramine aggregates; nevertheless they were still aggregates. For 10% API blends (Figure 7-13b), more aggregates were observed when compared to the 3% API blends. The same trend was obtained for the chlorpheniramine aggregates (mainly pure drug). For 30% API blends (Figure 7-13c), the APIs seemed to be much more uniform throughout. The chlorpheniramine blends still had large aggregates, most of which were pure drug. As the concentration of drug is increased, the influence of large aggregates becomes less important to the potency uniformity of a drug. Nevertheless, if large aggregates, such the ones detected here, were encountered inside tablets and capsules, variability in these processes would lead to failures (e.g. slower dissolution and potentially other effects as well). These examples are representative of what was observed for all rotation rates at the different concentrations.

(a)

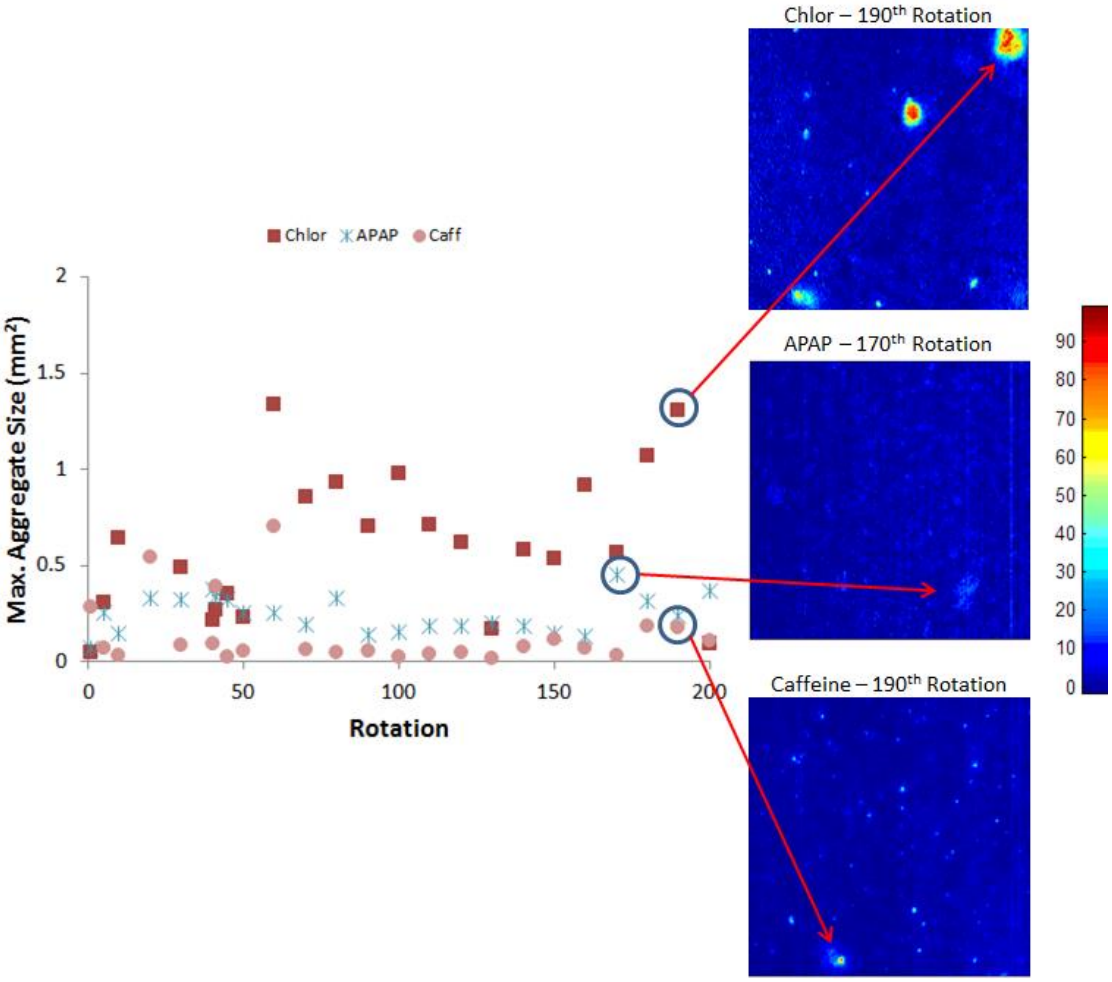
Chlor – 190th Rotation
APAP – 170th Rotation
Caffeine – 190th Rotation
Chlor
APAP
Caff
Max. Aggregate Size (mm²)
Rotation
0
0.5
1
1.5
2
0
50
100
150
200
90
80
70
60
50
40
30
20
10
0

(b)

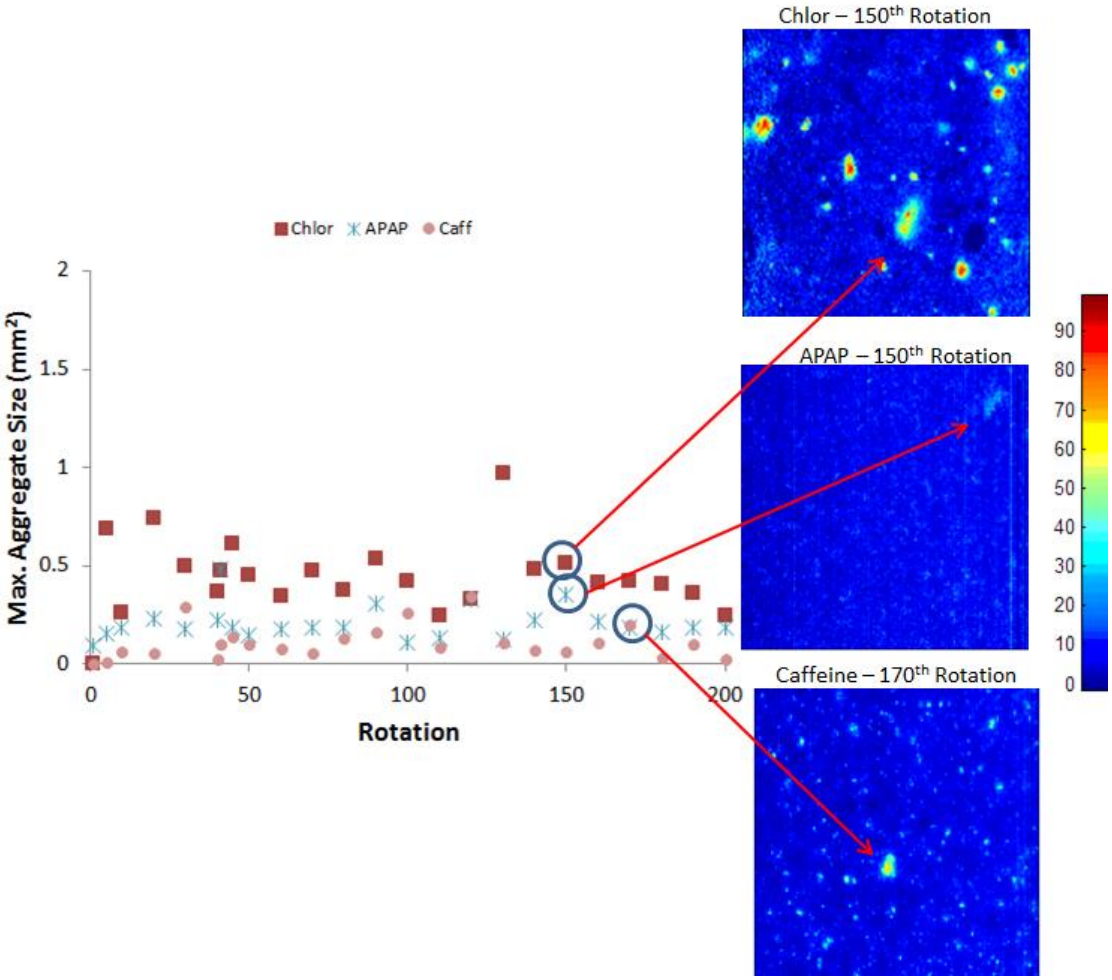
Chlor – 150th Rotation
APAP – 150th Rotation
Caffeine – 170th Rotation
Chlor
APAP
Caff
Max. Aggregate Size (mm²)
Rotation
0
0.5
1
1.5
2
0
50
100
150
200
90
80
70
60
50
40
30
20
10
0

(c)

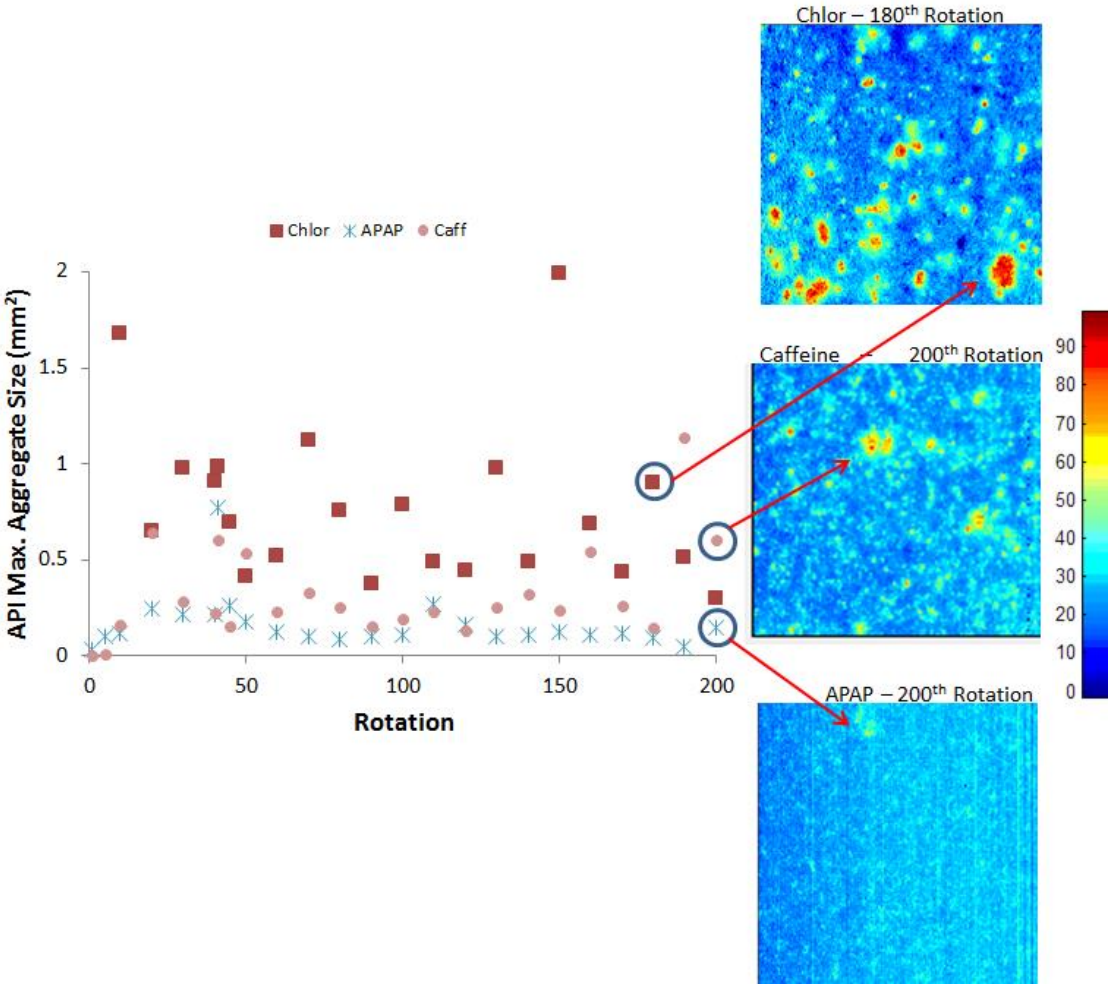

Figure 7-13. Maximum aggregate size for (a) 3%, (b) 10% and (c) 30% API at 25 RPM with sample chemical images towards the end of the blending process. Scale is 0-100% API.

The maximum aggregate size (area) was also compared to the mean particle area (Table 7-5) as previously described. A large number of chlorpheniramine particles were found in aggregates even at the end of the process. Although this number was lower for acetaminophen and caffeine, the number of particles present in large aggregates was still substantial. If these were potent APIs, especially for the 3% API blends, the presence of these large aggregates would adversely influence the content uniformity of the drug.

7.3.2 Excipients

Most frequently, only the gross uniformity of what is thought to be the critical ingredient (i.e. APIs) in powder blends are reported. This can be mainly attributed to the extensive labor required to test each of the ingredients in a blend using techniques such as chromatography. NIR spectroscopy in general and the NIR-CI method used in this study, allowed us to further study any component within a powder blend. Next, the main observations of the main excipients are described. It is understood that the API is, indeed, the most critical ingredient in the blend, but the rest of the components sometimes can be critical as well.

Chemical images showed the progression of mixing of the main excipients. These chemical images were omitted for the sake of brevity. Since the concentration of the main excipients was always high, the blending progression was detected quite efficiently with the chemical images. To see examples of the chemical images for lactose and Avicel as well as for MgSt and Cab-O-Sil, please refer back to Chapter 6.

7.3.2.1 Concentration statistics

The average lactose concentration increased with an increasing number of rotations toward its nominal value. The results for lactose concentration as a function of the number of rotations for all three concentrations at 25 RPM are shown in Figure 7-14. It is interesting to note that, in blends with low API concentrations, the lactose blending was very similar for blends with different APIs (Figure 7-14a). For the higher concentration chlorpheniramine blends (10% and 30%), lactose took longer to reach the target concentration (Figures 7-14b and 7-14c). The lactose blending time increased with

increasing API concentration, and differences among blends for the different APIs were also more prominent. The progression of lactose in the chlorpheniramine blends stood out the most from the other API blends.

(a)

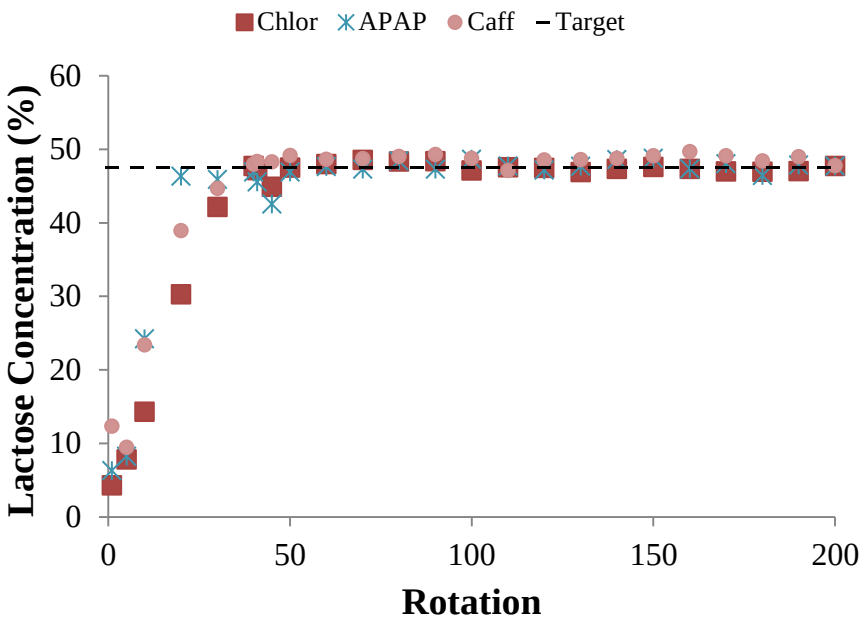

(b)

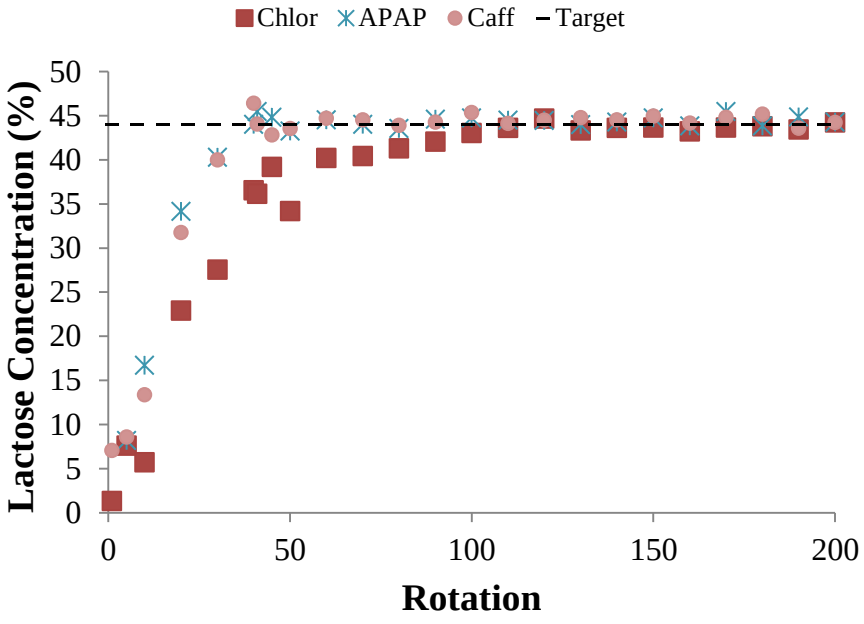

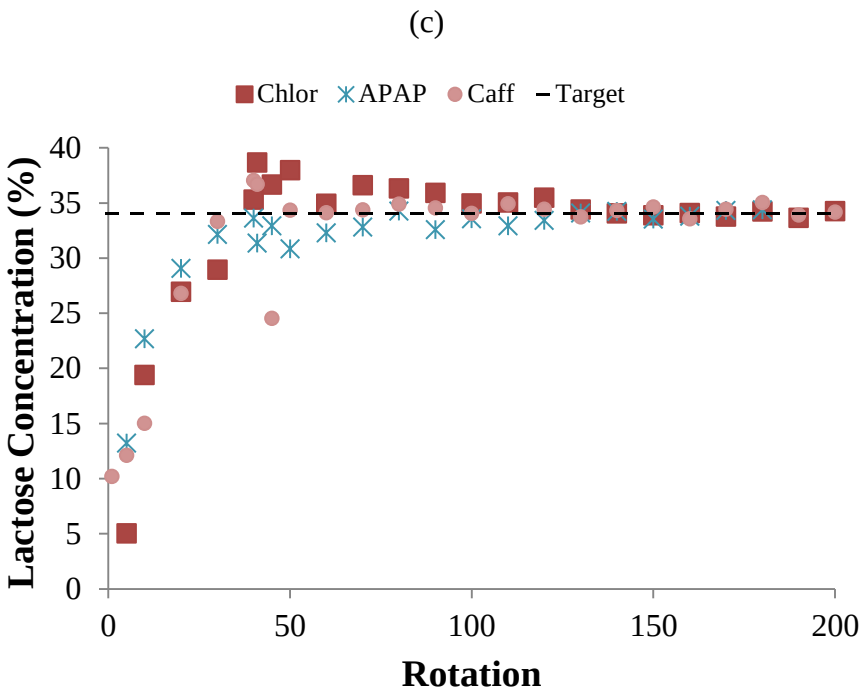

Figure 7-14. Blending profiles for lactose with blends of (a) 3%, (b) 10% and (c) 30% API at 25 RPM.

The average concentration of Avicel decreased with an increasing number of rotations toward its nominal value. The mixing of Avicel in blends with low API concentrations (Figure 7-15a) was very similar across blends with different APIs. When the API concentration was increased to 10% (Figure 7-15b), there was a more noticeable difference between the blends, with chlorpheniramine blends taking the longest to reach the target concentration for Avicel, followed by the APAP and caffeine blends. When the API concentration was increased to 30% (Figure 7-15c), the Avicel mixing was not affected significantly by different APIs. Nevertheless, APAP had a stronger influence on the Avicel mixing by increasing the amount of time needed to reach the target concentration.

(a)

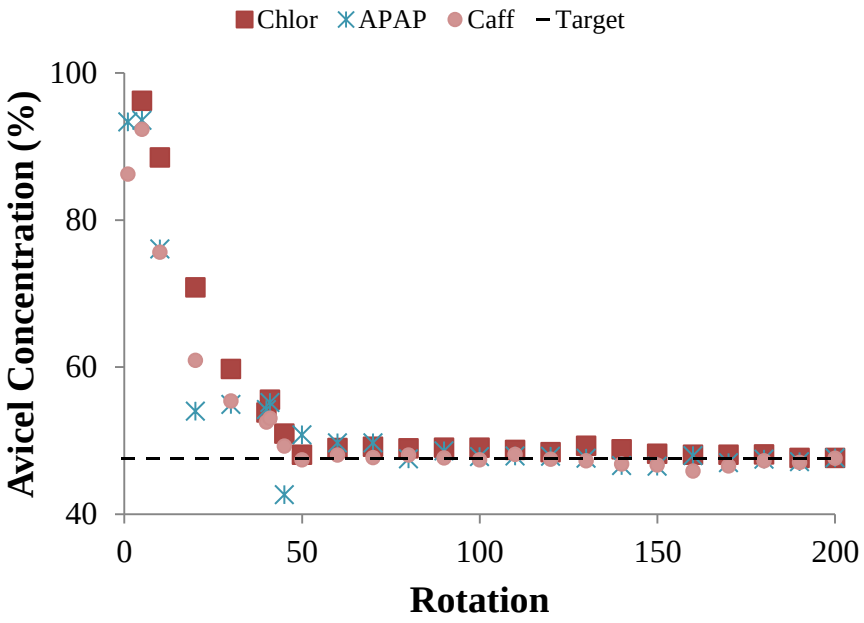
Chlor
APAP
Caff
Target
Avicel Concentration (%)
100
80
60
40
0
50
100
150
200
Rotation

(b)

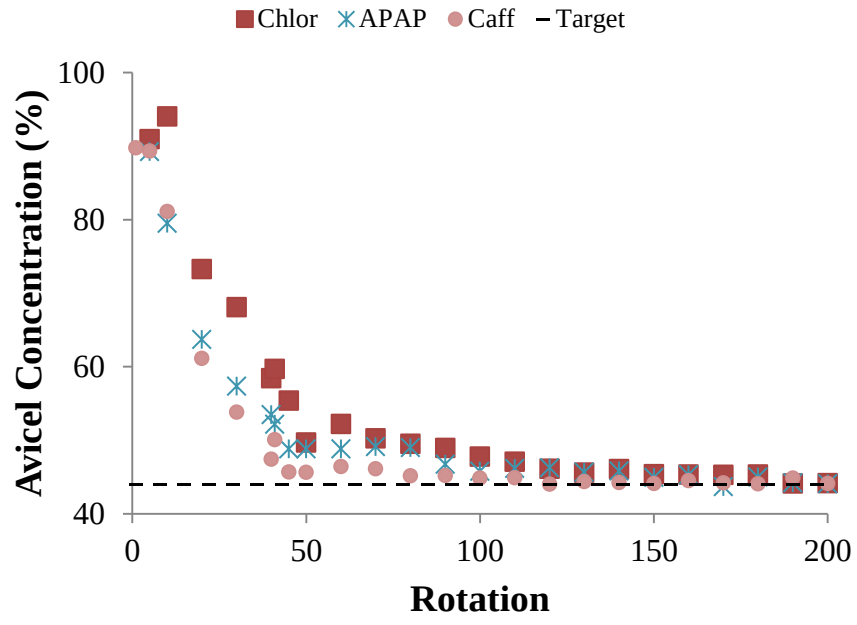
Chlor
APAP
Caff
Target
Avicel Concentration (%)
100
80
60
40
0
50
100
150
200
Rotation

(c)

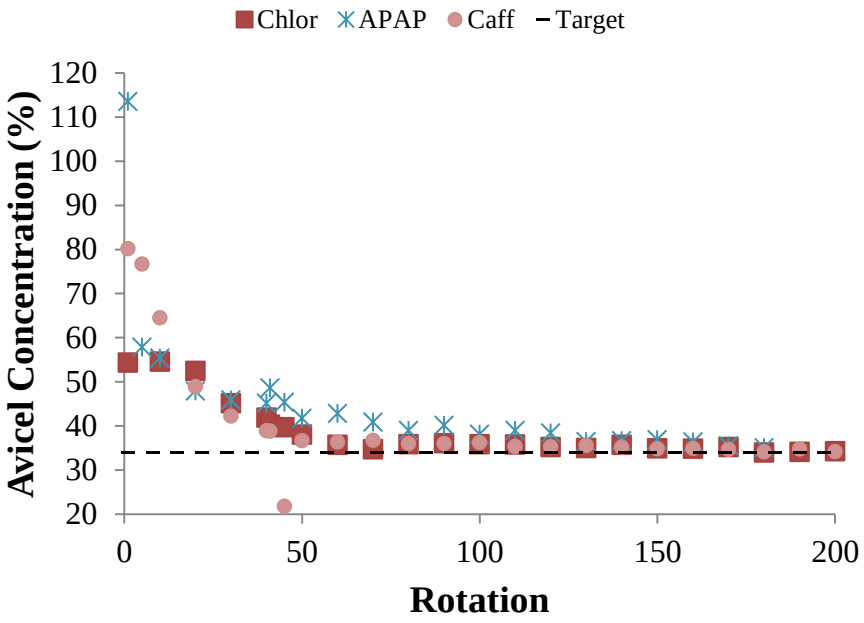

Figure 7-15. Blending profiles for Avicel with blends of (a) 3%, (b) 10% and (c) 30% API at 25 RPM.

To demonstrate the RSD results for both lactose and Avicel, the results for all three API concentrations at 25 RPM are shown in Figure 7-16 and Figure 7-17, respectively. The lactose RSD decreased with an increasing number of rotations (Figure 7-16). The lactose RSD was lower for all blends with APAP at all concentrations of API. The lactose RSD for chlorpheniramine and caffeine blends was quite similar for all concentrations and rotation rates used. The Avicel RSD increased with an increasing number of rotations (Figure 7-17). In blends with a higher API concentration (10% and 30%), the Avicel RSD was higher in APAP blends (Figures 7.17b and 7.17c). The similarity in particle size between Avicel and APAP might be causing this strong interaction between the two materials. The RSD for both lactose and Avicel increased with increasing API concentration. This increase was most prominent in the RSD for Avicel in the APAP

blends as the concentration increased. This confirms that Avicel had a stronger interaction with APAP than with the other APIs. The grade of Avicel used had similar particle size and flow properties to those of the APIs, while the grade of lactose used had better flow properties than all the APIs and Avicel used in these experiments.

(a)

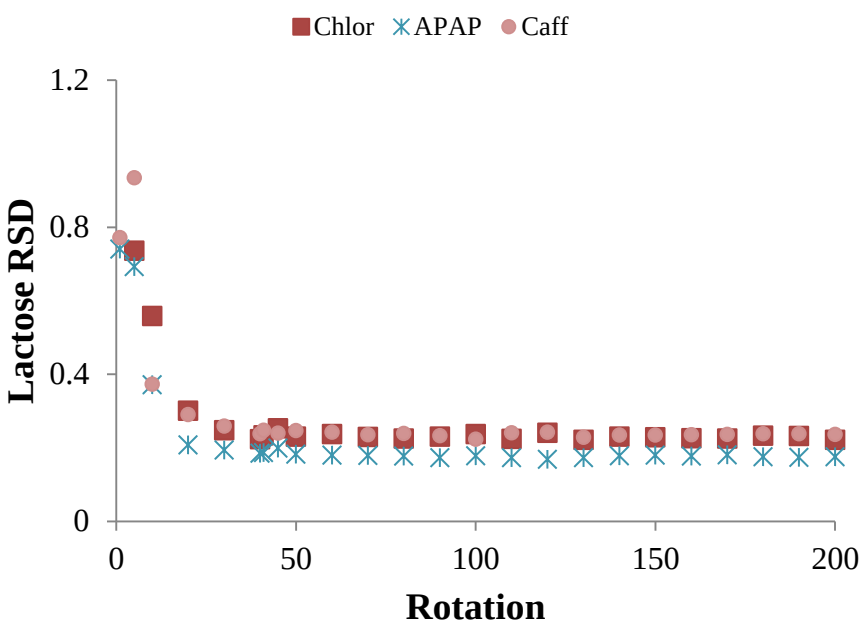

(b)

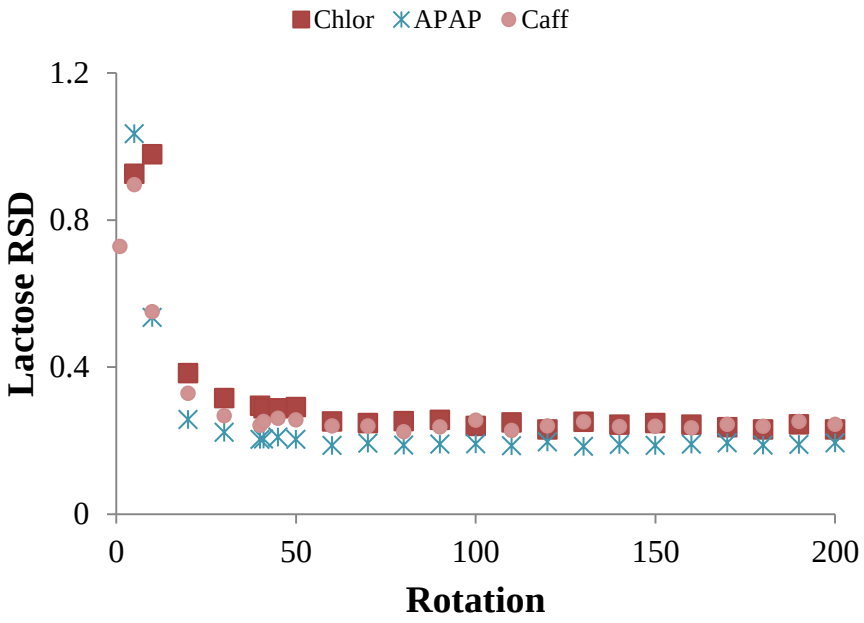

(c)

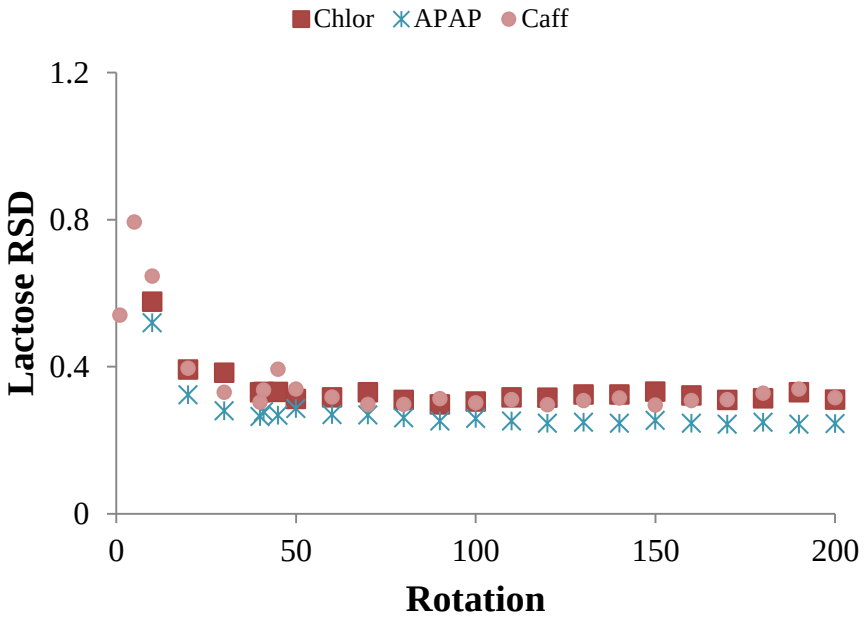

Figure 7-16. Sample RSD for lactose for (a) 3%, (b) 10% and (c) 30% API blends and 25 RPM.

(a)

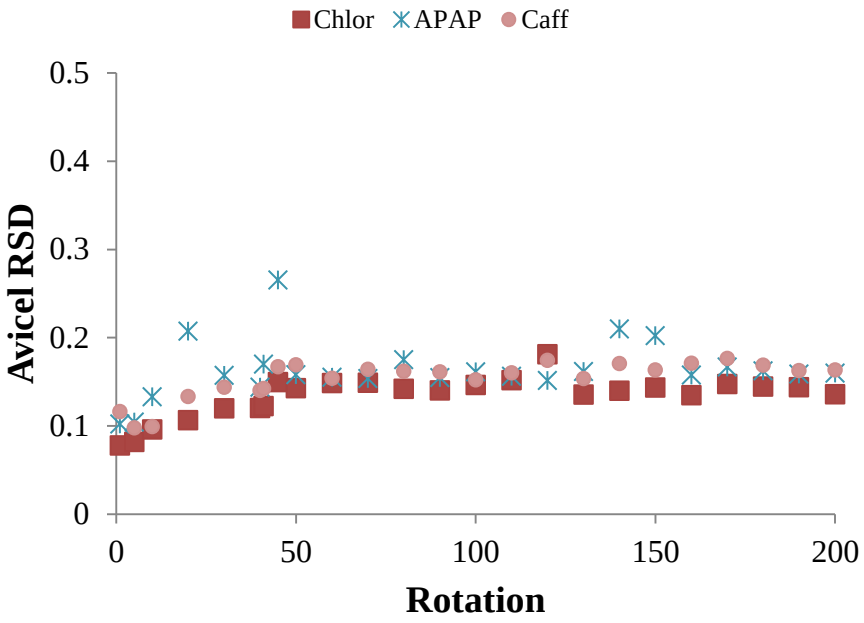
Chlor
APAP
Caff
Avicel RSD
0.5
0.4
0.3
0.2
0.1
0
0
50
100
150
200
Rotation

(b)

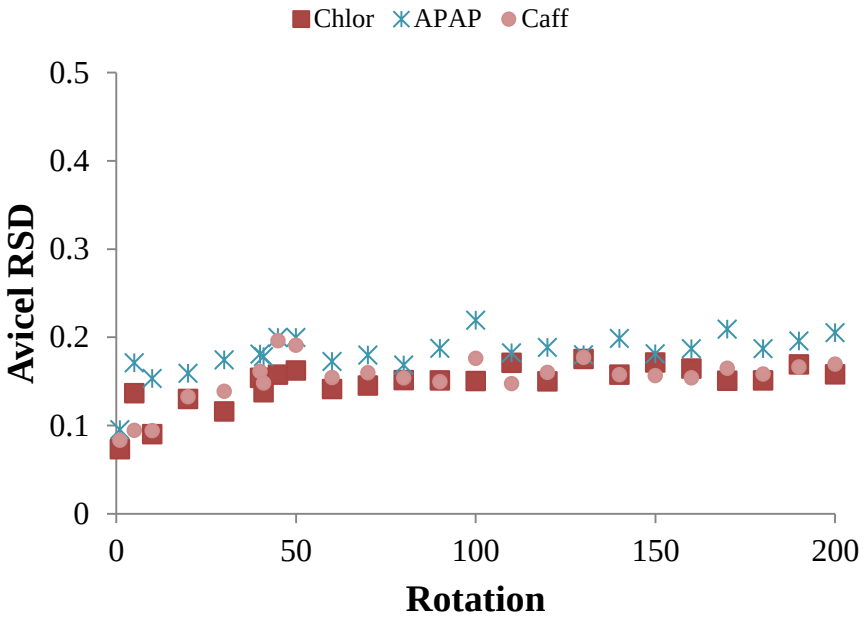
Chlor
APAP
Caff
Avicel RSD
0.5
0.4
0.3
0.2
0.1
0
0
50
100
150
200
Rotation

(c)

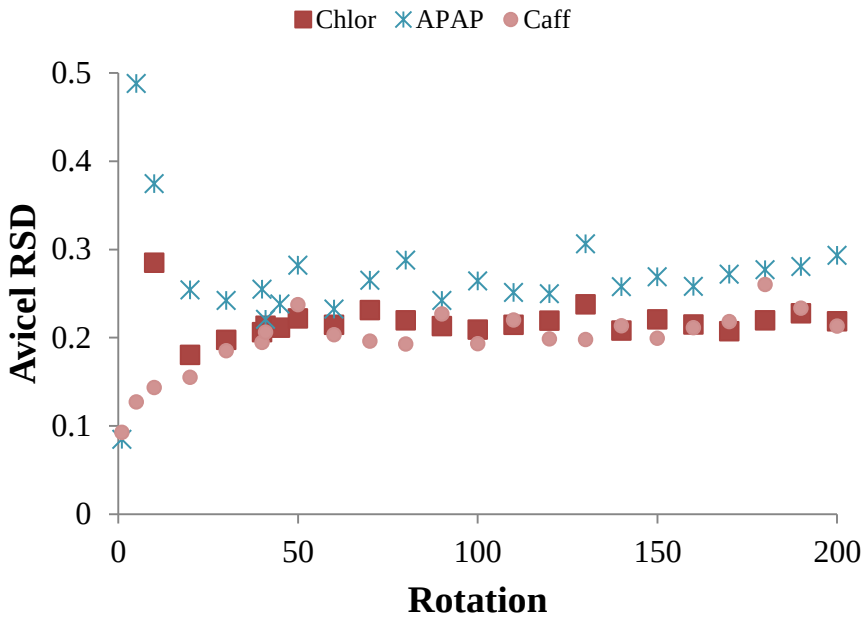

Figure 7-17. Sample RSD for Avicel for (a) 3%, (b) 10% and (c) 30% API blends and 25 RPM.

7.3.2.2 Fraction of pixels

For lactose, the fraction of pixels within the defined threshold increased with an increasing number of rotations (not shown). For the 3% API blends, the final fraction of pixels of lactose within the threshold was higher for APAP blends than for chlorpheniramine and caffeine blends. For the 10% API blends, the results were very similar using this metric and could not be differentiated. For the 30% API blends, the fraction of pixels within the threshold was again higher for the APAP blends.

The fraction of pixels within the threshold for Avicel at 25 RPM for all three API concentrations are shown in Figure 7-18. This fraction increased with an increasing number of rotations. Of the 3% API blends, the APAP blend had the highest fraction of

pixels within the threshold for Avicel (Figure 7-18a). Also in the 3% APAP blends, the fraction of pixels within the threshold for Avicel reached a plateau more quickly than for blends with chlorpheniramine or caffeine. The results for 3% chlorpheniramine and caffeine blends were very similar. Of the 10% API blends (Figure 7-18b), the blends with chlorpheniramine seemed to take the longest to reach the maximum fraction of pixels within the threshold for Avicel. The rates for the blends with APAP and caffeine were very similar for all three rotation rates. Of the 30% API blends (Figure 7-18c), the APAP blend took the longest to reach the maximum fraction of pixels within the threshold for Avicel. The rates for the chlorpheniramine and caffeine blends were very similar. The interaction of Avicel with the different APIs changed as a function of concentration.

(a)

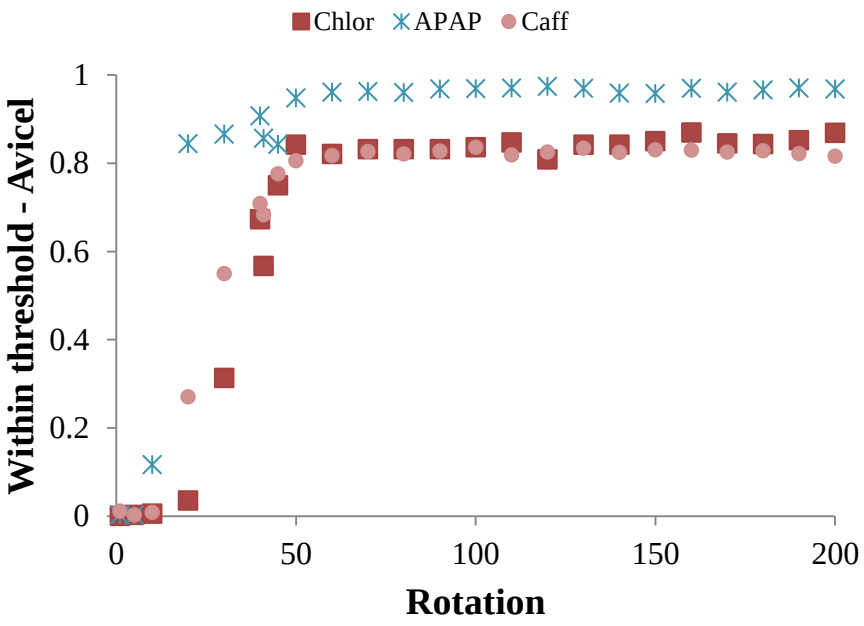

(b)

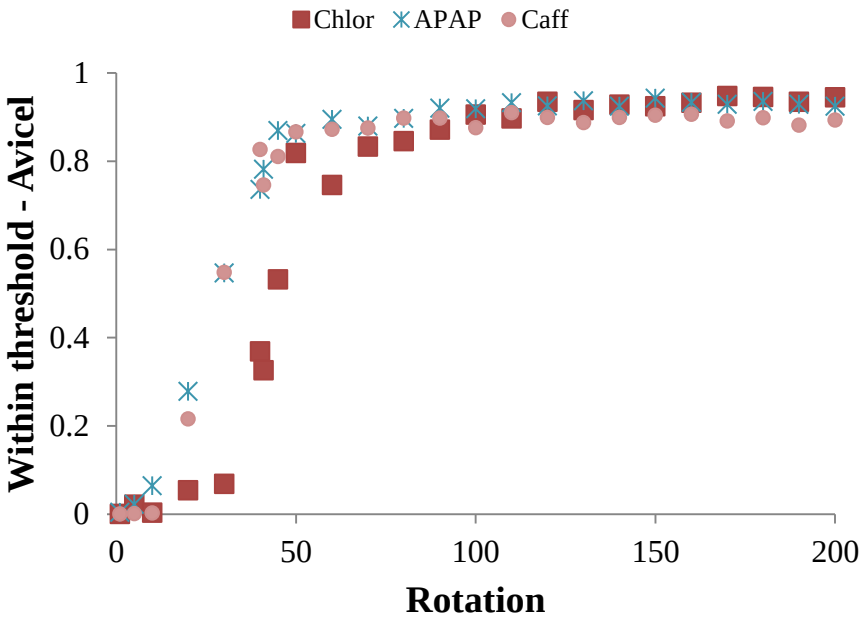

(c)

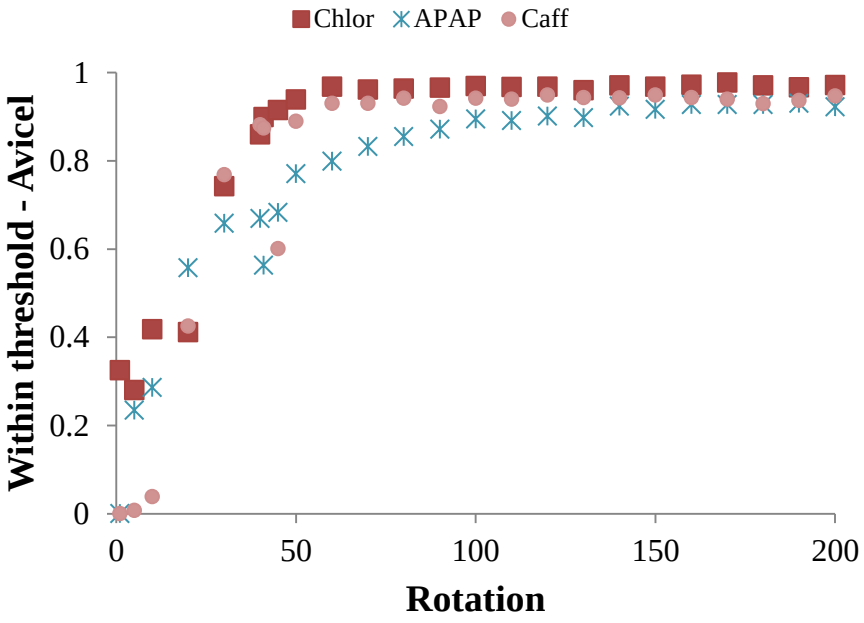

Figure 7-18. Fraction of pixels within threshold for Avicel for (a) 3%, (b) 10% and (c) 30% API blends at 25 RPM.

Interestingly, in some blends, the fraction of pixels above the threshold for lactose increased with an increasing number of rotations. The results had no clear differences between the different API blends. For Avicel, the fraction of pixels above the threshold decreased with an increasing number of rotations. Of the 3% API blends (Figure 7-19a), the APAP blend had the lowest fraction of pixels, while the chlorpheniramine and caffeine blends yielded very similar results. For the 10% API blends, the final fraction of pixels within the threshold was very similar for all of the API blends (Figure 7-19b). For 3% and 10% API blends, chlorpheniramine took longer to reach the minimum fraction of pixels value. For the 30% API blends (Figure 7-19c), the results indicated that the final fraction of pixels for Avicel was very similar for all APIs. The only noticeable difference in these results was the dynamics observed for the APAP blends. The fraction of pixels decreased at a lower rate for the 30% APAP blends than for the chlorpheniramine and caffeine blends. This demonstrated, once again, the stronger interaction between Avicel and APAP, when compared to the other two APIs at higher concentrations.

(a)

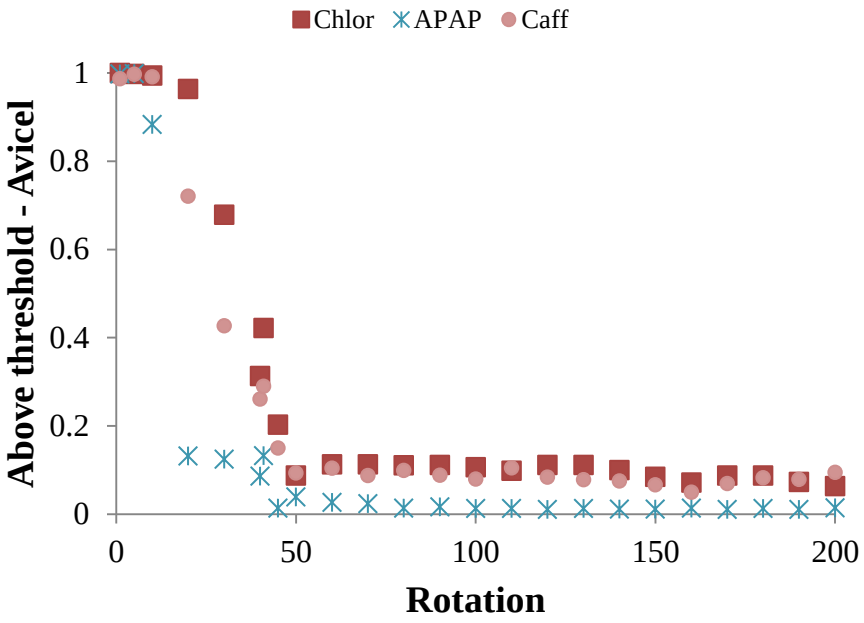
Chlor
APAP
Caff
Above threshold - Avicel
1
0.8
0.6
0.4
0.2
0
0
50
100
150
200
Rotation

(b)

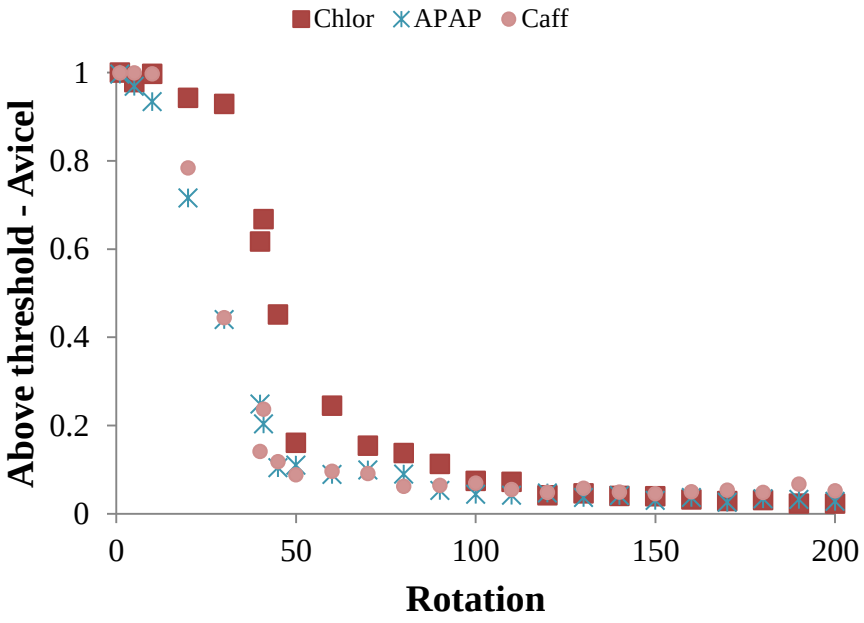
Chlor
APAP
Caff
Above threshold - Avicel
1
0.8
0.6
0.4
0.2
0
0
50
100
150
200
Rotation

(c)

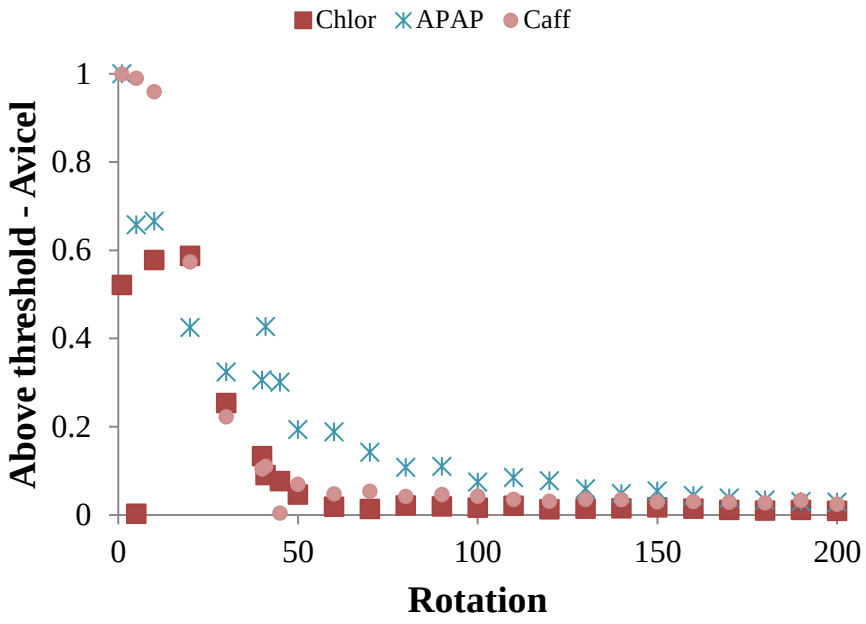

Figure 7-19. Fraction of pixels above threshold for Avicel for a) 3%, b) 10% and c) 30% API blends at 25 RPM.

7.3.2.3 Aggregate size

The mean aggregate size of lactose did not show any strong effects of API, concentration, or rotation rate. Overall, the final mean aggregate size of lactose was 0.015-0.03 mm^2 for all concentrations and rotations rates. When this is compared to the mean particle size of lactose (180 µm or ~ 0.025 mm^2), we can see that most of the lactose was found as a small group of particles or single particles within the blend. This is possible due to the good flowability (large particle size) of lactose used.

The mean aggregate size of Avicel decreased with an increasing number of rotations (Figure 7-20). Of the 3% and 10% API blends, most of the chlorpheniramine blends had the highest mean aggregate size for Avicel. Of the 30% API blends, APAP blends at 25

and 35 RPM had the highest mean aggregate size for Avicel. Overall, the final mean aggregate size of Avicel was 0.01 – 0.03 mm^2. Surprisingly, this was very similar to the mean aggregate size of lactose. When we follow the same analogy using the mean particle size of Avicel (50 µm or 0.00196 mm^2), the number of particles within an aggregate of Avicel was in the range 5-15. The average aggregate was ~ 10 times larger than the average size of an Avicel particle. These measurements are approximations since the aggregates detected by this method are 2-dimensional pictures while agglomerates are 3-dimensional.

(a)

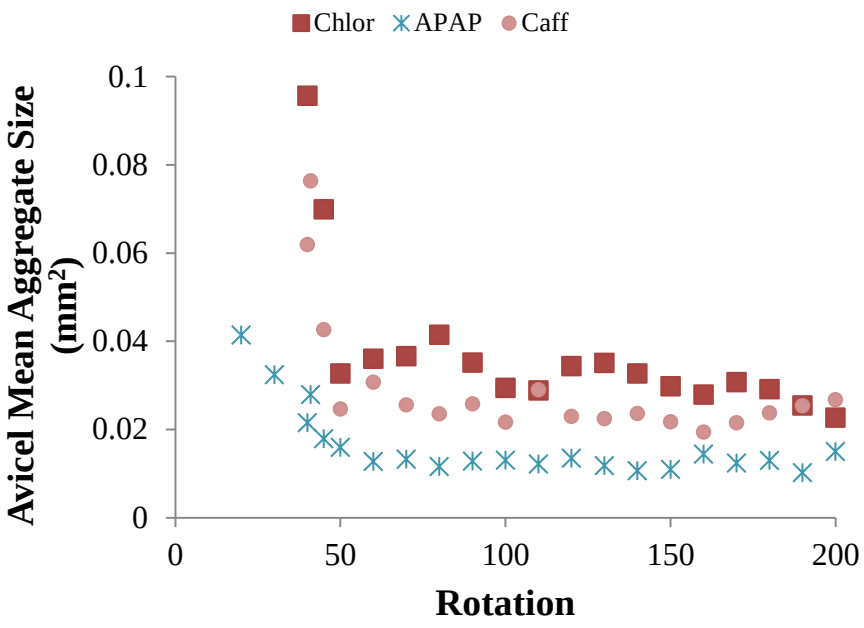

(b)

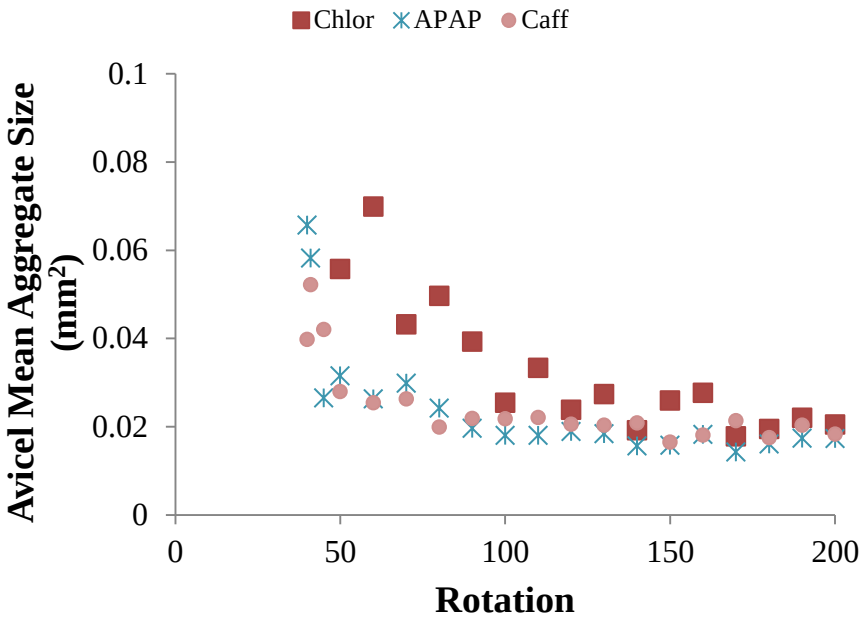

(c)

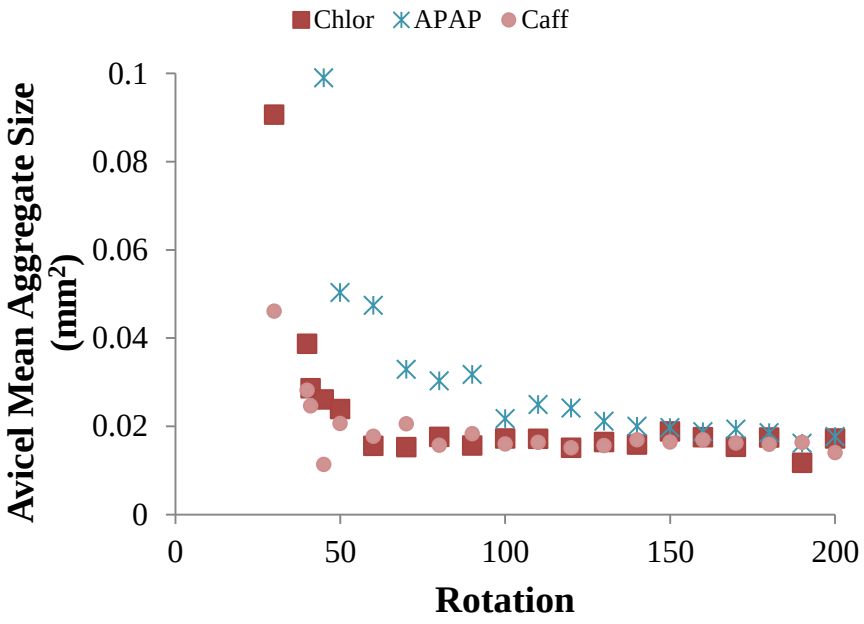

Figure 7-20. Mean aggregate size of Avicel for (a) 3%, (b) 10% and (c) 30% API blends at 25 RPM.

The maximum aggregate size of lactose did not show any clear effects of API, concentration, or rotation rate. The range of the maximum aggregate size of lactose was 0.05 – 0.30 mm^2. If we use the same analogy of the mean particle size (180 μm or 0.025 mm^2) as the single particle diameter, then a range of 2-12 particles composed the large lactose aggregates. The average aggregate was ~ 6 times larger than the average size of a lactose particle. These results indicated that lactose was always present as small aggregates throughout the blending process. The maximum aggregate size for Avicel decreased with increasing number of rotations. To illustrate the results, the maximum Avicel aggregate size at 25 RPM for all three concentrations is shown in Figure 7-21. Of the 3% API blends, the APAP blends had the lowest maximum Avicel aggregate size (~22 particles in an aggregate), while the chlorpheniramine and caffeine blends had larger aggregates (~ 200 particles in an aggregate). For the 10% API blends, the maximum Avicel aggregate size was very similar for all three API blends, with a range of ~ 56 – 138 particles in an aggregate. It is interesting to see how the APIs and the change in their concentration affect the mixing dynamics of the Avicel. The maximum Avicel aggregate size seemed to increase as the concentration of APAP increased, though for chlorpheniramine and caffeine blends, it seemed to decrease as the concentration of the API increased.

(a)

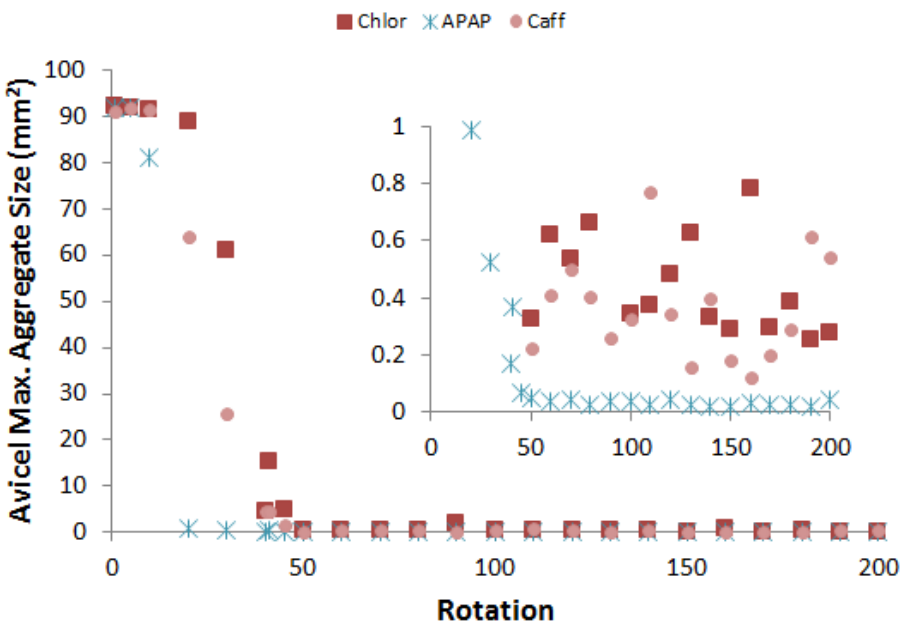
Chlor
APAP
Caff
Avicel Max. Aggregate Size (mm²)
Rotation
0
10
20
30
40
50
60
70
80
90
100
0
50
100
150
200
0
0.2
0.4
0.6
0.8
1

(b)

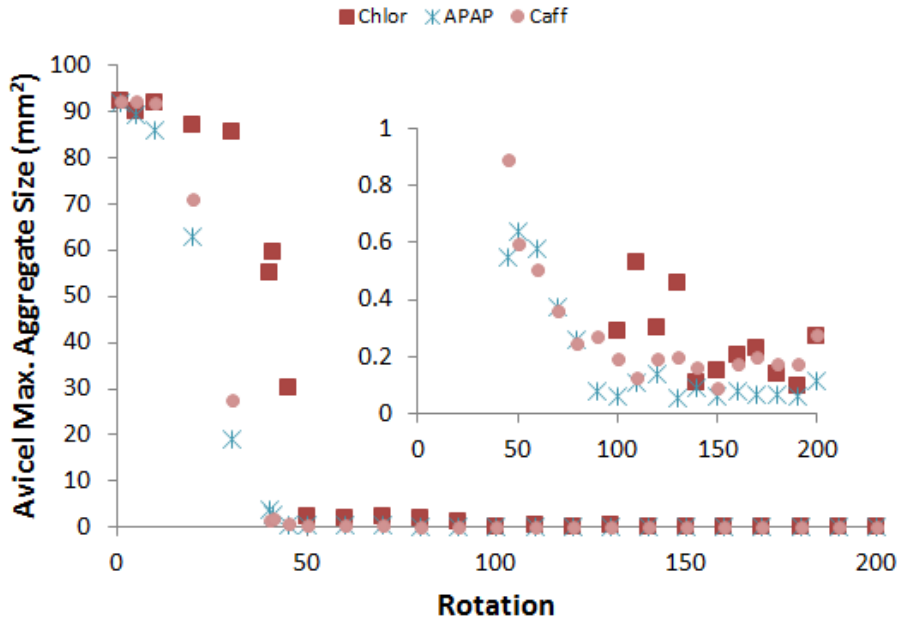
Chlor
APAP
Caff
Avicel Max. Aggregate Size (mm²)
Rotation
0
10
20
30
40
50
60
70
80
90
100
0
50
100
150
200
0
0.2
0.4
0.6
0.8
1

(c)

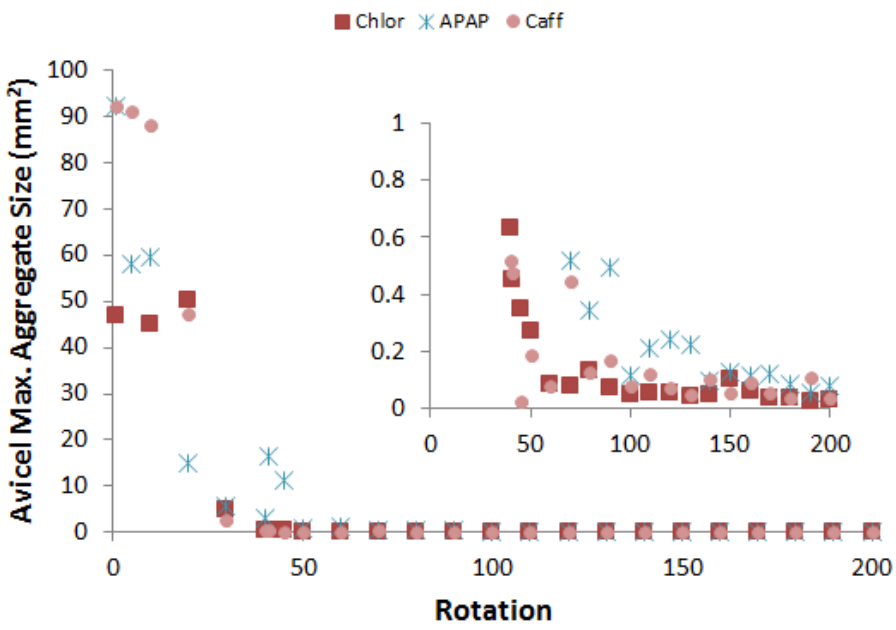

Figure 7-21. Avicel maximum aggregate size for Avicel for (a) 3%, (b) 10% and (c) 30% API blends at 25 RPM.

7.3.2.4 Minor excipients

No major trends were observed with MgSt and Cab-O-Sil; thus their results are not included. The MgSt average concentration was calculated, showing that MgSt reached its nominal concentration after a few rotations. MgSt usually coats the other particles, due to its small particle size and low melting point. In some later rotations, however, there were lingering large aggregates. In addition to MgSt being a lubricant, it also improves the powder flow within the blending of the materials. In this case, it seemed that most of the API blending was already complete before the addition of MgSt and no significant effect was observed upon its addition. While this is true for the blends presented here, in other instances we have noticed the effect of MgSt, which helped break up other ingredients' aggregates, improving blending overall.

7.4 Conclusions

The effects of material properties of cohesive APIs on micro-mixing in a 1-L bin-blender were characterized using near-infrared chemical imaging (NIR-CI). The APIs were characterized as very cohesive (chlorpheniramine), cohesive (acetaminophen) and slightly cohesive (caffeine), using particle size, bulk density and compressibility measurements. The *in situ* NIR-CI technique was able to measure the differences in micro-mixing dynamics caused by the material properties of the APIs throughout the blending process.

This NIR-CI technique was used to calculate the concentration maps of all components in the blends. Typical analysis such as concentration averages and relative standard deviation trends were characterized. In addition, the aggregate statistics - the mean and maximum aggregate sizes - calculated from each image described the mixing profiles as aggregate size changes occurred throughout the blending. The maximum aggregate size is a good metric to detect residual aggregates that might cause issues in a final blend, especially when these aggregates are from the active ingredient. Overall, the number of particles within an aggregate decreased with increasing concentration. This means that higher concentrations of APIs disperse and mix much more efficiently than APIs at lower concentrations. This phenomenon known as agglomeration was proven using this technique and it was stronger for the most cohesive API (chlorpheniramine).

The comparison between the APIs showed that chlorpheniramine (most cohesive API) resulted in the highest RSD for all concentrations. For 3% API blends, caffeine (least cohesive API) presented the lowest RSD, followed by APAP. The RSD for APAP and caffeine were very similar for the 10% API blends. The APAP RSDs were lower than

caffeine RSDs for 30% API blends. Chlorpheniramine remained in large aggregates throughout the blending process. Overall, the most cohesive API, chlorpheniramine, required a longer blending time (number of rotations) for the other ingredients (e.g. Avicel) to become well dispersed, as evidenced by the aggregate size measurements. The effect of cohesion on the micro-mixing state of blends as measured by NIR-CI was demonstrated here. The most cohesive API followed the expected trends (i.e. higher RSDs and larger aggregate sizes) while the trends for APAP and caffeine were dependent on their concentrations.

The NIR-CI technique introduced here can be used with high-shear blenders or larger size blenders that are closer to actual production batch sizes. In addition to being used in batch blending, this technology can be used to monitoring the performance of continuous mixing as well as different phases of continuous solid pharmaceutical manufacturing.

Chapter 8 Conclusions and Recommendations for Future Work

8.1 Conclusions

The primary objective of this thesis was to characterize the macro- and micro-mixing behavior of a newly developed blender (the resonant acoustic mixer - RAM) as well as the micro-mixing behavior of several APIs in one of the most common blending processes, bin-blending. All of the work presented here involved the study of cohesive active pharmaceutical ingredients (APIs) in lubricated blends. Although this work was focused on pharmaceutical processing, the methods are general and apply to other powder-based industries as well.

No work on the RAM had been reported in previous peer-reviewed literature. Overall, blend uniformity of acetaminophen (APAP) and magnesium stearate (MgSt), as measured by the relative standard deviation (RSD), significantly decreased with increasing mixing time and acceleration. It was found that up to one minute of mixing time, acceleration had a significant effect on the APAP and MgSt blend uniformity. After two minutes of blending, acceleration no longer had a significant effect on the RSDs. Mixing performance was found to be independent of fill level, which is not the case in most other blender types (e.g. tumbling mixers or shear mixers). Typical mixing curves were obtained in the RAM, both as functions of mixing time and acceleration. The effect of total energy to the blend per unit mass on the blend uniformity was also studied. A negative power law trend was obtained. It is recommended that the energy to the blend per unit mass to be used as the input parameter to predict and control the blend uniformity in the RAM.

Overall, resonant acoustic mixing was able to blend APAP and MgSt efficiently. Care must be taken when blending MgSt in the RAM since blend over-lubrication was obtained when mixing at higher accelerations (> 40 g's) and longer blending times (> 1 minute). It is also recommended to use low concentrations of MgSt, < 1 % w/w, in this mixer. The RAM was able to blend a moderately cohesive API, semi-fine APAP, although fluctuations in the RSD results might indicate agglomeration for some mixing parameters.

The effects of acceleration, blending time and total energy dissipated per unit mass on the blend material properties and tablet characteristics were assessed. The average temperature of the powder bed in the blends significantly increased with increasing acceleration and blending time. The particle size, the bulk density, the tapped density and the compressibility were considered as the blend material properties. The tableting compression force, tablet hardness, weight and dissolution were considered as the tableting and tablet characteristics. Overall, powder blend material properties and tablet characteristics were affected by changes in blending parameters during resonant acoustic mixing.

The particle size significantly changed due to acceleration and blending time. An increase in the d_{10} fraction was found with increasing acceleration and blending time. The same trend was also observed for bulk density and tapped density of the powder blends. The compressibility of the powder blends decreased with increasing blending time. These differences can be attributed to the effect of shear and strain during the rapid movement of the particles caused by the high input energy going to the blend during resonant acoustic mixing. An improvement in flowability of the blend was obtained with an

increase in acceleration and blending time. Owing to higher shear and shearing intensity, an increase in blend hydrophobicity was observed with increases in acceleration and mixing time.

The increase in hydrophobicity is known to indicate overlubrication, which accounted for a subsequent decrease in tablet hardness. At constant fill volume and tablet thickness, the tableting compression force and tablet weight significantly increased with increasing acceleration and blending time. These results were caused by the higher blend density obtained. The dissolution of the tablets indicated some interesting results. At lower accelerations and a mixing time of 0.5 minutes, large variations in the amount of drug dissolved were observed. Variability decreased and the amount of drug dissolved reached the nominal blend concentration at higher accelerations at the same mixing time. However, for blending times of one minute or greater, the amount and rate of drug dissolved was found to decrease with increasing acceleration.

Increases in acceleration and blending time increased the density of the powder blends. However, they also increased the blend hydrophobicity, which lowers the tablet hardness and dissolution. Hence, optimum blending parameters depend on the formulation requirements. A mixing time of one to two minutes at 40 g's of acceleration fulfilled the criteria for good blend homogeneity and tablet content uniformity as well as desirable hardness and dissolution performance. All the material properties of the blend and the tableting and tablet properties were also correlated to the total energy per unit mass dissipated into the blend. All measured properties, except hydrophobicity, yielded a power law when correlated to the energy per unit mass.

Resonant acoustic mixing significantly reduces blending time, making it a good candidate for improving the efficiency of powder mixing processes, especially during product development. The total energy dissipated per unit mass should be used as the input and control variable in resonant acoustic mixing. Prediction of powder blend flow properties and lubrication, tableting and tablet properties are possible by using the total amount of energy per unit mass.

The micro-mixing state of powder blends generated in a resonant acoustic mixer was also studied using near-infrared chemical imaging. Both qualitative (chemical images) and quantitative analyses (e.g. mean API aggregate area) were considered. First, a preliminary study was used to characterize the feasibility of using this technique to measure the aggregation of a cohesive API (APAP) and lubricant (MgSt). The second set of conditions studied was used to determine the main effects of resonant acoustic mixing, including acceleration and total blending time, on the aggregation of the API and lubricant. It was found that APAP showed less aggregation (higher dispersion) at higher accelerations and longer blending times. These results were in accordance with the mixing performance characterization of the RAM. The RAM was shown to efficiently reduce API aggregation, which is commonly done through milling after blending. It was also shown that MgSt was well dispersed (no evident aggregates) throughout the blend for all the conditions explored.

In this thesis, in addition to the comprehensive characterization of resonant acoustic mixing, a new *in situ* near-infrared chemical imaging (NIR-CI) technique, imMix™, designed to characterize micro-mixing in pharmaceutical powder blends, was also introduced. This technique used non-contact monitoring of the blending process in a bin-

blender, eliminating the bias introduced when using typical extractive sampling techniques. The spectral data was analyzed using the Science-Based Calibration (SBC) method to obtain concentration images of the ingredients in nine different blends. Each image allowed the estimation of the size of agglomerates and was used as a visual tool to help determine a suitable mixing time when all the components have formed a well-mixed blend. The mean concentration and RSD as a function of blending time were obtained from all images to further characterize the blending process. The time required for a blend to reach the nominal composition of the main excipients (Avicel and lactose) increased with the increase in APAP concentration. It was concluded that the rotation rate, using a 1-liter bin-blender, did not have an impact on the RSD, but the number of revolutions affected the blend homogeneity (RSD) of the main components.

Statistical analysis of each image was used to obtain detailed information about the blending progression of each of the components in the blends. The number of pixels above a predetermined concentration threshold and the fraction of pixels within a specified range of the nominal composition were used to characterize the blending progression. The fraction of pixels within the threshold was independent of APAP concentration. The fraction of pixels both within the threshold and above the threshold indicated that Avicel blended at a significantly slower rate than lactose. Avicel blended in fewer revolutions when the concentration of APAP was lower. The mean aggregate size statistics also supported the finding that Avicel blended at a slower rate than lactose. The maximum aggregate size analysis of the near-infrared chemical images provided a sensitive tool to detect aggregates of low-dose active materials that could pose a hazard if they remained unblended. Large APAP aggregates were detected in some blends even at

later rotations. This was an indication that APAP was still present in the blend in the form of agglomerates.

Using the same NIR-CI technique, the effects of material properties of cohesive APIs on the micro-mixing in a bin-blending process were studied. The APIs were characterized as very cohesive (chlorpheniramine), cohesive (acetaminophen) and slightly cohesive (caffeine) using particle size, bulk density and compressibility measurements. The *in situ* NIR-CI technique was able to measure the differences in micro-mixing dynamics caused by the material properties of the APIs throughout the blending process.

The NIR-CI technique was used to calculate the concentration maps of all components in the blends. Typical analysis such as concentration averages and relative standard deviation trends were characterized. In addition, the aggregate statistics, the mean and maximum aggregate sizes, calculated from each image described the mixing profiles as aggregate size changes occurred throughout the blending process. The maximum aggregate size is a good metric to detect residual aggregates that might cause issues in a final blend, especially when these aggregates are from the active ingredient.

The comparison between the APIs showed that chlorpheniramine (most cohesive) resulted in the highest RSD for all concentrations. For 3% API blends, caffeine (least cohesive) presented the lowest RSDs, followed by APAP. The RSDs for APAP and caffeine were very similar for 10% API blends. The APAP RSDs were lower than caffeine RSDs for 30% API blends. Chlorpheniramine remained in large aggregates throughout the blending process. Overall, blends with the most cohesive API, chlorpheniramine, required a longer blending time (number of rotations) for the other ingredients (Avicel and lactose) to become well dispersed, as evidenced by the aggregate

size measurements. The effect of cohesion on the micro-mixing state of blends as measured by NIR-CI was demonstrated here. The most cohesive API followed the expected trends (e.g. higher RSDs and larger aggregate sizes) while the trends for APAP and caffeine were dependent on their concentrations. The phenomenon known as agglomeration was proven using this technique and it was stronger for the most cohesive API (chlorpheniramine) at lower concentrations.

The micro-mixing characterization of both the RAM and bin-blending processes has expanded the knowledge and understanding of powder mixing. The micro-mixing state of powder blends is important and should be characterized in all powder mixing processes, especially during formulation and process development. NIR-CI was capable of characterizing the effects of blending parameters and material properties on the micro-mixing state of blends. It was also used to quantify the differences in macro- and micro-mixing dynamics caused by cohesive APIs, differing slightly in cohesion. This technique can further assist in the design, development and scale-up of industrial powder mixing processes.

In conclusion, this dissertation introduced the characterization of a resonant acoustic mixer. The macro-mixing, mixing curves, and the micro-mixing (e.g. API aggregation) were characterized as a function of blending parameters (acceleration, fill volume, and blending time). The effects of resonant acoustic mixing on powder blends and tablets properties were also characterized. This was the first time that any work on the RAM was reported. The RAM has the potential to mix small amounts of low concentration of cohesive APIs, which is a challenging task during product development. The amount of total energy to the blend per unit mass can be accurately calculated for the RAM. It was

found that this metric can be efficiently used to predict and control mixing performance in the RAM as well as powder blend material properties and tablet characteristics from blends produced in the RAM. In addition, a new *in situ* near-infrared chemical imaging technique was introduced and used to characterize the micro-mixing in a bin-blending process. The technique was able to differentiate the mixing dynamics from cohesive APIs. This technique has the potential to be used for scale-up purposes and should be considered as a PAT tool in powder mixing processes.

8.2 Recommendations for Future Work

Development of scale-up principles for resonant acoustic mixing – The hypothesis is that there should be a direct scale-up correlation if the same energy per unit mass is achieved in different sizes of resonant acoustic mixers. Work to prove this hypothesis would require further studies on the LabRAM, the RAM5, and the RAM55. The RAM5 is a 5-gallon resonant acoustic mixer, while the RAM55 is a 55-gallon resonant acoustic mixer. If successful scale-up correlations were obtained, this would be the very first time that such principles would be proven for a powder mixing process. Scale-up correlations would be based on the mixing performance, the material properties of blends and the final tablet properties.

Optimization of lubricant used in pharmaceutical powder blends – Lubrication, with the most common lubricant being magnesium stearate, is an everyday process in the pharmaceutical industry. Therefore, the optimization of the lubrication process as a function of lubricant concentration and total energy input in the blender is of great interest. This would prevent possible issues such as overlubrication of the blend, leading

to out-of-specification dissolution rates as well as low tablet hardness. Since only one concentration of MgSt (1% w/w) was used in the work in this dissertation, the powder blend and tablet properties should be studied as a function of lubricant concentration with variations in energy input. The hypothesis here is that the amount of MgSt used could be minimized while the amount of lubrication in the RAM could be controlled by adjusting the total energy input per unit mass.

Numerical modeling of resonant acoustic mixing - Experimental studies are limited by the capabilities of the analytical techniques; therefore, numerical modeling should be used to further understand resonant acoustic mixing. Such investigations should be performed using Discrete Element Method, which is a well-established numerical technique to study particle systems [120]. These simulations will allow the understanding of the particle-to-particle interactions, particle positions, trajectories, velocities and accelerations, as well as bulk flow behavior including shear rates, stress and strain histories in the RAM.

Use of resonant acoustic mixing for continuous powder blending - The use of resonant acoustic mixing for continuous processing is an option that is being explored by Resodyn [121]. Therefore, the conversion of the LabRAM technology for continuous processing should be considered. Integration of the LabRAM technology for a low throughput (< 5 kg/hr) continuous direct compression line ("micro-line") should be explored. The hypothesis here is that the energy dissipation and residence time could be controlled, yielding better quality in final blends and products.

Integration of *in situ* near-infrared chemical imaging as a PAT tool – The integration of *in situ* near-infrared chemical imaging (NIR-CI) for both batch and continuous

processing should be explored. Going forward, this NIR-CI technique can be used with high-shear blenders or larger sized blenders that are closer to actual production batch sizes. In addition to being used in batch blending, this technology can be used to monitor the performance of continuous mixing as well as different phases of continuous solid pharmaceutical manufacturing. In batch processing, the micro-mixing properties obtained could be used to develop more rigorous scale-up criteria. NIR-CI should be considered as a PAT tool since it can measure both the micro-mixing and macro-mixing properties of powder blends.

REFERENCES

1. J. Duran, *Sands, Powders, and Grains: An Introduction to the Physics of Granular Materials*2000, New York: Springer.
2. Muzzio, F.J., et al., *Evaluating the mixing performance of a ribbon blender.* Powder Tech., 2008. **186**: p. 247-254.
3. Mehrotra, A. and F.J. Muzzio, *Comparing mixing performance of uniaxial and biaxial bin blenders.* Powder Tech., 2009. **196**: p. 1-7.
4. Muzzio, F.J., et al., *Sampling practices in powder blending.* Int. J. Pharm., 1997. **155**: p. 153-178.
5. Beer, T.D., et al., *Near infrared and Raman spectroscopy for the in-process monitoring of pharmaceutical production processes.* Int. J. Pharm., 2011. **417**: p. 32-47.
6. Karande, A.D., P.W.S. Heng, and C.V. Liew, *In-line quantification of micronized drug and excipients in tablets by near infrared (NIR) spectroscopy: Real time monitoring of tabletting process.* International Journal of Pharmaceutics, 2010. **396**(1–2): p. 63-74.
7. Forterre, Y.a.O.P., *Flows of dense granular media.* Annual Review of Fluid Mechanics, 2008. **40**: p. 1-24.
8. Rietema, K., *Powders, what are they?* Powder Tech., 1984. **37**(1): p. 5-23.
9. Muzzio, F.J., et al., *Solids Mixing*, in *Handbook of Industrial Mixing - Science and Practice*, E.L. Paul, V.A. Atiemo-Obeng, and S.M. Kresta, Editors. 2003, John Wiley & Sons Inc. p. 887-985.
10. Mendez, A.S.L., G.d. Carli, and C.V. Garcia, *Evaluation of powder mixing operation during batch production: Application to operational qualification procedure in the pharmaceutical industry.* Powder Tech., 2010. **198**: p. 310-313.
11. Muzzio, F.J., T. Shinbrot, and B.J. Glasser, *Powder technology in the pharmaceutical industry: the need to catch up fast.* Powder Tech., 2002. **124**: p. 1-7.
12. Kale, K., K. Hapgood, and P. Stewart, *Drug agglomeration and dissolution – What is the influence of powder mixing?* European Journal of Pharmaceutics and Biopharmaceutics, 2009. **72**(1): p. 156-164.
13. Siraj, M.S., et al., *Effect of blade angle and particle size on powder mixing performance in a rectangular box.* Powder Tech., 2011. **211**: p. 100-113.
14. Hogg, R., *Mixing and Segregation in Powders: Evaluation, Mechanisms and Processes.* KONA Powder and Particle J., 2009. **27**: p. 3-17.
15. Vasilenko, A., B.J. Glasser, and F.J. Muzzio, *Shear and flow behavior of pharmaceutical blends - Method comparison study.* Powder Tech., 2011. **208**: p. 628-636.

16. Llusa, M., et al., *Measuring the hydrophobicity of lubricated blends of pharmaceutical excipients.* Powder Tech., 2010. **198**: p. 101-107.

17. Pingali, K.C., et al., *An observed correlation between flow and electrical properties of pharmaceutical blends.* Powder Tech., 2009. **192**: p. 157-165.

18. Sudah, O.S., D. Coffin-Beach, and F.J. Muzzio, *Quantitative characterization of mixing of free-flowing granular material in tote (bin)-blenders.* Powder Technology, 2002. **126**(2): p. 191-200.

19. Alexander, A., F.J. Muzzio, and T. Shinbrot, *Segregation patterns in V-blenders.* Chemical Engineering Science, 2003. **58**(2): p. 487-496.

20. Alexander, A., et al., *V-blender segregation patterns for free-flowing materials: effects of blender capacity and fill level.* International Journal of Pharmaceutics, 2004. **269**(1): p. 19-28.

21. Brone, D. and F.J. Muzzio, *Size segregation in vibrated granular systems: A reversible process.* Physical Review E, 1997. **56**: p. 1059-1063.

22. Brone, D. and F.J. Muzzio, *Enhanced mixing in double-cone blenders.* Powder Tech., 2000. **110**: p. 179-189.

23. Brone, D., et al., *Using flow perturbations to enhance mixing of dry powders in V-blenders.* Powder Technology, 1997. **91**(3): p. 165-172.

24. Arratia, P.E., et al., *Characterizing mixing and lubrication in the Bohle Bin blender.* Powder Technology, 2006. **161**(3): p. 202-208.

25. Chaudhuri, B., et al., *Cohesive effects in powder mixing in a tumbling blender.* Powder Tech., 2006. **165**: p. 105-114.

26. Hardy, E.H., J. Hoferer, and G. Kasper, *The mixing state of fine powders measured by magnetic resonance imaging.* Powder Tech., 2007. **177**: p. 12-22.

27. Perrault, M., F. Bertrand, and J. Chaouki, *An investigation of magnesium stearate mixing in a V-blender through gamma-ray detection.* Powder Tech., 2010. **200**: p. 234-245.

28. Li, W., et al., *Measurement of drug agglomerates in powder blending simulation samples by near infrared chemical imaging.* Inter. J. Pharm., 2007. **350**: p. 369-3873.

29. Ma, H. and C.A. Anderson, *Characterization of Pharmaceutical Powder Blends by NIR Chemical Imaging.* J. Pharm. Sci., 2008. **97**: p. 3305-3320.

30. Massol-Chaudeur, S., H. Berthiaux, and J.A. Dodds, *Experimental study of the mixing kinetics of binary pharmaceutical powder mixtures in a laboratory hoop mixer.* Chem. Eng. Science, 2002. **57**: p. 4053-4065.

31. Lemieux, M., et al., *Comparative study of the mixing of free-flowing particles in a V-blender and a bin-blender.* Chemical Engineering Science, 2007. **62**(6): p. 1783-1802.

32. Chester, A.W., et al., *Mixing dynamics in catalyst impregnation in double-cone blenders.* Powder Technology, 1999. **102**(1): p. 85-94.

33. Masiuk, S., *Power consumption, mixing time and attrition action for solid mixing in a ribbon mixer.* Powder Technology, 1987. **51**(3): p. 217-229.

34. Zainuddin, I.M., et al., *Experimental Study on Powder Flowability Using Vibration Shear Tube Method.* Particle & Particle Systems Characterization, 2012. **29**(1): p. 8-15.

35. Yuksel, N., et al., *Lubricant Efficiency of Magnesium Stearate in Direct Compressible Powder Mixtures Comprising Cellactose® 80 and Pyridoxine Hydrochloride.* J. of Pharm. Sci., 2007. **32**: p. 173-183.

36. Pingali, K., et al., *Mixing order of glidant and lubricant – Influence on powder and tablet properties.* Inter. J. Pharm., 2011. **409**: p. 269-277.

37. Mixer, R.A. *ResonantAcoustic® Mixing*. 2009 [cited 2012 October 4, 2012]; Available from: http://www.resodynmixers.com/wp-content/uploads/2009/05/ram-technical-white-paper1.pdf.

38. Lacey, P.M.C., *Developments in the Theory of Particle Mixing.* J. App. Chem., 1954. **4**: p. 257-268.

39. Kalman, H. and G.I. Tardos, Part. Sci. Technol., 2005. **23**: p. 1–19.

40. Alonso, M. and F.J. Alguacil, *Dry mixing and coating of powders.* Rev. Metal., 1999. **35**: p. 315-328.

41. Crosby, T., *Designing for the future of continuous processing.* PharmPro, 2006. **2006**(January).

42. Kumar, A., et al., *Model-based analysis of high shear wet granulation from batch to continuous processes in pharmaceutical production – A critical review.* European Journal of Pharmaceutics and Biopharmaceutics, (0).

43. FDA, *Code of Federal Regulations Part 21 Section 210*, 1978, Government Printing Office: Washington, DC.

44. FDA, *Code of Federal Regulations Part 21 Section 211*, 1978, Government Printing Office: Washington, DC.

45. Faure, A., P. York, and R.C. Rowe, *Process control and scale-up of pharmaceutical wet granulation processes: a review.* European Journal of Pharmaceutics and Biopharmaceutics, 2001. **52**(3): p. 269-277.

46. *Pharmaceutical Dosage Forms: Tablets*. Second ed. Vol. 1. 1989, New York: Marcel Dekker, Inc.

47. Mehrotra, A., et al., *Influence of shear intensity and total shear on properties of blends and tablets of lactose and cellulose lubricated with magnesium stearate.* Inter. J. Pharm., 2006. **336**: p. 284-291.

48. *Handbook of Pharmaceutical Granulation Technology*. Drugs and Pharmaceutical Sciences, ed. J. Swarbrick. Vol. 81. 1997, New York: Marcel Dekker, Inc.

49. Moreyra, R. and M. Peleg, *Physical properties of food powders.* Revista Agr. y Tecol. Alim. , 1980. **21**: p. 322- 329.

50. Sandler, N., et al., *Effect of Moisture on Powder Flow Properties of Theophylline.* Pharmaceutics, 2010. **2**(3): p. 275-290.

51. Porion, P., et al., *Dynamics of size segregation and mixing of granular materials in a 3D-blender by NMR imaging investigation.* Powder Technology, 2004. **141**(1–2): p. 55-68.

52. Ehrhardt, N., et al., *Assessing the homogeneity of powder mixtures by on-line electrical capacitance.* Chem. Eng. and Proc., 2005. **44**: p. 303-313.

53. FDA. *FDA Guidance for Industry - Powder Blends and Finished Dosage Units - Stratified Sampling In-Process Dosage Unit Sampling and Assessment*. 2003 [cited 2013 13 June]; Available from: http://www.fda.gov/cder/guidance/index.htm.

54. Gao, Y., M. Ierapetritou, and F. Muzzio, *Determination of the Confidence Interval of the Relative Standard Deviation Using Convolution.* Journal of Pharmaceutical Innovation, 2013. **8**(2): p. 72-82.

55. Lionberger, R., et al., *Quality by Design: Concepts for ANDAs.* The AAPS Journal, 2008. **10**(2): p. 268-276.

56. FDA, *Guidance for Industry Q8 (R2) Pharmaceutical Development*, FDA, Editor 2009.

57. *Guidance for Industry Quality Systems Approach to Pharmaceutical CGMP Regulations*. September 2006 [cited 2012 October 3, 2012]; Available from: http://www.fda.gov/downloads/Drugs/.../Guidances/UCM070337.pdf.

58. FDA, *Guidance for Industry: PAT — A Framework for Innovative Pharmaceutical Development, Manufacturing, and Quality Assurance.* 2004.

59. Wightman, C. and F.J. Muzzio, *Mixing of granular material in a drum mixer undergoing rotational and rocking motions - I. Uniform particles.* Powder Tech., 1998. **98**: p. 113-124.

60. Sudah, O.S., D. Coffin-Beach, and F.J. Muzzio, *Effects of blender rotational speed and discharge on the homogeneity of cohesive and free-flowing mixtures.* International Journal of Pharmaceutics, 2002. **247**(1–2): p. 57-68.

61. Perrault, M., F. Bertrand, and J. Chaouki, *An investigation of magnesium stearate mixing in a V-blender through gamma-ray detection.* Powder Technology, 2010. **200**(3): p. 234-245.

62. Danckwerts, P.V., *The definition and measurement of some characteristics of mixtures.* Appl. Sci. Res., 1952. **3**: p. 279-296.

63. Palzer, S., *Agglomeration of pharmaceutical, detergent, chemical and food powders — Similarities and differences of materials and processes.* Powder Technology, 2011. **206**(1–2): p. 2-17.

64. Daumann, B., et al., *Determination of the mixing time in a discontinuous powder mixer by using image analysis.* Chem. Eng. Sci., 2009. **64**: p. 2320-2331.

65. Realpe, A. and C. Velazquez, *Image processing and analysis for determination of concentrations of powder mixtures.* Powder Tech., 2003. **134**: p. 193-200.

66. Boschetto, A. and V. Giordano, *Powder sampling and characterization by digital image analysis.* Measurement, 2012. **45**(5): p. 1023-1038.

67. Daumann, B. and H. Nirschl, *Assessment of the mixing efficiency of solid mixtures by means of image analysis.* Powder Technology, 2008. **182**(3): p. 415-423.

68. Sommier, N., et al., *Magnetic resonance imaging investigation of the mixing-segregation process in a pharmaceutical blender.* Int. J. Pharm., 2001. **222**: p. 243-258.

69. Reich, G., *Near-infrared spectroscopy and imaging: Basic principles and pharmaceutical applications.* Adv. Drug Del. Reviews, 2005. **57**: p. 1109-1143.

70. Krämer, K. and S. Ebel, *Application of NIR reflectance spectroscopy for the identification of pharmaceutical excipients.* Analytica Chimica Acta, 2000. **420**(2): p. 155-161.

71. Porfire, A., et al., *High-throughput NIR-chemometric methods for determination of drug content and pharmaceutical properties of indapamide powder blends for tabletting.* Journal of Pharmaceutical and Biomedical Analysis, 2012. **70**(0): p. 301-309.

72. Ravn, C., E. Skibsted, and R. Bro, *Near-infrared chemical imaging (NIR-CI) on pharmaceutical solid dosage forms—Comparing common calibration approaches.* Journal of Pharmaceutical and Biomedical Analysis, 2008. **48**(3): p. 554-561.

73. Offroy, M., Y. Roggo, and L. Duponchel, *Increasing the spatial resolution of near infrared chemical images (NIR-CI): The super-resolution paradigm applied to pharmaceutical products.* Chemometrics and Intelligent Laboratory Systems, 2012. **117**(0): p. 183-188.

74. Gendrin, C., Y. Roggo, and C. Collet, *Content uniformity of pharmaceutical solid dosage forms by near infrared hyperspectral imaging: A feasibility study.* Talanta, 2007. **73**(4): p. 733-741.

75. El-Hagrasy, A.S., et al., *Near-Infrared Spectroscopy and Imaging for the Monitoring of Powder Blend Homogeneity.* J. Pharm. Sci., 2001. **90**: p. 1298-1307.

76. Šaŝić, S., A. Kong, and G. Kaul, *Determining API domain sizes in pharmaceutical tablets and blends upon varying milling conditions by near-infrared chemical imaging.* Anal. Methods, 2013. **5**: p. 2360-2368.

77. Lyon, R.C., et al., *Near-Infrared Spectral Imaging for Quality Assurance of Pharmaceutical Products: Analysis of Tablets to Assess Powder Blend Homogeneity.* AAPS PharmSciTech., 2002. **3**(3): p. 1-15.

78. Cruz, J., et al., *Nir-chemical imaging study of acetylsalicylic acid in commercial tablets.* Talanta, 2009. **80**(2): p. 473-478.

79. Cruz, J. and M. Blanco, *Content uniformity studies in tablets by NIR-CI.* Journal of Pharmaceutical and Biomedical Analysis, 2011. **56**(2): p. 408-412.

80. Awa, K., et al., *Self-modeling curve resolution (SMCR) analysis of near-infrared (NIR) imaging data of pharmaceutical tablets.* Analytica Chimica Acta, 2008. **619**(1): p. 81-86.

81. Sabin, G.P., et al., *Analysis of pharmaceutical pellets: An approach using near-infrared chemical imaging.* Anal. Chim. Acta, 2011. **706**: p. 113-119.

82. Rozo, J.I.J., et al., *Complementary Near-Infrared and Raman Chemical Imaging of Pharmaceutical Thin Films.* J. Pharm. Sci., 2011. **100**: p. 4888-4895.

83. Jaeger, H.M. and S.R. Nagel, *PHYSICS OF THE GRANULAR STATE.* Science, 1992. **255**(5051): p. 1523-1531.

84. Rietema, K., *Powders, what are they?* Powder Technology, 1984. **37**(1): p. 5-23.

85. Bridsona, R.H., et al., *The effects of high shear blending on α-lactose monohydrate.* Int. J. Pharm., 2007. **339**: p. 84-90.

86. Ridgway, K. and R. Rupp, *The effect of particle shape on powder properties.* Journal of Pharmacy and Pharmacology, 1969. **21**(S1): p. 30S-39S.

87. Fernandes, C.M., A.M.R. Senos, and M.T. Vieira, *Particle surface properties of stainless steel-coated tungsten carbide powders.* Powder Technology, 2006. **164**(3): p. 124-129.

88. Akapo, S., et al., *A novel method for determining the particle density of porous aeratable powders.* Powder Technology, 1989. **58**(4): p. 237-242.

89. Boschung, P. and M. Glor, *Methods for investigating the electrostatic behaviour of powders.* Journal of Electrostatics, 1980. **8**(2–3): p. 205-219.

90. Mendez, R., F.J. Muzzio, and C. Velazquez, *Powder hydrophobicity and flow properties: Effect of feed frame design and operating parameters.* AIChE Journal, 2012. **58**(3): p. 697-706.

91. Pingali, K., et al., *Evaluation of strain-induced hydrophobicity of pharmaceutical blends and its effect on drug release rate under multiple compression conditions.* Drug Dev. and Ind. Pharm., 2011. **37**: p. 428-435.

92. Carr, R.L., *Evaluating flow properties of solids.* Chem. Eng., 1965. **72**: p. 163-168.

93. Zhou, Y.C., et al., *An experimental and numerical study of the angle of repose of coarse spheres.* Powder Technology, 2002. **125**(1): p. 45-54.

94. Podczeck, F. and Y. Mia, *The influence of particle size and shape on the angle of internal friction and the flow factor of unlubricated and lubricated powders.* International Journal of Pharmaceutics, 1996. **144**(2): p. 187-194.

95. Vasilenko, A., B.J. Glasser, and F.J. Muzzio, *Density Effects in Characterization of Unconfined Flow Behavior* 2012, Rutgers University.

96. Vasilenko, A., B.J. Glasser, and F.J. Muzzio, *Shear and flow behavior of pharmaceutical blends — Method comparison study.* Powder Technology, 2011. **208**(3): p. 628-636.

97. Vasilenko, A., et al., *Role of consolidation state in the measurement of bulk density and cohesion.* Powder Technology, 2013. **239**(0): p. 366-373.

98. Fassihi, A.K. and I. Kanfer, *Effect of compressibility and powder flow properties on tablet weight variation.* Drug Dev. and Ind. Pharm., 1986. **12**: p. 1947-1966.

99. Osorio, J.G. and F.J. Muzzio, *Effects of powder flow properties on capsule filling weight uniformity.* Drug Dev. and Ind. Pharm., 2013. **39**: p. 1464-1475.

100. Freeman, T., et al., *Capsule filling performance of powdered formulations in relation to flow characteristics*, in *Particulate Materials: Synthesis, Characterisation, Processing and Modelling*, C.-Y. Wu and W. Ge, Editors. 2011, Royal Society of Chemistry. p. 131-136.

101. Andrews, G.P., *Advances in solid dosage form manufacturing technology.* Phil. Trans. R. Soc. A, 2007. **365**: p. 2935-2949.

102. Hersey, J.A., *Problems of powder flow in tabletting processes.* Rheologica Acta, 1965. **4**(3): p. 235-239.

103. Figueroa, I., H. Li, and J. McCarthy, *Predicting the impact of adhesive forces on particle mixing and segregation.* Powder Technology, 2009. **195**(3): p. 203-212.

104. Laurent, B.F.C. and J. Bridgwater, *Convection and segregation in a horizontal mixer.* Powder Tech., 2002. **123**: p. 9-18.

105. Miller, J.T., A.L.S. Coguill, and P. Lucon. *Mix Power*. in *2013 Resodyn Forum: Industrial Outcomes in ResonantAcoustic® Mixing*. 2013. Butte, Montana.

106. Xu, H., *A Catalogue of Three-Level Fractional Factorial Designs.* Mathematics Subject Classifications, 2004. **2000**: p. 1-25.

107. Osorio, J.G. and M. F.J., *Evaluation of Resonant Acoustic Mixing Performance.* To be submitted, 2013.

108. *ASTM E2503 - 13 "Standard Practice for Qualification of Basket and Paddle Dissolution Apparatus," ASTM International* 2013 [cited 2013 May 28, 2013]; Available from: www.astm.org.

109. Muzzio, F.J., et al., *Sampling and characterization of pharmaceutical powders and granular blends.* Int. J. Pharm., 2003. **250**(1): p. 51-64.

110. Susana, L., P. Canu, and A.C. Santomaso, *Development and characterization of a new thief sampling device for cohesive powders.* Int. J. Pharm., 2011. **416**: p. 260-267.

111. Venables, H.J. and J.I. Wells, *Powder Sampling.* Drug Dev. and Ind. Pharm., 2002. **28**: p. 107-117.

112. Marbach, R. *Multivariate Calibration: Science-Based Method - Part 1*. 2007.

113. Marbach, R. *Multivariate Calibration: A science-Based Method - Part 2*. 2007.

114. Hyvärinen, T., E. Herrala, and J. Jussila. *High Speed Hyperspectral Chemical Imaging*. 2011 [cited 2012 September 3, 2012]; Available from: www.specim.fi.

115. Wu, H., et al., *Quality-by-Design (QbD): An integrated multivariate approach for the component quantification in powder blends.* International Journal of Pharmaceutics, 2009. **372**(1–2): p. 39-48.

116. Osorio, J.G., et al., *Characterization of In Situ Near-Infrared Imaging to Aid Pharmaceutical Powder Blend Formulation Development.* Chem. Eng. Sci., 2013. **Submitted**.

117. Technology, F. *FT4 Powder Rheometer System*. 2011 [cited 2012 March 20]; Available from: http://www.freemantech.co.uk/en/ft4-system/ft4-powder-rheometer.html.

118. Ashton, M.D., et al., *Some investigations into the strength and flow properties of powders.* Rheologica Acta, 1965. **4**(3): p. 206-218.

119. Fitzpatrick, J.J., S.A. Barringer, and T. Iqbal, *Flow property measurement of food powders and sensitivity of Jenike's hopper design methodology to the measured values.* Journal of Food Engineering, 2004. **61**(3): p. 399-405.

120. Bharadwaj, R., *Using DEM to solve bulk material handling problems*, in *Chemical Engineering Progress*2012, AIChE. p. 54-57.

121. Mixers, R.A. *Resodyn Announces Transformational Continuous Acoustic Reactor Technology*. 2013 [cited 2013 December 13]; Available from: http://www.resodynmixers.com/general/2013/resodyn-announces-transformational-continuous-acoustic-reactor-technology/.